

**CONTRAST ENHANCEMENT FOR DIFFUSE OPTICAL  
SPECTROSCOPY AND IMAGING: PHASE CANCELLATION  
AND TARGETED FLUORESCENCE IN CANCER DETECTION**

A Dissertation in Bioengineering

University of Pennsylvania

**Yu Chen**

**2003**

CONTRAST ENHANCEMENT FOR DIFFUSE OPTICAL  
SPECTROSCOPY AND IMAGING: PHASE CANCELLATION AND  
TARGETED FLUORESCENCE IN CANCER DETECTION

**Yu Chen**

A DISSERTATION

in

BIOENGINEERING

Presented to the Faculties of the University of Pennsylvania in Partial Fulfillment of  
the Requirements for the degree of Doctor of Philosophy

2003

---

**Britton Chance**

Supervisor of Dissertation

---

**Gershon Bushsbaum**

Graduate Group Chairperson

COPYRIGHT

Yu Chen

2003

## ABSTRACT

### CONTRAST ENHANCEMENT FOR DIFFUSE OPTICAL SPECTROSCOPY AND IMAGING: PHASE CANCELLATION AND TARGETED FLUORESCENCE IN CANCER DETECTION

Yu Chen

Britton Chance

Diffuse optical spectroscopy (DOS) and tomography (DOT) using Near-Infrared (NIR) light provide promising tools for non-invasive imaging and clinical diagnosis of deep tissue. These techniques are capable of quantitative reconstructions of tissue absorption and scattering properties, thus can map *in vivo* tissue oxygen saturation level and hemoglobin concentration. Potential clinical applications of DOS/DOT include functional neuro-imaging and tumor detection.

DOS and DOT target the contrasts from intrinsic tissue chromophores such as oxygenated and deoxygenated hemoglobin and extrinsic optical contrast agents such as Indocyanine Green (ICG). Fluorescence imaging also gives high sensitivity and specificity for biomedical diagnosis. Recent developments on specific-targeting fluorophores such as molecular beacons offer high contrast between normal and cancerous tissues, hence provide promising means for early tumor detection.

In this work, we study the contrast enhancement by applying the dual-interfering-source or so called phased array method. In-phase and out-of-phase sources generate an interference-like pattern, which cancels the background signals. The perturbation introduced by small objects allows for enhanced detection

sensitivity. A frequency-domain instrument has been developed to realize the absorption and fluorescence detection. We compare the detection sensitivity for single- and dual-source by signal to noise analysis and show that the dual-source method provides higher detection sensitivity. Also, two or three-dimensional localization of an absorptive or fluorescent object embedded in the turbid media is achieved by mechanical scanning of the phased array.

To account for the effects of the heterogeneous background and finite boundaries, we also developed an amplitude modulation phased array system with electro-optic sweeping of the cancellation plane. The ability of tumor detection is demonstrated by an *in vivo* mouse tumor model with the systematic administration of fluorescence contrast agent, NIRF-2DG, which targets the tumor hyper-metabolism. Using the mouse tumor model and matching fluid having similar optical properties as the human breast tissue, we further explore the relations between fluorophore concentration and the detection signal.

## ACKNOWLEDGEMENTS

My interest in Biomedical Optics dates back to 1995, when I was a physics undergrad at Peking University. At that time I was studying the Raman spectroscopy of hemoglobin under the guidance of Professor Shu-Lin Zhang and Biophysicist Kwok-To Yue (Ph.D., UIUC). In 1996, when I was considering future research directions for graduate study, I had a stimulating conversation with To's colleague and friend, Dr. Linda Powers. I still remember what she had emphasized: "you should pursue some frontier research". To her, "frontier" means Britton Chance.

I could not agree more. The six years I have spent with Brit has been an unforgettable life adventure. Brit is, in many aspects, a true legend. His numerous titles and awards range from Member of the National Academy of Science to Olympic Gold Medal winner in Sailing. It is under his guidance that I grow both intellectually and personally. I was educated in many fields including engineering and biology, and obtained a wider perspective in science and research. Brit's abundant knowledge exhilarates every discussion projecting new ideas and keeping the research in the direction of progress. Whenever help is needed, he is always accessible. I could not accomplish this thesis work without his advising. I also explored further professional activities including presenting at various meetings, helping to organize conferences, and writing research grants, owing to the opportunities created generously by my advisor. Besides the daily lab work, I really enjoyed the experience of sailing with the Olympic medallist and the exciting trip to China, which I was fortunate to spend with Brit. Also, I was proud of the endowment of Honorary Professorship to Dr. Chance by Peking University, my *Alma Mater*. In retrospect, I am deeply grateful to Brit's mentorship in the past years.

I would like to acknowledge the support and help from my thesis committee members. I should thank Dr. Arjun Yodh for his teaching through group seminars as well as the Optics and Laser Spectroscopy classes. His critical comments sharpened my thinking and presentation to become more concise and precise. I also thank Dr. John Schotland for his generous kindness to serve as the chair of my committee, and the valuable conversation about the career. I am grateful to Dr. Ed Pugh for sharing his keen insights into the medical research and to Dr. Hanli Liu for her help and efforts made for my thesis.

I also want to thank the faculty of the Bioengineering Department for providing the interdisciplinary education. Particular thanks to Dr. Gershon Bushsbaum, Graduate Group Chair, for his encouragement and assistance with the graduate affairs, and Dr. Leif Finkel for his kind help in my preliminary exam and scholarship application. Lisa Halterman and Jennifer Laverty have provided tremendous support on my course registration and other educational routine procedures.

I wish to thank all of my coworkers and collaborators during my thesis research. I should first thank previous Post-docs and Ph.D.s in BC's lab for sharing their valuable experience with me, including Dr. Nimmi Ramanujam, Dr. Xingde Li and Dr. Vasilis Ntziachristos. In particular, Dr. Xavier Intes has been a helpful colleague and friend in the past four years, for not only the many projects and manuscripts we worked on together, but the constant exchanging of ideas, excitements and encouragements through the ups and downs in the research. I should also thank Dr. Shoko Nioka for bringing me to the clinical experiments and the hospitality she has provided. I would like to thank Shuoming Zhou and Chenpeng Mu for their help in the electronics and instrumentations for my research. Other

engineering experts in BC's lab have provided numerous efforts of assistance, including Yunsong Yang, Bin Guan, Hongyan Ma, Xuhui Ma, Dr. Quan Zhang, Tao Tu, Dr. Yueqing Gu, Yuanqing Lin, Jiangsheng Yu, Pengcheng Li, Zhongyao Zhao, Jun Zhao, Qian Liu, Ping Huang, Barry John-Chuan, Cindy Wang, Theresa Mawn and Dr. Simon Wen. The experiments could not have been accomplished without the assistance of biology and clinic experts including Yutao Zhang, Qing Xu, Shuning Huang, Jun Zhang, Dana Blessington, Dr. Hui Li, David Nelson, Lanlan Zhou and Zhihong Zhang. Chilton Alter has been helpful in providing research necessities and volunteering as an experimental subject. I should also thank Dot Coleman for efficiency and reliability in almost all laboratory affairs, Casey Tan for help on the text revision and Mary Leonard for expert drawings which appear in this thesis and other papers. Mike Carmen and Bill Penney at the Instrument Shop have designed and constructed the perfect parts for the experiments.

I would like to extend my acknowledgement to the colleagues in Arjun's lab, including Dr. Joe Culver, Turgut Durduran, Regina Choe, Dr. Guoqiang Yu, Dr. Hsing-Wen Wang, Ulas Sunar and Chao Zhou for frequent intellectual and social interactions. Also I would like to thank Drs. Gang Zheng and Min Zhang in Penn Radiology for the glucose contrast agents and Dr. Endla Anday for her assistance in neonatal study. My fellow classmate Dharmesh Tailor has been very pivotal in bringing the MRI together with the optical methods.

I should also thank Professor Shu-Lin Zhang and Dr. Kwok-To Yue for preparing me with a solid physics background, and Dr. Linda Powers for prompting me to this exciting interdisciplinary research field.

Last but not least, I could not have accomplished the doctoral degree without the love and care from my dearest family members and relatives. I would never forget

my granduncle, Dr. Dai-Sun Chen (1900-1997; Ph.D., Harvard University; former Professor and Dean, School of Economics, Peking University) for his encouragement on pursuing the doctoral degree in the United States. I would like to thank my Mom and Dad for their love and support in my education. Most importantly, I wish to thank my wife and best friend, Ning, for her love, care, patience, understanding and encouragement. We share our future together.

## TABLE OF CONTENTS

<b>1</b>	<b>INTRODUCTION .....</b>	<b>1</b>
<b>2</b>	<b>OPTICAL METHOD IN BREAST CANCER DETECTION .....</b>	<b>4</b>
2.1	Introduction of Breast Cancer and Detection Modalities .....	4
2.2	Optical Method and Intrinsic Contrast .....	5
2.3	Extrinsic Contrast .....	7
2.3.1	<i>Non-specific Contrast Agents</i> .....	7
2.3.2	<i>Molecular Specific Contrast Agents</i> .....	8
<b>3</b>	<b>BASIC THEORY OF PHOTON MIGRATION .....</b>	<b>10</b>
3.1	Diffusion Approximation .....	11
3.2	Diffuse Photon Density Waves .....	12
3.3	Boundary Conditions .....	15
3.4	Solutions with Boundary .....	16
3.4.1	<i>Solutions in Semi-infinite Geometry</i> .....	17
3.4.2	<i>Solutions in Slab Geometry</i> .....	18
3.4.3	<i>Perturbation by Spherical Object</i> .....	19
3.5	Fluorescence Diffuse Photon Density Waves .....	19
<b>4</b>	<b>INTERFERENCE OF DIFFUSE PHOTON DENSITY WAVES .....</b>	<b>24</b>
4.1	Solution with Dual Interfering Sources .....	25
4.1.1	<i>Solutions in Infinite Homogeneous Media</i> .....	26
4.1.2	<i>Solutions in Semi-infinite Homogeneous Media</i> .....	26
4.1.3	<i>Perturbation from Small Heterogeneity</i> .....	29
4.2	Sensitivity Analysis for Single- and Dual-source Systems .....	32
4.2.1	<i>Noise Model for Single- and Dual-source Systems</i> .....	32
4.2.2	<i>Signal to Noise Analysis</i> .....	37
4.3	Detection Limit for Dual-source System .....	38
4.3.1	<i>Detection Limit for Absorptive Perturbation</i> .....	38
4.3.2	<i>Detection Limit for Fluorescence Perturbation</i> .....	44
4.4	Object Localization using Phased Array System .....	50
4.5	Optimization of Phased Array System .....	52
4.5.1	<i>Amplitude and Phase Control for Dual-source System</i> .....	53
4.5.2	<i>Frequency Dependency of Phased Array System</i> .....	54
4.5.3	<i>Geometric Arrangement</i> .....	56
<b>5</b>	<b>DIFFUSE OPTICAL SPECTROSCOPY AND TOMOGRAPHY .....</b>	<b>59</b>
5.1	Calculation of Optical Properties .....	62
5.1.1	<i>Frequency Domain Measurement</i> .....	62
5.1.2	<i>Continuous Wave Measurement</i> .....	64
5.2	Spectroscopic Analysis .....	66

5.2.1	<i>Calibration of Scattering Coefficients</i> .....	66
5.2.2	<i>Blood Volume and Oxygenation Saturation</i> .....	67
5.3	Approximation for Heterogeneous Media .....	69
5.3.1	<i>Absorption Heterogeneity</i> .....	69
5.3.2	<i>Scattering Heterogeneity</i> .....	71
5.4	Matrix Inversion .....	73
5.4.1	<i>Algebraic Reconstruction Techniques (ART)</i> .....	75
5.4.2	<i>Singular Value Decomposition (SVD)</i> .....	77
5.5	Fluorescence Diffuse Optical Tomography .....	79
5.5.1	<i>Normalized Born Approximation</i> .....	79
5.5.2	<i>Dual-source System</i> .....	80
<b>6</b>	<b>EXPERIMENTAL METHODS</b> .....	<b>82</b>
6.1	Hardware Basics .....	83
6.1.1	<i>Photon Detection – Photomultiplier Tube</i> .....	83
6.1.2	<i>Photon Detection – Photodiode</i> .....	85
6.1.3	<i>Light Source – Laser Diode</i> .....	85
6.1.4	<i>Phase Detection</i> .....	86
6.1.5	<i>Amplitude Modulation</i> .....	87
6.1.6	<i>Interference Filter</i> .....	89
6.2	Apparatus .....	91
6.2.1	<i>I &amp; Q Homodyne System</i> .....	92
6.2.2	<i>Phased Array Localization System</i> .....	94
6.2.3	<i>Fluorescent Phased Array Goniometry</i> .....	96
6.2.4	<i>Phased Array Tomographer and Topographer</i> .....	99
6.2.5	<i>Amplitude Cancellation System</i> .....	103
6.3	Fluorescent Contrast Agents Development .....	106
6.3.1	<i>Non-specific Fluorophores</i> .....	106
6.3.2	<i>Molecular Targeting Contrast Agents</i> .....	107
<b>7</b>	<b>EXPERIMENTAL RESULTS</b> .....	<b>110</b>
7.1	Adaptive Calibration for Phased Array Localizer .....	111
7.1.1	<i>Adaptive Calibration</i> .....	114
7.1.2	<i>Sensitivity Analysis</i> .....	119
7.1.3	<i>Three Cases</i> .....	121
7.1.4	<i>Discussion</i> .....	128
7.2	Tumor Localization with Phased Array Goniometry .....	130
7.2.1	<i>Phantom Studies</i> .....	130
7.2.2	<i>System Performance</i> .....	134
7.2.3	<i>Animal Model I – Intra-tumor Injection</i> .....	136
7.2.4	<i>Animal Model II – In Vivo Systematic Administration</i> .....	138
7.2.5	<i>Discussion</i> .....	142

7.3	Breast Cancer Detection with Amplitude Cancellation System .....	143
7.3.1	<i>Blood Model Experiments</i> .....	144
7.3.2	<i>Preliminary Human Studies</i> .....	146
7.4	Tomographic Image Reconstruction .....	148
7.4.1	<i>Imaging Absorptive Heterogeneity</i> .....	148
7.4.2	<i>Imaging Fluorescent Heterogeneity</i> .....	154
7.5	Rat Brain Oxygenation Correlated with BOLD MRI .....	155
7.5.1	<i>Experimental Protocol and Set-up</i> .....	156
7.5.2	<i>Near-Infrared (NIR) Spectroscopy Data</i> .....	157
7.5.3	<i>Correlation with MRI BOLD Signals</i> .....	161
7.6	Brain Mapping with Phased Array Topography .....	164
7.6.1	<i>Phantom Experiment</i> .....	167
7.6.2	<i>Functional Imaging for Neonate</i> .....	168
<b>8</b>	<b>SUMMARY AND PERSPECTIVE .....</b>	<b>174</b>
8.1	Image Fusion .....	175
8.2	Molecular Imaging .....	175
8.3	Future Prospects of Phased Array Imaging .....	176
<b>9</b>	<b>REFERENCES .....</b>	<b>178</b>

## LIST OF FIGURES

3-1	Three kinds of source functions .....	13
3-2	Extrapolated boundary condition .....	17
3-3	Amplitude and phase profiles for the DPDW .....	18
3-4	Jablonski diagram .....	20
4-1	Phased array configuration .....	28
4-2	Amplitude and phase profiles for the phased array DPDW .....	28
4-3	Vector diagram and perturbation analysis for dual-source signals .....	30
4-4	Phase measurement through zero-crossing time interval .....	34
4-5	Noise model for summation of two vectors .....	36
4-6	Transmission and remission geometry for single- and dual-interfering- source configurations .....	39
4-7	Contour plot of the signal-to-noise ratio equals to one for amplitude and phase signals in single- and dual-source configurations .....	41
4-8	Diameter of the smallest detectable absorber plotted as a function of $\mu_a^{\text{out}}$ and $\mu_a^{\text{in}}$ for single- and dual-source systems in transmission mode .....	42
4-9	Diameter of the smallest detectable absorber plotted as a function of $\mu_a^{\text{out}}$ and $\mu_a^{\text{in}}$ for single- and dual-source systems in remission mode .....	43
4-10	Geometrical set-up for the simulation .....	46
4-11	Contour plot of the fractional amplitude and phase difference for single source system and phased array system .....	47
4-12	Point-object functions (POF) for different object positions .....	51
4-13	Illustration of the back projection method for localization image .....	52
4-14	Amplitude and phase profile for varying the source strength ratio .....	53
4-15	Amplitude and phase responses for different modulation frequencies .....	54
4-16	Fractional amplitude and phase difference versus the sources modulation frequency .....	56
4-17	Dual-source phase shift sensitivity versus the separation between the two anti-phase sources .....	57
5-1	Spectra of oxygenated hemoglobin, deoxygenated hemoglobin and water .....	61
5-2	Illustration of the sensitivity matrix for one source-detector pair	

in DOT .....	74
5-3 Illustration of the projection method .....	76
6-1 Schematic of an I & Q demodulator .....	86
6-2 Amplitude modulation of RF waves .....	88
6-3 Illustration of amplitude modulated RF waves .....	88
6-4 The diagram of interference filter .....	90
6-5 Attenuation versus incident angle for the interference filter .....	91
6-6 Block diagram of the collimator for angle selection .....	91
6-7 Schematic of the frequency-domain homodyne system .....	93
6-8 Block diagram of the phased array localizer .....	95
6-9 Schematic of 50 MHz fluorescent phased array system .....	97
6-10 Photo of the 50 MHz phased array imaging system .....	98
6-11 Two-dimensional goniometric probe .....	99
6-12 Source-detector arrangement for phased array tomographer .....	100
6-13 System diagram for the single-wavelength phased array imager .....	101
6-14 System diagram of the dual-wavelength phased array imager .....	102
6-15 Schematic of dual-wavelength amplitude cancellation imaging system .....	104
6-16 The structure and the absorption/fluorescence spectrum of ICG .....	107
6-17 Chemical structure of Cypate .....	107
6-18 Chemical structures of NIR804-2DG and Cypate-2DG .....	109
7-1 The phase transition slope vs. the object diameter .....	112
7-2 Dual-interfering-source detection on homogenous medium and heterogeneous medium .....	113
7-3 Illustration of adaptive calibration .....	118
7-4 Plot of phase resolution versus the data collection time interval with different sources phase offsets .....	120
7-5 The geometry and adaptive calibration of finite size phantom .....	123
7-6 The geometry and adaptive calibration of heterogeneous phantom .....	126
7-7 The geometry and adaptive calibration of the animal model .....	129
7-8 Illustration of the goniometric probe and the experimental set-up for the phantom test .....	131
7-9 Amplitude and phase signals from the scanning of phased array	

probe in one dimension .....	132
7-10 The two-dimensional localization of the fluorescent object .....	133
7-11 Illustration of localization accuracy by fine needle insertion .....	134
7-12 The relationship of phase signal, localization error and limit of detection versus the object depth .....	135
7-13 Experimental set-up for animal tumor model test .....	137
7-14 The two-dimensional localization of the submerged mouse tumor .....	137
7-15 Illustration of the fine needle localization of RIF-1 tumor .....	138
7-16 Experimental set-up for <i>in vivo</i> animal tumor model test .....	139
7-17 The two-dimensional localization of the submerged mouse tumor with tail vein injection of NIR804-2-D-Glucosamide and ICG .....	140
7-18 The two-dimensional localization of the submerged mouse tumor with tail vein injection of Cypate-mono-2-D-Glucosamide .....	141
7-19 The two-dimensional localization of the submerged mouse tumor with tail vein injection of BChl-2-D-Glucosamide and the negative control .....	142
7-20 The set-up of blood model test .....	145
7-21 The relationship between the real position and measured position for both oxygenated and deoxygenated blood .....	145
7-22 Imaging of deoxygenated blood and oxygenated blood .....	146
7-23 Breast tumor image .....	147
7-24 Image reconstruction using SIRT .....	149
7-25 Reconstructed absorption vs. iteration number .....	150
7-26 Image reconstruction using TSVD .....	151
7-27 L-Curve analysis for TSVD .....	151
7-28 Singular value spectra for phased array .....	153
7-29 Image reconstruction of fluorescent object using TSVD .....	154
7-30 Diagram illustrating the NIR probe position and the selection of region of interest (ROI) in the coronal MR images .....	157
7-31 Time traces of the optical coefficients .....	158
7-32 Changes of deoxygenated hemoglobin, oxygenated hemoglobin and total hemoglobin concentrations .....	159
7-33 Changes of oxygen saturation during the inspiration of gas with different FiO <sub>2</sub> .....	160
7-34 The MRI signal of the selected ROI during the inspiration of gas with different FiO <sub>2</sub> .....	162

7-35	Correlation between the normalized BOLD signal change and the normalized deoxygenated hemoglobin concentration change .....	162
7-36	The co-registration of the single-wavelength phased array image with a concurrent fMRI image .....	166
7-37	Finger-tapping test .....	167
7-38	$ \Delta\Phi(830\text{ nm})  -  \Delta\Phi(750\text{ nm}) $ vs. the displacement of absorber .....	168
7-39	Response to stimulation task from normal and abnormal subjects .....	170
7-40	Results of phased array imaging before and after seizure .....	171
7-41	The summation of total signals from four stimulus on one day versus the date of testing .....	173
8-1	Proposed patient-device interface for phased array imaging system .....	177

## LIST OF TABLES

3-1	Average optical properties of human tissues .....	12
3-2	Values for $R_{\text{eff}}$ on different interfaces .....	16
4-1	Chromophore optical properties .....	45
4-2	Fluorophore properties .....	45
4-3	Parameters for POF calculation .....	50
6-1	Technical specifications for three PMTs .....	84
6-2	Noise level for single- and dual-source configurations .....	96
6-3	Photophysical properties of NIRF-2DG .....	109
7-1	Localization accuracy for different object locations .....	124
7-2	Localization accuracy for different object absorptions .....	125

# 1 Introduction

In this work I would like to present the various applications of diffuse optical technologies in biomedicine. The diffuse photons offer novel tools to probe tissue physiology and pathophysiology non-invasively. Although optical techniques have been applied in biomedicine for more than 150 years, most of the applications are limited in surface layers or non-scattering medium. The multiple scattering nature of the biological tissues demands for the developments of sensitive instrumentation and sophisticated physical model to qualitatively, semi-quantitatively or quantitatively understand the underlying physiological events. The field of diffuse optical imaging has been continuously developed since the 1980s owing to the advances in novel laser technology, sensitive photon detectors and mathematical algorithm, among others. This work reflects the past 6 years of exciting research I have undertaken at the University of Pennsylvania.

The theme of this thesis is the contrast enhancement in diffuse optical spectroscopy and imaging. Contrast is important in differentiating the targeted object

(for instance, the tumor) from the background. Specifically, there are two kinds of contrast enhancement involved in this study. The first is to enhance the object detection sensitivity through the manipulation of dual-interfering sources. The resultant interference-like pattern converts the conventional absorption and scattering contrasts to perturbations of the cancellation plane, thus improving the ability in detecting small heterogeneity. The second kind of contrast enhancement lies in the recent advances in the molecular specific, fluorescent contrast agents. These novel probes will yield elevated tumor-to-normal contrast through various biological principles, and enhance the sensitivity and specificity in tumor detection. The content of this thesis is organized as follows.

**Chapter 2** presents the motivation for development of diffuse optical spectroscopy and image techniques for early breast cancer detection, and briefly reviews the exciting advances in the molecular targeting contrast agents. **Chapter 3** provides the basic physical model of the photon migration in highly scattering media such as human tissue and describes the fundamental solutions of diffuse photon density wave under different measurement geometries, as well as the solution of fluorescence medium. **Chapter 4** analyzes the theory, detection sensitivity and limitation using the interference-like pattern of diffuse photon density wave. Object localization using the dual-interfering-source configuration is also presented. **Chapter 5** reviews the algorithms for diffuse optical spectroscopy (DOS) and diffuse optical tomography (DOT). The physiological relevant parameters (blood volume and oxygenation) are calculated from the optical measurements. **Chapter 6** overviews the instruments and key materials utilized in the research work. Both frequency-domain and continuous-wave instruments are introduced to perform the DOS and DOT. Also, the contrast agents used in tumor imaging are illustrated. **Chapter 7** demonstrates the

experimental results of several research projects, including the optimization of phased array detection and localization, tumor imaging in animal models with the metabolism enhanced contrast agents, detection of human breast cancer with intrinsic contrasts, image reconstruction with absorption and fluorescent phantoms, monitoring of rat brain oxygenation modulation and correlation with BOLD MRI, functional brain mapping using phased array topography and the clinical application in evaluation of neonatal brain developments. **Chapter 8** concludes the current work and discusses the future outlook of diffuse optical technologies and the biomedical applications.

## **2 Optical Method in Breast Cancer Detection**

This chapter introduces the motivation of the continuous efforts in the development of advanced optical technology for clinical diagnosis. The history and current applications of optical techniques are also briefly surveyed.

### **2.1 Introduction of Breast Cancer and Detection Modalities**

Breast cancer is the most commonly diagnosed cancer among women in the United States and worldwide. It is the second leading cause of cancer death for women in the U.S.; there was an estimation of 203,500 new invasive cases of breast cancer occurring among women and approximately 40,000 women in the U.S. died from the disease in 2002 [1].

Early detection through mammography and clinical breast exams are essential for effective breast cancer screening. For women between the ages of 50-69, regular mammograms can reduce the chance of death from breast cancer by approximately 30% [2]. X-ray mammography may miss up to 25% of breast tumors in women in their 40s, and about 10% of women over age 50. Digital mammography may offer

better resolution. Surgical biopsies are considered as the “gold standard”, while 80% of U.S. women who undergo surgical biopsies do not have cancer. Image-guided needle breast biopsy, also called stereotactic biopsy, is being studied as an alternative to the more invasive surgical biopsies. Other non-invasive imaging techniques, such as magnetic resonance imaging (MRI) and ultrasound (US), have been developed for breast cancer detection and staging without using X-rays [3,4]. In general, mammography, MRI and US provide more anatomic information, rather than quantitative tissue function and composition [5]. Positron Emission Tomography (PET) could provide the metabolic information, but requires the injection of exogenous radionuclides [6].

## **2.2 Optical Method and Intrinsic Contrast**

Compared with other modalities, the optical method has its own merits of non-ionizing, economic and biochemical specificity. The use of optics in breast cancer detection dates back into the 1920s [7]. In the past two decades, the field of probing the tissue physiology with diffusive near-infrared (NIR) light (600 nm – 1000 nm) has been developing rapidly [8,9]. The spectrum window in the NIR range, which corresponds to lower absorption from major tissue chromophores such as oxygenated and deoxygenated hemoglobin, allows light to penetrate deep into the tissue, up to several centimeters [10]. The advances in optical technology and mathematical algorithms make the new imaging method – diffuse optical tomography (DOT) available. In DOT, the light propagation in the turbid media (such as human tissue) is well modeled by the diffusion equation, and the diffuse photons received from multiple projections are measured and compared with the forward model. Through the inversion techniques, the optical properties of the medium can be quantified in three-

dimension [11]. DOT has been applied to breast cancer detection and shows great promise to be complementary to current imaging modalities [12-14].

In the NIR window, the principle chromophores accounted for absorption in breast tissue are oxygenated and deoxygenated hemoglobin ( $\text{HbO}_2$  and  $\text{Hb}$ ), water ( $\text{H}_2\text{O}$ ) and lipids [15,16]. The concentration of each composition can be derived through the absorption spectrum analysis using multiple wavelengths (at least the same number of wavelengths as the number of unknowns). Those intrinsic contrasts can indicate significant functional information. Usually tumor cells will need more nutrition to grow, which results in the increase of blood vessels. This process is called angiogenesis [17]. While the supply of oxygen is still not enough for the tumor growth, thus lower oxygen partial pressure ( $\text{pO}_2$ ) values are observed in human breast tumors *in situ* than that in a normal breast, which is due to the hyper-metabolic activities in tumor cells [18,19].

Optical imaging can probe the concentrations of those chromophores, especially the oxygenated and deoxygenated hemoglobin. Hence, it can provide the biochemical specificity in breast cancer diagnosis [20,21]. Typically, two important parameters are given by optical spectroscopy and imaging, the blood volume (the sum of the oxygenated and deoxygenated hemoglobin concentration) and the oxygen saturation (the ratio of oxygenated hemoglobin to the blood volume). Statistical data indicate that there are two to four folds of contrast between normal and tumor structures for the blood volume, and the oxygen saturation in the tumor is also less than normal [5,16,21]. Also, those parameters are age and hormonal status related [5,22]. Thus NIR optical signals can reveal unique physiologic information that could not be obtained elsewhere non-invasively.

The scattering properties of tissue also contain important information for lesion diagnosis. The scattering coefficients are related to the tissue structure properties and the concentration or size of organelles [23]. The *in vivo* measurements show that scattering coefficients are wavelength dependent [5]. While *ex vivo* studies suggest that the scattering coefficients alone do not provide sufficient information to discriminate the small breast tumors from normal breast tissue [24,25].

## **2.3 Extrinsic Contrast**

Like other imaging modalities, contrast enhancement through contrast agents, either for absorption or fluorescence, have shown great promise for improving the sensitivity and specificity of breast cancer detection [14]. The use of exogenous probes to gain a better understanding of the physiological process has been an active field of research in the past years [23,26-29].

### **2.3.1 Non-specific Contrast Agents**

The most commonly used contrast agent in the NIR spectral window is Indocyanine Green (ICG). ICG is an FDA (Food and Drug Administration) approved fluorescent dye for imaging of retinal vasculature and hepatic function [30]. The absorption contrast provided by ICG mainly probes the permeability and vascularization [31] of tissue blood vessels, as well as indicates the blood flow [32]. ICG has been applied in human subjects clinically. The ICG-enhanced optical images coregistered accurately with Gadolinium-enhanced MRI images validate the ability of DOT to detect breast cancer [14]. Although ICG and its hydrophilic derivatives are not designed for specific target seeking, the effect of contrast enhancement for tumor detection has been successfully demonstrated [33].

Recently, fluorescent contrast agents have also been considered as a means to enhance the sensitivity and specificity for tumor detection [27,34]. Li *et al* [35] detected the fluorescence signal from a low dose ICG ( $\sim 80 \mu\text{g}/\text{kg}$  body weight) injection into the rat model with a subcutaneous mammary tumor. They reported a contrast around 2.5 between the fluorescence intensities of the tumor and control tissues, and monitored the longitudinal trend during the tumor exponential growth. It has been demonstrated that the contrast imparted by exogenous fluorescent agents can exceed the contrast from absorption [36]. For example, Ebert *et al* [24] reported a 6:1 tumor-to-tissue contrast ratio in fluorescent imaging of a highly hydrophilic cyanine dye derivative. These contrasts come from the preferential uptake of fluorescent contrast agents by the disease tissue and also the kinetics of fluorescence decay can be environmentally specific to different tissue volumes. Using intensity-modulated frequency-domain imaging with a gain-modulated image-intensified CCD camera, Reynolds *et al* [37] located the canine spontaneous mammary tumor *in vivo* from the ICG distribution. With similar instrumentation and animal model, Gurfinkel *et al* [38] tracked the pharmacokinetics of ICG using a double-exponential model. They mapped the fluorescence intensity of the dye during the uptake (wash-in) and release (wash-out) through the tissue, and observed a delayed wash-out of ICG up to 72 hours.

### **2.3.2 Molecular Specific Contrast Agents**

While ICG is mainly a blood-pooling agent and is cleared out by the liver rapidly, numerous efforts have been invested to improve the affinity and the retention time of contrast agents in the tumor cells, including the increasing of the hydrophilicity [33] and binding to macromolecules [39]. To further improve the performance of contrast agents, target-specific conjugates have been developed to

study the molecular specificity [26,28,29]. Cancer cells will over-express certain receptors, and increase the uptake of the corresponding ligands. This process will result in the accumulation of those ligands in a certain type of cells, thus providing high detection specificity [26]. Conjugation of a fluorophore to those ligands can give high fluorescent contrast for tumor cells versus the normal cells. For instance, Achilefu *et al* [40,41] and Becker *et al* [42] have developed a highly somatostatin (sst2) receptor-specific tricarbo-cyanine based peptide-dye conjugate to image the tumor that tends to over-express the sst2 receptor. Zheng *et al* [43] have targeted another kind of receptor, LDLr, which also tends to over-express on several types of tumor cells. They incorporated tricarbo-cyanine cholesteryl laurate within the lipid core of LDL that could be internalized by tumor cells via LDLr-mediated endocytosis. Another interesting type of molecular fluorescent marker has been developed by Weissleder *et al* [44]. They use the protease-activated probes containing auto-quenched fluorescent molecules through fluorescence resonance energy transfer (FRET) that can be cleaved by tumor-specific proteases and then fluoresce. Through this kind of approach, the high fluorescent contrast (12 folds) has been demonstrated in the tumor.

The combination of molecular probes and optical imaging techniques will yield the high sensitivity and specificity for cancer detection [45]. The significance lies in the early detection of cancerous tissue cells at the molecular level, before the anatomic changes become apparent. Thus the therapy can be applied in the very early stage of neoplasia to achieve high survival rates.

### 3 Basic Theory of Photon Migration

This chapter reviews the basic theories of the photon migration in the highly scattering media, as well as the fluorescence diffuse photon density wave. The review is mainly based on the publication of Patterson *et al* [48], Fishkin *et al* [49], Haskel *et al* [53], and the dissertations of David Boas [51], Maureen O’Leary [65] and Xingde Li [70].

This chapter is organized as follows: **Section 3.1** describes the diffusion approximation to the photon transport in the scattering media. **Section 3.2** derives the analytical solutions of diffuse photon density wave (DPDW) in the infinite homogeneous media. **Section 3.3** states the commonly chosen boundary conditions and **Section 3.4** provides the solutions with the boundary condition. In **Section 3.5**, we outline the analytical solutions for the fluorescence diffuse photon density wave (FDPDW) in the highly scattering media.

### 3.1 Diffusion Approximation

When light enters into a turbid medium (such as biological tissues), the photons travel in the form of a random walk due to the multiple scattering process. The mathematical description of photon migration is the linear transport equation [46]. While the transport equation is usually difficult to solve analytically and numerically. Fortunately, the propagation of the photons can be approximated by the diffusion equation when the scattering effect predominates the absorption [47-51]. In homogeneous turbid medium, the diffusion equation is written as [48,50]:

$$\frac{1}{c} \frac{\partial}{\partial t} \Phi(\mathbf{r}, t) - \nabla \cdot \mathbf{D} \nabla \Phi(\mathbf{r}, t) + \mu_a \Phi(\mathbf{r}, t) = \mathbf{S}(\mathbf{r}, t), \quad (3-1)$$

where  $\Phi(\mathbf{r}, t)$  is the photon fluence [ $\text{W} \cdot \text{cm}^{-2} \cdot \text{s}^{-1}$ ] at the position  $\mathbf{r}$  and time  $t$ ;  $c$  is the speed of light in the medium [ $\text{cm} \cdot \text{s}^{-1}$ ];  $\mu_a$  is the absorption coefficient [ $\text{cm}^{-1}$ ] (the reciprocal of absorption length);  $\mu'_s = (1-g)\mu_s$  is the reduced scattering coefficient [ $\text{cm}^{-1}$ ], with  $g$  the mean cosine of the photon scattering angle and  $\mu_s$  the scattering coefficient (the reciprocal of scattering length) [ $\text{cm}^{-1}$ ];  $\mathbf{D} = [3\mu'_s]^{-1}$  is the diffusion coefficient [ $\text{cm}$ ] and  $\mathbf{S}(\mathbf{r}, t)$  is the source term [ $\text{W} \cdot \text{m}^{-3} \cdot \text{s}^{-1}$ ].

The conditions for diffuse approximation are: the albedo  $\alpha = \mu'_s / (\mu'_s + \mu_a)$  is close to 1 (*i.e.*,  $\mu'_s \gg \mu_a$ ) and the source-detector separation  $\rho \gg 1/\mu'_s$ . These conditions are generally satisfied in the measurement of biological tissues such as breast and brain with the source-detector separation larger than 1 cm. Table 3-1 lists the average optical properties of several representative tissue types.

Hielscher *et al* [81] has validated the diffusion approximation to the transport equation under various  $\mu_a/\mu'_s$  ratios, and the diffusion approximation is broken down

in highly absorbing regions (such as hematoma) or void-like spaces with low absorption and scattering (such as ventricles).

Table 3-1: Average optical properties of human tissues

Tissue Type	Wavelength (nm)	$\mu_a$ (cm <sup>-1</sup> )	$\mu'_s$ (cm <sup>-1</sup> )	Ref
Breast	753	0.046 ± 0.014	8.9 ± 1.3	[55]
Breast (pre-menopausal)	806	0.090 ± 0.008	8.2 ± 0.6	[5]
Breast (post menopausal)	806	0.030 ± 0.008	6.0 ± 0.1	[5]
Breast	786	0.041 ± 0.025	8.5 ± 2.1	[56]
Breast	830	0.046 ± 0.027	8.3 ± 2.0	[56]
Brain (adult skull)	800	0.22 ± 0.01	18.5 ± 1.0	[57]
Brain (piglet)	758	0.15 ± 0.01	7.0 ± 0.5	[58]
Brain (grey matter)	800	0.25 ± 0.01	8.0 ± 1.0	[194]
Brain (white matter)	800	1.00 ± 0.10	40.0 ± 5.0	[194]

### 3.2 Diffuse Photon Density Waves

There are three kinds of source functions commonly employed in measuring photon migration in tissue, as illustrated in Figure 3-1. The simplest approach is using the continuous wave (CW) light source, in which the light intensity in the source or the detector is constant. Another approach is the frequency domain technique, or phase modulation system (PMS), in which the light intensity is sinusoidally modulated, thus both the amplitude and phase of the sinusoidal wave are

measurement parameters. The third technique, the time-resolved system (TRS), utilizes a short pulse (sub-nanosecond) and the broadening of the light pulse due to the multiple scattering is recorded.

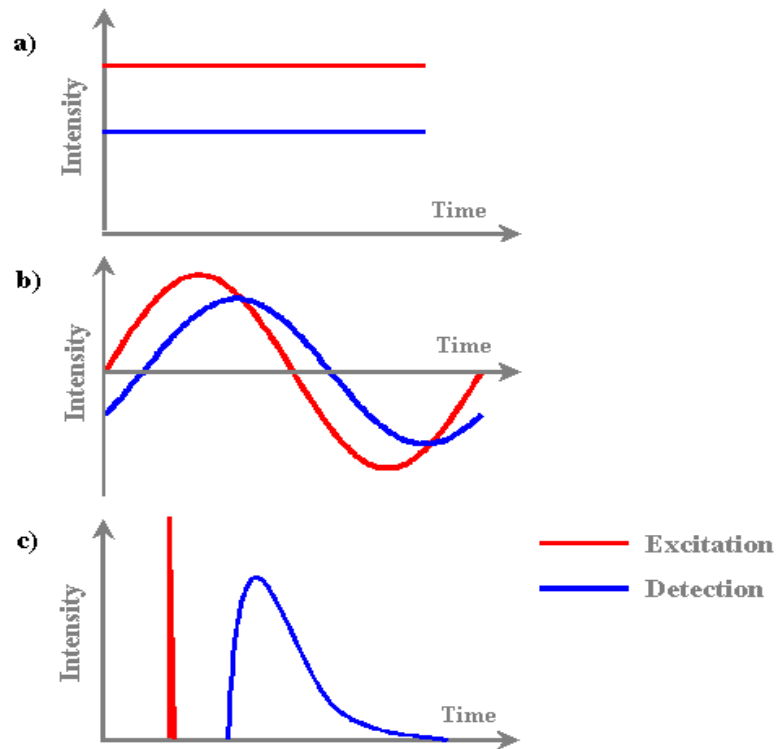


Figure 3-1: Three kinds of source functions: (a) Continuous wave (CW); (b) Phase modulation system (PMS); (c) Time-resolved system (TRS).

The three types of source functions are related. The frequency domain technique and the time domain technique are the Fourier transforms of each other, and the frequency domain technique is reduced to CW technique when the modulation frequency is zero. Thus we will focus on the frequency domain technique in the analysis and derivation of the solutions for the photon migration in multiple scattering media.

In the phase modulation system (PMS), the source intensity is modulated by a sinusoidal wave, *i.e.*,  $S(\mathbf{r},t)=\delta(\mathbf{r}_s)S_0(1+Ae^{-i\omega t})$ , where  $S_0$  is the source strength,  $A$  is the

modulation depth and  $\omega$  is the modulation frequency. The AC component of Eq. (3-1) will be rewritten as [10]:

$$(\nabla^2 + \mathbf{k}^2)\Phi_{ac}(\mathbf{r}) = -\mathbf{S}_0 \mathbf{A} \delta(\mathbf{r}_s) / \mathbf{D}, \quad (3-2)$$

where  $\mathbf{k}^2 = (-c\mu_a + i\omega) / c\mathbf{D}$ . The solution of this Helmholtz equation, amplitude  $M_{ac}(\rho)$  and phase  $\phi(\rho)$ , in an infinite medium, is given by [49]:

$$\mathbf{M}_{ac}(\rho) = \frac{\mathbf{S}_0 \mathbf{A}}{4\pi \mathbf{D} \rho} \exp[-\rho \Pi \cos(\frac{\vartheta}{2})], \quad (3-3)$$

$$\phi(\rho) = \rho \Pi \sin(\frac{\vartheta}{2}), \quad (3-4)$$

where  $\rho = |\mathbf{r} - \mathbf{r}_s|$  is the radial distance away from the point source,  $\vartheta = \tan^{-1}(\omega / \mu_a c)$

$$\text{and } \Pi = \left( \frac{\mu_a^2 c^2 + \omega^2}{c^2 \mathbf{D}^2} \right)^{1/4}.$$

Eq. (3-3) and Eq. (3-4) suggest that even though microscopically the photon migration in the highly scattering medium behaves like a random walk, macroscopically the photon density is distributed in the manner of a damped outgoing spherical wave, with a well-defined phase front. This distribution is referred as the diffuse photon density wave (DPDW).

The DPDW has the features of traditional waves, such as scattering [50], refraction [59] and interference [60]. These properties have been applied to achieve object localization [61-64] and imaging [65-67].

In the CW system, the intensity measured by a detector with a radial distance,  $\rho$ , is [49]:

$$\mathbf{M}_{dc}(\rho) = \frac{\mathbf{S}_0}{4\pi \mathbf{D} \rho} \exp(-\rho \sqrt{\mu_a / \mathbf{D}}). \quad (3-5)$$

It is clear that Eq. (3-5) is equivalent to Eq. (3-3) when the modulation frequency  $\omega = 0$ . And for the TRS system, the solution in an infinite medium is [48]:

$$\Phi(\rho, t) = \frac{c}{(4\pi Dct)^{3/2}} \exp\left(-\frac{\rho^2}{4Dct} - \mu_a ct\right). \quad (3-6)$$

The solutions given by Eqs. (3-3) – (3-6) describe the propagation of the diffuse photon density wave in the infinite media from a point source. These solutions can serve as the Green's function in solving the problems under more complicate conditions.

### 3.3 Boundary Conditions

In clinical usage, the realistic measurement geometry is the semi-infinite or slab geometry [52]. In this circumstance, a proper boundary condition should be chosen in order to obtain the correct solution. Generally, there are three kinds of boundary conditions: zero boundary condition [60], extrapolated zero boundary condition [48,54], and partial current boundary condition [68]. In zero boundary condition, the photon fluence vanishes at the interface between the scattering and non-scattering media; it is simple but not generally correct. In extrapolated zero boundary condition, the photon fluence vanishes in a virtual plane at a distance  $z_b$  away from the physical boundary; it provides a more accurate approach while in a simple format. In partial current boundary condition, the radiance vanishes at the boundary. The radiance consists of an isotropic fluence and a small directional flux [53]:

$$\mathbf{L}(\mathbf{r}, \hat{\mathbf{s}}, t) = \frac{1}{4\pi} \Phi(\mathbf{r}, t) + \frac{3}{4\pi} \mathbf{J}(\mathbf{r}, t) \cdot \hat{\mathbf{s}}, \quad (3-7)$$

where  $\Phi(\mathbf{r}, t)$  is the photon fluence [ $\text{W}\cdot\text{cm}^{-2}\cdot\text{s}^{-1}$ ] and  $\mathbf{J}(\mathbf{r}, t)$  is a vector representing the directional photon flux [ $\text{W}\cdot\text{cm}^{-2}\cdot\text{s}^{-1}$ ]. In turbid media, the flux is related to the fluence by the Fick's law:

$$\mathbf{J}(\mathbf{r},t) = -\mathbf{D}\nabla\Phi(\mathbf{r},t). \quad (3-8)$$

Partial current boundary condition is the most exact physical expression, but it is difficult to incorporate in the diffusion equation. Haskell *et al* [53] have shown that the partial current and the extrapolated boundary condition give almost similar solutions within 3%. In our study, the extrapolated zero boundary condition is mostly used.

The position of the extrapolated boundary depends on the scattering properties of the medium and the index of mismatch at the interface. The distance  $z_b$  is given by [53]:

$$z_b = \frac{2}{3\mu_s'} \frac{1 + R_{\text{eff}}}{1 - R_{\text{eff}}}, \quad (3-9)$$

where  $R_{\text{eff}}$  is the effective reflection coefficient on the interface. The values of  $R_{\text{eff}}$  with different interfaces are listed in Table 3-2 [53].

Table 3-2: Values for  $R_{\text{eff}}$  on different interfaces

Interface Type	$n_{\text{in}}$	$n_{\text{out}}$	$R_{\text{eff}}$	$z_b (1/\mu_s')$
Air-Air	1.00	1.00	0	0.667
Water-Air	1.33	1.00	0.431	1.677
Tissue-Air	1.40	1.00	0.493	1.963

### 3.4 Solution with Boundary

Using the diffuse photon density wave solution for the infinite medium, and applying extrapolated boundary condition and the image source-object pair technique

[48], we can derive the analytical expressions for the planar boundary geometry. Specifically, we set the photon fluence drops to zero at a distance  $z_b$  away from the physical boundary, and use a pair of positive and negative sources located below and above the extrapolated boundary symmetrically, then superpose the individual solutions from different sources.

### 3.4.1 Solution in Semi-infinite Geometry

In semi-infinite geometry, a collimated beam is modeled by an isotropic source located at  $z_0 = 1/\mu'_s$  inside the surface. And an image source needs to be added at the position  $z = -z_0 - 2z_b$  as illustrated in Figure 3-2(a) [48,73].

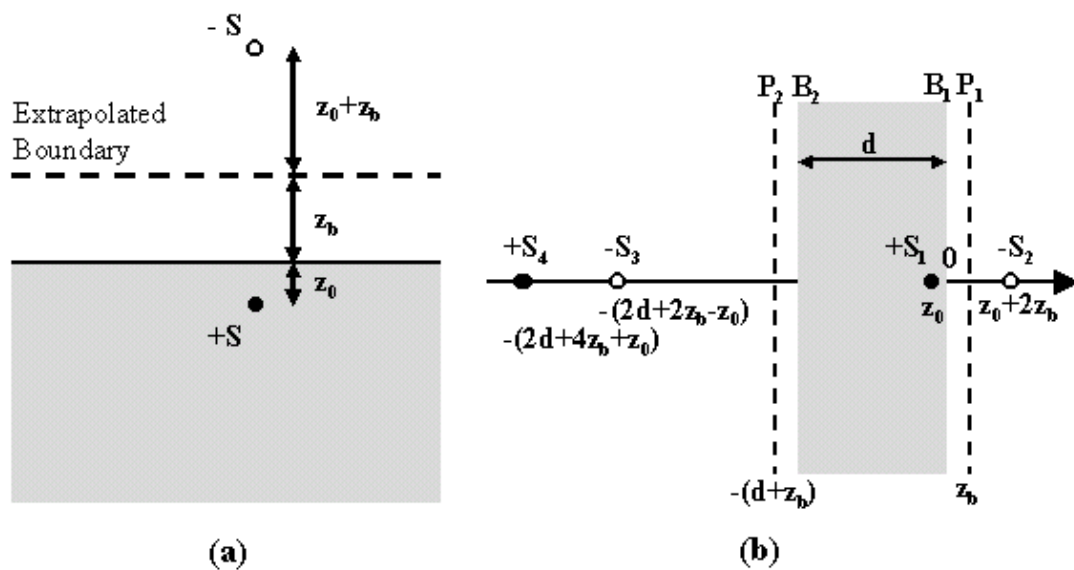


Figure 3-2: Extrapolated boundary condition for (a) semi-infinite geometry and (b) slab geometry. (Shaded area represents the scattering media; Filled circle represents the source and the open circle refers to the image source;  $B_1$ ,  $B_2$  are physical boundaries and  $P_1$ ,  $P_2$  are extrapolated boundaries)

The DPDW in the medium can be derived from the sum of the DPDWs in infinite homogeneous medium generated by the source pairs. The amplitude and phase profiles of solution in semi-infinite geometry are illustrated in Figure 3-3.

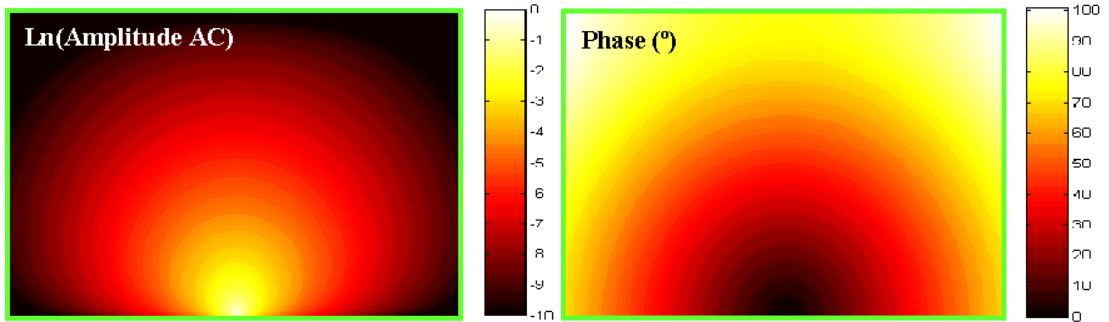


Figure 3-3: Amplitude and phase profiles for the DPDW generated in the semi-infinite geometry. (The parameters for the simulation:

$$\mu_a = 0.04 \text{ cm}^{-1}, \mu'_s = 8.0 \text{ cm}^{-1}, \omega = 200 \text{ MHz})$$

### 3.4.2 Solution in Slab Geometry

Slab geometry is another commonly used geometry in clinical measurement, for instance, the compressed breast geometry [14]. Here we consider an infinite slab with the thickness  $\mathbf{d}$  illustrated in Figure 3-2(b). Two extrapolated boundaries,  $P_1$  and  $P_2$ , need to be satisfied  $\Phi(\mathbf{r},t)$ . To meet these requirements, a series of image source pairs are added. As illustrated in Figure 3-2(b), the source  $\mathbf{S}_1$  is at the distance  $-z_0$  inside the diffuse medium, and an image source ( $\mathbf{S}_2$ ) located at  $z = z_0 + 2z_b$  is added as the mirror symmetric about plane  $P_1$ . And the mirror images of  $\mathbf{S}_1$ - $\mathbf{S}_2$  about plane  $P_2$  are further added at  $z = -(2d + 2z_b - z_0)$  and  $z = -(2d + 4z_b + z_0)$  as indicated by  $\mathbf{S}_3$ - $\mathbf{S}_4$ . For demonstration purposes, we only show two pairs of sources; theoretically, more source pairs need to be considered (such as the mirror of  $\mathbf{S}_3$ - $\mathbf{S}_4$  regarding to plane  $P_1$ , and so forth). In practice, the number of source pairs required depends on the slab size

and optical properties [48]. Contini *et al* [195] suggested that 7 dipoles are sufficient to maintain the truncate error within 0.1%. The final solution of DPDW should be the summation of all those image source pairs.

### 3.4.3 Perturbation by Spherical Object

One of the purposes for development of the theoretical analysis of diffuse photon density wave is to localize and characterize inhomogeneities embedded inside the scattering media. Boas *et al* [50,74] and Feng *et al* [75] have derived the analytical solution for the case of spherical inhomogeneities within the turbid media. The general solution for the measured DPDW outside the object is the superposition of the incident DPDW plus the diffusive wave scattered from the object [50]:

$$\Phi_{\text{out}} = \Phi_{\text{inc}} + \Phi_{\text{scatt}} . \quad (3-10)$$

The scattering diffusive wave depends on the diameter of the spherical object, the optical properties of the object and the background medium, and the source modulation frequency. A detailed expression of the scattering wave has been given in Ref. [74]. The analytical solution for the infinite circular, cylindrical inhomogeneity embedded in a homogeneous highly scattering turbid medium has also been provided [76].

## 3.5 Fluorescence Diffuse Photon Density Waves

Besides the scattering and absorption, biological tissue also contains intrinsic fluorophores. Even though most of them are not available in the NIR region, the exogenous fluorescent contrast agents in the NIR region have been considered as a means to enhance the sensitivity and specificity for tumor detection [27-29,36]. Thus many interests have been invested on the fluorescence photons due to the high

sensitivity and molecular specificity [36,77-80]. Fluorescence methods have been applied widely in biochemical, chemical, and medical research due to its inherent sensitivity and favorable time scale [82]. The re-radiation of DPDW in turbid media by the fluorescent dye has been reported [69] and the theoretical analysis has been developed [65,70,71].

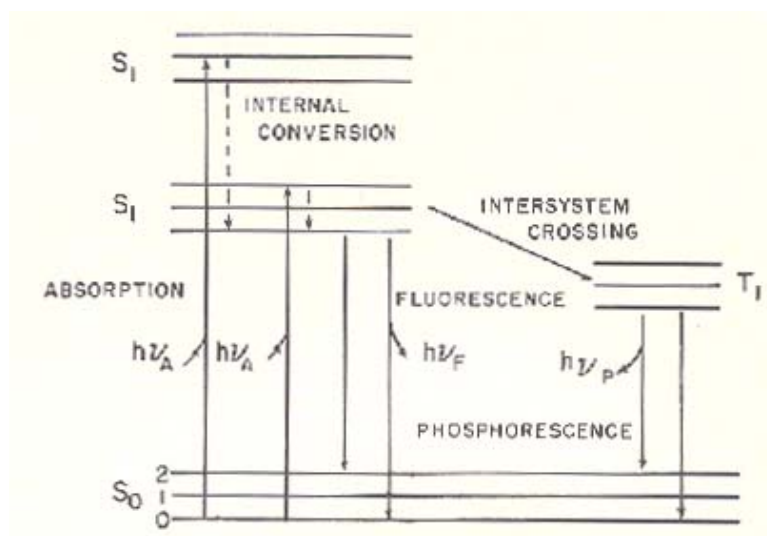


Figure 3-4: Jablonski diagram for absorption, fluorescence and phosphorescence.

(Adopted from Ref. [82])

Figure 3-4 illustrates the Jablonski diagram describing the transitions responsible for absorption, fluorescence, and phosphorescence interactions [72]. After absorbing an excitation photon ( $\lambda_{ex}$ ) in the UV-VIS-NIR region, an activated chromophore is instantly elevated to its excited state. Relaxation can occur via nonradiative or radiative processes, depending upon the local environment of the molecule. In the radiative processes (fluorescence), the relaxation is accompanied by the release of a reemission photon ( $\lambda_{em}$ , and  $\lambda_{em} > \lambda_{ex}$ ). The mean time between absorption and reemission of the fluorescence photon is known as the fluorescence lifetime  $\tau$ .

Assuming the fluorescent re-radiation is well separated from that of incident photons, the excited fluorophores have a single lifetime, and the fluorophores are treated as a two level quantum system and the saturation effect is ignored, the number of excited fluorophores,  $N$ , obeys the linear diffusion equation [65]:

$$\frac{\partial \mathbf{N}(\mathbf{r}, \mathbf{t})}{\partial \mathbf{t}} = -\Gamma \mathbf{N}(\mathbf{r}, \mathbf{t}) + \eta \varepsilon \Phi_{\text{inc}}(\mathbf{r}, \mathbf{r}_s) \mathbf{N}_t(\mathbf{r}) \quad (3-11)$$

where  $\Gamma$  is the excited dye decay rate;  $\Phi_{\text{inc}}(\mathbf{r}, \mathbf{r}_s)$  is the incident photon fluence;  $N_t$  is the number of dye molecules per unit volume; and  $\eta$  the fluorescent yield, and  $\varepsilon$  is the absorption cross section. For the case of amplitude modulated source,  $N(\mathbf{r}, \mathbf{t}) = N(\mathbf{r}) \exp(-i\omega t)$ , Eq. (3-11) can be rewritten as:

$$-i\omega \mathbf{N}(\mathbf{r}, \mathbf{t}) = -\Gamma \mathbf{N}(\mathbf{r}) + \eta \varepsilon \Phi_{\text{inc}}(\mathbf{r}, \mathbf{r}_s) \mathbf{N}_t(\mathbf{r}). \quad (3-12)$$

and the rate of production of fluorescent photons is:

$$\Gamma \mathbf{N}(\mathbf{r}) = \frac{\eta \varepsilon \Phi_{\text{inc}}(\mathbf{r}, \mathbf{r}_s) \mathbf{N}_t(\mathbf{r})}{1 - i\omega \tau}. \quad (3-11)$$

where  $\tau = 1/\Gamma$  is the fluorescent lifetime.

The term  $\Gamma \mathbf{N}(\mathbf{r})$  is now a source of fluorescent DPDW. These photons will propagate to the detector position  $\mathbf{r}_d$  so that the detected fluorescent signal is:

$$\begin{aligned} \Phi_n(\mathbf{r}_d, \mathbf{r}_s) &= \int_v \Gamma \mathbf{N}(\mathbf{r}) \mathbf{G}^n(\mathbf{r}, \mathbf{r}_d) / \mathbf{D}^n d\mathbf{r} \\ &= \int_v \Phi_{\text{inc}}(\mathbf{r}, \mathbf{r}_s) \frac{\eta \varepsilon \mathbf{N}_t(\mathbf{r})}{(1 - i\omega \tau) \mathbf{D}^n} \mathbf{G}^n(\mathbf{r}, \mathbf{r}_d) d\mathbf{r}. \end{aligned} \quad (3-13)$$

The detected fluorescent signal can be expressed through the following parameters:

- a) The incident photon density wave from the source to the fluorophore,  $\Phi_{\text{inc}}(\mathbf{r}, \mathbf{r}_s)$ .

- b) The fluorescent term, including  $N_f(\mathbf{r})$  the fluorophore concentration and  $\eta$  the fluorescent yield,  $\varepsilon$  the absorption cross section of the dye and  $\tau$  the fluorescent lifetime.
- c) The outgoing fluorescent diffuse photon density wave from the fluorophore to the detector, where the Green's function  $G(\mathbf{r}, \mathbf{r}_d) = \exp(ik|\mathbf{r} - \mathbf{r}_d|)/4\pi|\mathbf{r} - \mathbf{r}_d|$ . The superscript “fl” denotes the parameters in FDPDW are governed by the optical properties of the medium at the fluorescent wavelength.

The general solution for fluorescent diffuse photon density wave (FDPDW) has been provided by Li *et al* [77]. The solution for the case of a single source excitation has the following form:

$$\begin{aligned} \Phi_{\text{hetero}}^{\text{flr}}(\mathbf{r}_s, \mathbf{r}_d, \omega, \mathbf{a}) &= \Phi_{\text{hom o}}^{\text{flr}}(\mathbf{r}_s, \mathbf{r}_d, \omega) + \Phi_{\text{sc}}^{\text{flr}}(\mathbf{r}_s, \mathbf{r}_d, \omega, \mathbf{a}) \\ &= \frac{\varepsilon \mathbf{q}_1 \eta_1 N_1}{\mathbf{1} - i\omega\tau_1} \mathbf{F}_1(\mathbf{r}_s, \mathbf{r}_d, \omega) + \frac{\varepsilon \mathbf{q}_2 \eta_2 N_2}{\mathbf{1} - i\omega\tau_2} \mathbf{F}_2(\mathbf{r}_s, \mathbf{r}_d, \omega, \mathbf{a}) \end{aligned} \quad (3-15)$$

where  $\Phi_{\text{hom o}}^{\text{flr}}(\mathbf{r}_s, \mathbf{r}_d, \omega)$  is the homogeneous FDPDW,  $\Phi_{\text{sc}}^{\text{flr}}(\mathbf{r}_s, \mathbf{r}_d, \omega, \mathbf{a})$  is the scattered FDPDW.  $\mathbf{r}_s$  and  $\mathbf{r}_d$  are the source and the detector positions, respectively,  $\mathbf{a}$  is the radius of the inhomogeneity, and  $\omega$  is the angular source modulation frequency.  $N_1$  and  $\tau_1$  are the fluorophore concentration and lifetime in the homogeneous background medium (*i.e.*, outside the spherical inhomogeneity);  $N_2$  and  $\tau_2$  are the concentration and lifetime inside the inhomogeneity.  $\varepsilon$  is the fluorophore extinction coefficient at the excitation wavelength  $\lambda_{\text{ex}}$ .  $\eta_1$  ( $\eta_2$ ) is the fluorescence quantum yield outside (inside) the object.  $\mathbf{q}_1$  ( $\mathbf{q}_2$ ) is the fluorescence quenching factor outside (inside) the object. Expression of  $\mathbf{F}_1(\mathbf{r}_s, \mathbf{r}_d, \omega)$  and  $\mathbf{F}_2(\mathbf{r}_s, \mathbf{r}_d, \omega, \mathbf{a})$  could be found in

Ref. [77]. Li *et al* [78] also have demonstrated that the fluorescence measurement mode is superior to the absorption mode in terms of the limits for detection and characterization of fluorescent (phosphorescent) inhomogeneities embedded in tissue-like highly scattering turbid media.

## **4 Interference of Diffuse Photon Density Waves**

As mentioned in Chapter 3, DPDW can interfere and refract in the turbid media. To detect a small object embedded inside the turbid media, dual-interfering-source configuration (also termed “phased array” geometry) is considered because it is basically a cancellation technology. Previous studies have explored this topic theoretically [50,60,83-85] and experimentally [61-64,86]. The experimental results reported that the phased array (dual-interfering-source) system can detect 20 picomole of ICG in a 3-mm diameter tube in the scattering medium [63] or 1 mm displacement of a small object embedded at a depth of 10 mm [61]. Studies show that the dual-interfering-source system could provide higher detection sensitivity than a single-source configuration from numeric simulations and signal-to-noise analysis [87-89]. The phased array system has been applied to the breast tumor phantom [90], functional brain imaging [91,92] and fluorescence detection [69,93], experimentally. Also, tomographic image reconstruction using phased array geometry has been demonstrated using the simulated and experimental data [94,95].

The basic phased array unit consists of a pair of in-phase and out-of-phase amplitude modulated sources, thus amplitude null and  $180^\circ$  phase transition will be generated in the plane bisecting these two sources in a homogeneous medium, and this pattern can be sensitively perturbed by the presence of an absorbing or fluorescent object to form the signal for detection and localization. In this chapter, I first introduce the analytical solution for interfering of the DPDW (**Section 4.1**); then develop the noise model for signal-to-noise analysis of the perturbation (**Section 4.2**), hence derive the detection limit for the dual-interfering-source system (**Section 4.3**). **Section 4.4** provides the algorithm for two-dimensional object localization using a dual-interfering-source. Also, the optimization of the dual-interfering-source system is discussed in **Section 4.5**.

## 4.1 Solution with Dual Interfering Sources

In the phased array configuration, where two out-of-phase sources are placed with a distance  $R$  between them, the diffuse photon density wave (DPDW) generated from two out-of-phased sources created an interference-like pattern. Generally, the expressions for those two sources are  $S_1 \exp(-i\omega t)$  and  $S_2 \exp(-i(\omega t + \Delta\phi_0))$  respectively, where  $\Delta\phi_0$  is the phase offset between those two sources. The total DPDW field is equal to the superposition of two independent solutions of those source terms based on the solution provided in Chapter 3. The analytical solutions for the infinite medium and semi-infinite medium with extrapolated zero boundary condition have been described as follows.

#### 4.1.1 Solutions in Infinite Homogeneous Media

Schmitt *et al* [60] first derived the solutions with dual-interfering-source in both infinite and semi-infinite medium (with zero boundary condition) in detail. In an infinite medium, the amplitude and phase of the interference DPDW can be expressed as:

$$\begin{aligned} \mathbf{M}_{\text{sum}}^{\text{fs}}(\rho) = & \{S_1^2 \mathbf{M}_{\text{ac}}^2(\rho_1) + S_2^2 \mathbf{M}_{\text{ac}}^2(\rho_2) + 2S_1 S_2 \mathbf{M}_{\text{ac}}(\rho_1) \mathbf{M}_{\text{ac}}(\rho_2) \\ & \times \cos[\phi(\rho_2) - \phi(\rho_1) + \Delta\phi_0]\}^{1/2}, \end{aligned} \quad (4-1)$$

$$\begin{aligned} \phi_{\text{sum}}^{\text{fs}}(\rho) = & \tan^{-1}(\{S_1 \mathbf{M}_{\text{ac}}(\rho_1) \sin[\phi(\rho_1)] + S_2 \mathbf{M}_{\text{ac}}(\rho_2) \sin[\phi(\rho_2) + \Delta\phi_0]\} \\ & / \{S_1 \mathbf{M}_{\text{ac}}(\rho_1) \cos[\phi(\rho_1)] + S_2 \mathbf{M}_{\text{ac}}(\rho_2) \cos[\phi(\rho_2) + \Delta\phi_0]\}), \end{aligned} \quad (4-2)$$

where  $\mathbf{M}_{\text{ac}}$  and  $\phi$  are expressed as in Eq. (3-3) and (3-4),  $\rho$  is the distance between the detecting point and the mid-point of the two sources and  $\rho_1, \rho_2$  are the distance between the detector and each source.

#### 4.1.2 Solutions in Semi-infinite Homogeneous Media

To model large biological organs such as human breast and brain, the semi-infinite boundary condition is most commonly applied [52]. As illustrated in Figure 4-1, a collimated beam is simulated by an isotropic source located at  $z_0 = 1/\mu'_s$  inside the surface (assuming the photon will lose the initial direction after one scattering event), and the photon fluence vanishes at a distance  $z_b$  away from the medium surface. The total DPDW in the medium can be derived from the summation of the DPDWs in infinite homogeneous medium generated by those two sources and their image sources [60,83]:

$$\begin{aligned}
\mathbf{M}_{\text{sum}}^{\text{hs}}(\rho) = & \{ \{ \mathbf{S}_1 \mathbf{M}_{\text{ac}}(\rho_1) \cos[\phi(\rho_1)] - \mathbf{S}_1 \mathbf{M}_{\text{ac}}(\rho_1') \cos[\phi(\rho_1')] \} \\
& + \mathbf{S}_2 \mathbf{M}_{\text{ac}}(\rho_2) \cos[\phi(\rho_2) + \Delta\phi_0] - \mathbf{S}_2 \mathbf{M}_{\text{ac}}(\rho_2') \cos[\phi(\rho_2') + \Delta\phi_0] \}^2 \\
& + \{ \mathbf{S}_1 \mathbf{M}_{\text{ac}}(\rho_1) \sin[\phi(\rho_1)] - \mathbf{S}_1 \mathbf{M}_{\text{ac}}(\rho_1') \sin[\phi(\rho_1')] \} \\
& + \mathbf{S}_2 \mathbf{M}_{\text{ac}}(\rho_2) \sin[\phi(\rho_2) + \Delta\phi_0] - \mathbf{S}_2 \mathbf{M}_{\text{ac}}(\rho_2') \sin[\phi(\rho_2') + \Delta\phi_0] \}^2 \}^{1/2}
\end{aligned} \tag{4-3}$$

and

$$\begin{aligned}
\phi_{\text{sum}}^{\text{hs}}(\rho) = & \tan^{-1} \{ \{ \mathbf{S}_1 \mathbf{M}_{\text{ac}}(\rho_1) \sin[\phi(\rho_1)] - \mathbf{S}_1 \mathbf{M}_{\text{ac}}(\rho_1') \sin[\phi(\rho_1')] \} \\
& + \mathbf{S}_2 \mathbf{M}_{\text{ac}}(\rho_2) \sin[\phi(\rho_2) + \Delta\phi_0] - \mathbf{S}_2 \mathbf{M}_{\text{ac}}(\rho_2') \sin[\phi(\rho_2') + \Delta\phi_0] \} / \\
& \{ \mathbf{S}_1 \mathbf{M}_{\text{ac}}(\rho_1) \cos[\phi(\rho_1)] - \mathbf{S}_1 \mathbf{M}_{\text{ac}}(\rho_1') \cos[\phi(\rho_1')] \} \\
& + \mathbf{S}_2 \mathbf{M}_{\text{ac}}(\rho_2) \cos[\phi(\rho_2) + \Delta\phi_0] - \mathbf{S}_2 \mathbf{M}_{\text{ac}}(\rho_2') \cos[\phi(\rho_2') + \Delta\phi_0] \} \}
\end{aligned} \tag{4-4}$$

where the distance parameters are:

$$\rho_1 = [(\mathbf{r} + \mathbf{R}/2)^2 + (\mathbf{z} - \mathbf{z}_0)^2]^{1/2}, \tag{4-5a}$$

$$\rho_1' = [(\mathbf{r} + \mathbf{R}/2)^2 + (\mathbf{z} + \mathbf{z}_0 + 2\mathbf{z}_b)^2]^{1/2}, \tag{4-5b}$$

$$\rho_2 = [(\mathbf{r} - \mathbf{R}/2)^2 + (\mathbf{z} - \mathbf{z}_0)^2]^{1/2}, \tag{4-5c}$$

$$\rho_2' = [(\mathbf{r} - \mathbf{R}/2)^2 + (\mathbf{z} + \mathbf{z}_0 + 2\mathbf{z}_b)^2]^{1/2}. \tag{4-5d}$$

The amplitude and phase profiles of the solution in semi-infinite geometry illuminated by dual-interfering-source are illustrated in Figure 4-2.

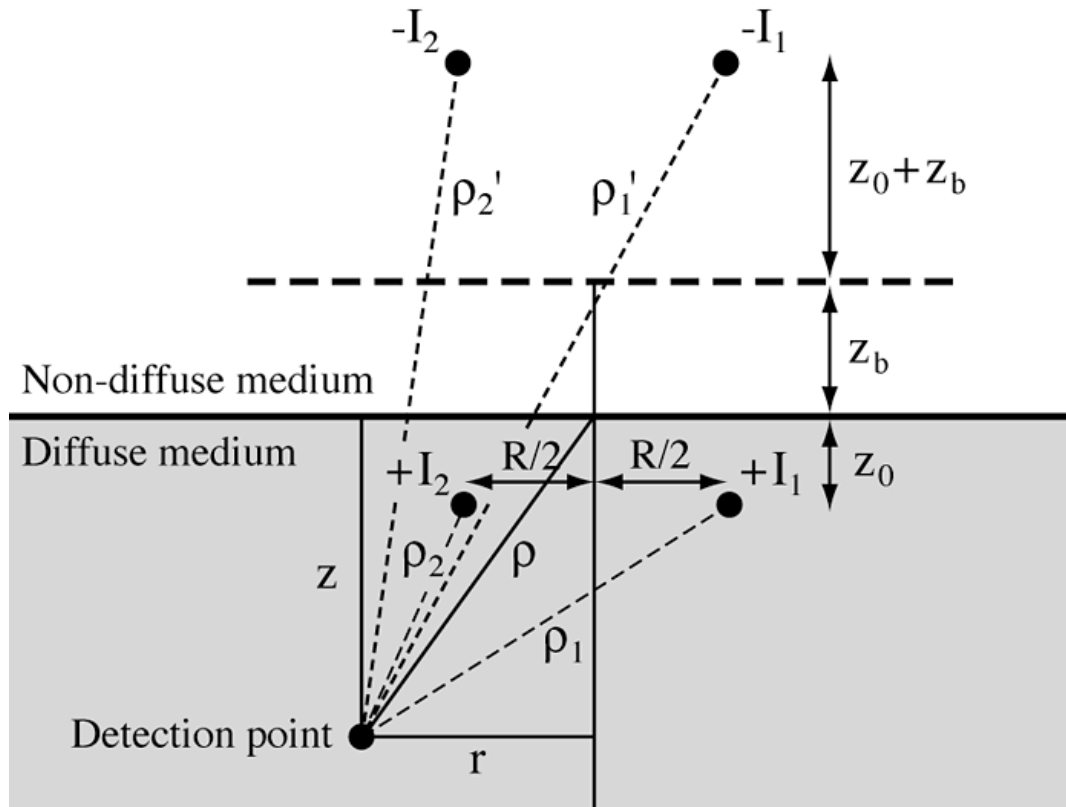


Figure 4-1: Phased array configuration in semi-infinite medium with extrapolated zero boundary condition (two sources are separated by a distance  $R$ ).

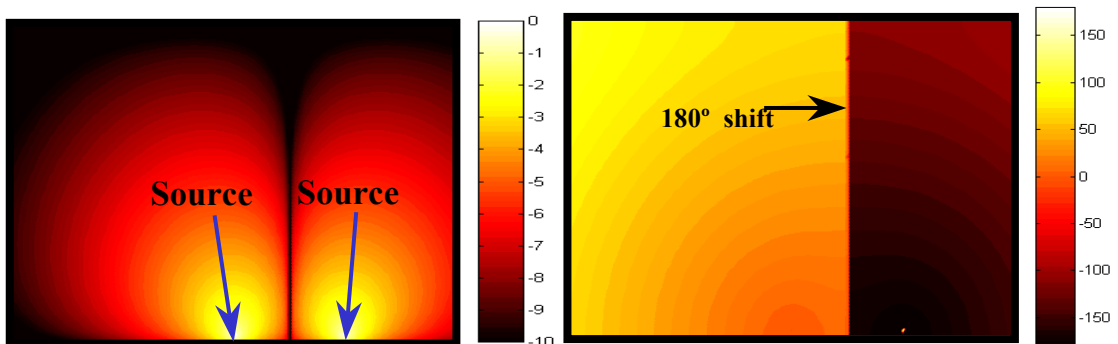


Figure 4-2: Amplitude and phase profiles for the DPDW generated by dual-interfering-source in the semi-infinite geometry. (The parameters for the simulation:

$$\mu_a = 0.04 \text{ cm}^{-1}, \mu'_s = 8.0 \text{ cm}^{-1}, \omega = 200 \text{ MHz, source separation} = 2 \text{ cm})$$

### 4.1.3 Perturbation from Small Heterogeneity

Since the dual-interfering-source data are the summation of the DPDW (scalar wave) from the two phased sources, we can analyze the relationship between the signals coming from single-source and dual-interfering-source schemes using the vector diagram (Figure 4-3(a)). In the dual-interfering-source system, we sum up two vectors, each of which represents the signal obtained from each single-source measurement. As shown in Figure 4-3(a), vectors  $\overline{\mathbf{AB}}$  and  $\overline{\mathbf{BC}}$  represent the signals from two sources, S1 and S2 respectively, with a phase difference of  $(180^\circ - \alpha)$ . The length of the vector represents the amplitude and the orientation indicates the relative phase. Usually there is some phase mismatch in the practical system so that the two sources are not exactly  $180^\circ$  out of phase (*i.e.*,  $\alpha = 1^\circ \sim 2^\circ$ ). In Figure 4-3(a), we exaggerate the phase deviation  $\alpha$  for better visualization.

In the homogeneous background, the amplitudes from equidistant sources should be the same, *i.e.*,  $|\overline{\mathbf{AB}}| = |\overline{\mathbf{BC}}|$ , so their sum will be the vector  $\overline{\mathbf{AC}}$ . Assuming that there is a small absorbing object present in the optical path between S2 and the detector, the vector  $\overline{\mathbf{BC}}$  will change (supposing the phase change is negligible) to  $\overline{\mathbf{BC}'}$ , while  $\overline{\mathbf{AB}}$  remains the same (supposing the perturbation is small enough that the changes in  $\overline{\mathbf{AB}}$  can be neglected), the result will be that the sum of the vectors will also change from  $\overline{\mathbf{AC}}$  to  $\overline{\mathbf{AC}'}$ , which is measured by the amplitude variation  $|\overline{\mathbf{AC}'} - \overline{\mathbf{AC}}|$  and phase shift  $\phi'$ . Applying the relations of trigonometry, we can express the phase shift  $\phi'$  and amplitude variation  $\delta I = (|\overline{\mathbf{AC}'}| - |\overline{\mathbf{AC}}|)$  by the amplitude from signal-source,  $M (=|\overline{\mathbf{BC}}|)$  and its variation  $\delta M (=|\overline{\mathbf{C}'\mathbf{C}}|)$ :

$$\tan \phi' = \frac{\overline{\mathbf{C}'\mathbf{D}'}}{\overline{\mathbf{AD}'}} = \frac{|\delta M| \cos(\alpha/2)}{2M \sin(\alpha/2) - \delta M \sin(\alpha/2)} = \frac{|\delta M / M|}{2 - (\delta M / M)} \cot\left(\frac{\alpha}{2}\right),$$

So that

$$\phi' = \tan^{-1} \left[ \frac{|\Delta|}{2 - \Delta} \cot \left( \frac{\alpha}{2} \right) \right]. \quad (4-6)$$

where  $\Delta = \delta M/M$ . And for amplitude, from

$$\delta I = \overline{AC'} - \overline{AC} = \frac{|\delta M| \cos(\alpha/2)}{\sin \phi'} - 2M \sin \left( \frac{\alpha}{2} \right) = \delta M \left( \frac{M}{\delta M} \right) \cdot \left[ \frac{|\delta M/M| \cos(\alpha/2)}{\sin \phi'} - 2 \sin \left( \frac{\alpha}{2} \right) \right],$$

so that:

$$\frac{\delta I}{\delta M} = \frac{1}{\Delta} \left[ \frac{|\Delta|}{\sin \phi'} \cos \left( \frac{\alpha}{2} \right) - 2 \sin \left( \frac{\alpha}{2} \right) \right]. \quad (4-7)$$

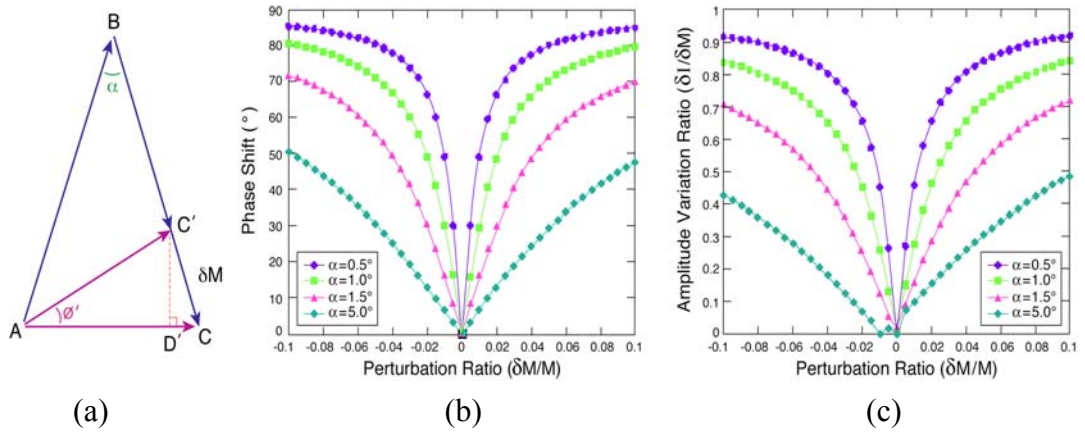


Figure 4-3: (a) Vector diagram for summing up two single-source signals,  $\overline{AB}$  and  $\overline{BC}$ , and resulting in the dual-interfering-source signal,  $\overline{AC}$ . When the DPDW from single-source has been perturbed, *i.e.*,  $\overline{BC}$  changes to  $\overline{BC'}$ , then the result of dual-source also changes to  $\overline{AC'}$ ; (b) Phase shift (absolute value) and (c) Amplitude variation ratio (absolute value) for dual-interfering-source signal vs. the perturbation in single-source signal, with different phase offset ( $180^\circ - \alpha$ ).

Here,  $\delta I/\delta M$  stands for the ratio of change in the dual-interfering-source amplitude to the variation in single-source amplitude. From the equations above, we can analyze how the phase shift  $\phi'$  and amplitude change  $\delta I$  in the dual-interfering-

source scheme is related to the amplitude change in a single source-detector channel,  $\delta M$ , with different perturbation ratio  $\Delta (= \delta M/M)$ .

Figure 4-3(b) and (c) plot the relations between the dual-interfering-source signal (phase and amplitude) variations and the perturbation ratio in single-source, under different phase offsets ( $180^\circ - \alpha$ ). Figure 4-3(b) shows the response of the dual-interfering-source phase shift to different perturbations. For instance, in the case of phase difference of  $178^\circ$  ( $\alpha = 2^\circ$ ), we can see that the phase shift increases with the increase in perturbation ratio  $\delta M/M$ , and the rate of increase is very rapid especially when the perturbation is small, resulting in a  $30^\circ$  phase shift on a 2% perturbation, while the rate of increase slows down when the perturbation gets bigger. This trend agrees with the experiment and simulation results [96]. Also, if we vary the phase offset  $\alpha$ , the sensitivity of the dual-interfering-source phase shift will change. When the phase difference is close to  $180^\circ$  (perfect cancellation), for example,  $\alpha = 0.5^\circ$ , there will be a large response to a small perturbation ( $70^\circ$  for 2% perturbation), while it asymptotically approaches  $85^\circ$  under a larger perturbation. In this case, the system is very sensitive to the presence of small perturbations, but it could not discriminate the intensity difference for larger perturbations ( $> 5\%$ ). On the contrary, if the phase offset is larger ( $\alpha = 5^\circ$ ), the response of the dual-interfering-source phase shift is smaller (only  $10^\circ$  for 2% perturbation) compared with the case of  $0.5^\circ$  offset, but the sensitivity to perturbation is more evenly distributed so as to be able to indicate the intensity of perturbation. The result suggests that by adjusting the phase difference offset, we can change the system's sensitivity to probing different perturbation intensities. This trend agrees with the experimental results reported by Morgan *et al* [97]. And from Figure 4-3(c), we can see that the dual-interfering-source amplitude behaves similarly in response to different perturbations. A slight difference exists in

that the zero phase shift will occur only when the perturbation  $\delta M/M = 0$ , but the amplitude variation of zero will happen at two positions, corresponding to the vectors  $\overline{AC}$  and  $\overline{AC'}$  in Figure 4-3(a) where  $\overline{AC} = \overline{AC'}$ . This can be seen clearly in the green plot of Figure 4-3(c) when  $\alpha$  is large.

## 4.2 Sensitivity Analysis for Single- and Dual-source Systems

Many investigators have compared the sensitivity of single- and dual-interfering-source systems [61,62,75,87,98]. For example, Erickson *et al* [87] demonstrated that a dual-interfering-source system could provide higher detection sensitivity than a single-source configuration from numeric simulations, while Papaioannou *et al* [98] observed a comparable sensitivity for an optically scanned phased array system and a continuous wave system, which suggests that this topic needs further detailed analysis.

### 4.2.1 Noise Model for Single- and Dual-source Systems

In the detection of photons using a single-source system, the noise level will determine the detection threshold. There are some relevant noise sources in experimental and clinical situations. Shot noise is the dominant factor for an ideal experiment system, which is due to the randomness in photon multiplication and the fluctuation of the dark current, and is related to the square root of the number of photons detected. For a clinically relevant system (1 Hz bandwidth), the estimated shot noise level is about 0.1% in amplitude and  $0.05^\circ$  in phase [74]. For the input light power ( $\sim 3$  mW) used clinically and the experimental temperature, the shot noise is the major source from the ideal electronic circuit, and is determined mostly by the detector. The signal current from a photon detector is:

$$\mathbf{i}_{\text{sig}} = \frac{\eta q}{h\nu} (\mathbf{R}\Phi) \cdot \mathbf{G} \quad (4-8)$$

where  $\eta$  is the quantum efficiency of the detector,  $q$  is the elementary charge,  $h\nu$  is the energy of a single photon,  $\Phi$  is the photon fluence given by Eq. (3-1),  $R$  is the detecting area ( $\text{cm}^2$ ) and  $G$  is the internal gain of the detector.

The shot noise can be expressed as [99]:

$$\mathbf{i}_{\text{shot}} = \sqrt{2q(\mathbf{i}_{\text{sig}} / A)\mathbf{B}} \quad (4-9)$$

where  $i_{\text{shot}}$  is the shot noise current from the signal  $i_{\text{sig}}$ ,  $A$  is the modulation of the source,  $B$  is the system bandwidth (we choose 1 Hz).

Thermal noise and other signal-independent noise can be approximated by the Noise Equivalent Power of the detection system [99]. The expression for signal-independent noise is:

$$\mathbf{i}_{\text{NEP}} = \text{NEP} \cdot \mathbf{B}^{1/2} \mathbf{K} \quad (4-10)$$

where  $K$  is photoelectric conversion efficiency and  $B$  is the system bandwidth.

When put together, the noise from the photoelectric measurement in fractional amplitude can be expressed as:

$$\mathbf{N}_1 = \sqrt{\mathbf{i}_{\text{shot}}^2 + \mathbf{i}_{\text{NEP}}^2} / \mathbf{i}_{\text{sig}} \quad (4-11)$$

While in practice, there are other sources for the noise, such as the variation in source amplitude due to the fluctuation in RF power and laser light intensity, and the position error during the scanning of source and detector fibers. Here we estimate those effects as random error  $N_2 = 0.5\%$  from our experimental calibration.

Phase noise is composed of the amplitude independent part (phase noise floor) and the amplitude dependent part [99]. In our system, the phase is detected by the heterodyne method (the heterodyne method shifts the radio frequency (RF) to a lower frequency for phase detection, while the homodyne method detects the phase shift at

the radio frequency, see Chapter 6 for details) [100], using a zero-crossing phase meter (Krohn-Hite Corp.). The phase meter measures the phase angle by measuring the time ratios (Figure 4-4) [101]:

$$\phi = (T_T / T_R) \times 2\pi \quad (4-12)$$

where  $T_T$  is the time interval between the positive going zero-crossing of  $V_R$  (reference signal) and  $V_T$  (measured signal), and  $T_R$  is the period of  $V_R$ .

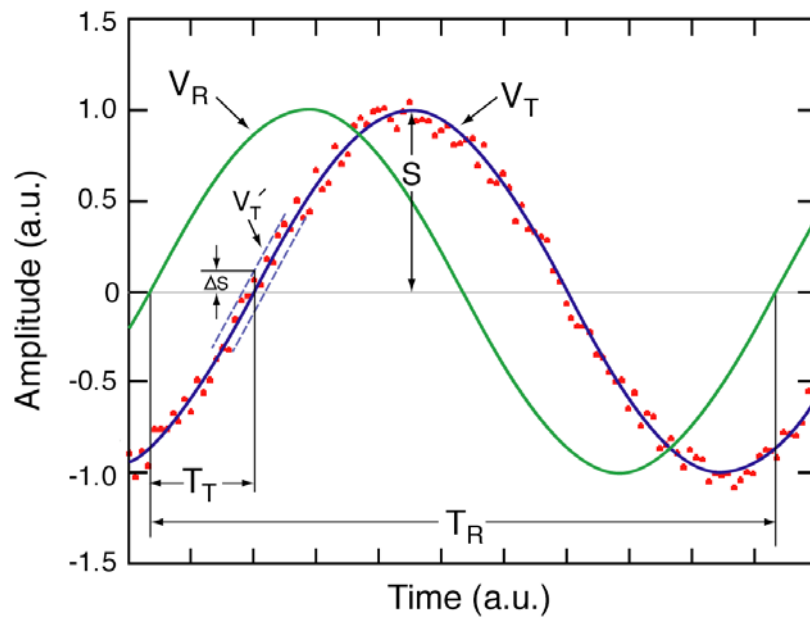


Figure 4-4: Phase measurement through zero-crossing time interval.

When the tested signal contains amplitude variation with a standard deviation  $\Delta S$  from the ideal intensity  $S$  (the peak value of  $V_T$ ), as shown in Figure 4-4, the variance of the amplitude will cause the shift of the zero-crossing point, and hence the phase reading. We can calculate the related phase standard deviation in terms of the fractional amplitude variation  $N_s = \Delta S / S$  as follows:

For the signal in pure sine wave,  $V_T = S \cdot \sin(\omega t + \phi)$ , at the zero-crossing point  $T_T$ , we have:

$$0 = S \cdot \sin(\omega T_T + \phi), \quad (4-13)$$

When the signal is contaminated by noise variation  $\Delta S$ , which will also introduce the shift of zero-crossing points that causes the phase noise  $\sigma_1$ . We can represent the noisy data within the envelope  $V'_T$ , by shifting  $V_T$  with a phase error  $\sigma_1$ . For  $V'_T$  we have:

$$\Delta S = S \cdot \sin(\omega T_T + \phi + \sigma_1). \quad (4-14)$$

Comparing Eqs. (4-13) and (4-14), we can solve  $\sigma_1$  expressed as:

$$\sigma_1(N_s) = \sin^{-1}(N_s). \quad (4-15)$$

From Eq. (4-15), the phase noise is inversely proportional to the signal-to-noise ratio when the signal-to-noise ratio is larger than 10, and increases more rapidly when the signal gets even smaller [99]. When the signal is less than or equal to the noise level, the phase will vary randomly in a range of  $180^\circ$ . We verified the Eq. (4-15) with experiments (data not shown here). The standard deviation for total phase noise is then [99]:

$$\sigma_\phi(N_s) = \sigma_1(N_s) + \sigma_0, \quad (4-16)$$

where  $\sigma_0 = 0.05^\circ$  is the phase noise floor according to the specifications.

For single source, we calculate the noise level with:

$$N_{s-s} = \sqrt{N_1^2 + N_2^2}, \quad (4-17)$$

and the phase noise from the circuit:

$$\sigma_{s-s} = \sigma_\phi(N_{s-s}). \quad (4-18)$$

For the dual-source case, we first obtained the scattered waves from each single source (amplitude and phase), and then synthesized them by vector summation. From the noise-free data, we obtained the difference between with and without the presence of the object, which is the signal perturbation we would like to detect. The

noise level for the homogeneous background in dual-source detection can be obtained through the standard deviation of the summation vector from single source data added with the noise from Eqs. (4-17) and (4-18) (see Figure 4-5).

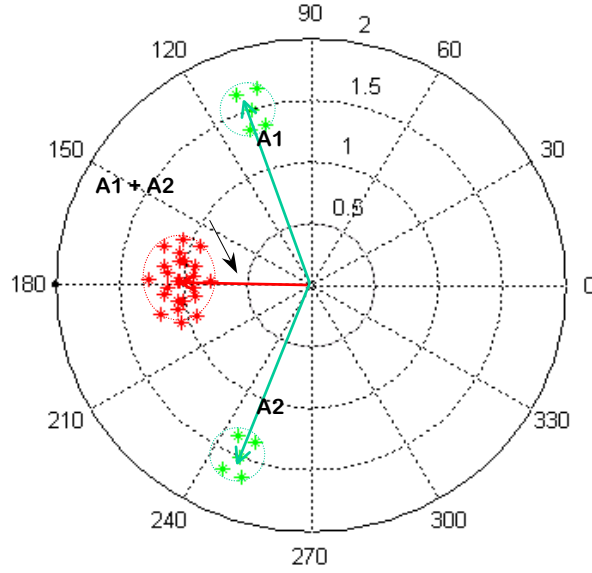


Figure 4-5: Noise model for summation of two vectors. The vectors are the average signals and the dotted circles are the distribution of sampling values. The standard deviation of the green spots is the noise distribution for single-source. The standard deviation of the red spots gives the amplitude and phase noise of the dual-source measurement.

Suppose we sample the signal from source S1, the vector  $\overline{\mathbf{A1}}$  can be expressed by the normal distribution with the mean value of A1 (including amplitude and phase) and the amplitude standard deviation  $N_{s-s}^{S1}$  and the phase standard deviation  $\sigma_{s-s}^{S1}$ :

$$\overline{\mathbf{A1}} \sim N(\mathbf{A1}, N_{s-s}^{S1}, \sigma_{s-s}^{S1}), \quad (4-19)$$

as shown in Figure 4-4. Similarly, for source S2, we have:

$$\overline{\mathbf{A2}} \sim N(\mathbf{A2}, N_{s-s}^{S2}, \sigma_{s-s}^{S2}). \quad (4-20)$$

If we sum them together, we will get the dual-source signal:

$$\overline{\mathbf{A3}} = \overline{\mathbf{A1}} + \overline{\mathbf{A2}} \sim \mathbf{N}(\mathbf{A3}, \mathbf{N}_{d-s}, \sigma_{d-s}), \quad (4-21)$$

which can also be approximated as a normal distribution where  $\mathbf{N}_{d-s}$  and  $\sigma_{d-s}$  represent the fractional amplitude and phase noise for the dual-source system that can be calculated if we have enough sampling points. Note that when we calculate the shot noise in (4-19) and (4-20), there is a  $\sqrt{2}$  factor due to the increase of the dc component.

#### 4.2.2 Signal to Noise Analysis

For detection and location of the heterogeneity, we compare the signals (fractional amplitude  $[|\Phi_{\text{hetero}} - \Phi_{\text{homo}}| / \Phi_{\text{homo}}]$  and phase  $[|\text{Arg}(\Phi_{\text{hetero}}) - \text{Arg}(\Phi_{\text{homo}})|]$ ) to the noise threshold from the homogeneous background. In other words, suppose we scan an object with different optical properties from the background, there will be some variations or perturbations in the signals (amplitude and phase deviate from the values in a homogeneous case), and the perturbation will be related to the level of heterogeneity. The less the object's optical properties deviate from the background, the less perturbation signals we can detect. If  $\Delta\mu_a$  and  $\Delta\mu'_s$  are small enough, the perturbation signals obtained from the detector will be less than the detection noise level, then the object is beyond our system's detection limit that we could not detect the object.

The forward simulation was performed using the photon migration imaging software (PMI) developed by Boas D.A., O'Leary M.A. and Li X.D. at the University of Pennsylvania [65]. For both single-source and dual-interfering-source cases, we calculated the signal variations due to the scanning of the absorbing or fluorescent object. Then, we compared the perturbation with the noise floor in the homogeneous

background. If the perturbation in amplitude or phase is larger than the noise floor in the homogeneous background, then the presence of the object will be detected [74,78].

### **4.3 Detection Limit for Dual-source System**

#### **4.3.1 Detection Limit for Absorptive Perturbation**

The geometry for the simulation model is illustrated in Figure 4-6. The background medium is an infinite slab with a thickness of 5 cm, and its optical properties are chosen to mimic the human breast tissue with  $\mu_a = 0.05 \text{ cm}^{-1}$  and  $\mu'_s = 10.0 \text{ cm}^{-1}$  [55]. We considered two clinical relevant set-ups: transmission mode and remission mode. For the transmission mode, as shown in Figure 4-6, the source and detector face each other in the single-source configuration, and in the dual-interfering-source configuration, two out-of-phase sources ( $0^\circ$  and  $179^\circ$ ) are separated by 2 cm and the detector is placed in the middle plane of two sources. The reason we choose  $179^\circ$  is that if the two sources are exactly  $180^\circ$  out of phase, the signal in homogenous medium will be zero, so that the phase noise will be  $180^\circ$ , which will be too noisy for detection. By selecting  $179^\circ$  between the two sources, we bring the amplitude signal down about 40dB, but can still detect the signal. The modulation frequency is 50 MHz, which corresponds to our current apparatus. For the remission mode, sources and detector are placed on the same side of the slab, with a constant source-detector separation of 5 cm to ensure the constant depth sensitivity. The source separation for dual-source configuration is also 2 cm. In each case, we scan an absorbing object (with scattering being the same as the background) to create the perturbation. The image source-object pair technique is used, with the extrapolated zero boundary condition.

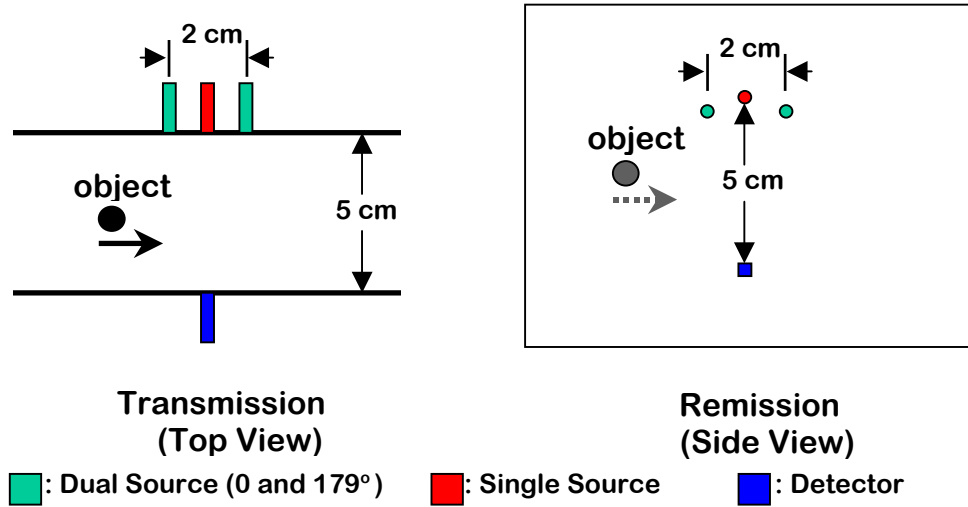


Figure 4-6: Transmission and remission geometry for single- and dual-interfering-source configurations.

We study the detection sensitivity for single- and dual-interfering-source systems in both transmission and remission geometries. The background medium and object's optical properties are kept the same:  $\mu_a^{Background} = 0.05 \text{ cm}^{-1}$ ,  $\mu_s^{Background} = 10.0 \text{ cm}^{-1}$  and  $\mu_a^{Object} = 0.20 \text{ cm}^{-1}$ ,  $\mu_s^{Object} = 10.0 \text{ cm}^{-1}$ . The objects are scanned with i) different sizes; ii) different depths from the source plane (source-detector plane in remission case).

*Detecting the Object with Different Depth and Size:* In Figure 4-7 we plot the contours for the detection threshold from amplitude and phase signals in both single- and dual-source configurations. For the transmission case with single-source conditions, the amplitude signal gives better sensitivity than the phase signal to detect the absorption heterogeneity, and the threshold contour is symmetrical to the central plane between the source and detector, which is due to the reciprocity of the source and detector in single-source setup. The detection sensitivity becomes worse when the

object is closer to the middle plane (depth = 2.5 cm). Generally, the detection limit in this case is about 3 to 4 mm, which is similar to the results given by Boas *et al* [74]. For dual-interfering-source geometry, we can see that the phase signal gives a better sensitivity than the amplitude signal, which is due to the larger transition of phase signal when the object scans through the null line. Note that the detection ability for the dual-source system is non-symmetrical from the higher detection sensitivity (2.3 mm) when the object is closer to the source plane, to the lower sensitivity (4 mm) when the object is closer to the detector plane. This can be explained by the non-symmetrical spatial sensitivity profile created by the interference of two sources (*cf.* Figure 4-2). And when the object is closer to the source plane, the dual-source system provides better detection sensitivity than the single-source system, but when the object is far from the sources, the sensitivity for dual-source actually becomes weaker than the single-source case. The reason is due to the fact that the photon paths from source 1 to the detector and source 2 to the detector get closer (intermingled with each other) when approaching the detector, hence the scanning of the object will affect the signals from both sources, which results in the decrease of the perturbation signal.

For the remission case, both single- and dual-source contours are non-symmetrical, and could not detect the object depth larger than 3 cm for a 1 cm diameter object, which is limited by the source-detector separation (here it is 5 cm). While in this case, the dual-source system always shows higher sensitivity than the single-source system.

From the two charts in Figure 4-7, we can see that different systems give different detectability for the same model, which might be helpful when we design our detection systems in terms of the selection of either transmission or remission geometry, and single- or dual-source configuration.

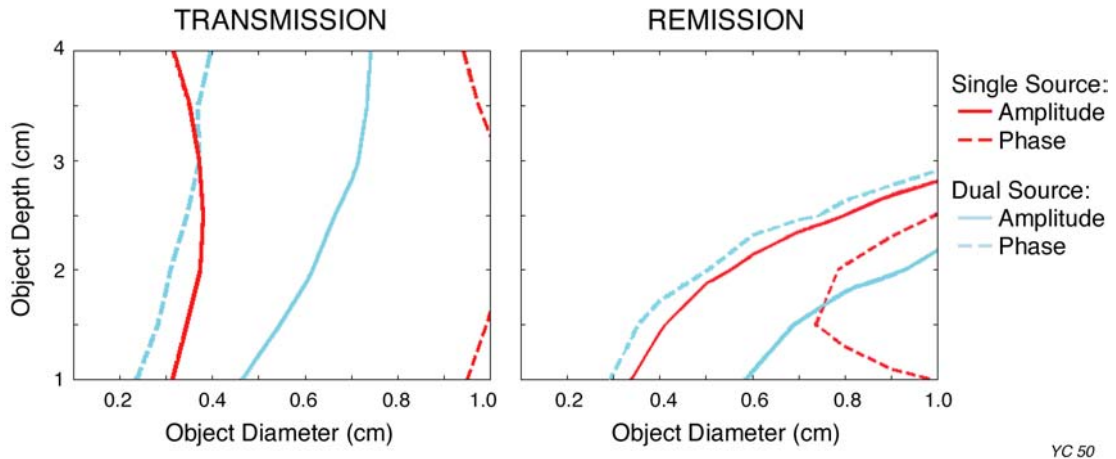


Figure 4-7: Contour plot of the signal-to-noise ratio equals to one for amplitude and phase signals in single- and dual-source configurations. To the right side of the curve indicates a signal-to-noise ratio larger than 1 and the object with those parameters will be detected.

*Detecting the Object with Different Absorption Contrast:* Figure 4-8 shows the contours indicating the smallest detectable absorber diameters as a function of absorption of the outside background,  $\mu_a^{\text{out}}$  and inside the object,  $\mu_a^{\text{in}}$  under transmission mode. In this case, the object depth is fixed to 2.5 cm, which is the central plane between the source and detector. The detection sensitivity reaches to the minimum at the central plane for single-source; for dual-interfering-source, the lowest detection sensitivity can also be measured at the central plane because we can replace the sources and detector plane to overcome the poorer sensitivity near the detector plane. The shaded area indicates the detectable region. From the contour plots, we can see that for the single-source results, the sensitivity of detection decreases with the increase of background absorption, which will give higher shot noise and lower absorption contrast. The trend of the contour agrees with the results reported in Ref.

[74], though the numbers are not exactly the same since we use different modulation frequency and slab thickness. When we compare it with the dual-source's contour, the pattern is similar but the sensitivity has increased. This is indicated by the shifting of the contours towards the upper-left direction. The smaller the object diameter, the larger the difference. This is due to  $a^3 \mu_a^{\text{in}}$ , which accounts for the perturbation signal, so that for a smaller object, the dual-source detection will be more sensitive in terms of absorption contrast.

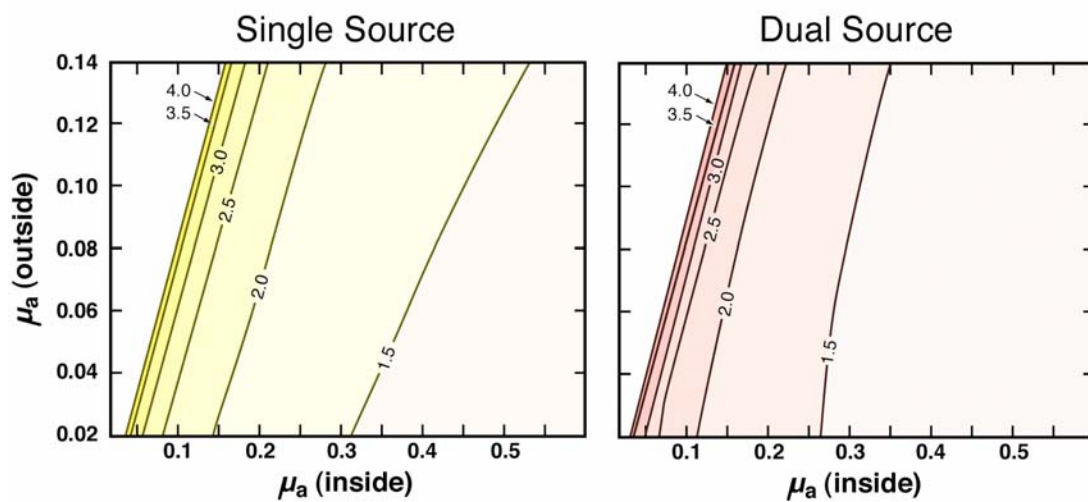


Figure 4-8: Diameter of the smallest detectable absorber plotted as a function of  $\mu_a^{\text{out}}$  and  $\mu_a^{\text{in}}$  for single- and dual-source systems in transmission mode. The background and object scattering coefficients are kept same ( $10 \text{ cm}^{-1}$ ) and the modulation frequency is 50 MHz. (Bandwidth = 1 Hz)

Figure 4-9 compares the contours of the diameter for the smallest detectable absorber as a function of  $\mu_a^{\text{out}}$  and  $\mu_a^{\text{in}}$  under remission mode. Also in this case, the object depth is fixed at 2.5 cm. Generally, the detection with the transmission mode will give a higher sensitivity than the remission mode, if we compare the contours with the same object diameter to the corresponding one in Figure 4-8. And the detection sensitivity deteriorates faster with the decrease of absorption contrast in the

remission case (the contour bends towards the lower right direction in Figure 4-9) due to the reason that the remission measurement is less sensitive than transmission, as shown in Figure 4-7. Similar to Figure 4-8, the dual-interfering-source system still gives better sensitivity than the single-source system.

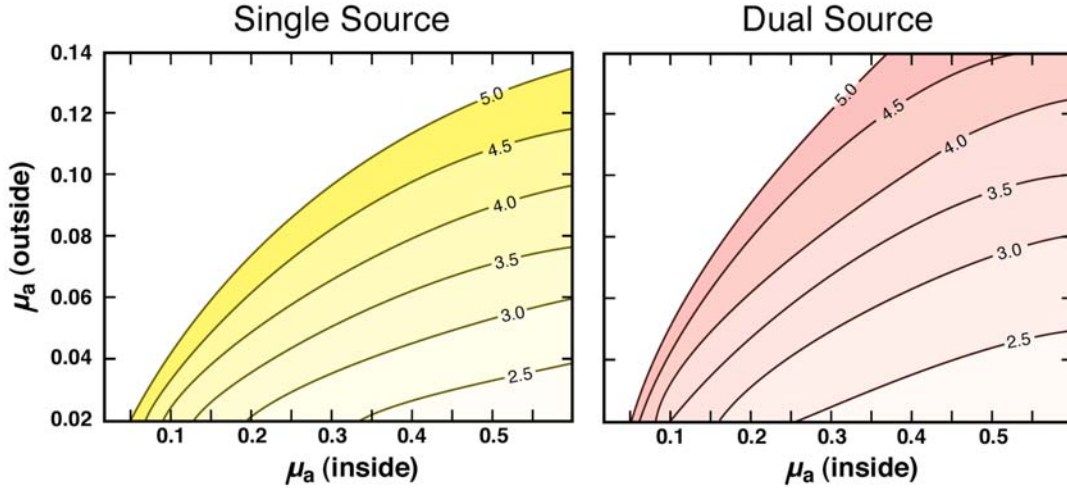


Figure 4-9: Diameter of the smallest detectable absorber plotted as a function of  $\mu_a^{\text{out}}$  and  $\mu_a^{\text{in}}$  for single- and dual-source systems in remission mode. The background and object scattering coefficients are kept same ( $10 \text{ cm}^{-1}$ ) and the modulation frequency is 50 MHz. (Bandwidth = 1 Hz)

In this section we focused on the detection sensitivity analysis for absorptive perturbation and hence provided information for detection and localization of absorbing objects. The signal-to-noise ratio is the limiting factor for detection. It is difficult to directly compare the performance of single- and dual-interfering-source systems, since there are many parameters involved regarding the optimal configuration for the dual-source system such as the sources' separation and modulation frequency [96]. Instead, we have studied the detectability for the same model (background and absorber) under practical experimental setups. The analysis of the amplitude and phase signals suggests that the dual-interfering-source phase

component can sensitively amplify the small perturbation to a larger phase signal, which could yield higher signal-to-noise ratio for the purpose of detection. The sensitivity of the dual-interfering-source detection might provide complementary information for the conventional single-source detection, in both the detection and characterization.

### 4.3.2 Detection Limit for Fluorescence Perturbation

We also perform a quantitative comparison between the single source and the dual-interfering-source configurations for the detection of fluorescent heterogeneities embedded in a piecewise highly scattering homogeneous fluorescent background. The models used in this study were derived from Ref. [78]. The medium considered in this analysis is an infinite long slab with a finite width of 5 cm. A single spherical inhomogeneity is embedded in the center of the slab. Extrapolated zero boundary conditions with image sources were employed in the analysis. The analytical solution for the fluorescence DPDW in dual-interfering-source configuration is the summation of two phased fluorescence DPDWs from each source [89]:

$$\Phi_{\text{hetero}}^{\text{fir}}(\mathbf{r}_{s1}, \mathbf{r}_{s2}, \mathbf{r}_d, \omega, \mathbf{a}) = \Phi_{\text{hetero}}^{\text{fir}}(\mathbf{r}_{s1}, \mathbf{r}_d, \omega, \mathbf{a}) + \Phi_{\text{hetero}}^{\text{fir}}(\mathbf{r}_{s2}, \mathbf{r}_d, \omega, \mathbf{a}) \quad (4-22)$$

where  $\Phi_{\text{hetero}}^{\text{fir}}(\mathbf{r}_s, \mathbf{r}_d, \omega)$  is the heterogeneous FDPDW given by Eq. (3-15),  $\mathbf{r}_{s1}$  and  $\mathbf{r}_{s2}$  are the positions of the two out-of-phase sources.

Optical properties of the chromophore at the excitation wavelength ( $\lambda_{\text{ex}}$ ) and the emission wavelength ( $\lambda_{\text{em}}$ ) are presented in Table 4-1. The optical properties related to the homogeneous medium are indicated by a subscript 1; optical properties related to the object are indicated by a subscript 2; optical values related to the fluorescent DPDW are indicated with an extra subscript f. We use a superscript c to indicate chromophore-related parameters. Other parameters as indicated in Table 4-2

were chosen to be close to one of the most commonly used NIR dyes — Indocyanine Green (ICG), although the values are not exactly the same (*i.e.*  $\tau_1 \approx 0.5\text{ns}$  and  $\eta \approx 5\%$  for ICG) [37,38].

Table 4-1: Chromophore optical properties (units in  $\text{cm}^{-1}$ )

Background				Inhomogeneity			
$\lambda_{\text{ex}}$		$\lambda_{\text{em}}$		$\lambda_{\text{ex}}$		$\lambda_{\text{em}}$	
$\mu_{\text{a1}}^{\text{c}}$	$\mu_{\text{s1}}^{\text{'}}$	$\mu_{\text{a1f}}^{\text{c}}$	$\mu_{\text{s1f}}^{\text{'}}$	$\mu_{\text{a2}}^{\text{c}}$	$\mu_{\text{s2}}^{\text{'}}$	$\mu_{\text{a2f}}^{\text{c}}$	$\mu_{\text{s2f}}^{\text{'}}$
0.02	8.0	0.025	8.0	0.0205	8.0	0.0256	8.0

Table 4-2: Quantum yield  $\eta$ , background fluorophore concentration  $N_1$ , lifetime  $\tau_1$  and extinction coefficients  $\varepsilon$  and  $\varepsilon_f$ .

$\eta$	$N_1$	$\tau_1$	$\varepsilon$ (at $\lambda_{\text{ex}}$ )	$\varepsilon_f$ (at $\lambda_{\text{em}}$ )
10%	0.1 $\mu\text{M}$	1.0 ns	$0.5 \times 10^5 \text{ cm}^{-1}\text{M}^{-1}$	$0.05 \times 10^5 \text{ cm}^{-1}\text{M}^{-1}$

In the case of a single source, the object was located in the middle between the source and the detector. For the case of dual-interfering-source configuration, the two sources were separated by 2cm and modulated at 200MHz. The object in the dual-interfering configuration was placed in front of a source. This position corresponds to the maximum of sensitivity in terms of object position at  $\lambda_{\text{ex}}$ . The detector was placed 0.25cm off the cancellation plane (plane bisecting the two sources) closer to the

source in front of the object to avoid the large phase noise when placed right at the cancellation plane [88] (*cf.* Figure 4-10).

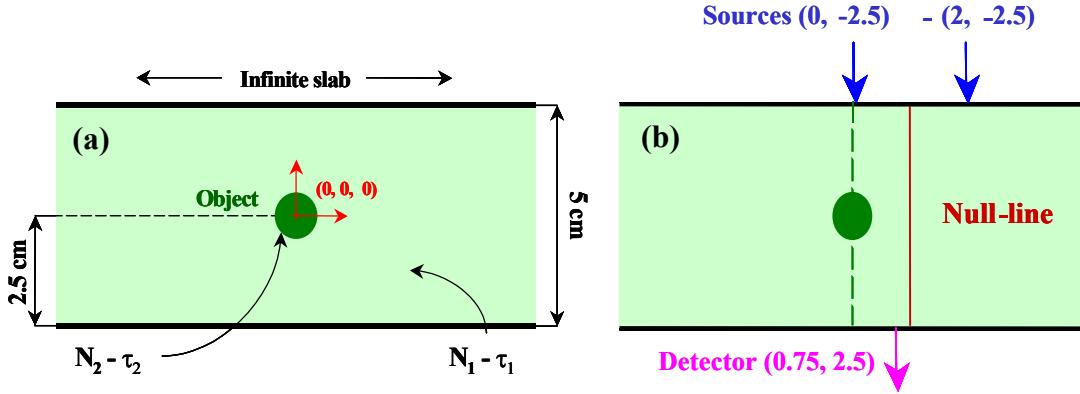


Figure 4-10: Geometrical set-up for the simulation. The background (inhomogeneity) medium is characterized by the fluorophore concentration  $N_1$  ( $N_2$ ) and lifetime  $\tau_1$  ( $\tau_2$ ).

For dual-sources configuration, the detector is 0.25 cm off the null-line on the side closer to the object. (Adapted from Ref. [89])

The criteria that we use to determine the detection and characterization limits are based on a signal-to-noise analysis similar to the previous approach [78]. The noise model considered has a fractional amplitude random noise of  $N_{s-s} = 1\%$  and an absolute phase random noise of  $\phi_{s-s} = 0.5^\circ$ . Thus the heterogeneity was detectable when the relative amplitude and phase of the FDPDW, were above the noise threshold ( $[\left| \Phi_{\text{hetro}}^{\text{nr}} / \Phi_{\text{homo}}^{\text{nr}} \right| - 1] > N_{s-s}$  and  $|\text{Arg}(\Phi_{\text{hetro}}^{\text{nr}}) - \text{Arg}(\Phi_{\text{homo}}^{\text{nr}})| > \sigma_{s-s}$ ). For dual-interfering-source configuration, we use the same noise model aforementioned. With the optical parameters of Table 4-1 and fluorophore characteristics of Table 4-2, we get a noise of 1.5% in amplitude and  $0.7^\circ$  in phase. Thus the criteria employed in the

dual-interfering-source configuration were:  $\left| \Phi_{\text{hetro}}^{\text{fir}} / \Phi_{\text{hom o}}^{\text{fir}} \right| - 1 > 1.5\%$  and  $\left| \text{Arg} \left( \Phi_{\text{hetro}}^{\text{fir}} \right) - \text{Arg} \left( \Phi_{\text{hom o}}^{\text{fir}} \right) \right| > 0.7^\circ$ .

We have investigated a broad range of fluorophore concentration and lifetime contrast using the same signal-to-noise considerations. The fractional amplitude perturbation and relative phase change contours for different inhomogeneity radii are presented in Figure 4-11.

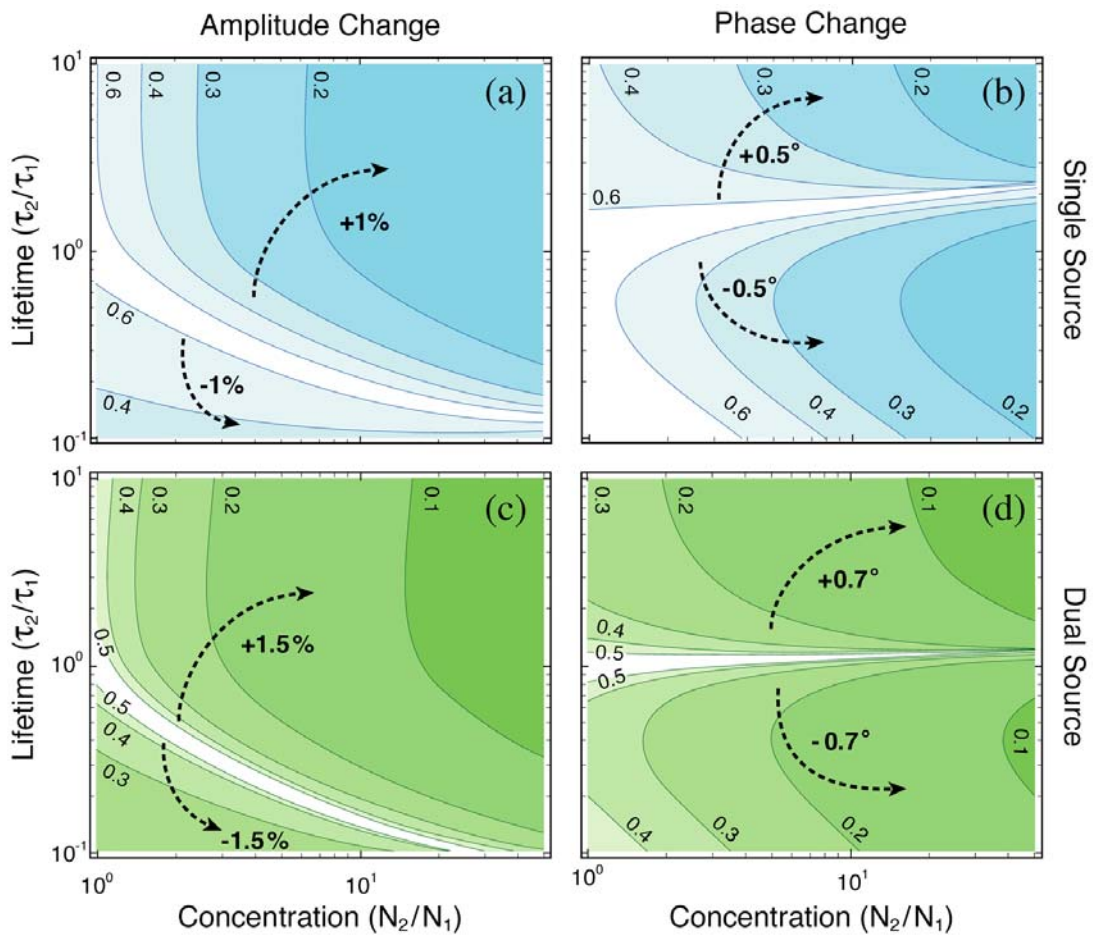


Figure 4-11: Contour plot of the fractional amplitude ((a) and (c)) and phase difference ((b) and (d)) for single source system ((a) and (b)) and phased array system ((c) and (d)). The legends on the iso-contours correspond to the radius of the inhomogeneity. The filled areas correspond to the parameter space where the perturbation is higher than the criteria used. (Adapted from Ref. [89])

Both single-source and dual-source configurations are considered in these simulations. The results for the single source configuration are in accordance with those presented in Ref. [78]. The filled areas correspond to the concentration and lifetime contrasts allowing detection of the inhomogeneity.

First, we note that in both cases, single- and dual-interfering-source, the increase of concentration and lifetime contrast result in an increase in both amplitude and phase perturbation. Thus, the higher the concentration contrast and the higher the lifetime contrast, the smaller the detectable object.

Fluorophore concentration increase induces two opposite effects [78]. The first one is the increase of fluorescent photons due to a higher number of fluorophores excited. The second one is the photon fluence decreasing due to the increase of absorption both at the excitation and fluorescent wavelengths. In all the simulations herein, the second effect is small as long as the absolute concentrations are low. This is depicted in the fractional amplitudes contours (Figure 4-11 (a) and (c)). The higher the concentration, the higher the perturbation signal. Moreover, this perturbation is positive indicating that the detected fluence increases compared to the homogeneous state (higher deflection of the null line in the phased array). So, for a given lifetime  $\tau_2$ , as the fluorophore concentration  $N_2$  increases, the object size required to produce the same amount of amplitude and phase perturbation decreases, and therefore a smaller object can be detected.

In the same manner, the fluorophore lifetime increase leads to two opposite effects on the FDPDW amplitude. On one hand, the fluorescence fluence increases with longer lifetimes due to less quenching. On the other hand, the fluorescence fluence decreases with longer lifetimes due to greater demodulation ( $\propto 1/(1 - i\omega\tau_2)$ ).

For a given fluorophore concentration  $N_2$ , the fluorescent amplitude will increase until the two effects described above cancel and the fluorescent fluence reaches a saturation state.

Concerning the relative phase shift, the same statement similar to that in Ref. [78] could be made: the lower-left corner of the phase contours plots corresponds to the area where the concentration contrast predominates (negative phase change due to increase of absorption) and the upper-right corner corresponds to the areas where the lifetime contrast predominates (positive phase change due to longer lifetime in the tumor).

Although the same trends could be found in both single- and dual-interfering-source configurations, there are quantitative differences. For instance, let us consider the detection of a 2 mm radius inhomogeneity. In the case without lifetime contrast, which is relevant to ICG as long as this dye does not appear to exhibit lifetime sensitivity related to tissue state [37], the concentration contrast needed falls from 8.5 in single-source configuration to 3 in case of dual-interfering-source when amplitude is used. Thus, the threshold of detection is improved roughly by a factor of 3 in this case. This enhancement decreases with the increase of the radius of the heterogeneity. It falls to 2 for a 3 mm radius and to roughly 1.5 for a 4 mm radius. When phase changes are considered in this specific case ( $\tau_1 = \tau_2 = 1$  ns), no obvious enhancement in threshold detection is achieved. On the other hand, if the lifetime contrast increases, even if the amplitude enhancement is not improved, the phase sensitivity is highly enhanced. For a 2 mm radius heterogeneity, and for a lifetime contrast of 5, the detection threshold in terms of concentration contrast falls from 20 to 2 comparing single- and dual-interfering-source configuration. As stated above, this enhancement also decreases with the increase of the heterogeneity radius.

It was shown that dual-interfering-source configuration out-performs single-source technique for detecting a small spherical object. The detection threshold enhancement was up to 3 times if amplitude was considered. Moreover, if a lifetime contrast was induced, this enhancement was even more appreciable. In both cases, the enhancement was inverse proportional to the size of the heterogeneity.

#### 4.4 Object Localization using Phased Array System

One of the goals of developing the high sensitivity phased array system is for accurate object localization [22,23]. We employ the fitting method to estimate the object position from the scanning data. Here we use a fluorescent object as an illustration. This approach can be applied to absorptive and scattering heterogeneity. First we generate the one-dimensional point-object functions (POF) through the analytical solutions for a small fluorescent object (1 mm in diameter) placed at various positions [77]. Figure 4-12 illustrated the normalized POF for position  $x = 2, 3$  and  $4$  cm, assuming the parameters used in Table 4-3.

Table 4-3: Parameters for POF calculation

Background		Object		Fluorophore		
$\mu_a$ (cm <sup>-1</sup> )	$\mu'_s$ (cm <sup>-1</sup> )	$\mu_a$ (cm <sup>-1</sup> )	$\mu'_s$ (cm <sup>-1</sup> )	[C] ( $\mu$ M)	$\tau$ (ns)	$\eta$ (%)
0.05; 0.05	10.0; 10.0	0.35; 0.41	10.0; 10.0	1.0	0.56	10

Note: The 1<sup>st</sup> and 2<sup>nd</sup> values in optical properties are respect to excitation and emission wavelength; [C]: concentration;  $\tau$ : lifetime;  $\eta$ : quantum yield.

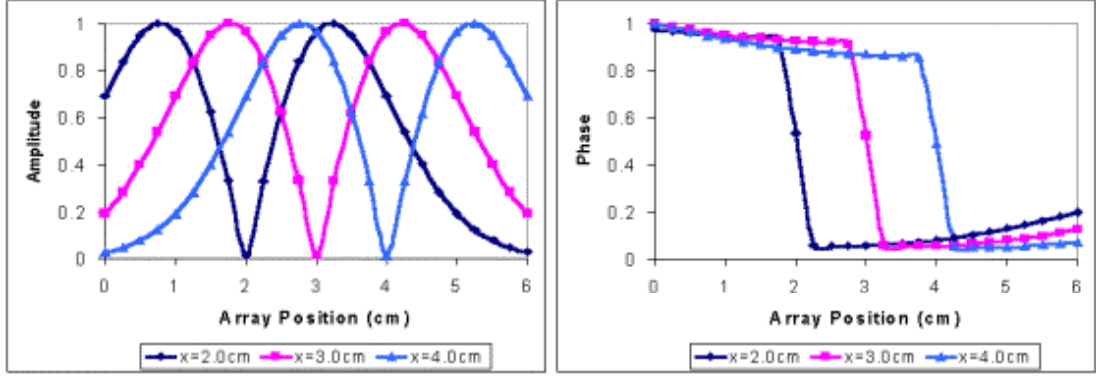


Figure 4-12: Point-object functions (POF) for object positions at  $x = 2, 3$  and  $4$  cm.

Then, after we acquire the amplitude and phase signals with the phased array system for each position of the probe scanned, the chi-square ( $\chi^2$ ), indicating the mismatch between the signals and the POF at each position  $\rho$  along the scanning direction  $\theta$ , is calculated by:

$$\chi_{\theta}^2(\rho) = \frac{1}{2N} \sum_{i=1}^N \left\{ \left[ \frac{A_{\theta}^{\text{SIG}}(\mathbf{i}) - A_{\theta}^{\text{POF}}(\rho, \mathbf{i})}{\sigma_A} \right]^2 + \left[ \frac{P_{\theta}^{\text{SIG}}(\mathbf{i}) - P_{\theta}^{\text{POF}}(\rho, \mathbf{i})}{\sigma_P} \right]^2 \right\}. \quad (4-23)$$

where A and P denote the normalized amplitude and phase (from 0 to 1) respectively, superscript ‘‘SIG’’ and ‘‘POF’’ refer to the measured signal or the calculated point-object function and N is the total number of sampling points,  $\sigma_A$  and  $\sigma_B$  are errors in the measurements. The two-dimensional localization image of the detected fluorescent object can be obtained by scanning the probe in at least two orthogonal dimensions.

For a given data set, we can generate the  $\chi^2$  for a continuum of a predicted position  $\rho$ , and the minimum of the  $\chi^2$  gives the best-estimated object position. For a one-dimensional scan, the estimated object position locates in a plane perpendicular to the scanning direction. When there are multiple scan directions, the averaged object

position is obtained using the back-projection method, *i.e.*, projecting the  $\chi^2$  curve back into the direction perpendicular to the direction of probe scanning:

$$\mathbf{I}(\mathbf{x}, \mathbf{y}) = \frac{1}{\mathbf{K}} \sum_{i=1}^{\mathbf{K}} -\lg[\chi_{\theta_i}^2(\rho)] \quad (4-24)$$

where  $\mathbf{I}$  is the parameter indicating the object position;  $\rho = \mathbf{x} \cdot \cos \theta_i + \mathbf{y} \cdot \sin \theta_i$  is the radius in the polar plot;  $(\mathbf{x}, \mathbf{y})$  is the position index;  $\theta_i$  is the angle of the  $i^{\text{th}}$  scanning direction ( $\theta = 0$  for horizontal scanning) and  $\mathbf{K}$  is the total number of scanned directions. The logarithm of  $\chi^2$  is taken and inverted for better visualization. Four scans as illustrated in Figure 4-13 are applied to obtain sufficient localization accuracy.

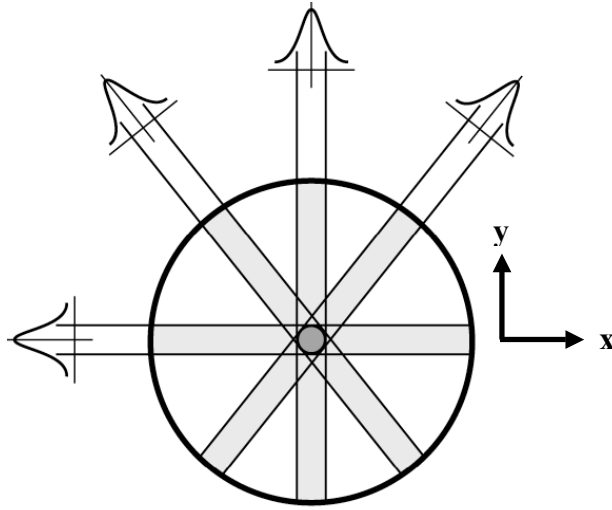


Figure 4-13: Illustration of the back projection method for localization image.

#### 4.5 Optimization of Phased Array System

Since dual-interfering-source arrangement is basically an interference-like procedure, the interference pattern and the detection sensitivity are influenced by several factors such as amplitude ratio and phase offset between two sources, modulation frequency, inter-source separation and source-detector separation, etc. In

this section, we will discuss the impact of those parameters on the interference of DPDW.

#### 4.5.1 Amplitude and Phase Control for Dual-source System

The interference of DPDW is calculated by Eqs. (4-3) and (4-4) with different values of amplitude ratio  $S_1/S_2$  and phase offset  $\Delta\phi_0$ . Figure 4-14 shows the amplitude and phase profiles with different source intensity ratios while keeping the phase offset  $\Delta\phi_0 = 180^\circ$ . The cancellation plane will be deflected towards the source with less strength. The amplitude and phase for a given detector position in the medium illuminated by the phased array sources are functions of the relative source intensity  $S_1/S_2$  between those two sources. Thus the interference pattern will change through modifying the source intensity ratio.

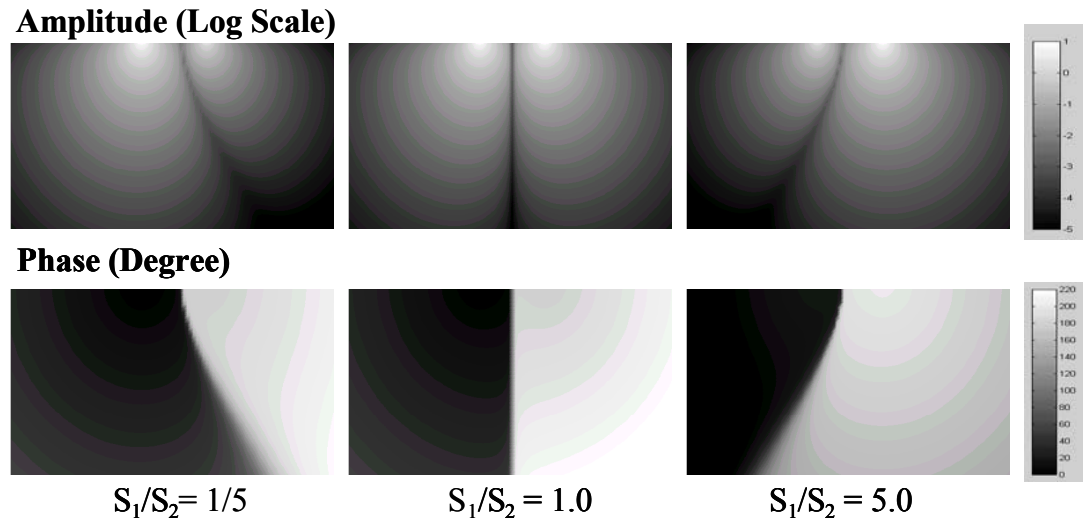


Figure 4-14: Amplitude and phase profile for varying the source strength ratio  $S_1/S_2$ , the cancellation plane will be deflected towards the weaker source (the optical properties of the medium are:  $\mu_a = 0.05 \text{ cm}^{-1}$ ,  $\mu_s = 10.0 \text{ cm}^{-1}$ ).

Morgan *et al* [97] has analyzed the dependence of phase offset on the interference profile. The closer the phase offset is to  $180^\circ$ , the higher the phase transition slope, and the higher the detection sensitivity. When the phase offset is away from  $180^\circ$ , the phase transition slope decreases. This result is in agreement with the perturbation analysis in Section 4.1.3.

#### 4.5.2 Frequency Dependency of Phased Array System

We also calculated the response with different modulation frequencies, from 350 MHz down to 60 Hz. The amplitude and phase signals are plotted in Figure 4-15. It is clear that the amplitude null and phase transition are well presented in the whole frequency range. In terms of amplitude, the higher frequency modulation (larger than 100 MHz) results in a decrease in the absolute intensity; and the higher frequency brings the larger phase shift during the scanning of the probe (*cf.* 350 MHz and 50 MHz in Figure 4-15(b)). Nevertheless, the  $180^\circ$  phase shifts in three different frequencies are in similar sensitivity.

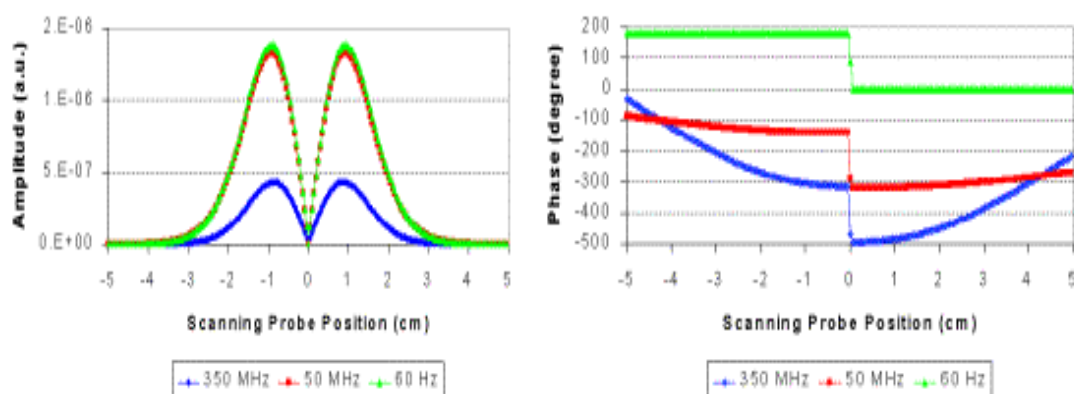


Figure 4-15: Amplitude and phase responses for different modulation frequencies.

In the case of fluorescence measurement, modulation frequency will associate with the lifetime of the fluorophore. The modulation frequency of the sources is an important factor as it has been shown that optimal modulation frequency can be derived for single-source system when phase detection is concerned in fluorescent mode [78]. An example of the dependence of perturbation upon the modulation frequency for both the single-source and dual-source system are presented in Figure 4-16, using the geometry described in Figure 4-10(b). For these specific cases, the concentration contrast is set to 5 cm and the separation of the sources is 2 cm for a 0.2 cm radius inhomogeneity.

From Figure 4-16 one can see that as stated by Li *et al.* [78], a simple estimate of the maximum perturbation can be done using  $\omega\tau_2 \approx 1$ . This rule is important to optimize the system for a given lifetime contrast. Inadequate modulation frequency can tremendously hamper the ability to detect the inhomogeneity in the phased array system. Moreover, even if the amplitude perturbation decreases with the increase of modulation frequency, the rule of thumb proposed in Ref. [78], allows the maximum of phase perturbation without degrading the amplitude perturbation significantly.

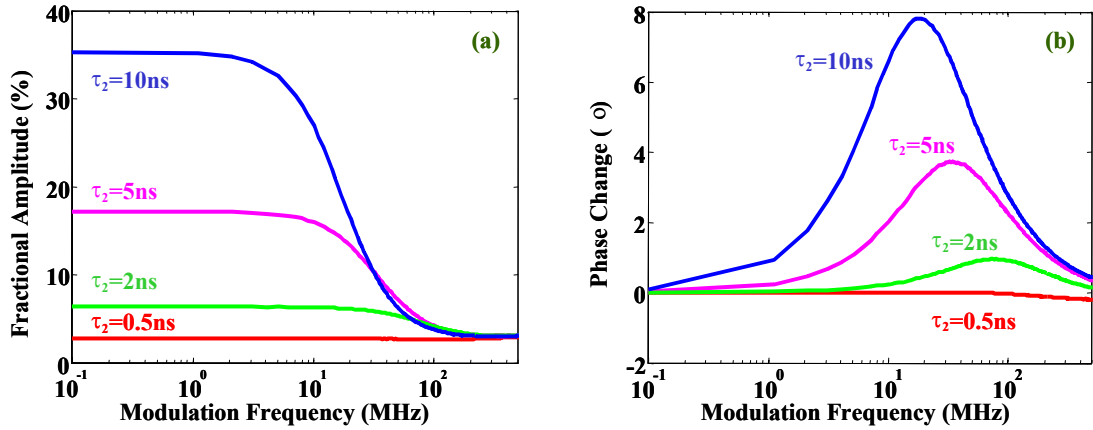


Figure 4-16: (a) fractional amplitude and (b) phase difference versus the sources modulation frequency. The legends on the curves correspond to lifetime contrast. The inhomogeneity radius is set to 0.2 cm with a concentration contrast of 5 ( $N_2 = 0.5 \mu\text{M}$ ).

(Adapted from Ref. [89])

### 4.5.3 Geometric Arrangement

Another important parameter to consider is the inter-source separation (separation between two sources). In Figure 4-17 we showed the relation between the phase transition sensitivity (phase shift divided by the separation between phase maximum and minimum, in the unit of degree/mm) and the separation between two interfering sources. The data are from simulation results based on clinical relevant situations and phantom experiments (the details of the experimental method is described in Chapter 6 and 7). The background tissue properties are:  $\mu_a = 0.04 \text{ cm}^{-1}$ ,  $\mu'_s = 10.0 \text{ cm}^{-1}$ , and the scanning object has  $\mu_a = 0.10 \text{ cm}^{-1}$  and same  $\mu'_s$  as the background. The diameter of the spherical object is 0.5 cm and scanned in two different depths from the source plane (1.5 cm and 3.5 cm respectively). From the chart we can see that for different depths, the sensitivity profiles are different, while

both achieve the maximum sensitivity when the source separation is roughly equal to the depth of the object. Hence the best configuration will be related to the magnitude of the perturbation (including the size, contrast and location of the object, etc) and should be analyzed case by case.

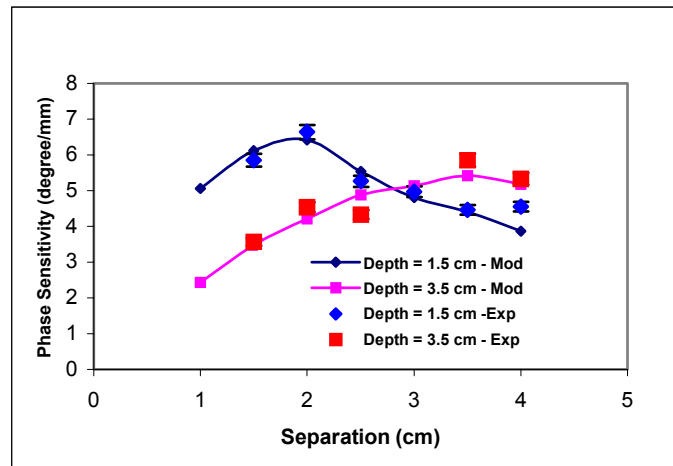


Figure 4-17: Dual-source phase shift sensitivity versus the separation between the two anti-phase sources. Results from two object depths are demonstrated with both the theoretical and experimental data.

In this chapter we focused on the detection sensitivity analysis of dual-interfering-source configuration and provide the algorithm for accurate object localization. The signal-to-noise ratio was the limiting factor for detection. The noise threshold can be reduced by repeating the measurement several times or narrowing the measurement bandwidth (increasing the signal integrating time). The analysis of the amplitude and phase signals suggests that the dual-interfering-source phase component can sensitively amplify the small perturbation to a larger phase signal, which could yield a higher signal-to-noise ratio for the purpose of detection, in both absorption and fluorescence modes. The sensitivity of the dual-interfering-source

detection might provide complementary information for the conventional single-source detection, in both the detection and characterization.

## **5 Diffuse Optical Spectroscopy And Tomography**

This chapter will focus on the review of two major types of technologies utilizing the diffuse photons: Diffuse Optical Spectroscopy (DOS) and Diffuse Optical Tomography (DOT). Generally, spectroscopic techniques assume that the medium of interest is homogeneous; therefore, the measurement is related to the average or the global optical properties. Tomography, on the other hand, is targeted to differentiate the focal changes in contrast with the global background. Relatively spectroscopic techniques require simpler instruments and algorithms, and are more convenient for the clinical implementation. While tomography can provide more accurate and localized information at the expenses of more sophisticated instruments and complex image reconstruction algorithms.

Spectroscopy has been widely used in probing the biological tissue for a long time. Various spectroscopic technologies have been developed including near-infrared spectroscopy (NIRS) [119], fluorescence spectroscopy [125], light scattering spectroscopy [126] and Raman spectroscopy [127]. Our work mainly focused on the

NIRS, and with the multiple scattering nature of tissue, photon diffusion theory is employed to decouple the absorption and scattering effects.

Basically DOS can provide the global information of the absorption coefficient  $\mu_a$  and the reduced scattering coefficient  $\mu'_s$ . Figure 5-1 illustrates the absorption spectra of the major chromophores in the NIR region. From absorption coefficients, we can estimate the oxygenated and deoxygenated hemoglobin concentrations (hence total hemoglobin concentration and the oxygen saturation) [16,105], water and lipid concentration [16,106], cytochrome oxidase [107], as well as the concentration of exogenous contrast agents [31]. From scattering coefficients, we can reveal the organelle density such as membrane, mitochondria and nuclei population [112].

Although DOS can provide some information of the averaged optical properties, it could not retrieve the spatial area where the inhomogeneous variation originates. To accurately quantify those changes with spatial resolution, DOT needs to be implemented [128].

In principle, DOT is similar to other tomographic schemes such as computerized tomography, and involves two parts of the procedure: the forward problem and the inverse problem. The forward problem describes the photon propagation in the interested medium from the solution of the diffusion equation. The inverse problem uses the appropriate forward solution to construct an operator that is applied to the measurement data from an unknown medium to yield the internal optical properties of this medium. This operator could be the direct inverse of a matrix, the numerically calculated inverse of a matrix or a minimization/data-fitting process [11, 138].

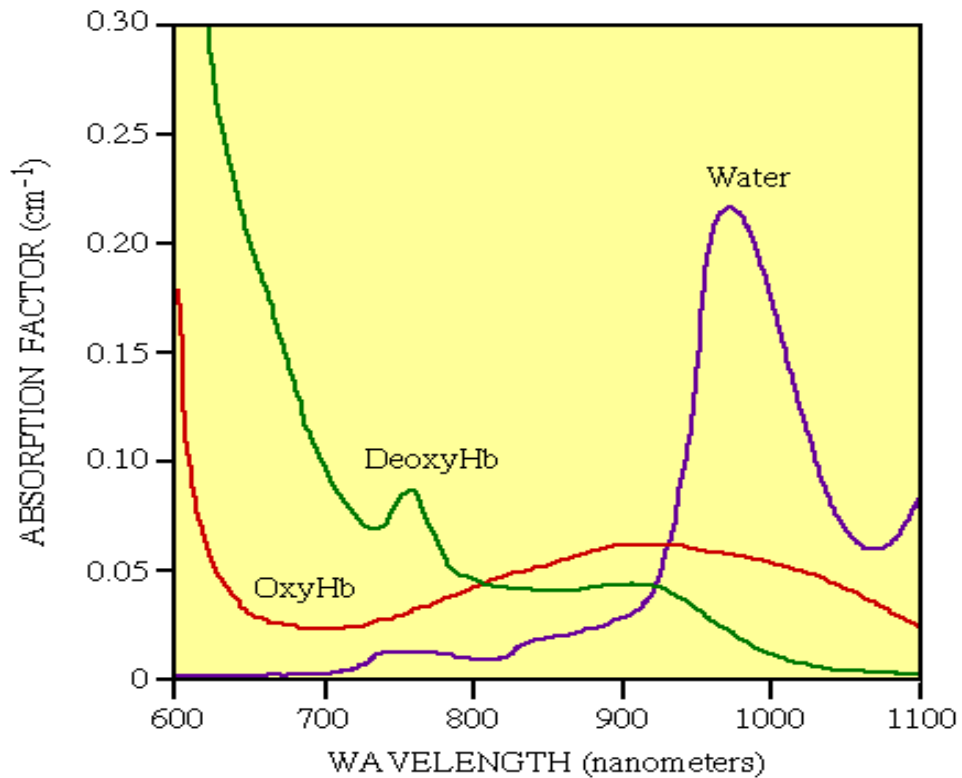


Figure 5-1: Spectra of oxygenated hemoglobin, deoxygenated hemoglobin and water. (Adapted from Ref. [10])

In **Section 5.1**, I first introduce the algorithm to recover the bulk absorption and scattering coefficients from the DOS measurements, especially using the frequency domain data. Estimation of the optical properties variation using the continuous wave (CW) technique is also discussed. **Section 5.2** gives the example on one of the most important medical applications of diffuse optical spectroscopy, calculations of the hemoglobin concentration and the oxygenation saturation. In **Section 5.3**, we change the gear to diffuse optical tomography by deriving the solutions for the heterogeneous diffusion equation, using two main kinds of approximations: Born and Rytov. **Section 5.4** introduces the common techniques for solving the inverse problem with two main categories: the algebraic techniques and

the subspace techniques. Then in **Section 5.5**, we demonstrate the algorithm for DOT with dual-source using the fluorescent data.

## 5.1 Calculation of Optical Properties

### 5.1.1 Frequency Domain Measurement

From the measured amplitude and phase of the DPDW, we can obtain the average or bulk optical properties of the sampled tissue assuming a homogeneous medium. The amplitude and phase ( $M_{ac}$  and  $\phi$ ) are functions of the medium optical properties as described in Eqs. (3-3) and (3-4), and also related to the initial amplitude and phase of the instrument. To account for the instrument functions, and recover the average  $\mu_a$  and  $\mu'_s$ , two major strategies are employed.

*1) Calibration with Known  $\mu_a$  and  $\mu'_s$ :* This method utilizes the *a-priori* optical properties information of the calibration phantom. Assume the instrumentation functions are the same for the phantom measurement and the actual measurement, we can eliminate the influence of the initial amplitude and phase of the instrument by fitting  $[M_{ac}^{(\text{medium})}/M_{ac}^{(\text{model})}]$  and  $[\phi^{(\text{medium})} - \phi^{(\text{model})}]$ , thus estimating the  $\mu_a$  and  $\mu'_s$  of the investigated medium [102]. Here I will use semi-infinite geometry as an illustration.

The analytical solution for homogeneous medium with the semi-infinite geometry is [52]:

$$\mathbf{R}(\mu_a, \mu'_s, \mathbf{c}, \rho, \omega) = \frac{1}{2(2\pi)^{3/2}} \left[ \frac{z_0(1 + \mathbf{k}\rho_0)}{\rho_0^3} \exp(-\mathbf{k}\rho_0) + \frac{z_p(1 + \mathbf{k}\rho_p)}{\rho_p^3} \exp(-\mathbf{k}\rho_p) \right] \quad (5-1)$$

where  $R$  is the number of photons crossing the tissue boundary [ $s^{-1} \cdot \text{cm}^{-2}$ ] at distance  $\rho$ , and  $\rho_0^2 = \rho^2 + z_0^2$ ,  $\rho_p^2 = \rho^2 + z_p^2$  with  $z_0 = 1/\mu'_s$  and  $z_p = z_0 + 4D/s$  ( $s \sim 0.426$  for tissue-air boundary).

From the measured reflectance  $R$  (which is a complex number), we obtain the amplitude and phase of the diffuse photon density wave. The amplitude and phase ( $M_{ac}$  and  $\phi$ ) are functions of the medium optical properties, and also relate to the initial amplitude and phase of the instrument. To account for the instrument parameters, calibration of the instrument on a phantom with known  $\mu_a$  and  $\mu'_s$  is performed, *i.e.*, from the measured data on the phantom with known  $\mu_a$  and  $\mu'_s$ , we can back-calculate the instrument initial amplitude and phase. And since these instrument parameters are the same for both phantom and the tissue medium, by fitting  $[M_{ac}^{(\text{medium})}/M_{ac}^{(\text{model})}]$  and  $[\phi^{(\text{medium})} - \phi^{(\text{model})}]$ , we can obtain the  $\mu_a$  and  $\mu'_s$  of the tissue medium.

2) Multiple Separation Method: By measuring the amplitude and phase at several source-detector separations, the  $\mu_a$  and  $\mu'_s$  can be also solved by fitting method [103]. Using this method, we can avoid the error introduced by the mis-estimation of the optical properties of the phantom in the previous approach.

From Eqs. (3-3) and (3-4), we can re-write them in the following forms:

$$\ln(M_{ac}\rho) = \ln\left(\frac{S_0 A}{4\pi D}\right) - \Pi \cos\left(\frac{\vartheta}{2}\right)\rho, \quad (5-2)$$

$$\phi = \Pi \sin\left(\frac{\vartheta}{2}\right)\rho. \quad (5-3)$$

where  $\vartheta = \tan^{-1}(\omega / \mu_a c)$  and  $\Pi = \left(\frac{\mu_a^2 c^2 + \omega^2}{c^2 D^2}\right)^{1/4}$ .

The slopes of the above two linear equations  $S_{ac}$  and  $S_\phi$  are expressed as:

$$S_{ac} = -\Pi \cos\left(\frac{\theta}{2}\right), \quad (5-4)$$

$$S_{\phi} = \Pi \sin\left(\frac{\theta}{2}\right). \quad (5-5)$$

After we obtain the values of these two slopes,  $\mu_a$  and  $\mu'_s$  of the probing media can be calculated as follows:

$$\mu_a = \frac{\omega}{c \cdot \tan\left[2 \tan^{-1}\left(\frac{S_{\phi}}{S_{ac}}\right)\right]}, \quad (5-6)$$

$$\mu'_s = \frac{\sqrt{\mu_a^2 c^2 + \omega^2}}{3c \cdot (S_{ac}^2 + S_{\phi}^2)}. \quad (5-7)$$

Similar approach can also be applied to semi-infinite geometry and the detailed solution has been provided by Fantini *et al* [73].

DOS is widely used in clinical applications due to its simplicity and convenience. It has been used to monitor the tissue oxygenation saturation in the vascular bed, providing the functional information of tissue [103,104]. Clinically relevant parameters, such as blood oxygenation saturation and blood volume, can be obtained for the diagnosis of certain diseases, for example, breast cancer [110], hematomas [108] and muscle dysfunctions [109].

### 5.1.2 Continuous Wave Measurement

Continuous wave measurements use the light source with constant intensity; therefore, only the amplitude attenuation is recorded, with no phase information. From Eq. (3-5), for infinite homogeneous diffuse media, the DC amplitude also has similar exponential decaying feature as Eq. (5-2) [49]:

$$\ln(M_{dc}\rho) = \ln\left(\frac{S_0}{4\pi D}\right) - \sqrt{\frac{\mu_a}{D}}\rho. \quad (5-8)$$

For the semi-infinite scattering medium, the diffuse reflectance  $R(\rho)$  is [123]:

$$\mathbf{R}(\rho) = \frac{S_0}{4\pi\mu'_t} \left[ \left( \mu_{\text{eff}} + \frac{1}{r_1} \right) \frac{\exp(-\mu_{\text{eff}} r_1)}{r_1^2} + \left( \frac{4}{3}A + 1 \right) \left( \mu_{\text{eff}} + \frac{1}{r_2} \right) \frac{\exp(-\mu_{\text{eff}} r_2)}{r_2^2} \right], \quad (5-9)$$

where  $r_1 = \sqrt{(1/\mu_t)^2 + \rho^2}$ ,  $r_2 = \sqrt{[(4A/3 + 1)/\mu_t]^2 + \rho^2}$ ,  $\mu'_t = \mu_a + \mu'_s$  and  $\mu_{\text{eff}} = \sqrt{3\mu_a\mu'_s}$ ;  $S_0$  is the initial source intensity;  $A$  is the internal specular reflection parameter, which depends only on the relative refractive index of the tissue and surrounding medium and  $\rho$  is the source-detector separation. For typical biological tissues with  $\mu_a \sim 0.05 - 0.5 \text{ cm}^{-1}$  and  $\mu'_s \sim 10 - 20 \text{ cm}^{-1}$ , the photon transport mean free path  $1/\mu'_t$  is in the range of  $0.05 - 0.1 \text{ cm}$ . When the source-detector separation  $\rho = 2 - 3 \text{ cm}$ , which is larger than  $20 - 40$  mean transport free path, approximation can be taken on  $r_1$  and  $r_2$  as  $r_1 \approx r_2 \approx \rho$ , Eq. (5-9) can be simplified as [124]:

$$\mathbf{R}_{\text{app}}(\rho) = \frac{1}{a\mu'_t} \left( \mu_{\text{eff}} + \frac{1}{\rho} \right) \frac{\exp(-\mu_{\text{eff}} \rho)}{\rho^2}, \quad (5-10)$$

where  $a = 2\pi/[S_0(1+2A/3)]$ , which is independent of  $\rho$ . It can be rewritten as:

$$\ln[\rho^2 \mathbf{R}_{\text{app}}(\rho)] = -\mu_{\text{eff}} \rho - \ln(a\mu'_t) + \ln\left( \mu_{\text{eff}} + \frac{1}{\rho} \right). \quad (5-11)$$

Liu *et al* [124] has analyzed the linear dependency of Eq. (5-11) with  $\rho$ . They concluded that when the source-detector separation is larger than  $2 \text{ cm}$ , the third term in the right hand side of Eq. (5-11), which is non-linear, can be approximated by a constant term with the error less than  $5\%$ , thus Eq. (5-11) reduces to:

$$\ln[\rho^2 \mathbf{R}_{\text{app}}(\rho)] = -\mu_{\text{eff}} \rho - \ln(a\mu'_t) + \ln\left( \mu_{\text{eff}} + \frac{1}{\rho_0} \right). \quad (5-12)$$

where  $\rho_0$  is the middle point of the minimum and maximum source-detector separations. Using the multiple separation measurement method as well as the calibration model, it is able to obtain the  $\mu_{\text{eff}}$  and  $\mu'_t$ , and thus  $\mu_a$  and  $\mu'_s$ .

## 5.2 Spectroscopic Analysis

From the methods given in Section 5.1, we can obtain the absorption and scattering coefficients of the medium under investigation. Absorption data is often used to derive the concentration of several chromophores, with multiple wavelengths measurement. Generally speaking, it is a spectroscopic analysis procedure. Because the scattering effects usually couple with the absorption, calibration is needed to remove the cross talk between the absorption and scattering.

### 5.2.1 Calibration of Scattering Coefficients

It has been shown that the reduced scattering coefficient  $\mu'_s$  can be well approximated by the Mie theory [111]. Several investigators have demonstrated that this approximation is applicable to cell suspension and liver tissue [112], breast tissue [5,113], and rat brain [114]. A simplified version of Mie scattering can be expressed as a power law when the size of the scattering particle is comparable to the optical wavelength (organelles such as mitochondria, which is in the size of  $0.5 \sim 1.0 \mu\text{m}$ ) [5,56]:

$$\mu'_s(\lambda) = a\lambda^{-b}, \quad (5-13)$$

where  $a$  and  $b$  are free parameters,  $\lambda$  is the wavelength. For multiple wavelengths measurements, after we obtain  $\mu_a$  and  $\mu'_s$  from methods provided by Section 5.1, the scattering coefficients  $\mu'_s$  in different wavelengths are fitted to Eq. (5-13) to obtain

values of a and b. Then from Eq. (5-13) with the estimated a and b, the corrected  $\mu'_s$  values are calculated and plugged back into the equations used before to calculate the optical properties; new  $\mu_a$  values are then re-calculated. This approach can be also regarded as fitting the data in both absorption and scattering spectra [56].

## 5.2.2 Blood Volume and Oxygen Saturation

Using the methods described in the previous section, we can derive the corrected absorption coefficient  $\mu_a$  of the tissue sampled. For multiple wavelengths, the concentration of deoxygenated and oxygenated hemoglobin can be estimated using the modified Beer-Lambert law:

$$\begin{bmatrix} \mu_a^{\lambda_1} \\ \mu_a^{\lambda_2} \\ \vdots \\ \mu_a^{\lambda_n} \end{bmatrix} = \begin{bmatrix} \epsilon_{\text{Hb}}^{\lambda_1} & \epsilon_{\text{HbO}_2}^{\lambda_1} \\ \epsilon_{\text{Hb}}^{\lambda_2} & \epsilon_{\text{HbO}_2}^{\lambda_2} \\ \vdots & \vdots \\ \epsilon_{\text{Hb}}^{\lambda_n} & \epsilon_{\text{HbO}_2}^{\lambda_n} \end{bmatrix} \begin{bmatrix} C_{\text{Hb}} \\ C_{\text{HbO}_2} \end{bmatrix} + \begin{bmatrix} \mu_a^{\text{B},\lambda_1} \\ \mu_a^{\text{B},\lambda_2} \\ \vdots \\ \mu_a^{\text{B},\lambda_n} \end{bmatrix} \quad (5-14)$$

where  $\mu_a^{\lambda_n}$  is the absorption coefficient at wavelength  $\lambda_n$  ( $n \geq 2$ ),  $\epsilon_x^{\lambda_n}$  is the extinction coefficient at wavelength  $\lambda_n$ ,  $C_x$  is hemoglobin concentration of the specific chromophore, and  $\mu_a^{\text{B},\lambda_n}$  is the background absorption coefficient at wavelength  $\lambda_n$ , which takes into account the absorption due to other chromophores except the hemoglobin, such as lipid, water, cytochrome oxidase, etc.

To quantify the oxygenation saturation, the absolute hemoglobin concentration is necessary. This will require knowledge of  $\mu_a^{\text{B}}$  in Eq. (5-14). There are two methods to estimate the background absorptions [58]: one is to assume that the background absorption is due entirely to water, which comprises 80% of the tissue [115]; the other is using the empirical values from a large population of subjects [116].

Eq. (5-14) can be generally extended to multiple chromophores as long as enough wavelengths' data are sampled. The general form of the modified Beer-Lambert law can be expressed as:

$$\begin{bmatrix} \mu_a^{\lambda_1} \\ \vdots \\ \mu_a^{\lambda_n} \end{bmatrix} = \begin{bmatrix} \epsilon_{C_1}^{\lambda_1} & \cdots & \epsilon_{C_m}^{\lambda_1} \\ \vdots & \ddots & \vdots \\ \epsilon_{C_1}^{\lambda_n} & \cdots & \epsilon_{C_m}^{\lambda_n} \end{bmatrix} \begin{bmatrix} C_1 \\ \vdots \\ C_m \end{bmatrix} + \begin{bmatrix} \mu_a^{B,\lambda_1} \\ \vdots \\ \mu_a^{B,\lambda_n} \end{bmatrix} \quad (5-15)$$

where  $C_x$  indicates concentrations for different chromophores (*i.e.* oxygenated and deoxygenated hemoglobin, lipid, water, cytochrome c oxidase, etc.).  $\epsilon_{C_x}^{\lambda_n}$  is the corresponding extinction coefficient at wavelength  $\lambda_n$ .

To solve the matrix equation (5-14) or (5-15), singular value decomposition (SVD) [117] is used to obtain the initial estimation of the chromophore concentrations and then a Nelder-Mead simplex search algorithm was followed to minimize a least square function as maximum likelihood estimator [118] to obtain the best fit for the chromophore concentrations.

From the estimated concentrations of the oxygenated and deoxygenated hemoglobin, we can further calculate the oxygen saturation ( $StO_2$ ) and the blood volume (BV) through [119]:

$$StO_2 = \frac{C_{Hb}}{C_{Hb} + C_{HbO_2}}, \quad (5-16)$$

$$BV = C_{Hb} + C_{HbO_2}. \quad (5-17)$$

Those values are valuable clinical parameters that can be used to monitor many physiological phenomena such as brain functions [120,121], tumor angiogenesis and hyper-metabolism [21], and muscle oxygenation during exercise [122].

### 5.3 Approximation for Heterogeneous Media

In the previous sections, we assume the medium is homogeneous and apply spectroscopic methods to recover the average optical properties of the tissue. When the medium is heterogeneous, we use the perturbation method to solve the heterogeneous diffusion equation:

$$\frac{1}{c} \frac{\partial}{\partial t} \Phi(\mathbf{r}, t) - \nabla \mathbf{D}(\mathbf{r}) \nabla \Phi(\mathbf{r}, t) + \mu_a(\mathbf{r}) \Phi(\mathbf{r}, t) = \mathbf{S}(\mathbf{r}, t). \quad (5-18)$$

#### 5.3.1 Absorption Heterogeneity

For absorptive heterogeneity, the spatial dependent absorption coefficient is divided into the average component and the heterogeneous part:

$$\mu_a(\mathbf{r}) = \mu_a^0 + \delta\mu_a(\mathbf{r}). \quad (5-19)$$

Substitute Eq. (5-19) back to Eq. (5-18) and assume the scattering is homogeneous, for a frequency modulated source, Eq. (5-18) reduces to:

$$\left( \nabla^2 + \mathbf{k}^2 + O(\mathbf{r}) \right) \Phi(\mathbf{r}) = -\mathbf{S}_0 \mathbf{A} \delta(\mathbf{r}_s) / \mathbf{D} \quad (5-20)$$

where

$$O(\mathbf{r}) = -\frac{\delta\mu_a(\mathbf{r})}{\mathbf{D}_0}. \quad (5-21)$$

here  $\mathbf{D}_0$  is the homogeneous diffusion coefficient.

There are two kinds of methods commonly used to solve Eq. (5-20): the Born (linear) and the Rytov (exponential) approximations [65,129].

Born Approximation: In Born expansion we rewrite the photon fluence as the sum of the incident part (homogeneous) and the scattered (heterogeneous) part, *i.e.*,

$$\Phi(\mathbf{r}, \mathbf{r}_s) = \Phi_0(\mathbf{r}, \mathbf{r}_s) + \Phi_{sc}(\mathbf{r}, \mathbf{r}_s) \quad (5-22)$$

Substituting Eq. (5-22) into Eq. (5-20), and subtracting the homogeneous Helmholtz equation (Eq. (3-2)) yields

$$(\nabla^2 + \mathbf{k}^2)\Phi_{sc}(\mathbf{r}, \mathbf{r}_s) = -O(\mathbf{r})\Phi(\mathbf{r}, \mathbf{r}_s) \quad (5-23)$$

For Born approximation,

$$\Phi_{sc}(\mathbf{r}, \mathbf{r}_s) \ll \Phi_0(\mathbf{r}, \mathbf{r}_s). \quad (5-24)$$

Thus,

$$\Phi(\mathbf{r}, \mathbf{r}_s) \approx \Phi_0(\mathbf{r}, \mathbf{r}_s), \quad (5-25)$$

By substituting Eq. (5-25) into Eq. (5-22), with Green's function solution for the homogeneous Helmholtz equation, the solution for the scattered field can be expressed as:

$$\Phi_{sc}(\mathbf{r}_s, \mathbf{r}_d) = \int \mathbf{G}(\mathbf{r}', \mathbf{r}_d) \frac{\delta\mu_a(\mathbf{r}')}{\mathbf{D}_0} \Phi_0(\mathbf{r}', \mathbf{r}_s) d\mathbf{r}'. \quad (5-26)$$

The Born approximation requires that the scattered field is small compared to the incident field as indicated in Eq. (5-24).

Rytov Approximation: In Rytov expansion we also divide the photon density into the incident part (homogeneous) and the scattered (heterogeneous) part, using the exponential expression:

$$\Phi(\mathbf{r}, \mathbf{r}_s) = \exp[\varphi_0(\mathbf{r}, \mathbf{r}_s) + \varphi_{sc}(\mathbf{r}, \mathbf{r}_s)], \quad (5-27a)$$

$$\Phi_0(\bar{\mathbf{r}}, \bar{\mathbf{r}}_s) = \exp[\varphi_0(\mathbf{r}, \mathbf{r}_s)]. \quad (5-27b)$$

Here  $\varphi_{sc}$  is the Rytov scattered wave. In the case of absorptive inclusions, Eq. (5-20) can be written as [65]:

$$(\nabla^2 + \mathbf{k}^2)\Phi_0(\mathbf{r}, \mathbf{r}_s)\varphi_{sc}(\mathbf{r}, \mathbf{r}_s) = -\Phi_0(\mathbf{r}, \mathbf{r}_s)((\nabla\varphi_{sc}(\mathbf{r}, \mathbf{r}_s))^2 + O(\mathbf{r})) \quad (5-28)$$

For Rytov approximation,

$$(\nabla\varphi_{sc}(\mathbf{r},\mathbf{r}_s))^2 \ll O(\mathbf{r}). \quad (5-29)$$

Similarly, the Rytov solution for the scattered field can be expressed as:

$$\varphi_{sc}(\mathbf{r}_s, \mathbf{r}_d) = \frac{1}{\Phi_0(\mathbf{r}_d, \mathbf{r}_s)} \int \mathbf{G}(\mathbf{r}', \mathbf{r}_d) \frac{\delta\mu_a(\mathbf{r}')}{\mathbf{D}_0} \Phi_0(\mathbf{r}', \mathbf{r}_s) d\mathbf{r}' \quad (5-30)$$

The Rytov approximation assumes that the variation of scattered field is slow as indicated in Eq. (5-29).

Approximation for Dual-source System: In the dual-interference-source system, similar solutions will be derived for both the Born and Rytov approximation. Note that the homogeneous field is the summation of the two independent DPDWs. Here we give the Rytov solution as an example [94]:

$$\varphi_{sc}^{DS}(\mathbf{r}_d, \mathbf{r}_{s1}, \mathbf{r}_{s2}) = \frac{1}{\Phi_0^{DS}(\mathbf{r}_d, \mathbf{r}_{s1}, \mathbf{r}_{s2})} \int \mathbf{G}(\mathbf{r}', \mathbf{r}_d) \frac{\delta\mu_a(\mathbf{r}')}{\mathbf{D}_0} \Phi_0^{DS}(\mathbf{r}', \mathbf{r}_{s1}, \mathbf{r}_{s2}) d\mathbf{r}' \quad (5-31)$$

where

$$\Phi_0^{DS}(\mathbf{r}, \mathbf{r}_{s1}, \mathbf{r}_{s2}) = \frac{S_0 A}{4\pi \mathbf{D}_0} \cdot \left[ \frac{\exp(i\mathbf{k}|\mathbf{r}_{s1} - \mathbf{r}|)}{|\mathbf{r}_{s1} - \mathbf{r}|} + \frac{\exp(i\mathbf{k}|\mathbf{r}_{s2} - \mathbf{r}| + i\Delta\phi_0)}{|\mathbf{r}_{s2} - \mathbf{r}|} \right]. \quad (5-32)$$

### 5.3.2 Scattering Heterogeneity

The derivation of solution for scattering heterogeneity is similar to the approach in Section 5.3.1. For scattering heterogeneity, the spatial dependent scattering coefficient can also be divided into the average component and the heterogeneous part (here we use the diffusion coefficient as the representative of scattering):

$$\mathbf{D}(\mathbf{r}) = \mathbf{D}_0 + \delta\mathbf{D}(\mathbf{r}). \quad (5-33)$$

Substitute Eq. (5-33) back to Eq. (5-18) and assume the absorption is homogeneous, for a frequency modulated source, Eq. (5-18) reduces to:

$$\left(\nabla^2 + \mathbf{k}^2\right)\Phi(\mathbf{r}) + \nabla\delta\mathbf{D}(\mathbf{r})\nabla\Phi(\mathbf{r})/\mathbf{D}_0 + \delta\mathbf{D}(\mathbf{r})\nabla^2\Phi(\mathbf{r})/\mathbf{D}_0 = -\mathbf{S}_0\mathbf{A}\delta(\mathbf{r}_s)/\mathbf{D}_0, \quad (5-34)$$

Born Approximation: In Born expansion,

$$\Phi(\mathbf{r}, \mathbf{r}_s) = \Phi_0(\mathbf{r}, \mathbf{r}_s) + \Phi_{sc}(\mathbf{r}, \mathbf{r}_s). \quad (5-35)$$

Substitute Eq. (5-35) into Eq. (5-34), and subtract the homogeneous Helmholtz equation (Eq. (3-2)) yields:

$$\begin{aligned} \left(\nabla^2 + \mathbf{k}^2\right)\Phi_{sc}(\mathbf{r}, \mathbf{r}_s) = & -\nabla\delta\mathbf{D}(\mathbf{r})\left(\nabla\Phi_0(\mathbf{r}, \mathbf{r}_s) + \nabla\Phi_{sc}(\mathbf{r}, \mathbf{r}_s)\right)/\mathbf{D}_0 \\ & - \delta\mathbf{D}(\mathbf{r})\left(\nabla^2\Phi_0(\mathbf{r}, \mathbf{r}_s) + \nabla^2\Phi_{sc}(\mathbf{r}, \mathbf{r}_s)\right)/\mathbf{D}_0. \end{aligned} \quad (5-36)$$

For Born approximation,

$$\Phi_{sc}(\mathbf{r}, \mathbf{r}_s) \ll \Phi_0(\mathbf{r}, \mathbf{r}_s). \quad (5-37)$$

Thus Eq. (5-36) reduces to

$$\left(\nabla^2 + \mathbf{k}^2\right)\Phi_{sc}(\mathbf{r}, \mathbf{r}_s) = -\nabla\delta\mathbf{D}(\mathbf{r})\nabla\Phi_0(\mathbf{r}, \mathbf{r}_s)/\mathbf{D}_0 - \delta\mathbf{D}(\mathbf{r})\nabla^2\Phi_0(\mathbf{r}, \mathbf{r}_s)/\mathbf{D}_0, \quad (5-38)$$

From Eq. (5-38) and using Green's first identity, the solution for the scattered field can be expressed as [65]:

$$\Phi_{sc}(\mathbf{r}_s, \mathbf{r}_d) = \int \nabla\mathbf{G}(\mathbf{r}', \mathbf{r}_d) \frac{\delta\mathbf{D}(\mathbf{r}')}{\mathbf{D}_0} \nabla\Phi_0(\mathbf{r}', \mathbf{r}_s) d\mathbf{r}'. \quad (5-39)$$

Rytov Approximation: In Rytov expansion, again we have:

$$\Phi(\mathbf{r}, \mathbf{r}_s) = \exp[\varphi_0(\mathbf{r}, \mathbf{r}_s) + \varphi_{sc}(\mathbf{r}, \mathbf{r}_s)], \quad (5-40a)$$

$$\Phi_0(\bar{\mathbf{r}}, \bar{\mathbf{r}}_s) = \exp[\varphi_0(\mathbf{r}, \mathbf{r}_s)]. \quad (5-40b)$$

Here  $\varphi_{sc}$  is the Rytov scattered wave. In the case of scattering inclusions, it has been demonstrated [65]:

$$\varphi_{sc}(\mathbf{r}_s, \mathbf{r}_d) = \frac{1}{\Phi_0(\mathbf{r}_d, \mathbf{r}_s)} \int \nabla \mathbf{G}(\mathbf{r}', \mathbf{r}_d) \frac{\delta \mathbf{D}(\mathbf{r}')}{\mathbf{D}_0} \nabla \Phi_0(\mathbf{r}', \mathbf{r}_s) d\mathbf{r}'. \quad (5-41)$$

Approximation for Dual-source System: In the dual-interference-source system, the solution is similar to both the Born and Rytov approximations except the homogeneous field is now the summation of the two independent DPDWs.

For a heterogeneous system with both the absorption and scattering perturbations, the final solution will be the linear superposition with the scattering fields resulted from the absorption and scattering heterogeneity (for either the Born or the Rytov approximation).

## 5.4 Matrix Inversion

In DOT, we divide the unknown media into discrete volume elements (voxels). Thus the integral equation in the solution for heterogeneous medium can be discretized to a set of linear equations. We will use the Rytov solution (Eq. (5-30)) as the example. The measurement dataset and the optical properties of each voxel can be related by the following matrix equation [65] (for  $m$  sets of measurements and  $n$  voxels):

$$\begin{bmatrix} \varphi_{sc}(\mathbf{r}_{s1}, \mathbf{r}_{d1}) \\ \vdots \\ \varphi_{sc}(\mathbf{r}_{sm}, \mathbf{r}_{dm}) \end{bmatrix} = \begin{bmatrix} \mathbf{W}_{11} & \cdots & \mathbf{W}_{1n} \\ \vdots & \ddots & \vdots \\ \mathbf{W}_{m1} & \cdots & \mathbf{W}_{mn} \end{bmatrix} \begin{bmatrix} \delta\mu_a(\mathbf{r}_1) \\ \vdots \\ \delta\mu_a(\mathbf{r}_n) \end{bmatrix} \quad (5-42)$$

where  $\varphi_{sc}(\mathbf{r}_{si}, \mathbf{r}_{di})$  is the Rytov perturbative scattered wave for the  $i^{\text{th}}$  source-detector pair (we use  $\Theta$  to denote the vector),  $\mathbf{W}_{ij}$  is the weight function for the  $j^{\text{th}}$  voxel and the  $i^{\text{th}}$  source-detector pair (we use  $\mathbf{W}$  to denote the matrix), which can be expressed as [65]:

$$\mathbf{W}_{ij} = \frac{\mathbf{h}^3}{\mathbf{D}_0} \cdot \frac{\mathbf{G}(\mathbf{r}_j, \mathbf{r}_{di}) \cdot \Phi_0(\mathbf{r}_j, \mathbf{r}_{si})}{\Phi_0(\mathbf{r}_{di}, \mathbf{r}_{si})}, \quad (5-43)$$

where  $h$  is the voxel dimension.  $\delta\mu_a(\mathbf{r}_j)$  is the differential absorption coefficient of the  $j^{\text{th}}$  voxel (we use  $\Delta\mu_a$  to denote this vector).

Figure 5-2 illustrates the geometry of DOT in one projection. The weight function  $\mathbf{W}_{ij}$  is also the sensitivity for absorptive perturbation at the  $j^{\text{th}}$  voxel for  $i^{\text{th}}$  source-detector pair.

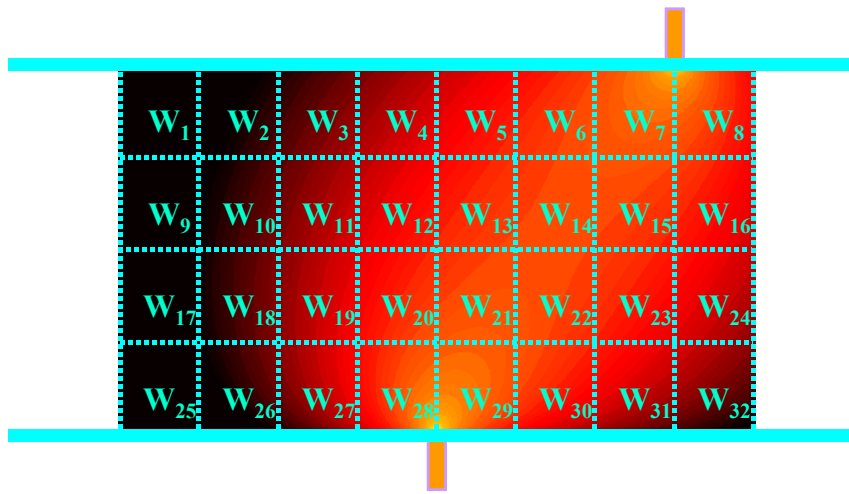


Figure 5-2: Illustration of the sensitivity matrix for one source-detector pair in DOT.

In the case of the dual-interfering-source system, the corresponding Rytov weight function is expressed as:

$$\mathbf{W}_{ij}^{\text{DS}} = \frac{\mathbf{h}^3}{\mathbf{D}_0} \cdot \frac{\mathbf{G}(\mathbf{r}_j, \mathbf{r}_{\text{di}}) \cdot \Phi_0^{\text{DS}}(\mathbf{r}_j, \mathbf{r}_{\text{si}})}{\Phi_0^{\text{DS}}(\mathbf{r}_{\text{di}}, \mathbf{r}_{\text{si}})}. \quad (5-44)$$

The goal of DOT is to invert the matrix denoted in Eq. (5-42) to obtain an estimate of  $\Delta\mu_a$ . Several techniques are suitable to solve this linear set of equations

[11]. Two commonly used methods in our lab are: the algebraic reconstruction techniques and the subspace methods [131].

#### 5.4.1 Algebraic Reconstruction Techniques (ART)

The algebraic methods have been widely used for DOT and as well as many other tomographic problems [129]. Specifically, we apply the Simultaneous Iterative Reconstruction Technique (SIRT) to solve Eq. (5-42). This iterative method can be described mathematically as:

$$\Delta\mu_a^{(k+1)} = \Delta\mu_a^{(k)} + \frac{\lambda}{\mathbf{m}} \sum_{i=1}^{\mathbf{m}} \frac{\Theta_i - \mathbf{W}_i \Delta\mu_a^{(k)}}{\mathbf{W}_i \mathbf{W}_i^T} \mathbf{W}_i^T. \quad (5-45)$$

where  $\Delta\mu_a^{(k)}$  is the  $k^{\text{th}}$  estimate of the object function,  $\mathbf{W}_i$  is the  $i^{\text{th}}$  row of the  $\mathbf{m} \times \mathbf{n}$  weight matrix  $\mathbf{W}$ , and  $\lambda$  is the relaxation parameter.

Eq. (5-45) describes the projections method (Kaczmarz method) [129] for solving a set of linear equations. For illustration purpose, the solution for a set of two linear equations is demonstrated in Figure 5-3.

The projection method consists of first starting with an initial guess, projecting this initial guess onto the first line, re-projecting the resulting point onto the second line, and then projecting back onto the first line, and so forth. If a unique solution exists, the iterations will converge to that point.



This equation says that the projection of a vector  $\overrightarrow{\mathbf{OC}}$  (for any point C on the hyper-plane) on the vector  $\mathbf{W}_1$  is of constant length. The unit vector  $\overrightarrow{\mathbf{OU}}$  along  $\mathbf{W}_1$  is given by:

$$\overrightarrow{\mathbf{OU}} = \frac{\mathbf{W}_1}{\sqrt{\mathbf{W}_1 \cdot \mathbf{W}_1}}. \quad (5-47)$$

The perpendicular distance of the hyper-plane from the origin, is given by:

$$|\overrightarrow{\mathbf{OA}}| = \overrightarrow{\mathbf{OU}} \cdot \overrightarrow{\mathbf{OC}} = \frac{\mathbf{W}_1 \cdot \overrightarrow{\mathbf{OC}}}{\sqrt{\mathbf{W}_1 \cdot \mathbf{W}_1}} = \frac{\Theta_1}{\sqrt{\mathbf{W}_1 \cdot \mathbf{W}_1}}, \quad (5-48)$$

because C is on the hyper-plane described by Eq. (5-46). The initial guess  $\Delta\mu_a^{(0)}$  and the next estimation  $\Delta\mu_a^{(1)}$  is related by:

$$\Delta\mu_a^{(1)} = \Delta\mu_a^{(0)} + \overrightarrow{\mathbf{GH}} \quad (5-49)$$

where the vector  $\overrightarrow{\mathbf{GH}}$  is given by:

$$\begin{aligned} \overrightarrow{\mathbf{GH}} &= |\overrightarrow{\mathbf{GH}}| \overrightarrow{\mathbf{OU}} = \left( |\overrightarrow{\mathbf{OF}}| - |\overrightarrow{\mathbf{OA}}| \right) \overrightarrow{\mathbf{OU}} = \left( \Delta\mu_a^{(0)} \cdot \overrightarrow{\mathbf{OU}} - |\overrightarrow{\mathbf{OA}}| \right) \overrightarrow{\mathbf{OU}} \\ &= \frac{\Delta\mu_a^{(0)} \cdot \mathbf{W}_1 - \Theta_1}{\sqrt{\mathbf{W}_1 \cdot \mathbf{W}_1}} \overrightarrow{\mathbf{OU}} = \frac{\Delta\mu_a^{(0)} \cdot \mathbf{W}_1 - \Theta_1}{\mathbf{W}_1 \cdot \mathbf{W}_1} \mathbf{W}_1. \end{aligned} \quad (5-50)$$

Substituting Eq. (5-50) in Eq. (5-49), we get Eq. (5-45).

#### 5.4.2 Singular Value Decomposition (SVD)

The subspace methods are also used to solve the inverse problem [131]. We employ the singular value decomposition (SVD) method to perform the image reconstruction [65]. The Moore-Penrose generalized inverse of Eq. (5-42) is defined as:

$$\Delta\mu_a = (\mathbf{W}^T \mathbf{W})^{-1} * \mathbf{W}^T \Theta, \quad (5-51)$$

Since the inverse problem is ill-posed, regularization methods are used to obtain stabilized results [132]. The regularized weight matrix to be inverted is:

$$\mathbf{R} = (\mathbf{W}^T\mathbf{W} + \alpha\mathbf{I}), \quad (5-52)$$

where  $\alpha$  is the regularization parameter and  $\mathbf{I}$  is the identity matrix.  $\mathbf{R}$  can be rewritten through SVD as:

$$\mathbf{R} = \mathbf{U}\mathbf{S}\mathbf{V}^T, \quad (5-53)$$

where  $\mathbf{U}$  and  $\mathbf{V}$  are orthonormal matrices and  $\mathbf{S}$  is a diagonal matrix. The superscript “T” denotes the matrix transpose. The inverted matrix can be derived through:

$$\mathbf{R}^{-1} = \mathbf{V}\mathbf{S}^{-1}\mathbf{U}^T. \quad (5-54)$$

In truncated SVD (TSVD), Eq. (5-54) is computed with only the  $t$  largest singular values and singular vectors to approximate the inversion [117]. The selection of  $t$  is based on the singular value spectrum (plot of singular value versus the singular value index).

Pogue *et al* [136] have proposed a spatially variant regularization method to improve the image resolution in DOT. Here we choose our regularization parameter as:

$$\alpha(y) = \lambda_e[\exp(y/d) + \exp(1-y/d)] + \lambda_c \quad (5-55)$$

where  $y$  is the distance from the voxel to the detector plane, and  $d$  the slab thickness.  $\lambda_e$  and  $\lambda_c$  are free parameters to be empirically determined. An *a posteriori* method, L-curve analysis is used to determine the best regularization parameter [132]. In L-curve analysis, we plot the log of 2-norm of the residual versus the log of the 2-norm of the estimation with varying regularization parameters. The best parameter is chosen from the corner of the “L” shape, which is a good compromise between data fitting and penalizing the norm of the reconstruction. Mathematically we use the curvature function [137]:

$$\mathbf{K}(\lambda) = \frac{\xi''(\lambda)\zeta'(\lambda) - \xi'(\lambda)\zeta''(\lambda)}{(\xi'(\lambda)^2 + \zeta'(\lambda)^2)^{3/2}}, \quad (5-56)$$

where  $\xi(\lambda) = \ln \|\mathbf{W} \cdot \Delta\mu_a^{\text{est}} - \Theta\|$  and  $\zeta(\lambda) = \ln \|\Delta\mu_a^{\text{est}}\|$ . The superscripts ' and '' denote the first and second derivatives respectively. The minimum of the curvature function corresponds to the best regularization parameter.

## 5.5 Fluorescence Diffuse Optical Tomography

In Chapter 3 we have derived the fluorescent diffuse photon density wave in the scattering medium (Eq. (3-14)), which is also expressed in the form of an integral equation. In this section, we illustrate that it can also be expressed in the form of a matrix equation and then perform the inversion for fluorescent diffuse optical tomography.

### 5.5.1 Normalized Born Approximation

From Eq. (3-14), which basically describes the fluorescence fluence impinging to the detector fiber, we can estimate the fluorescence signal received by the detector as follows:

$$\Phi_{\text{fl}}(\mathbf{r}_d, \mathbf{r}_s) = \int \zeta_s(\mathbf{r}_s)\zeta_d(\mathbf{r}_d)\Omega_f\gamma^{\lambda_2}\Phi_0^{\lambda_1}(\mathbf{r}, \mathbf{r}_s)\frac{\eta\varepsilon\mathbf{N}(\mathbf{r})}{(\mathbf{1} - \mathbf{i}\omega\tau)\mathbf{D}^{\lambda_2}}\mathbf{G}^{\lambda_2}(\mathbf{r}, \mathbf{r}_d)d\mathbf{r}, \quad (5-57)$$

where  $\zeta_s$  ( $\zeta_d$ ) is the coupling coefficient [135] for the source (detector) fiber;  $\Omega_f$  is the fluorescent filter attenuation;  $\gamma$  is the quantum efficiency for the detector at a specific wavelength. Other symbols are the same as in Eq. (3-14).

Similarly, we can describe the expression for the excitation fluence detected by the same source-detector pair (without the fluorescent filter and assume the same coupling coefficients):

$$\Phi_{\text{inc}}(\mathbf{r}_d, \mathbf{r}_s) = \zeta_s(\mathbf{r}_s) \zeta_d(\mathbf{r}_d) \gamma^{\lambda 1} \Phi_0^{\lambda 1}(\mathbf{r}_d, \mathbf{r}_s). \quad (5-58)$$

Dividing Eq. (5-57) by Eq. (5-58), we get the normalized Born expression of the fluorescent field [133]:

$$\begin{aligned} \Phi^{\text{NB}}(\mathbf{r}_d, \mathbf{r}_s) &= \frac{\mathbf{1}}{\Omega_f} \cdot \frac{\Phi_{\text{fl}}(\mathbf{r}_d, \mathbf{r}_s)}{\Phi_{\text{inc}}(\mathbf{r}_d, \mathbf{r}_s)} \cdot \frac{\gamma^{\lambda 1}}{\gamma^{\lambda 2}} \\ &= \frac{\mathbf{1}}{\Phi_0^{\lambda 1}(\mathbf{r}_d, \mathbf{r}_s)} \int \Phi_0^{\lambda 1}(\mathbf{r}_s, \mathbf{r}) \cdot \frac{\eta \varepsilon \mathbf{N}(\mathbf{r})}{(\mathbf{1} - \mathbf{i} \omega \tau) \mathbf{D}^{\lambda 2}} \cdot \mathbf{G}^{\lambda 2}(\mathbf{r}, \mathbf{r}_d) \cdot \mathbf{d}^3 \mathbf{r}. \end{aligned} \quad (5-59)$$

We discretize the medium under investigation into  $n$  voxels, which can be expressed in the form of a matrix equation similar to Eq. (5-42) [133,134]:

$$\begin{bmatrix} \Phi^{\text{NB}}(\mathbf{r}_{s1}, \mathbf{r}_{d1}) \\ \vdots \\ \Phi^{\text{NB}}(\mathbf{r}_{sm}, \mathbf{r}_{dm}) \end{bmatrix} = \begin{bmatrix} \mathbf{W}_{11} & \cdots & \mathbf{W}_{1n} \\ \vdots & \ddots & \vdots \\ \mathbf{W}_{m1} & \cdots & \mathbf{W}_{mn} \end{bmatrix} \begin{bmatrix} \mathbf{N}(\mathbf{r}_1) \\ \vdots \\ \mathbf{N}(\mathbf{r}_n) \end{bmatrix} \quad (5-60)$$

where

$$\mathbf{W}_{ij} = \frac{\eta \varepsilon \mathbf{h}^3}{\mathbf{D}^{\lambda 2}} \cdot \frac{\mathbf{G}^{\lambda 2}(\mathbf{r}_j, \mathbf{r}_{di}) \cdot \Phi_0^{\lambda 1}(\mathbf{r}_j, \mathbf{r}_{si})}{\Phi_0^{\lambda 1}(\mathbf{r}_{di}, \mathbf{r}_{si}) \cdot (\mathbf{1} - \mathbf{i} \omega \tau)}. \quad (5-61)$$

### 5.5.2 Dual-source System

The difference between the weight function  $\mathbf{W}_{ij}$  for dual-interference-source and single-source configuration lies in that the  $\Phi_0$  here is now the linear summation of the DPDWs from two sources, respectively [130]. Similar to Eq. (5-32), the excitation field is:

$$\Phi_0^{\text{DS}, \lambda 1}(\mathbf{r}_j, \mathbf{r}_{si}) = \Phi_0^{\text{S1}, \lambda 1}(\mathbf{r}_j, \mathbf{r}_{si}) + \Phi_0^{\text{S2}, \lambda 1}(\mathbf{r}_j, \mathbf{r}_{si}). \quad (5-62)$$

The image reconstruction for fluorescent heterogeneity can also be achieved through the methods introduced in Section 5.4.

## 6 Experimental Methods

In this chapter I introduce the essential materials and instruments utilized in the research. **Section 6.1** gives the brief overview of some basic electronic and optical components commonly used in the opto-electronic instruments, including light sources, photon detectors, phase detectors, amplitude modulator and the fluorescence filter. This part of content will provide the basic concepts for further understanding of the construction of the instruments. **Section 6.2** outlines five instruments we have developed for different research purposes. *Section 6.2.1* describes the multi-wavelength frequency-domain homodyne system for a near-infrared spectroscopy measurement; *Section 6.2.2* introduces the heterodyne phased array localizer for object localization; the extension of the phased array localizer to fluorescence goniometry for two-dimensional localization of a subsurface mouse tumor labeled by fluorescent contrast agents is detailed in *Section 6.2.3*. *Section 6.2.4* includes the geometrical arrangement for tomographic imaging using the dual-interfering-source and the multi-unit phased array topography for brain mapping. Lastly, a continuous

wave instrument utilizes the cancellation principle – the Amplitude Cancellation system is also illustrated in *Section 6.2.5*.

The next part of this chapter overviews the basic chemistry and photo-physical properties of the contrast agents used in the enhancement of tumor-to-normal contrast for tumor detection and localization in the mouse model (**Section 6.3**).

## **6.1 Hardware Basics**

In this section we review the principles and specifications of some basic components commonly used in our opto-electronic system, including the photon detectors, light sources, phase detection, amplitude modulation and the fluorescence filter.

### **6.1.1 Photon Detection – Photomultiplier Tube**

The photomultiplier tube (PMT) is one of the most commonly used detectors for low-level light detection. Typically a PMT consists of a photocathode, an electron multiplier and an electron collector (anode). When a photon hits the photocathode, the photocathode emits photoelectrons through the photoemission process, which are multiplied by the electron multiplier and collected by the anode as an output signal.

In this section we summarize three types of PMTs used in our study: R928, R636-10 and H6780-02. Their features are compared and tabulated in Table 6-1.

R928 PMT: R928 PMT is one of the most commonly used PMTs in NIR spectroscopy and imaging applications. It features high current amplification (9 stages,  $4 \times 10^7$  at 1200 v) and provides the largest anode current among the three PMTs we tested ( $8 \times 10^5$  A/W for 780 nm and  $4 \times 10^5$  A/W for 830 nm at 1200 v). When a larger signal is desired, we can take advantage of the high internal low-noise

amplification from R928 without introducing extra noise power from the additional amplifiers [139].

R636-10 PMT: R636-10 PMT is made from GaAs, which has almost a flat quantum yield from 550 to 850 nm, and has the highest cathode radiant sensitivity (62 mA/W for 780 nm and 55 mA/W for 830 nm) among the three PMTs. The almost equal sensitivities on 780 nm and 830 nm will make the R636-10 PMT ideal for detecting both absorption and fluorescence signals in the NIR range, such as fluorescence detection of Indocyanine Green (ICG).

H6780-02 PMT: H6780-02 PMT is the most convenient to use among all the three since it is the photosensor module with built-in high voltage power supply. Because it uses similar photocathode material as R928 PMT, H6780-02 PMT has a similar spectrum response for the relative sensitivity of 780 nm and 830 nm. The anode current is smaller than the R928 PMT and the R636-10 PMT, due to the relatively lower gain compared to the R928 PMT, and lower cathode sensitivity compared with the R636-10 GaAs PMT.

Table 6-1: Technical specifications for three PMTs

	<b>R928</b>	<b>R636-10</b>	<b>H6380-02</b>	Units
Photocathode material	Multialkali	GaAs(Cs)	Bialkali	
Cathode radiant	20 (780 nm)	62 (780 nm)	5.4 (780 nm)	mA/W
sensitivity	10 (830 nm)	55 (830 nm)	3.3 (830 nm)	mA/W
Current gain	40 (1200 v)	2 (1500 v)	3.7 (1.0 v)	$\times 10^6$
Anode sensitivity	8 (780 nm)	1.2 (780 nm)	0.2 (780 nm)	$\times 10^5$ A/W
	4 (830 nm)	1.1 (830 nm)	0.1 (830 nm)	$\times 10^5$ A/W
Anode dark current	3	0.1	0.4	nA

### **6.1.2 Photon Detection – Photodiode**

Photodiodes are semiconductor light sensors which operate in different principles as PMTs. When a photon strikes the photodiode, the electron within the crystal structure becomes stimulated. If the light energy is greater than the band gap energy, the electrons are pulled up into the conduction band, leaving holes in their place in the valence band. This results in a positive charge in the P-layer and a negative charge in the N-layer. If an external circuit is connected between the P- and N-layers, electrons will flow away from the N-layer, and holes will flow away from the P-layer toward the opposite respective electrodes.

One of the common photodiodes used in our study is OPT202, which has a broad spectral response in the NIR region (500 nm – 900 nm), with the highest sensitivity at around 760 nm (0.48 A/W).

### **6.1.3 Light Source – Laser Diode**

Laser diodes use the semiconductor P-N junction in the laser system. In laser diodes, light is emitted from the transition of electrons from the conduction band of the semiconductor to the valence band, thus the photon has the energy equal to the band gap energy. The laser diodes we used with wavelengths between 750 nm and 830 nm are a direct-gap gallium aluminum arsenide (GaAlAs) crystal. In this type of semiconductor, the ratio of the Ga to Al can be adjusted to vary the band gap width and therefore control the wavelength.

To modulate the laser diode sinusoidally, we modulate the DC driving current to oscillate between the lasing threshold and the maximum current (usually the modulation depth is ~ 90%) using the capacitor coupling.

### 6.1.4 Phase Detection

Basically there are two kinds of phase detection methods which have been utilized in our systems, the homodyne and the heterodyne detection. A homodyne system detects the phase shift at the radio frequency (RF), while the heterodyne system down converts the RF to a lower frequency for phase detection [140]. Usually, the heterodyne technique has a higher accuracy in detecting the phase signal since phase error decreases with decreased oscillator frequency, but with the increase of system complexity [140].

Homodyne Detection: The homodyne detection in our system utilizes the in-phase and quadrature (I & Q) demodulation [104]. The diagram of the I & Q demodulator is depicted in Figure 6-1.

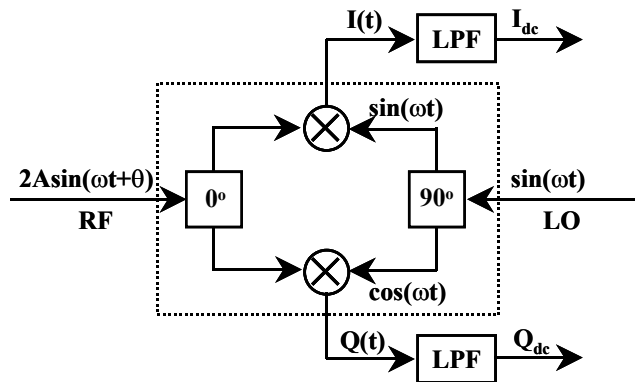


Figure 6-1: Schematic of an I & Q demodulator.

As illustrated in Figure 6-1, the amplitude and phase of the RF signal at the angular frequency of  $\omega$  are detected through the I & Q demodulator. The local oscillator (LO) reference signal is split into  $0^\circ$  and  $90^\circ$  (sin and cos), and mixed with RF signals through a pair of double balanced mixers. The in-phase and quadrature outputs are:

$$\mathbf{I}(t) = 2A\sin(\omega t + \theta)\sin(\omega t) = A\cos(\theta) - A\cos(2\omega t + \theta), \quad (6-1a)$$

$$\mathbf{Q}(t) = 2A\sin(\omega t + \theta)\cos(\omega t) = A\sin(\theta) + A\sin(2\omega t + \theta), \quad (6-1b)$$

After the low-pass filter (LPF), the  $2\omega$  frequency signals are removed; only the dc terms (the first term in the right hand side of Eq. (6-1)) are selected. Thus,

$$\theta = \mathbf{tan}^{-1}(\mathbf{Q}_{dc}/\mathbf{I}_{dc}), \quad (6-2a)$$

$$\mathbf{A} = \sqrt{\mathbf{I}_{dc}^2 + \mathbf{Q}_{dc}^2}. \quad (6-2b)$$

where  $\mathbf{I}_{dc} = A\cos(\theta)$  and  $\mathbf{Q}_{dc} = A\sin(\theta)$ .

Heterodyne Detection: In the heterodyne system, the RF signal is modulated with intermediate frequency (IF) signal (usually audio frequency) through the single side-band (SSB) modulation. After demodulation, the IF signal passes through the IF band-pass filter, and the phase difference between the signal and the reference is detected by a digital phase-meter (Krohn-Hite 6200). The phase meter detects the zero crossings of the sine wave signal to generate a square wave. The square waves of the two channels (signal and reference) are fed to a lead-lag flip-flop and a differential circuit to give the polarity sign and the DC voltage that is proportional to the phase difference between those two channels.

### 6.1.5 Amplitude Modulation

Adjusting the amplitude of the RF waves is important for calibration of frequency-domain instruments. Here, I present an example of amplitude modulation of the RF intensities in the dual-interfering-source system. The amplitude modulation is realized through modulating the RF signal with the external low frequency sinusoidal wave from function generator (Hewlett Packard 3310B) via a double balanced modulator (LM1496, National Semiconductor), as illustrated by Figure 6-2.

The  $0^\circ$  and  $180^\circ$  RF signals are modulated also by out-of-phase low frequency oscillations. The mathematical expressions for the low frequency modulation waves on two channels are:

$$S_1(t) = S_0[1 + m \cdot \cos(\Omega \cdot t)], \quad (6-3a)$$

$$S_2(t) = S_0[1 - m \cdot \cos(\Omega \cdot t)], \quad (6-3b)$$

where  $m$  is the low frequency modulation depth,  $S_0$  is the average source strength and  $\Omega$  is the low modulation frequency. Figure 6-3 illustrates the RF waveform intensities for two sources.

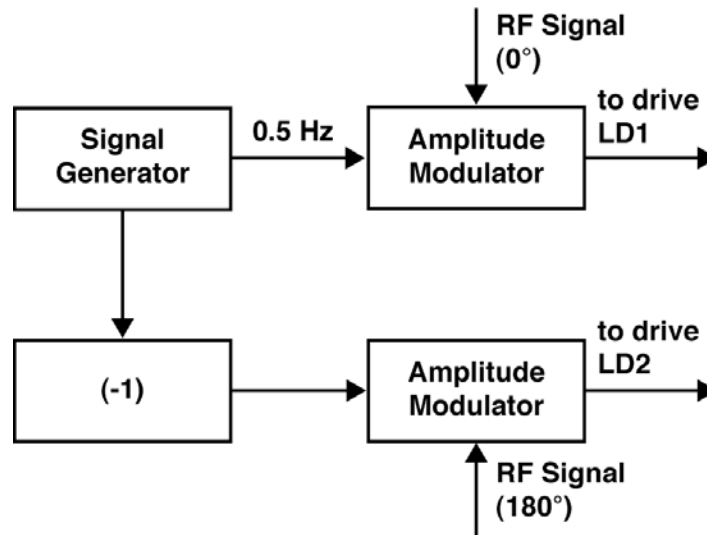


Figure 6-2: Amplitude modulation of RF waves.

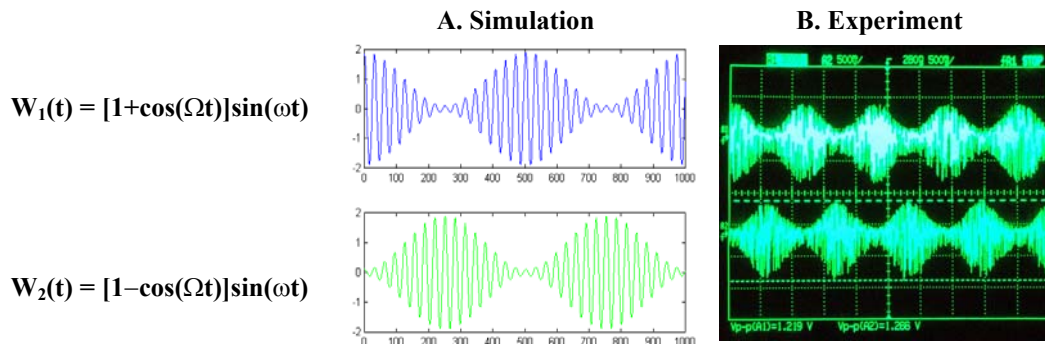


Figure 6-3: Illustration of amplitude modulated RF waves (A: simulation from the analytical expression; B: experiment results displayed on the oscilloscope).

As we can see from Figure 6-3, the intensities of RF waves  $W_1$  and  $W_2$  are periodical functions determined by the low frequency modulation waves. By this means, we can control the RF amplitude for both channels and also the relative intensity ratio between two sources to achieve the purpose of adjustment of the interference pattern (see Section 4.5.1).

### 6.1.6 Interference Filter

To select the photons at the fluorescence wavelength, a secondary filter is usually applied. The general requirements for the fluorescence filter are: 1) high transmission at the fluorescence band; 2) high blockage at the excitation wavelength. In our system, we use an interference filter to select the fluorescence photon and reject the excitation lights.

The principle of the interference filter is illustrated as follows. If a thin transparent spacer is placed between two semi-reflective coatings, multiple reflections and interference can be used to select a narrow frequency band, producing an interference filter. If the spacer is a half wavelength for the desired wavelength, then other wavelengths will be attenuated by destructive interference. Usually, an interference filter is designed for normal incidence, and will shift to shorter wavelengths if tilted.

The thickness for the designated pass-band wavelength  $\lambda_0$  is:

$$\mathbf{d} = \lambda_0 / 2\mathbf{n}, \quad (6-4)$$

where  $n$  is the index of the spacer and the incident angle is zero (Figure 6-4). For incident angle of  $\alpha$ , the passed wavelength is given by:

$$\lambda = \lambda_0 \cos\beta = \lambda_0 \sqrt{1 - \frac{\sin^2 \alpha}{n^2}}. \quad (6-5)$$

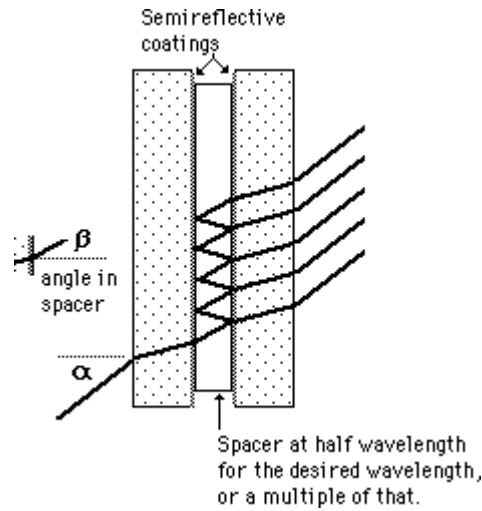


Figure 6-4: The diagram of interference filter.

The diffuse photons coming from the detector fiber tip are impinging into the filter at various angles (limited by the numerical aperture of the fiber), thus the passed wavelength will shift towards the shorter wavelength, *i.e.*, will cause the leakage of the excitation light. The transmission property of the interference filter is angular dependent, as shown in Figure 6-5, which plots the simulation of the transmittance of the interference filter (830DF10 thin film) at  $0^\circ$ ,  $10^\circ$ ,  $15^\circ$ ,  $20^\circ$ ,  $25^\circ$ , and  $30^\circ$  in angle of incidence (AOI) provided by the manufacturer. As the AOI increases, the coating shifts further and further to shorter wavelengths. Since the diffused photons coming from the tip of the detection fiber bundle will impinge on the filter film in various angles (for optical fiber with N.A. = 0.66 and  $n = 1.50$ , the maximum off-axis angle is  $\sim 26^\circ$ ), the photons in the excitation wavelength (780 nm) with larger incident angles ( $\sim 30^\circ$ ) will not be effectively blocked by the filter. Thus those leakage photons in the excitation wavelength will dominate the fluorescence signals in 830 nm. To overcome this problem, a specially designed collimator is employed, with the plano-convex lens

(Edmund Scientific, NJ) to collimate the incident photons and an angle selection of less than  $15^\circ$  to assure the blockage of excitation photons, which is shown in Figure 6-6. Also two 830 nm filters are stacked together to give an effective blocking OD of 6 at the excitation wavelength (780 nm).

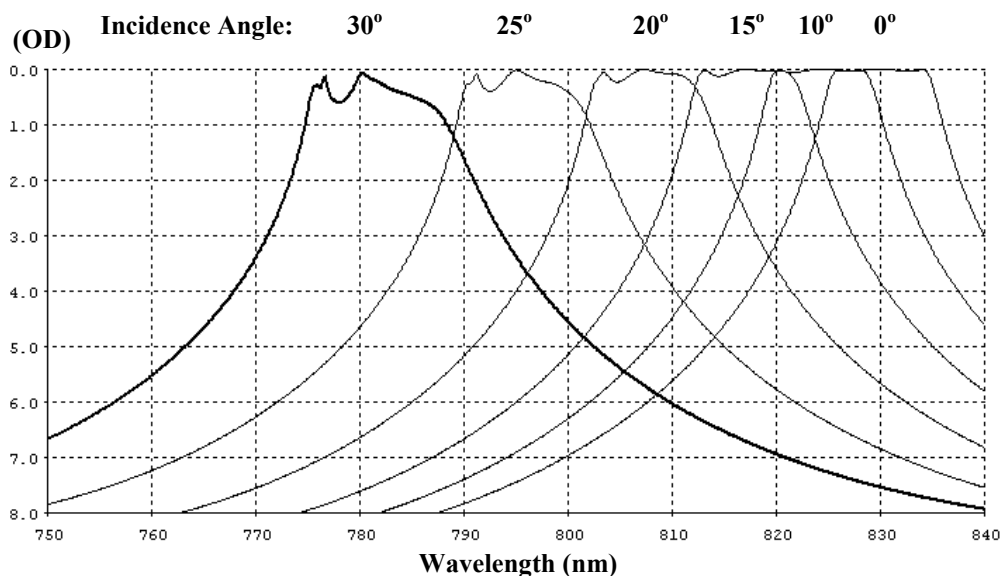


Figure 6-5: Attenuation (in optical density) versus incident angle for the 830 nm interference filter (courtesy of Mark Ziter from Omega Optical, Inc.).

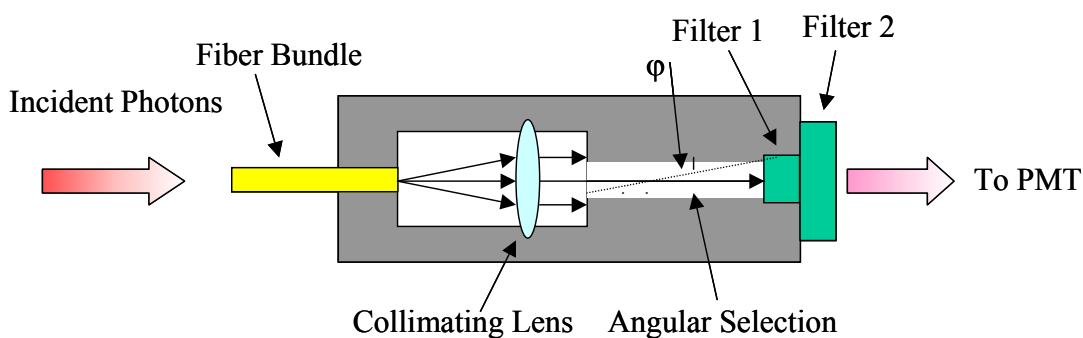


Figure 6-6: Block diagram of the collimator for angle selection.

## 6.2 Apparatus

In accordance to the three kinds of light sources described in Section 3.2, three major types of experimental instruments have been developed for NIR spectroscopy

and imaging. The simplest one is a continuous wave (CW) instrument where a constant intensity light source is used, and the attenuation of light intensity due to the tissue absorption and scattering is measured by an amplitude detector [141-143]. A more complex system, phase modulation system (PMS), employs the intensity modulation of the light source by a sinusoidal radio-frequency (RF) wave [104,142]. The detection circuitry consists the demodulator to give the amplitude attenuation and phase shift signals. The most complicate approach is the time-resolved techniques (TRS) [144,145]. In this case short light pulses are injected into tissue, and the detection involves a time-correlated photon counting system which generates a histogram of the number of arriving photons as a function of time.

From the CW instrument to the TRS instrument, the information content increases. The simple CW instrument could not differentiate the light attenuation due to the scattering or the absorption process. The PMS instrument can quantify the scattering and absorption from the amplitude and phase data. The TRS instrument contains the highest information content since it is equivalent to the multi-frequency intensity modulation method through Fourier transform. In terms of the cost and complexity, it also increases from the CW to TRS. In our study, in order to have an economical and portable instrument with enough information content, we mainly focus on the frequency-domain intensity modulation instrument and the CW instrument as the major tools in our research.

### **6.2.1 I & Q Homodyne System**

In this section we will introduce a homodyne system based on the I & Q phase detection (Section 6.1.4). The frequency-domain multi-wavelength I & Q system is illustrated in Figure 6-7. The light sources were 690 nm, 750 nm, 780 nm, 810 nm and

830 nm laser diodes, which were modulated at 140 MHz, time-multiplexed and coupled to a 1 mm diameter optical fiber (OZ Optics, Canada). The light was collected by a 3 mm fiber bundle, and a photomultiplier tube (PMT, Hamamatsu, R928) was used to detect the light signal. Homodyne detection was performed. After amplifying and filtering, the signal from the PMT was mixed with a reference channel through the in-phase and quadrature (I&Q) demodulator, and converted into I and Q components which carry the information of amplitude and phase. This system has been used to monitor the blood volume and oxygenation on piglet and rat models [116,148] (see Section 7.5).

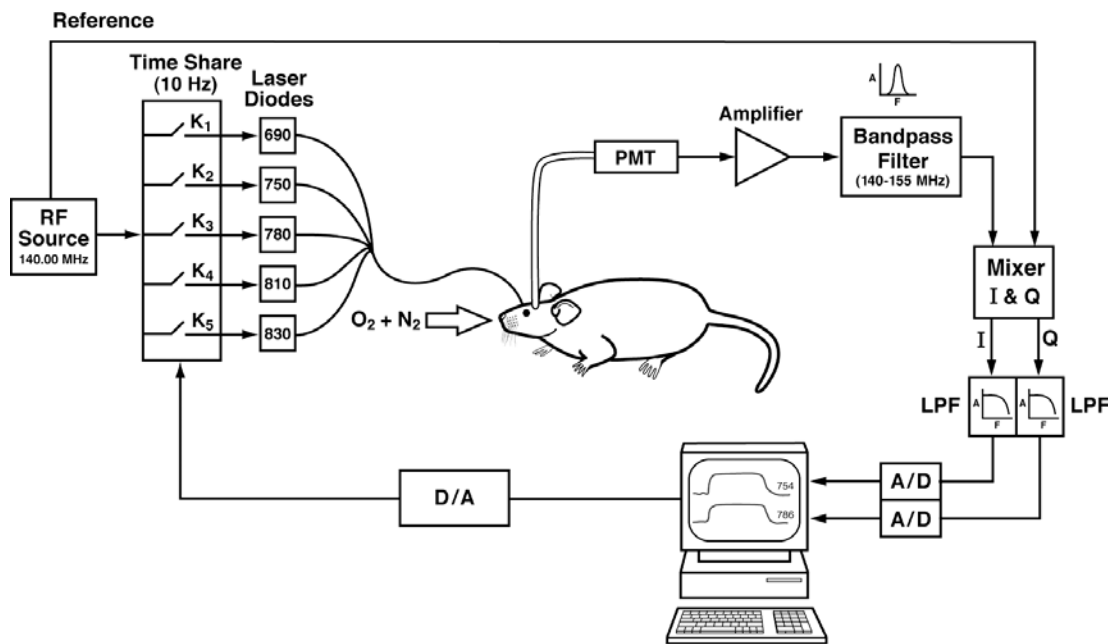


Figure 6-7: Schematic of the frequency-domain homodyne system (PMT: photomultiplier tube; LPF: low pass filter; I & Q: in-phase and quadrature).

## 6.2.2 Phased Array Localization System

In this section we present the frequency-domain phased array system which utilizes the dual-interfering-source principles detailed in Chapter 4. The purpose of this instrument is to accurately locate the position of the object in the diffuse media. Different from the homodyne system outlined above, this system is a heterodyne system (Section 6.1.4).

Figure 6-8 depicts the diagram of the apparatus. A 50 MHz oscillator is modulated in the single side-band (SSB) mode by 2 kHz sinusoidal wave and the upper side-band (USB) from the transmitter (FT-690R11, Yaesu Musen Co. Ltd., Japan) is selected and split into  $0^\circ$  and  $180^\circ$  by the RF splitter (ZSCJ-2, Mini-Circuits). The RF waves are amplitude modulated by a low frequency oscillator (0.5 Hz), and then modulate the laser diode sources (Sharp Laser Diode, 780 nm, 5 mw) with a modulation of 90%. The light is delivered to the medium through fiber optics, and the scattered photons are collected by a 3 mm diameter fiber bundle. The optical signal is then detected by a R928 photomultiplier tube (PMT, Hamamatsu Photonics, KK) and demodulated by a 50 MHz SSB receiver.

The amplitude of the RF waves can be modulated by the amplitude modulator described in Section 6.1.5. Usually, the calibration is performed on a homogeneous medium with the signals from two light sources equal in amplitude and  $\sim 180^\circ$  difference in phase, and then the amplitude modulation intensity is fixed during the entire scanning. In the case of heterogeneous background, adaptive calibration is applied using the low frequency amplitude modulation [139] (see Section 7.1).

The system uses the heterodyne technique to detect the phase signal since phase error decreases with decreased oscillator frequency. After demodulation, the IF

signal passes through a 2 kHz band-pass filter, and the phase difference between the signal and the 2 kHz reference is detected by a digital phase-meter (Krohn-Hite 6200). The accuracy of phase detection is  $0.5^\circ$ .

To obtain a substantial level of IF signal intensity for accurate phase detection, the automatic gain control (AGC) circuit is used. The actual signal amplitude is recovered from the AGC control voltage through a lookup table. The advantage of using AGC is the large dynamic range, which is around 90 dB for this system, while the disadvantage is the relatively long time constant, about 1.0 second, due to the feedback control.

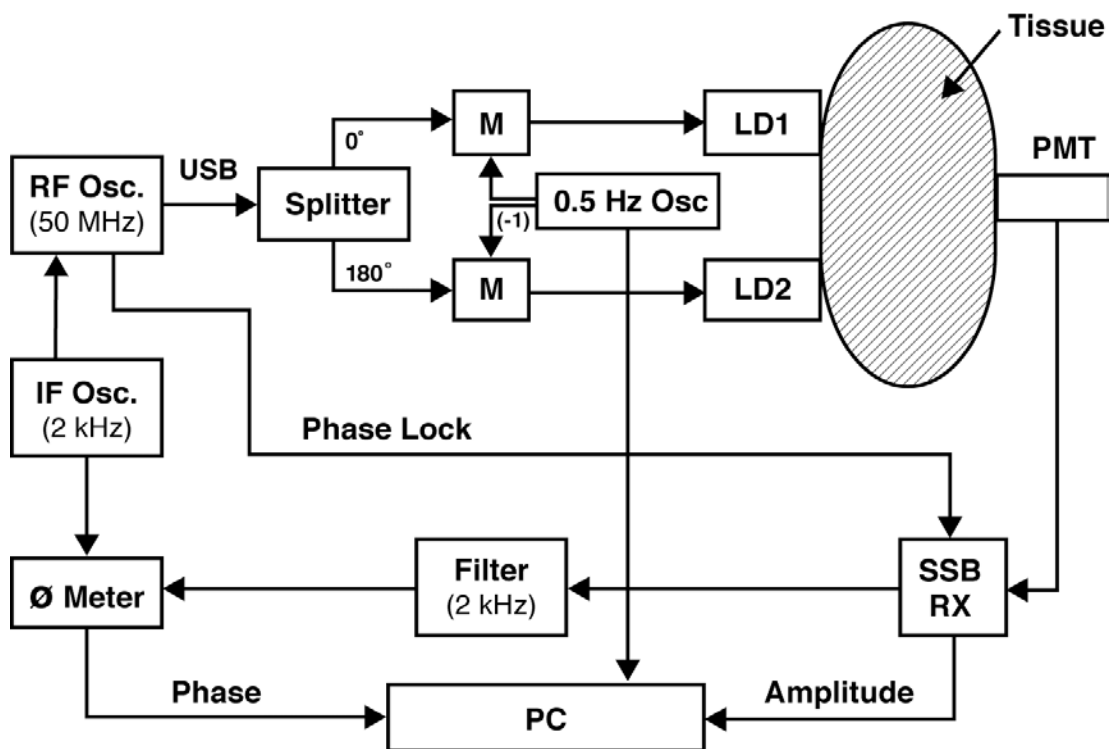


Figure 6-8: Block diagram of the phased array localizer. (Osc.: oscillator; M: amplitude modulator; LD: laser diode; PMT: photomultiplier tube; RX: receiver;  $\phi$  Meter: phase meter; PC: Intel Pentium based personal computer)

Table 6-2 lists the noise level for single- and dual-source configurations for this system, also compared with the simulation described in Chapter 4. The bandwidth is 1 Hz.

Table 6-2: Noise level for single- and dual-source configurations

	Single-Source		Dual-Source	
	Amplitude	Phase	Amplitude	Phase
Simulation	0.5%	0.15°	25%	10°
Experiment	0.3%	0.08°	6%	1.8°

Both the experiment and simulation results suggest that due to the increase of the sensitivity, the noise level of the dual-source system also becomes larger than the single-source. The ratio from the simulation is larger than the experiment because the cancellation between two single sources is better in the simulation, which will result in a smaller background signal; hence, the larger percentage in amplitude variation and phase noise. For the experiments, the balance of two sources (equal amplitude and 179° phase difference) is not ideal due to the resolution of the RF attenuator and the slight difference between the two cables' lengths.

### 6.2.3 Fluorescent Phased Array Goniometry

To detect and locate the fluorescent object in the diffuse media, similar instrument with slight modifications is employed. Figure 6-9 depicts the diagram of the instrument. The electronic components are almost similar to those described in

Section 6.2.2, except that we are using higher power laser diodes (LD, Philips CQL7840, 780 nm, 40 mW) for fluorescence excitation. The light is delivered to the breast tissue phantom ( $\mu_a = 0.05 \text{ cm}^{-1}$ ,  $\mu_s' = 10.0 \text{ cm}^{-1}$ ) through fiber optics. The fluorescence signal from the fluorophore embedded in the phantom is collected by a 3 mm diameter fiber bundle. An 830 nm  $\pm$  10 nm interference filter (830DF10, Omega Optical, Inc., VT) with a blocking OD of 6 in the excitation wavelength is used to select the fluorescent photons. The optical signal is then detected by a R928 photomultiplier tube (PMT, Hamamatsu Photonics, KK) and demodulated by a 50 MHz SSB receiver. The amplitude of the fluorescent signal is determined by the automatic gain control (AGC) voltage through a look-up table, and the phase is measured in 2 kHz by the phase-meter (Krohn-Hite 6200).

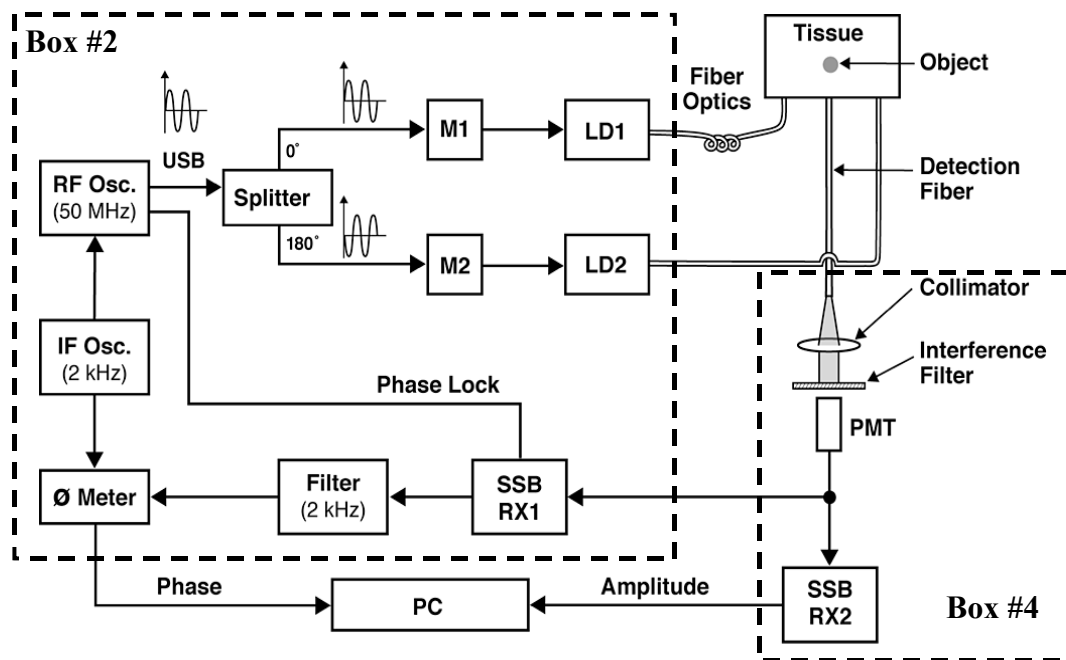


Figure 6-9: Schematic of 50 MHz fluorescent phased array system. (Osc: Oscillator; USB: Upper Side Band; M: Modulator; LD: Laser Diode; PMT: Photomultiplier Tube; SSB: Single Side Band). The dashed lines indicate the components inside the boxes as shown in Figure 6-10.

Figure 6-10 shows the photo of the phased array imaging system. The system is compact in size and portable to clinical access.

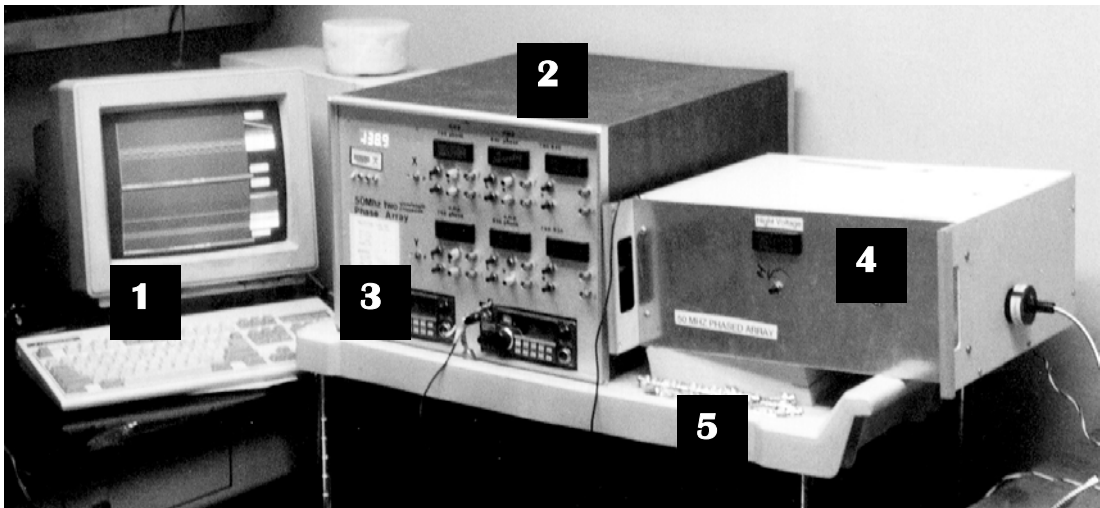


Figure 6-10: Photo of the 50 MHz phased array imaging system (1: Computer; 2: Box contains electronic components as illustrated in Figure 2; 3: RF transmitter and receiver 1; 4: PMT and receiver 2; 5: Wheel Cart).

The goniometric probe consists of two source fiber holders with a separation of 2 cm and a detection fiber bundle holder located in the plane bisecting those two sources with equal distance (4 cm) to each source. The source and detector fibers can be scanned together in tandem along the axis under the control of a stepper motor (NEMA17BSM, StepperControl.com). The spatial resolution is 0.5 mm and the scanning speed is usually 0.5 mm/s. After finishing one axial scan, the inner ring of the probe can be rotated to another direction and perform the next scan (see Figure 6-11). By this method, multiple scans in different directions can be obtained for the purpose of object localization (see Section 4.4).

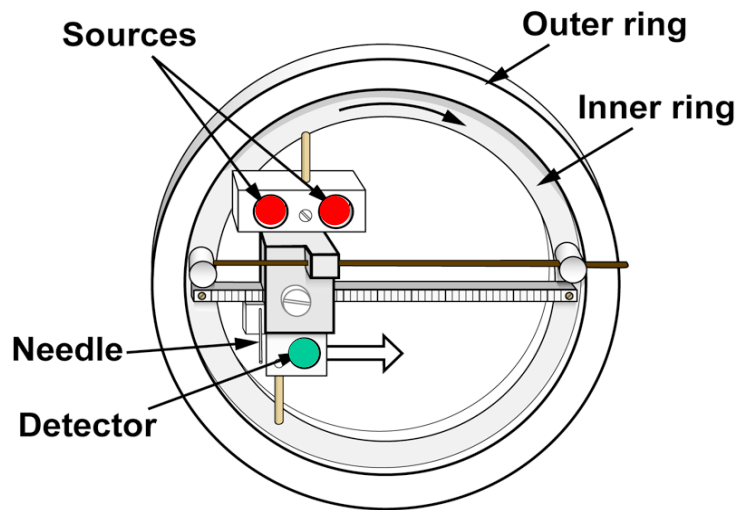


Figure 6-11: Two-dimensional goniometric probe.

The application of the phased array goniometry system includes the detection and localization of the tumor with the contrast enhanced by the fluorescent contrast agent (see Section 7.2).

#### 6.2.4 Phased Array Tomographer and Topographer

Phased Array Tomographer: In order to perform the tomographic image reconstruction using the phased array system, multiple projections with phased source pair and different detectors are utilized. The instrument used for tomographic imaging is similar to the one demonstrated in Section 6.2.2 and 6.2.3, and only the scanning scheme is modified to fulfill the data collection requirements as stated in Eq. (5-42).

The data measurement was performed on slab geometry with  $8 \text{ cm} \times 5 \text{ cm}$  rectangular area (Figure 6-12). The sources (source pairs) and detectors were scanned in parallel with 1 cm step (in total  $9 \times 9$  measurements) sequentially, *i.e.*, with one

source pair position, the detector is scanned for all 9 positions. The tomographic image reconstruction using this system is detailed in Section 7.4.

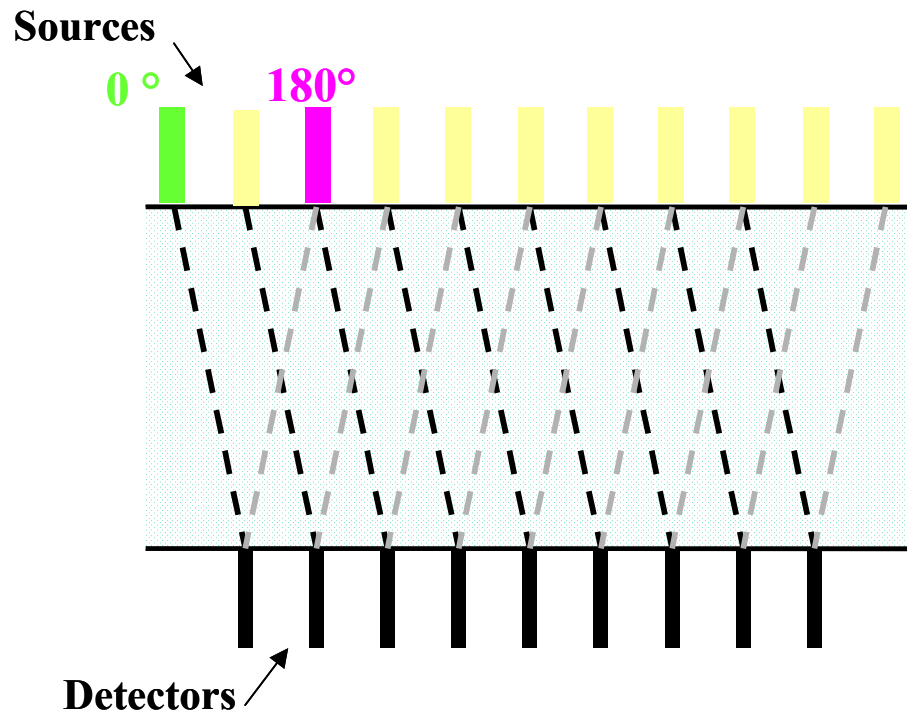


Figure 6-12: Source-detector arrangement for phased array tomographer.

The purpose of tomography is to resolve the three-dimensional position of the targeted object, while in many applications of detection and localization, a fast two-dimensional indication of the object position is also important. We have developed the phased array topography system, which maps the object position by placing multiple source-detector arrays over the probing area.

*Single-wavelength Phased Array Topographer:* Figure 6-13 illustrates the diagram of the single-wavelength phased array imager. The insert in the upper left depicts the source-detector geometry. 9 sources (780 nm laser diode) and 4 detectors

(H6380-02 PMT) are arranged in a  $9\text{ cm} \times 4\text{ cm}$  rectangular area. The  $0^\circ$  and  $180^\circ$  sources are placed adjacently and totally form 16 source-detector arrays (4 surrounding each detector). Each PMT has 4 sources around it, thus can form 4 phased array pairs. The detector is positioned appropriately to get an amplitude null and phase shift around  $90^\circ$ . A localized small change of absorption or scattering will cause significant perturbation in nearby phased array pairs and result in the phase shifts, which form the signals for imaging. The source-detector is in the remission mode with a separation of  $2.5\text{ cm}$  [91].

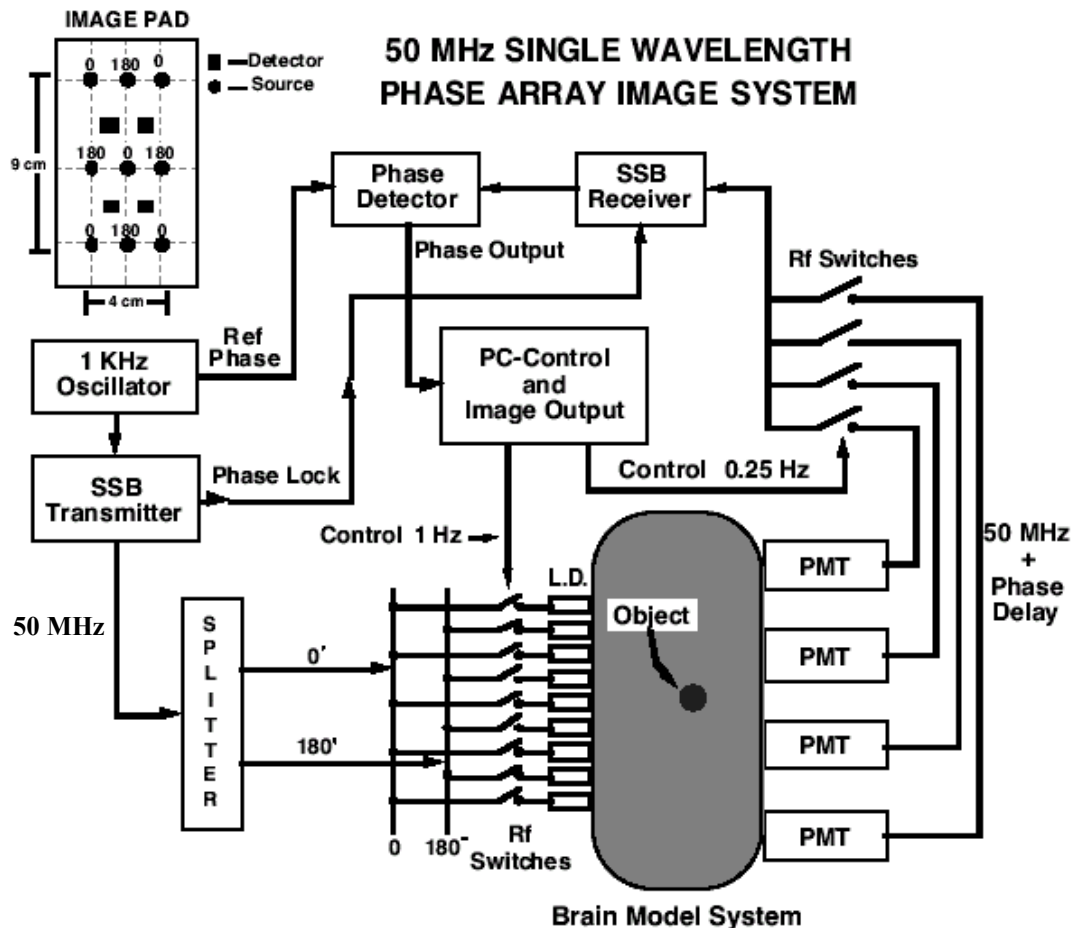


Figure 6-13: System diagram for the single-wavelength phased array imager.

The system also uses the SSB modulation of the 50 MHz RF signal. The difference between this system and the system described in Section 6.2.2 is that a series of RF switches (Radio Shack) control the on-off of the specific array. Each time a pair of  $0^\circ$  and  $180^\circ$  sources are turned on and the closest detector receives the signal. The time constant for each array is 1 second and the total time for one complete scan is 16 seconds. After the scanning of all the arrays, a two-dimensional image of the underlying area can be generated. The results of brain mapping are given in Section 7.6.

Dual-wavelength Phased Array Topographer: The next version of the phased array imager applies two wavelengths, because the different responses in those two wavelengths will indicate the changes in the oxygenated and deoxygenated hemoglobin [92].

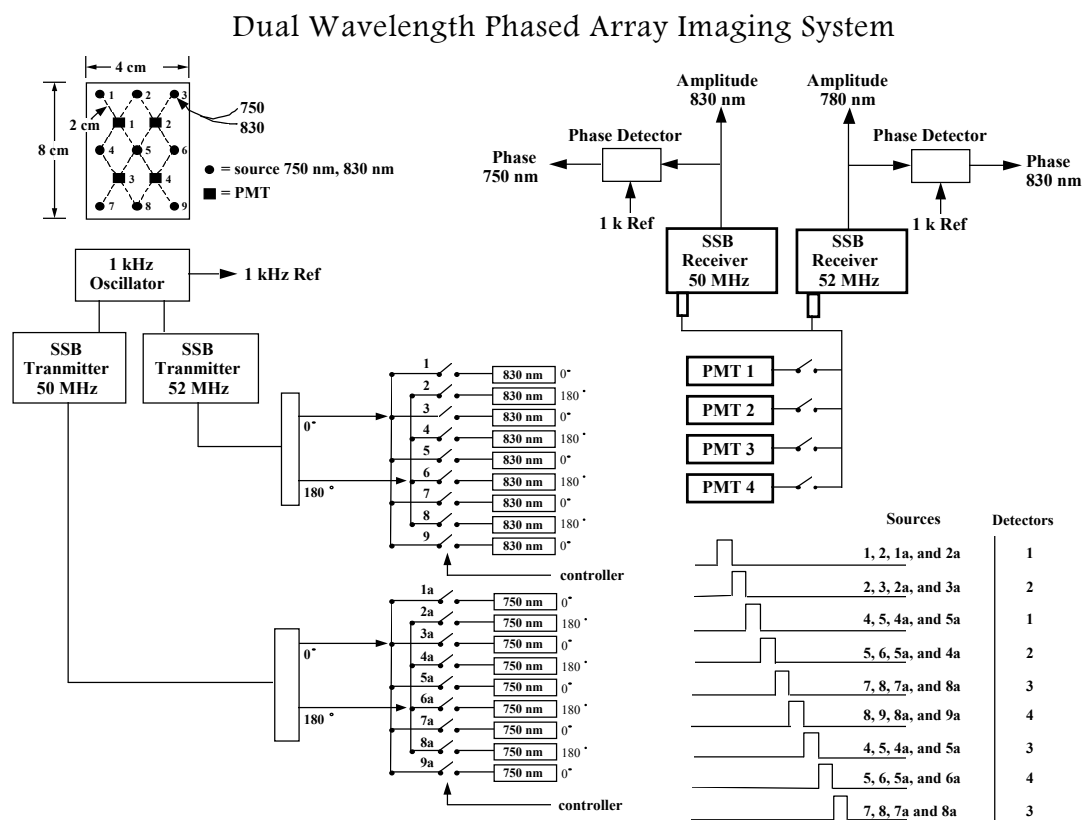


Figure 6-14: System diagram of the dual-wavelength phased array imager.

Figure 6-14 depicts the schematic of the two-wavelength phased array imaging system. The system uses two different radio frequencies (50 MHz and 52 MHz) to encode two wavelengths (750 nm and 830 nm), respectively. Both are modulated in the SSB (single side-band) mode (1 kHz). The upper side band (USB) is chosen and split into  $0^\circ$  and  $180^\circ \pm 1^\circ$  to achieve a sharp cancellation plane. There are 9 laser diode sources (Sharp Corp., Japan) for each wavelength (total of 18) and 4 detector fiber bundles mounted on a 7 cm  $\times$  4 cm rectangular rubber pad, with a source-detector separation of 2 cm. The fibers are then coupled into the R928 PMT (Hamamatsu Photonics, Japan). The output signals are sent to SSB receiver, which can detect the signal levels on the order of microvolts in a 2 kHz bandwidth, and then decoded for each wavelength. The phase of the 1 kHz sine wave can be detected through a zero-crossing phase meter (Krohn-Hite Corp.) and the amplitude measurement is based on the AGC (Automatic Gain Control) voltage. The combination of sources and detectors makes up 16 phase cancellation arrays in total. The sampling time for each cycle is 16 seconds. The two dimensional spatial resolution for this system is 1 cm and the signal to noise ratio is about 500 for a normal parietal response in 1 Hz bandwidth. The application of the dual-wavelength phased array imaging system for neonatal brain mapping is demonstrated in Section 7.6.

### **6.2.5 Amplitude Cancellation System**

The principle of interference of DPDW is not just limited to the frequency domain system. It can also be applied to the time domain [86] and the continuous

wave system [146]. In this section, we are illustrating a CW phased array system for breast tumor imaging.

The dual-wavelength amplitude cancellation system is demonstrated in Figure 6-15. This device has a probe (upper left insert) of 9 cm × 10 cm rectangular shape. The sources are laser diodes (750 nm and 830 nm). The probe consists of 8 sources and 21 silicon photodiodes. The sources and detectors were mounted in a sponge rubber pad which is flexible and afforded a close approach of the sources and detectors to the breast tissue.

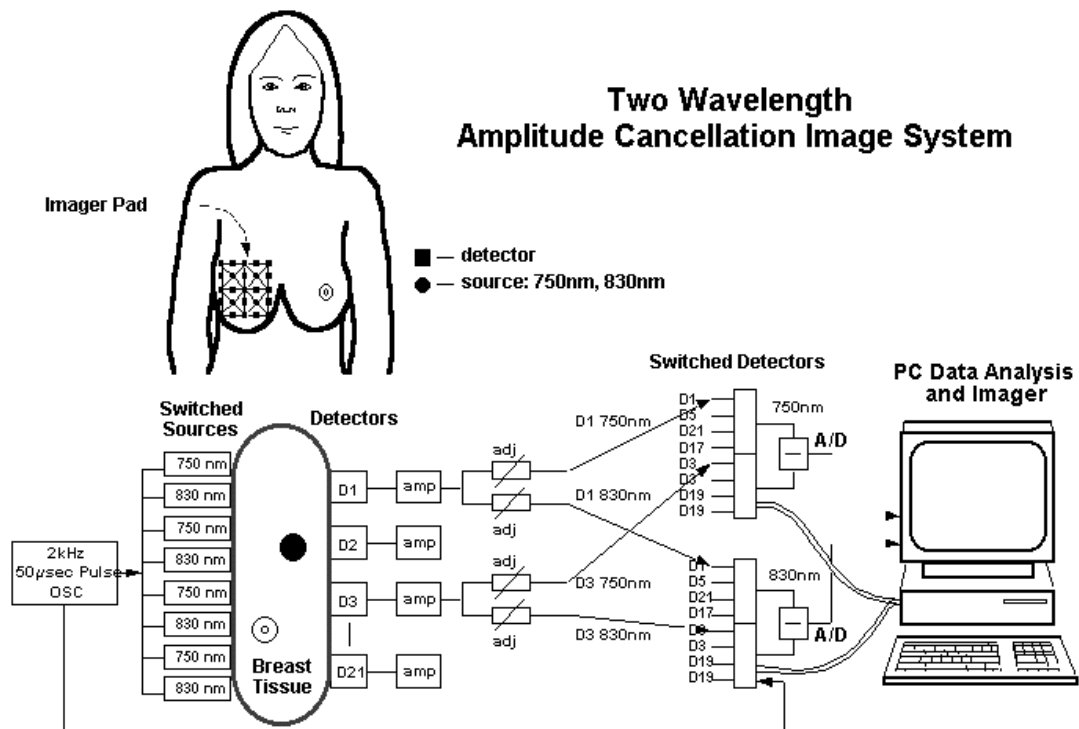


Figure 6-15: Schematic of dual-wavelength amplitude cancellation imaging system.

The probe has four units, each of which has a pair of sources (750 nm and 830 nm) placed next to each other and surrounded by 8 detectors. Based on the

cancellation principle, the signals from two equidistant detectors are subtracted to form zero in the homogeneous media. When there is a small perturbation on the photon path in the areas of the sources and detectors, there is a perturbation signal responding to the small object.

The sources are modulated by 50  $\mu\text{s}$  pulse encoding the dual wavelength (750 nm and 830 nm). The data from two corresponding detectors are subtracted by the differential amplifier. The imaging time is 8 seconds and the spatial resolution is less than 1 cm. Another feature of this system is the programmed amplifier to automatically adjust the gain for each channel [146]. The imaging system is first calibrated on a breast model by adjusting the gain through the programmed amplifier to ensure all outputs are equal; hence the differential amplifier outputs are zero. The sensitive null (zero) plane is applied to detect small objects. The system has a high signal-to-noise ratio (100) in detecting inhomogeneity of the breast with respect to the surrounding tissue or to the contralateral breast in voxels containing blood volume and oxygenation changes corresponding to the presence of tumors or related tissue pathologies (see Section 7.3).

We have also explored the amplitude cancellation through the low frequency modulation. From Eq. (3-3) and (3-5), when the modulation frequency  $\omega \ll \mu_a c$  (in practical biological situation with  $\mu_a \sim 0.05 \text{ cm}^{-1}$ ,  $\omega < 1 \text{ MHz}$ ), the solutions from frequency domain and CW are actually similar. Thus we can use the CW solutions to analyze the low frequency modulation to simplify the mathematical model. In addition, the phase cancellation using the low frequency modulation can be achieved through the photodetector, while in the CW system we need to construct the differential circuit or the subtraction algorithm. Besides, the electronic components in the low frequency range (audio frequency) are easily integrated into a small-scale

device compared with radio frequency components. A recent hand-held system applies two out-of-phased 3 kHz sinusoidal modulated two light emitting diodes (LED) and one silicon photodiode detector [147]. The model experiments indicate this system has affordable sensitivity for breast tumor and lymph node tumor detection.

### **6.3 Fluorescence Contrast Agents Development**

Exogenous contrast agents are utilized to enhance the tumor-to-normal contrast for increased detection sensitivity and specificity. This requires the design of the contrast agents according to the morphological and physiological properties of tumor tissue. One of the interesting tumor features is the increased tumor vasculature and leaky vessels. Thus a blood-pooling agent such as ICG could be used to enhance the imaging contrast in a means similar to that of angiography.

#### **6.3.1 Non-specific Fluorophores**

Indocyanine Green (ICG) is used as both the absorption and fluorescence contrast agent since it had been approved by the Food and Drug Administration (FDA) and is commercially available (Akorn Inc.). It has been widely used in ophthalmology for the purpose of angiography [30].

ICG is a non-specific contrast agent and mainly binds to the albumin in the blood. Figure 6-16 illustrates the structure and spectrum of ICG.

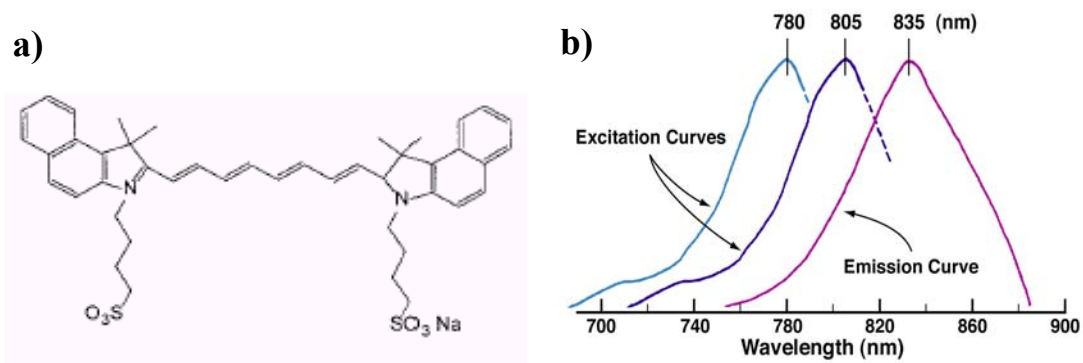


Figure 6-16: The structure (a) and the absorption/fluorescence spectrum (b) of ICG (the peak of absorption spectrum is at 780 nm in water or 805 nm in the plasma).

One of the ICG analogs is the dye Cypate reported by Achilefu *et al* [40,41]. Figure 6-17 provides the structure of Cypate. The similarity in the structures of ICG and Cypate is that there are carbon atoms linked between two nitrogen centers, which is named polymethine chromophore, or the carbocyanine dye [29]. Both ICG and Cypate are not tumor specific and will be cleared by the liver within one hour [41].

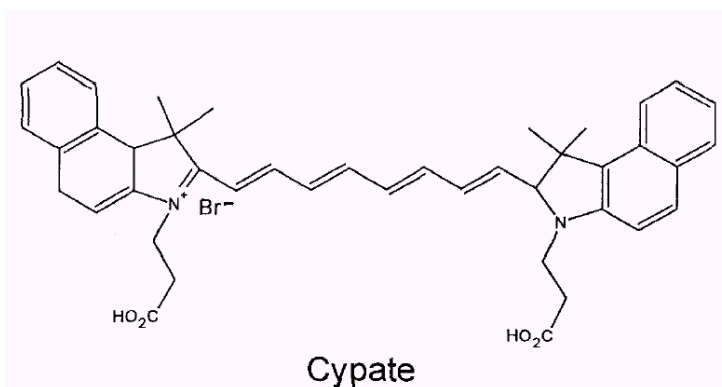


Figure 6-17: Chemical structure of Cypate. (Adopted from Ref. [40])

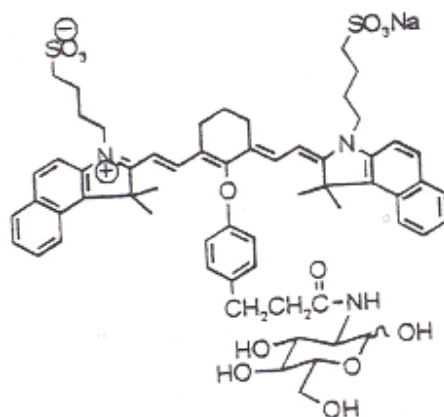
### 6.3.2 Molecular Targeting Contrast Agents

To increase the molecular specificity, other contrast agents with preferential uptake in tumor cells have been developed [26,29]. In this study, we focus on a family

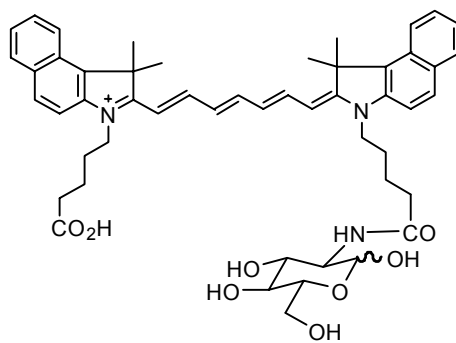
of NIR Fluorophore-2-D-Glucosamide conjugates (NIRF-2DG, developed by Dr. Gang Zheng and Min Zhang at the University of Pennsylvania) [150].

A common feature of malignant cells is the use of glycolysis for energy generation, and results in enhanced expression of glucose transporters (GLUTs) and activity of hexokinase in tumor cells. This mechanism is similar to the tumor detection using  $^{18}\text{F}$  2-fluoro-2-deoxyglucose ( $^{18}\text{F}$ FDG)-based positron emission tomography (PET), which is widely used for detecting and staging many human cancers [151]. This signature feature of tumor cells may also be utilized for detecting tumors using optical imaging based on the enhanced uptake and entrapment by phosphorylation of non-metabolizable 2DG in tumor cells.

For the fluorescence contrast agent, we mainly use the tricyanocyanine dyes as the fluorochrome because of their NIR spectrum. There are several examples: NIR804-2DG, Bacteriochlorophyll (BChl)-2DG and Cypate-mono-2DG. They all have similar spectral properties as ICG (the peak of the absorption spectrum is near 800 nm and the peak of the emission spectrum is near 830 nm, see Table 6-3). Figure 6-18 gives the schematics of NIR804-2DG and Cypate-2DG.



(a)



(b)

Figure 6-18: Chemical structures of (a) NIR804-2DG and (b) Cypate-2DG.

Table 6-3: Photophysical properties of NIRF-2DG

	Excitation Wavelength	Emission Wavelength
NIR804-2DG	805 nm	830 nm
BChl-2DG	825 nm	840 nm
Cypate-mono-2DG	780 nm	830 nm

## 7 Experimental Results

This chapter presents the experimental results of six research projects, which are all based on the theory and instrumentation introduced from Chapter 3 to Chapter 6. **Section 7.1** demonstrates the improvement of localization accuracy of the phased array localizer, through periodically sweeping the cancellation plane across the scattering media. The influence of the background heterogeneity on the balance of the phased array system with the fixed cancellation plane will be considered in this system and adaptive calibration is applied to minimize the effects. Results on tissue phantoms and animal models are presented. **Section 7.2** is one of the main themes of this dissertation – detection of a tumor labeled by fluorescence contrast agents. We have demonstrated the sensitivity and accuracy of the fluorescent phased array goniometric imaging system, and the preliminary results on the animal tumor model are presented. Our results suggest that metabolic targeting contrast agents could be

used for the enhancement of tumor-to-background contrast in early tumor detection. **Section 7.3** illustrates some clinical results obtained by the Amplitude Cancellation system, without the administration of exogenous contrast agents. The tumor detection is based on the increase of blood volume and deoxygenation, as well as the spatial congruence between these two parameters. **Section 7.4** gives the results of tomographic imaging of both absorption and fluorescence heterogeneity embedded inside the scattering media.

**Section 7.5** and **7.6** are focused on another interesting topic in diffuse optical imaging, the brain function. **Section 7.5** shows the spectroscopic measurements of the blood volume and oxygenation in the rat brain during the modulation of inhaling oxygen. Moreover, these results were correlated with the BOLD MRI signals on the co-localized region. **Section 7.6** gives the example of functional brain mapping using the phased array topography.

## **7.1 Adaptive Calibration for Phased Array Localizer**

In Chapter 4 we demonstrated that in the homogeneous medium, the higher sensitivity is achieved when the two sources are balanced with an intensity ratio of unity and a phase difference of  $180^\circ$ . Figure 7-1 shows the experimental measurement of object detection using the phased array localizer. This result suggests that the phased array system can sensitively detect a small wire down to 0.15 mm based on the phase transition. However, due to the boundary effects or heterogeneous background absorption (the presence of other absorbers), in real clinical situations the amplitude detected by the detector from each source, after propagation through the medium, will generally be unequal and the phase difference will not be  $180^\circ$ , thus the sensitivity will be degraded [88], and the localization error will be larger. In this case, calibration

is required to adjust the amplitude and phase of each source to make the source pair re-balanced.

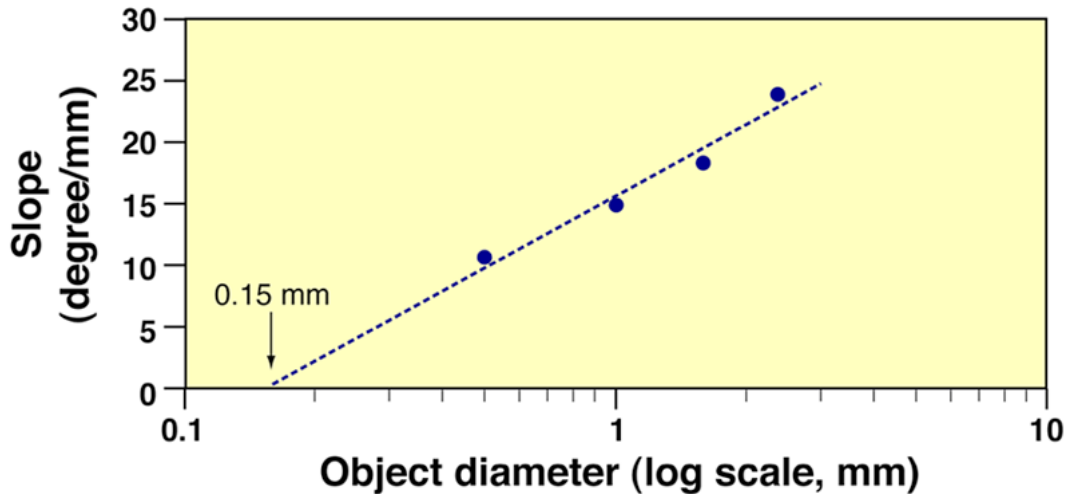


Figure 7-1: The phase transition slope vs. the object diameter. The objects are a series of iron wires with different diameters. Extrapolation of the signal gives the detection limit of the phased array system.

We can use an example to illustrate the necessity of the calibration procedure with simulation data. Figure 7-2 shows the case of the dual-interfering-source system calibration on the heterogeneous model. Figure 7-2(a) is a calibration on a homogeneous model, so the two sources are balanced (equal in amplitude) and can detect the perturbation of a small absorber (the signal is depicted as the blue curve in Figure 7-2(c)). While on a heterogeneous model (like calibrating on the brain, or other heterogeneous tissue, and a simplified model is illustrated by Figure 7-2(b) with the presence of another fixed absorber), the two sources will not be balanced so that the system is working on the asymptotical region of Figure 4-3(b)(c), thus the sensitivity is degraded (the signal is depicted as the black curve in Figure 7-2(c)). We can

rebalance the sources by adjusting the amplitude for each source and restore the high detection sensitivity (the signal is depicted as the red curve in Figure 7-2(c)).

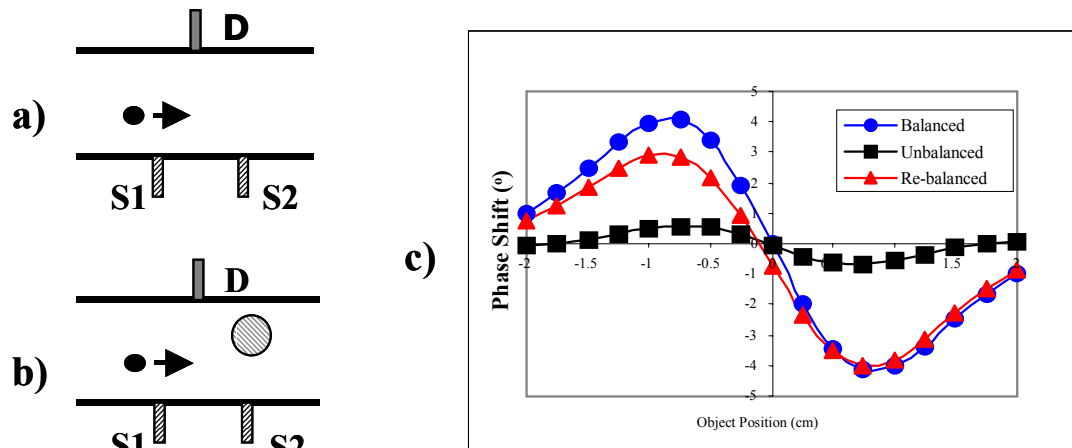


Figure 7-2: Dual-interfering-source detection on homogenous medium (a) and heterogeneous medium (b). The background optical coefficients are  $\mu_a = 0.08 \text{ cm}^{-1}$ ,  $\mu'_s = 12.0 \text{ cm}^{-1}$ . For the homogeneous case, the small scanning absorber has  $\mu_a = 0.5 \text{ cm}^{-1}$  and  $r = 0.1 \text{ cm}$ . The two sources are balanced ( $S1 = S2 = 1.0$ ). For the heterogeneous case, we introduce another larger fixed absorber ( $\mu_a = 0.5 \text{ cm}^{-1}$  and  $r = 0.5 \text{ cm}$ ) to simulate the inhomogeneous background, and the balance is disturbed. If we increase the strength of S2, the two sources will cancel each other again ( $S1 = 1.0$ ,  $S2 = 1.12$ ). The phase transition for the above three cases are plotted in (c). (Blue is

for case (a); Black is for case (b) with  $S1 = S2$ ;

Red is for case (b) with  $S2 = 1.12 * S1$ ).

Investigators have used various methods to modify the amplitude and phase of the two sources [61,64,97,98]. A suggested method is to modulate two RF waves

using a  $90^\circ$  shifted low frequency sinusoidal carrier wave [64,83]. This method is also called an electro-optic scan. The electro-optic scan has been utilized as an alternative to the mechanical scan of the phased array probe to detect the location of the object, thus avoiding the variation in the coupling coefficients between the optical fibers and the tissue in different scanning positions. While detection sensitivity is decreased when the cancellation plane (where the amplitude is minimum and the phase flips  $180^\circ$ ) is away from the detector [88]. To locate an object in a large medium (several centimeters in size), the phased array system needs to be adaptively calibrated on each scanning position due to different influences from coupling coefficients, boundary effects and a non-homogenous absorbing background. In this section we describe a method using the electro-optic scan as a convenient and accurate way of adaptive calibration to account for the amplitude imbalance due to the different attenuations from the media and increase the sensitivity and accuracy in localizing an embedded object.

### **7.1.1 Adaptive Calibration**

The principle and the instrumentation of electro-optic scan have been introduced in Section 6.1.5 and 6.2.2 respectively. Here we will mention the data analysis method for the adaptive calibration. In such a condition, the cancellation plane will continuously scan across the medium also with a frequency  $\Omega$ . When the intensities of two sources are equal, the cancellation plane is in the mid-plane between two sources, and deflects towards the source whose strength is less than the other's, and *vice versa*. Through amplitude modulation, the intensity ratio for those two sources varies periodically, *i.e.*,  $S_1/S_2$  is a function of time. Thus we can achieve a

desired intensity ratio by selecting a specific time point, which simplifies the instrument design and data analysis algorithm.

In phased array detection and localization, the highest sensitivity occurs when the detector is located in the cancellation plane [87]. A small perturbation will cause a shift of the cancellation plane so that sharp changes in amplitude and phase will be detected. When the detector is not placed on the cancellation plane, the signal difference induced by the presence of the object will be smaller (decrease in the detection sensitivity). In the experiment, the relative positions of source pair and detector are fixed and mechanically scanned across the medium in tandem to locate the position of the embedded object. In a homogeneous medium, usually the intensities of those two sources are calibrated to be equal and the detector is placed in the mid-plane of two sources. In this case, the amplitude of the DPDW from each single source will be equal upon the detector position, which will result in the formation of the cancellation plane (here cancellation plane is generally referred to the plane with amplitude minimum, *cf.* Figure 4-14) on the detector position. In a heterogeneous medium, if the source intensities are fixed during the scanning process, when one of the sources is closer to the boundary, or the background optical properties are not homogeneous, or the coupling coefficients of those two sources are varying along the scanning procedure, the DPDW received by the detector from each single source will not be equal in amplitude. Thus the cancellation plane is deflected and the detection sensitivity will be degraded. With electro-optic scanning of the cancellation plane by varying the relative intensities of the two sources, the cancellation plane can be restored to the position of the detector and thus regain the high detection sensitivity.

Object detection using phased array configuration relies on monitoring the perturbation signals (amplitude change and phase transition) induced by an object after the two sources are calibrated and the detector is on the cancellation plane. When the medium is heterogeneous, the signal intensity measured by the detector from each single source is usually unequal and varies from one location to the other during the scanning of the sources and detector together. Thus the condition that the detector is on the cancellation plane could not always be guaranteed. The purpose of calibration using electro-optic scan is to find out the specific time point when the detector is on the cancellation plane at each location, by sweeping the cancellation plane periodically. As mentioned before, the ratio of source intensities is a function of time, thus the specific time  $t'(x)$  at each location when the cancellation plane sweeps through the detector (amplitude minimum and phase transition) in the baseline scan (without object) will indicate the calibrated intensity ratio. Then, the signal at the same time  $t'(x)$  for the scan with an object is compared with the baseline. Since the calibration time  $t'(x)$  (when cancellation plane is on the detector) is generally different for different locations  $x$  in a heterogeneous medium, this procedure is referred to as the adaptive calibration.

The method for the adaptive calibration is listed as follows:

- i. Plot a period of the amplitude and phase signals versus the time index using the function generator's triggering signal (*cf.* Figure 6-8) as the reference.
- ii. Find the calibration time  $t'(x)$  for each location  $x$  from the baseline scan, using the amplitude minimum and phase transition criteria:

$$\mathbf{Log[Amp](x,t')} = \mathbf{min}\{\mathbf{Log[Amp](x,t)}\}; \quad (7-1a)$$

$$\Phi(\mathbf{x}, \mathbf{t}') = \phi_0 (= [\phi_1 + \phi_2]/2). \quad (7-1b)$$

where **min** indicates the minimum, and  $\phi_1$  or  $\phi_2$  is the phase signal when only the in-phase or the anti-phase source is illuminating. The phase transition is from  $\phi_1$  to  $\phi_2$ .  $\phi_0 = (\phi_1 + \phi_2)/2$  is the mid-point of the phase transition.

- iii. After selecting  $t'(x)$  for each location  $x$ , calculate the signals changes due to the presence of the object by subtracting the measurement signals at time index  $t'(x)$  between the scans with and without the object:

$$\Delta \text{Log}[\text{Amp}](\mathbf{x}, \mathbf{t}') = \text{Log}[\text{Amp}]^{\text{Obj}}(\mathbf{x}, \mathbf{t}') - \text{Log}[\text{Amp}]^{\text{Base}}(\mathbf{x}, \mathbf{t}'), \quad (7-2a)$$

$$\Delta \Phi(\mathbf{x}, \mathbf{t}') = \Phi^{\text{Obj}}(\mathbf{x}, \mathbf{t}') - \Phi^{\text{Base}}(\mathbf{x}, \mathbf{t}'). \quad (7-2b)$$

where the superscript *Obj* denotes the signals measured with the object and *Base* refers to the signals without the object (baseline).

Figure 7-3 illustrates the procedure of adaptive calibration for two source-detector locations **A** and **B** (see Figure 7-3(a)). Figure 7-3(b) plots the amplitude (in log scale) and phase as functions of time (since they are periodical, here we just plot half a period). A1 is the signal for baseline (without the object) when the source-detector is at location **A**, and A2 refers to the signals with the object. B1 and B2 refer to the signals without and with the object respectively when the source-detector is at location **B**. When the array is located at location **A**, which is in the central plane of the medium, the geometry is symmetric along the detector plane. In this case, the signals from the detector reach the amplitude minimum and phase transition point ( $\phi_0$ ) when the two sources are equal in strength, which corresponds to  $t_0$  in terms of time index (Figure 7-3(b)). This is also the time point in which the system reaches the highest

sensitivity. The presence of an object will cause the shift of the amplitude and phase profiles (A2 in Figure 7-3(b)), resulting in the perturbation signals:

$$\Delta \text{Log}[\text{Amp}](\mathbf{A}, t_0) = \text{Log}[\text{Amp}](\mathbf{A2}, t_0) - \text{Log}[\text{Amp}](\mathbf{A1}, t_0), \quad (7-3a)$$

$$\Delta \Phi(\mathbf{A}, t_0) = \Phi(\mathbf{A2}, t_0) - \Phi(\mathbf{A1}, t_0). \quad (7-3b)$$

where  $\text{Log}[\text{Amp}]$  and  $\Phi$  refer to the logarithm of amplitude and the phase curve versus the time scan in location  $\mathbf{A}$ .

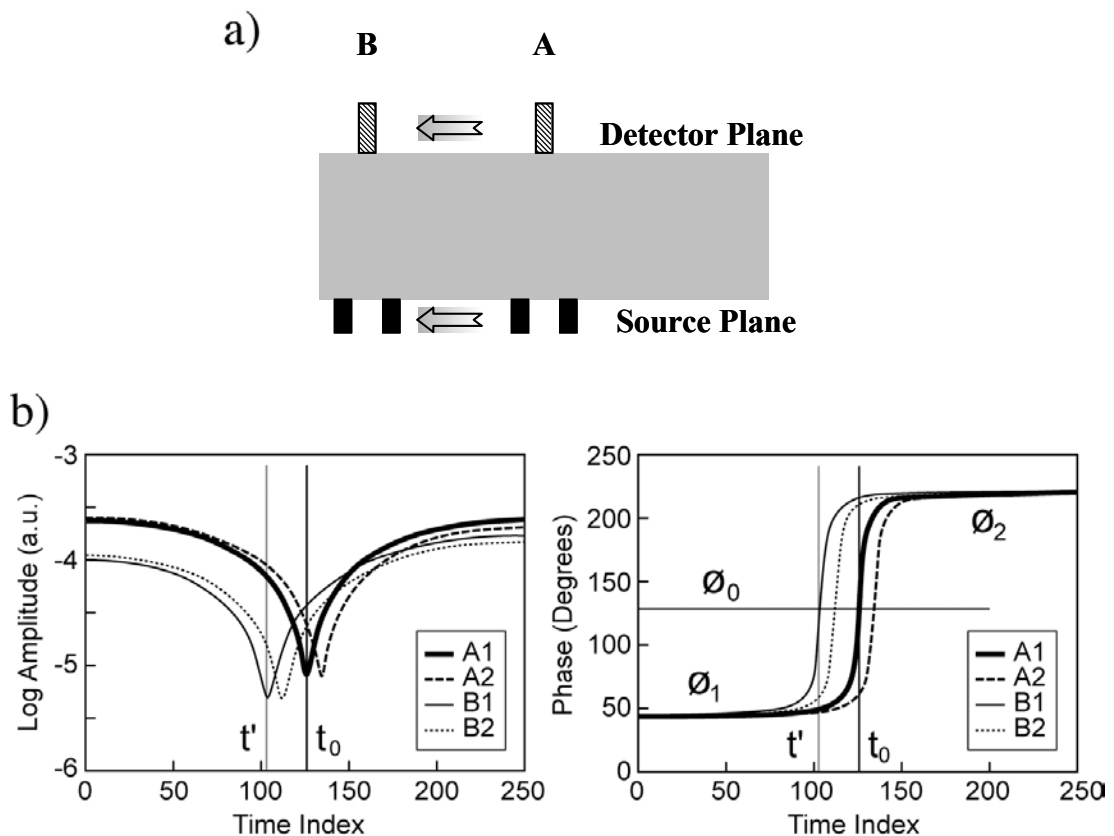


Figure 7-3: (a) Geometry for scanning of phased array from location  $\mathbf{A}$  (in the center) to location  $\mathbf{B}$  (close to boundary); (b) Illustration of adaptive selection of calibration time index  $t'$ . (A1: signals when array in location  $\mathbf{A}$  and without object; A2: signals when array in location  $\mathbf{A}$  and with object; B1: signals when array in location  $\mathbf{B}$  and without object; B2: signals when array in location  $\mathbf{B}$  and with object).

When the source-detector array is moved to location  $\mathbf{B}$ , which is close to the boundary, the different influence on the DPDW from two sources will cause an imbalance of the phased array in time  $t_0$ . In other words, the signals difference between with and without the object (B2 and B1) at time  $t_0$  (*i.e.*,  $\{Log[Amp](B2, t_0) - Log[Amp](B1, t_0)\}$  and  $\{\Phi(B2, t_0) - \Phi(B1, t_0)\}$ ) are smaller. At this position, to rebalance these two sources, their relative intensity ratio should be changed, *i.e.*, the amplitude minimum and phase transition time point will be different from  $t_0$ . As illustrated in Figure 7-3(b), the new time index for balance at location  $\mathbf{B}$  is changed to  $t'$ , which means the signal difference taken in time  $t'$  ( $\{Log[Amp](B2, t') - Log[Amp](B1, t')\}$  and  $\{\Phi(B2, t') - \Phi(B1, t')\}$ ) will be the most sensitive.

### 7.1.2 Sensitivity Analysis

The sensitivity of the signal detected using this method depends on the slope of the phase transition, which can be controlled by the relative phase offset between two sources [97]. While the accuracy of the detected signal also depends on the data collection time interval and the amplitude modulation carrier frequency. The phase transition will be sensitively perturbed by the object. If the time interval between two data points is too sparse, only a few points would be recorded during the transition, thus resulting in larger phase signal intervals between adjacent data points. This will introduce a larger phase error if there are some uncertainties in the time index gating. The term “phase resolution” is defined as the largest phase signal interval between two data points during the phase transition. Actually, the largest phase signal interval or phase slope will occur in the mid-point of phase transition,  $\phi_0$ , at time  $t'(x)$ . The mathematical expression for the phase resolution is:

$$\delta\phi = \frac{\partial\Phi(\mathbf{x}, \mathbf{t})}{\partial\mathbf{t}} \Big|_{\mathbf{t}=\mathbf{t}'} \Delta\mathbf{T}. \quad (7-4)$$

where  $\Delta T$  is the data collection time interval.

From Eq. (7-4), the phase resolution is related to the slope of phase transition in the mid-point, and the data collection time interval. The steeper the slope, the larger the resolution; while the smaller the data collection time interval, the smaller the resolution. In measuring and reconstructing of the phase transition curve, we would like to have a finer resolution. We can optimize the transition slope, phase resolution, data collection time interval and dataset size. Figure 7-4 plots the phase resolution versus the reciprocal of data collection time interval with different phase offsets between two sources, which determine the transition slopes.

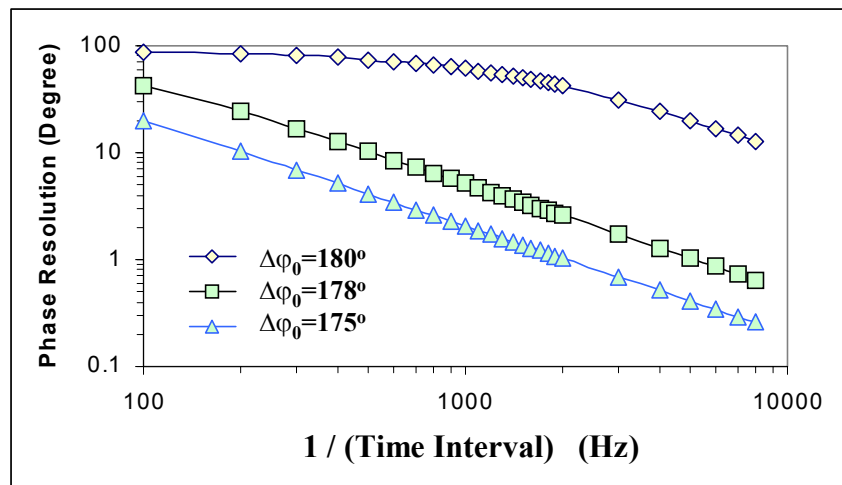


Figure 7-4: Plot of phase resolution versus the data collection time interval with different sources phase offsets (low frequency modulation frequency  $\Omega = 0.5$  Hz).

The closer the phase offset is to  $180^\circ$ , the higher the detection sensitivity, and the larger the phase resolution (as shown in Figure 7-4, about  $20^\circ$  phase resolution at 0.2 ms data collection time interval for phase offset of  $180^\circ$ ). The phase resolution

decreases with the decrease of the data collection time interval. To maintain relatively high detection sensitivity with reasonable data collection time interval and dataset size, a phase offset of  $178^\circ$  and time interval of 0.2 ms are chosen, which results in a phase resolution of  $1.0^\circ$ .

The other consideration is the phase noise. Usually the phase noise will be larger during the transition, where the amplitude is almost zero. By selecting  $178^\circ$  phase difference between two sources rather than  $180^\circ$ , the resultant amplitude during the transition is not exactly zero (-40 dB), and then amplified by the AGC to give enough intensity level for accurate phase measurement. Measurement noise can be further reduced by averaging the collected signals at the same position and interpolating the data points between the sampling interval, the final phase noise in our measurement is about  $0.5^\circ$ .

### 7.1.3 Three Cases

In this section we illustrate the improvements of detection sensitivity and accuracy of the optical scanning phased array system using two types of phantoms. One is a box phantom with finite size introducing the boundary effects. The other type of phantom is a heterogeneous system. Here we investigate the case when the background absorption is not homogeneous. Finally, we test our method on an animal model and demonstrate the possibility to detect the local accumulation of the absorbing dye in the tumor.

*Finite Boundary:* Figure 7-5(a) shows the configuration of the phantom #1 used in the study. We use a thin-wall container (10 cm  $\times$  10 cm  $\times$  15 cm) filled with Intralipid and ink to simulate the optical properties of the human breast tissue ( $\mu_a = 0.05 \text{ cm}^{-1}$ ,  $\mu'_s = 10.0 \text{ cm}^{-1}$ ). This geometry mimics the finite boundaries relevant to

biological tissues such as the human breast or arm. The phased array probe is arranged in a transmission mode with an inter-source separation of 2 cm. The probe is scanned from the detector position  $x = 1.0$  cm to  $x = 7.0$  cm. A 5 mm diameter black absorber is positioned between the source and detector plane at a lateral position of  $x = 3.50$  cm (the mechanical positioning error is 0.02 cm in all the experimental setups).

Figure 7-5(b) plots the raw data obtained from the scan on the finite size phantom without the adaptive calibration, *i.e.*, the intensity of source  $S_1$  and  $S_2$  remained unchanged during the scan. Due to the effect of the boundary, a large phase shift between detector positions at 1.0 cm to 3.0 cm has been observed (open triangle curve). The presence of the object pulls the signal down (closed square curve). While the system is unbalanced so that the difference between the object and background signals gives an unsymmetrical phase transition, as demonstrated in the differential curve plotted in Figure 7-5(c), which results in a 0.20 cm mean error in localization (averaged from 3 independent measurements).

Figure 7-5(d) depicts the results obtained using adaptive calibration. On the reference scan, the specific transition time  $t'$  at each position is determined by Eq. (7-2) and then applied to the object scan to find out the phase shift signals at each location. The resultant phase shift is plotted in Figure 7-5(d). Comparing Figure 7-5(c) and (d), adaptive calibration can enhance the signal contrast ( $40^\circ$  in Figure 7-5(d) versus  $32^\circ$  in Figure 7-5(c)) and the transition is much more symmetrical in Figure 7-5(d), so that the localization is more accurate (mean error = 0.05 cm).

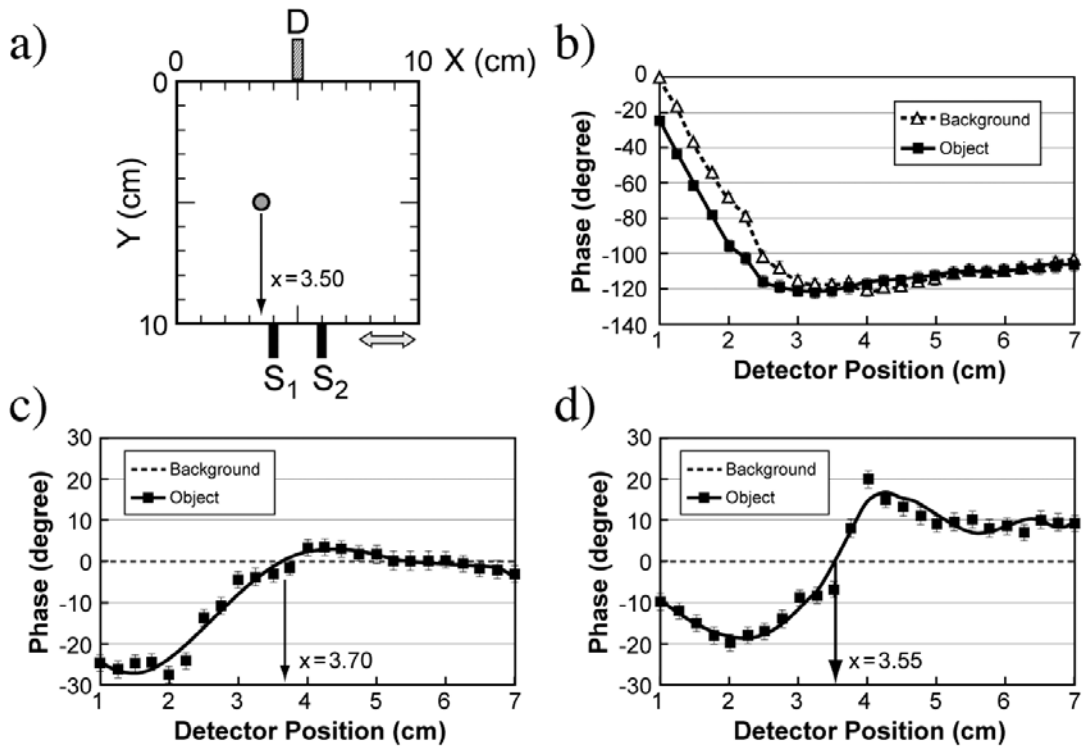


Figure 7-5: (a) The geometry of the finite size phantom (the object position is  $x = 3.50$  cm) (b) Raw phase data collected without adaptive calibration. (c) The subtraction of background scan from the object scan, the detected location of the object is  $3.70 \pm 0.08$  cm (mean error = 0.20 cm). (d) The signal obtained after the adaptive calibration using amplitude modulation, the detected location of object is  $3.55 \pm 0.07$  cm (mean error = 0.05 cm). The solid curves in (c) and (d) are the fitting of the data. (Note: The error bars are coming from the average of 5 independent measurements)

Extensive measurements on various object locations are performed and Table 7-1 illustrates the accuracy and repeatability of the 5 mm diameter object in different positions in X and Y axes. At each position, three measurements are obtained. In general, without adaptive calibration, the mean localization error is larger, especially when the object is closer to the boundary ( $x = 2.0$  cm, mean error  $\sim 0.3$  cm). With adaptive calibration, the mean localization error is less than 0.15 cm.

Table 7-1: Localization accuracy for different object locations

True Position in X Axis (cm)	Measured Position in X Axis (cm)			
	Y = 5.0 cm		Y = 7.0 cm	
	w/o calibration	w/ calibration	w/o calibration	w/ calibration
2.00	1.65 ± 0.18	1.88 ± 0.15	1.70 ± 0.15	1.90 ± 0.12
3.50	3.70 ± 0.09	3.55 ± 0.07	3.68 ± 0.10	3.46 ± 0.06
5.00	4.92 ± 0.08	4.94 ± 0.07	4.93 ± 0.07	4.95 ± 0.05

*Heterogeneous Background:* The influence from background heterogeneity is simulated by the presence of another absorber besides the targeted object. In phantom #2, as shown in Figure 7-6(a), the slab geometry is chosen for this study. The optical properties of the background medium are the same as that in phantom #1. Instead of the homogeneous background, we place an absorber **A**, 8 mm in diameter,  $\mu_a = 0.30 \text{ cm}^{-1}$ , at the position  $x = 4.50 \text{ cm}$  to create the heterogeneous background absorption. The “tumor” is simulated by another absorbing object **B** with a 5 mm diameter located at  $x = 3.50 \text{ cm}$ . The absorption of this target is varied by changing the concentration of the ICG filled in the object (500 nM, 1000 nM and 1500 nM, corresponding to the absorption coefficients of  $0.15 \text{ cm}^{-1}$ ,  $0.30 \text{ cm}^{-1}$  and  $0.45 \text{ cm}^{-1}$  respectively). A reference scan without the tumor object is also obtained (Figure 7-6(a)).

Figure 7-6(b) plots the results without adaptive calibration. The reference plot is obtained with absorber **A** only. The signal follows the normal pattern of phased array detection (*cf.* Figure 7-3(b)), and the position of the reference curve crossing the

baseline phase ( $-50^\circ$ ) is close to the true position of absorber **A** ( $x' = 4.40 \pm 0.05$  cm, *cf.* the true position  $x = 4.50 \pm 0.02$  cm, the mean error = 0.10 cm). From Figure 7-6(b), the presence of the “tumor” object **B** causes the shift of phase signal, resulting in the cross point of the signal and the baseline phase ( $-50^\circ$ ) lies between these two absorbers. Obviously, the presence of object **A** influences the detection of object **B**. In this case, the usual way to determine the position of object **B** is to find out the cross point of the phase signals with and without absorber **B** (Figure 7-6(b)). As summarized in Table 7-2, the mean localization errors for different object absorptions without adaptive calibration are from 1.5 to 3.5 mm.

Table 7-2: Localization accuracy for different object absorptions

ICG Concentration (nM)	Mean Localization Error (cm)	
	w/o adaptive calibration	w/ adaptive calibration
500	$0.15 \pm 0.06$	$0.05 \pm 0.03$
1000	$0.35 \pm 0.08$	$0.10 \pm 0.05$
1500	$0.25 \pm 0.05$	$0.05 \pm 0.04$

Using adaptive calibration, as shown in Figure 7-6(c), at each scanning position, the time at which the phase signal reaches the baseline phase ( $-50^\circ$ ) on the reference scan (only absorber **A** present) has been recorded. The phase signal at the same time point with both the background absorber **A** and the “tumor” object **B** present is then plotted versus the scanning position. From Table 7-2, the mean position errors of the “tumor” are from 0.5 to 1.0 mm.

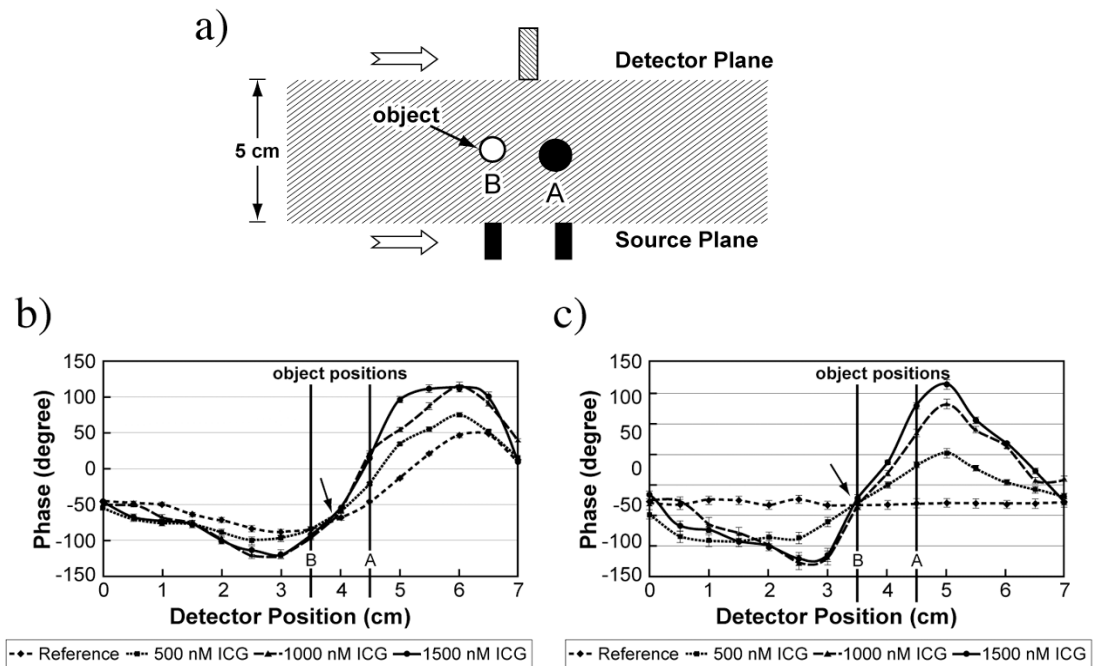


Figure 7-6: (a) The geometry of the heterogeneous background phantom (a fixed absorber **A** is located at  $x = 4.50$  cm, with  $\mu_a = 0.30$  cm<sup>-1</sup> and the “tumor” **B** located at  $x = 3.50$  cm, the  $\mu_a$  of the “tumor” object changes from 0.05 cm<sup>-1</sup> to 0.15 cm<sup>-1</sup>, 0.30 cm<sup>-1</sup> and 0.45 cm<sup>-1</sup>). (b) Raw phase data collected without adaptive calibration. (c) The signal obtained after the adaptive calibration using amplitude modulation (the vertical dotted line indicates the real object position). The arrows in (b) and (c) indicate the cross point of the object scan and the baseline scan.

Table 7-2 summarizes the localization errors for different object absorptions. In general, the object localization with the adaptive calibration is precise. Also, the phase transition becomes more symmetrical after adaptive calibration (Figure 7-6(c) vs. Figure 7-6(b)), which agrees with the results from experiments using phantom #1.

Animal Model: Afterwards, we conducted the intra-tumor ICG injection on an animal model (MMTV mouse with a spontaneous mammary tumor ~ 1 cm diameter in size). The mouse was euthanized and immersed in an intralipid and ink solution.

The distance from the center of tumor to the surface of the intralipid varied from 2 cm to 3 cm. In the first step, we scanned the phased array to acquire the baseline, and then we injected 200  $\mu$ l of 5  $\mu$ M ICG (= 1 nmol) in the tumor (ICG will diffuse throughout the tumor according to the literature [152]) to simulate the uptake of a high affinity dye or tumor specific binding molecular beacon. Then, we scanned again to locate the position of the ICG-labeled tumor. The experimental setup is illustrated in Figure 7-7(a). The source-detector separation is 5.0 cm and the source-source separation is 4.0 cm.

Figure 7-7(b) – (d) plot the results acquired from the animal model. Figure 7-7(b) gives an example of pre- and post-injection of ICG when the tumor is 2 cm deep inside the scattering medium. We are able to observe the phase shift due to the heterogeneous mouse body, and the difference is small after the injection of the absorbing dye. Figure 7-7(c) plots the difference between pre- and post-injection of ICG when the tumor is located at different depths. The signals in Figure 7-7(c) are fluctuating, indicating that the signal difference between pre- and post- injection of ICG is small compared with the heterogeneity of the tumor-bearing mouse. Thus it is difficult to locate the position even with the aid from the extrinsic contrast agent. Figure 7-7(d) depicts the results after the adaptive calibration using amplitude modulation. After applying the adaptive calibration, the influence from the heterogeneous background has been corrected, which is represented by the curve with the dashed line with diamond markers, almost equal to the balanced phase ( $0^\circ$  in this case). The solid line with diamond markers, the dashed line with square markers and the dotted line with triangle markers represent the results for tumor depths of 2.0 cm, 2.5 cm and 3.0 cm, respectively. We can determine the position of the ICG-labeled tumor by the crossing point of the post-ICG signal and the reference, and the

localization errors of 1.0 mm, 2.0 mm and 6.0 mm for 2.0 cm, 2.5 cm and 3.0 cm tumor depths respectively. When the tumor depth increases, the perturbation signal coming from the ICG-labeled tumor gets weaker, thus the localization error increases. Using the adaptive calibration method, we can effectively detect the presence of the embedded absorber from the heterogeneous background (Figure 7-7(d)), which would otherwise be hard to locate (Figure 7-7(c)).

#### **7.1.4 Discussion**

The amplitude cancellation method using dual out-of-phase sources (phased array system) can sensitively detect and locate small objects in the turbid media. The detection sensitivity will rely upon the balance of those two sources; thus, the calibration is very important in maintaining the high detection sensitivity of the phased array system, especially in the presence of heterogeneous background or vicinity of the boundary. The low frequency modulation provides a convenient way to adaptively calibrate the system at each position by periodically varying the source intensities. We have demonstrated the improvement of the localization sensitivity and accuracy on a finite boundary phantom, heterogeneous phantom and animal model. The localization error has been decreased about 3 – 5 folds to around a few mm.

Since this technique is a differential method that can sensitively detect the presence of small heterogeneity, it is appropriate for measuring local changes in optical properties, such as the contrast agent uptake and cortical activation. Thus this system can be applied to early breast cancer detection and functional brain mapping. To further increase the detection sensitivity, we can use higher power light sources, higher sensitivity detectors and higher quantum yield contrast agents. This method can also be applied to the detection of fluorescent objects embedded in the scattering

media to improve the sensitivity and accuracy of the detection and DOT using phased array configuration.

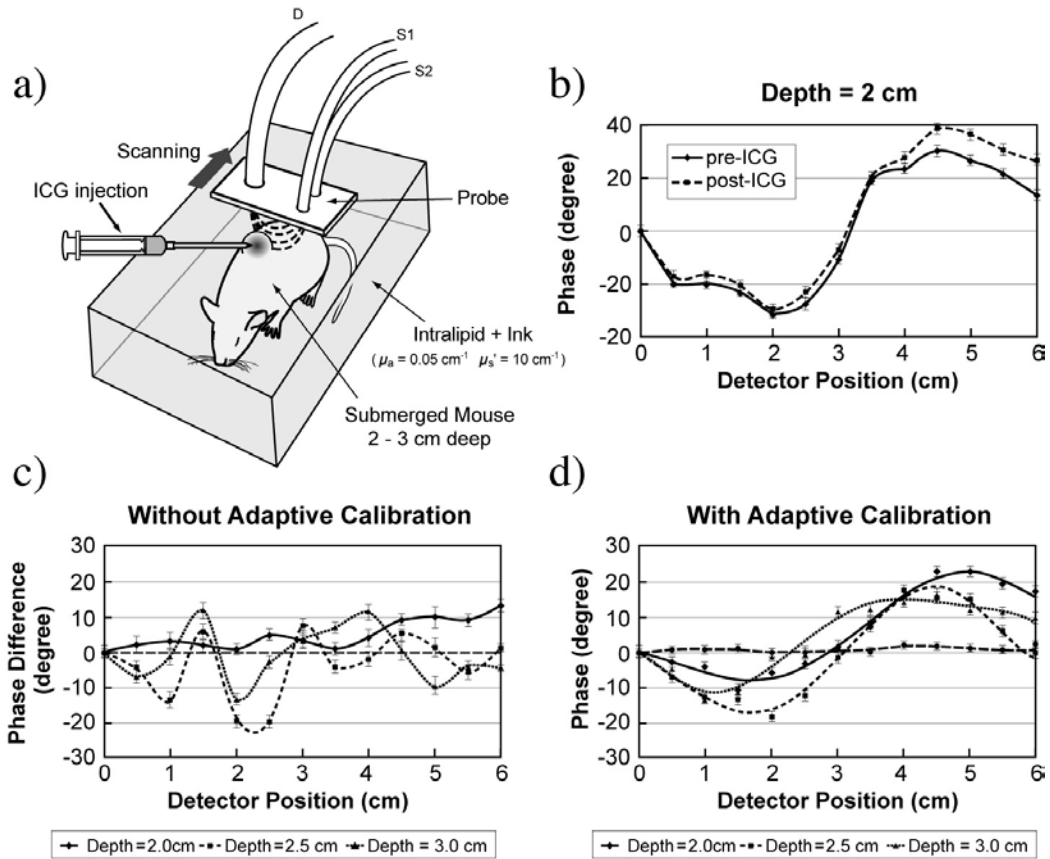


Figure 7-7: (a) The geometry of the submerged mouse model; the tumor position is  $x = 3.00 \text{ cm}$ . (b) Raw phase data collected without amplitude modulation before (pre-ICG) and after (post-ICG) the ICG injection with the tumor depth = 2.0 cm. (c) The subtraction of the pre-ICG signal from the post-ICG signal for different tumor depths, the difference is small and no clear pattern is observed. (d) The signal obtained after the adaptive calibration using amplitude modulation, the detected locations of object are 2.90 cm (depth = 2.0 cm, error = 1.0 mm), 3.20 cm (depth = 2.5 cm, error = 2.0 mm) and 2.40 cm (depth = 3.0 cm, error = 6.0 mm). The dashed line with diamond markers is the calibrated background.

## 7.2 Tumor Localization with Phased Array Goniometry

In this section we will present the possibility of using the fluorescence phased array goniometry for the detection and localization of the contrast agent labeled tumor inside the scattering media. The experiment protocol is designed according to the following logic: The instrument sensitivity and accuracy test is performed using the phantom study; then, the ability to detect fluorescent dye distributed in the tumor is performed using an intra-tumoral injection of ICG in the euthanized mouse model; finally, we use the anesthetized mouse model for *in vivo* testing with the NIRF-2DG contrast agent.

### 7.2.1 Phantom Studies

A 12 cm L x 5 cm W x 15 cm H tank filled with 1% Intralipid and a certain concentration of ink simulates the geometry and optical properties of a large breast (at 780 nm:  $\mu_a = 0.05 \text{ cm}^{-1}$ ,  $\mu_s' = 10 \text{ cm}^{-1}$ ). The phased array goniometry probe is placed outside the thin glass wall (thickness = 1 mm) of the tank with the reflectance geometry. The fluorescent object is a 1 cm<sup>3</sup> ball filled with 1.0  $\mu\text{M}$  concentration of the fluorescence contrast agent simulating the delivery of the molecular beacon to a tumor (1 cm<sup>3</sup>). The object is embedded inside the scattering media 2.0 cm away from the plane where the rotational probe was placed, while the depth can be modified through a slider (Figure 7-8). The probe is scanned in four different directions (45° apart from each other) to locate the position of the object in two-dimension. The size of the object, the concentration of the ICG, and the depth between the center of the object and the source-detector plane can all be varied to explore the detection sensitivity of the phased array localizer.

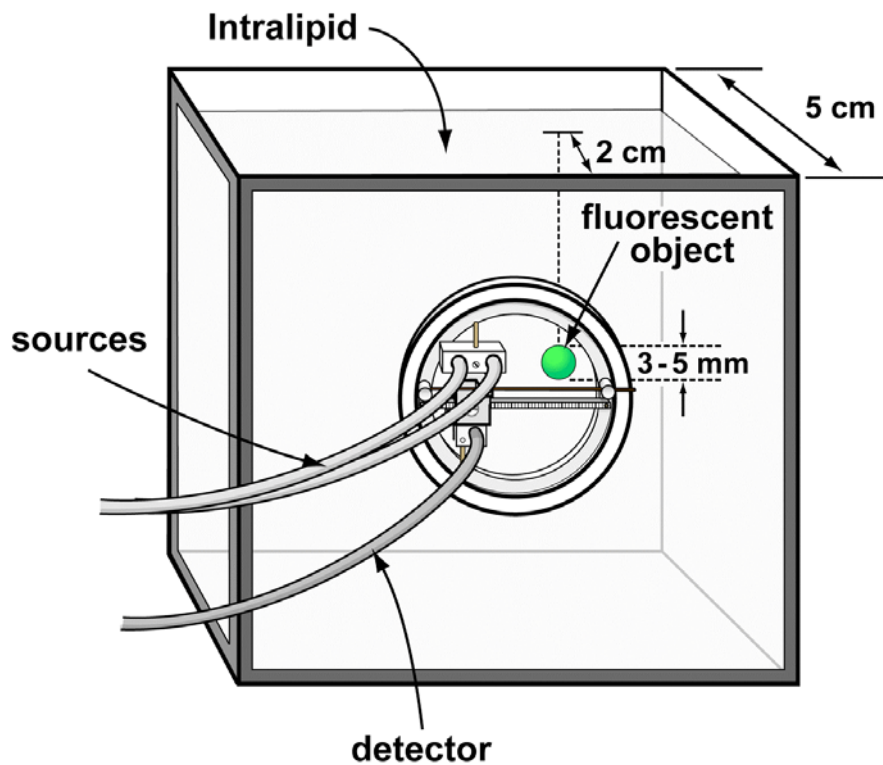
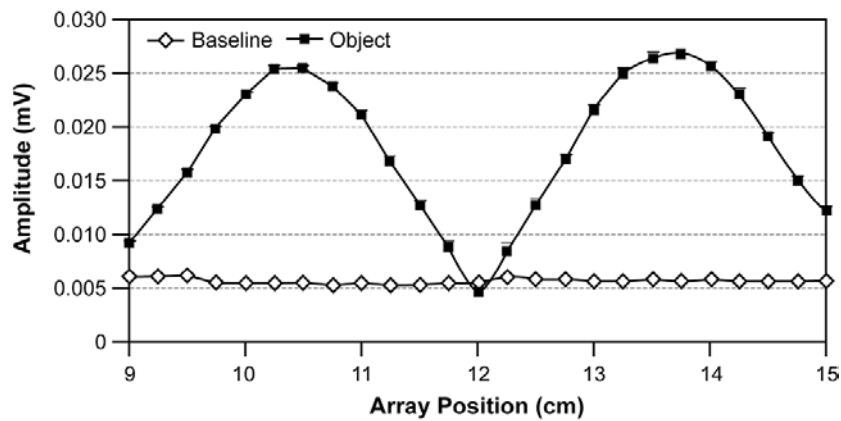


Figure 7-8: Illustration of the goniometric probe and the experimental set-up for the phantom test.

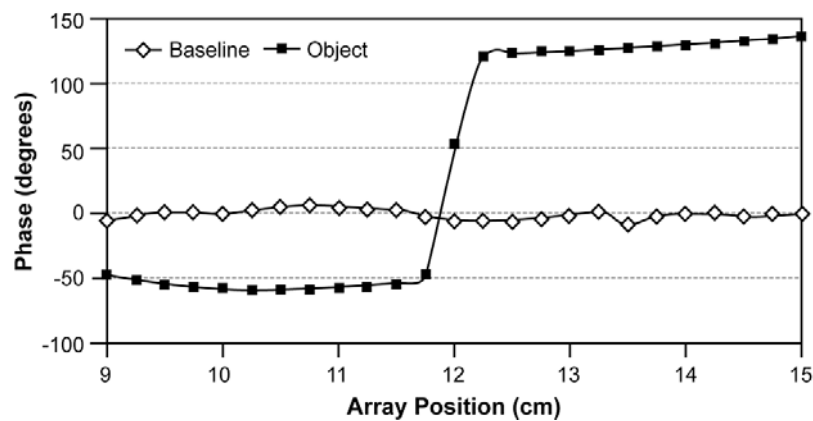
Figure 7-9 illustrates the amplitude and phase signals with the one-dimensional scanning of the source-detector block. The open diamond curve refers to the baseline scan, which is performed when the medium contains no fluorescent objects. The solid square curve is the signal when the fluorescent object ( $1 \text{ cm}^3$  ball with  $1 \mu\text{M}$  ICG) is placed 2.5 cm deep inside the scattering medium. The data demonstrate the features of the phased array fluorescence signal, with the amplitude null and phase transition slope maximum when the cancellation plane scans through the position of the fluorescent object.

Figure 7-10 plots the two-dimensional localization image of the detected fluorescent object using the method introduced in Section 4.4. The peak intensity indicates the position of the object. The fluorescent object is accurately localized with

a depth of 2.5 cm (here the depth is defined as the distance between the center of the object to the plane of the source-detector). The localization error for the ICG ball is 1.4 mm (Figure 7-10(a)). Figure 7-10(b) plots the three-dimensional  $\chi^2$  map to indicate the good agreement of the fitting procedure.



(a)



(b)

Figure 7-9: Amplitude (a) and phase (b) signals from the scanning of the phased array probe in one dimension. Open diamond curve refers to the background scan without the fluorescent object; solid square curve depicts the signal from the scan with the embedded fluorescent object.

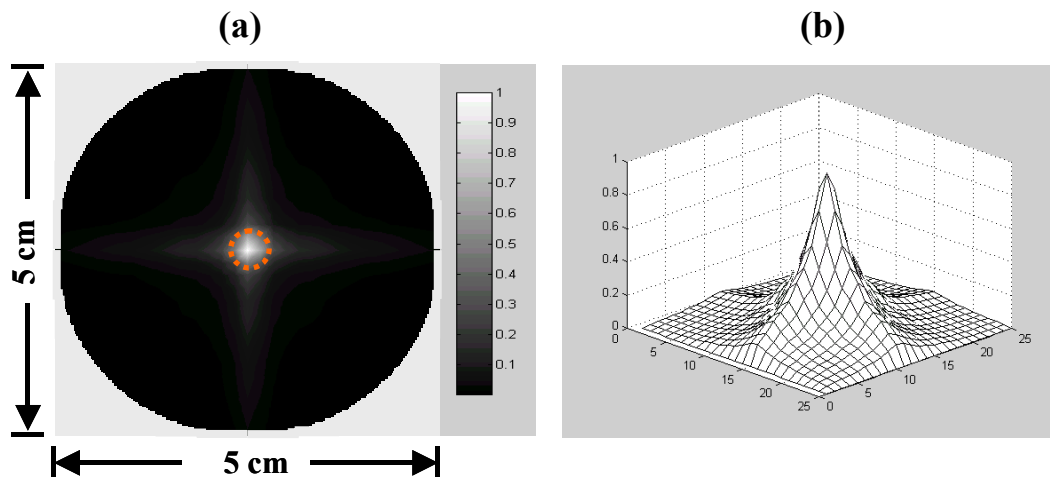


Figure 7-10: (a) The two-dimensional localization of the fluorescent object (5 mm diameter ICG ball). The concentration of ICG is 1  $\mu\text{M}$ . The peak in the image indicates the estimated center of the object and the dotted circle represents the true position and size of the object. (b) The  $\chi^2$  map of the fitting (plot in  $-\lg(\chi^2)$ ).

To verify the accuracy of the object localization, after determining the object position by the goniometry method, a needle is inserted to indicate the detected object position. Figure 7-11 illustrates the accuracy of the needle localization after removal of the plastic cover and the top part of the Intralipid. The mean localization error is 1.4 mm for the 5 mm sphere. There is a trade-off between the number of scanning directions and the localization error. Increasing the number of scans will improve the localization accuracy, while extending the scanning time. Empirically, we found that four scans with  $45^\circ$  in between each direction will provide sufficient accuracy with the most efficient scanning time.

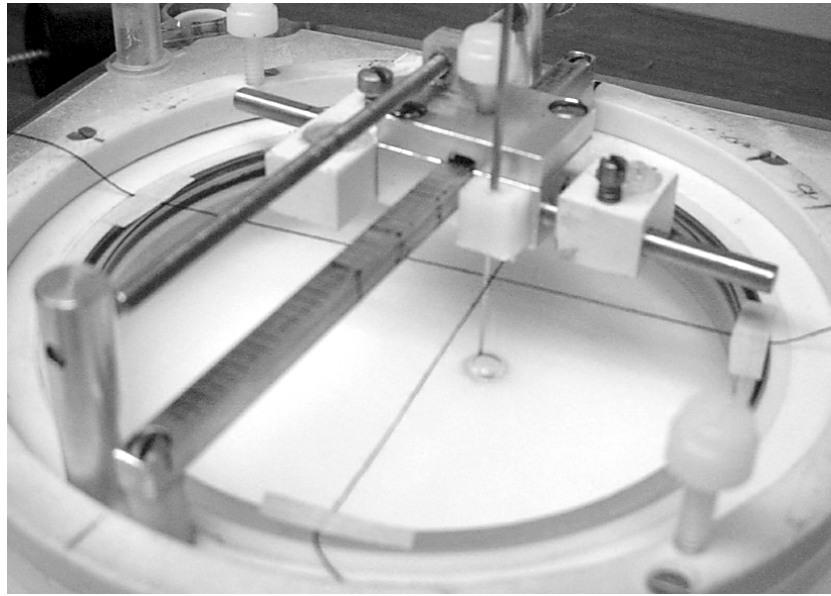
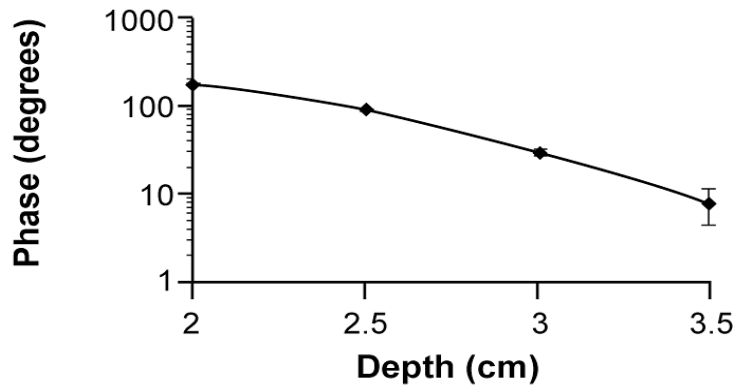


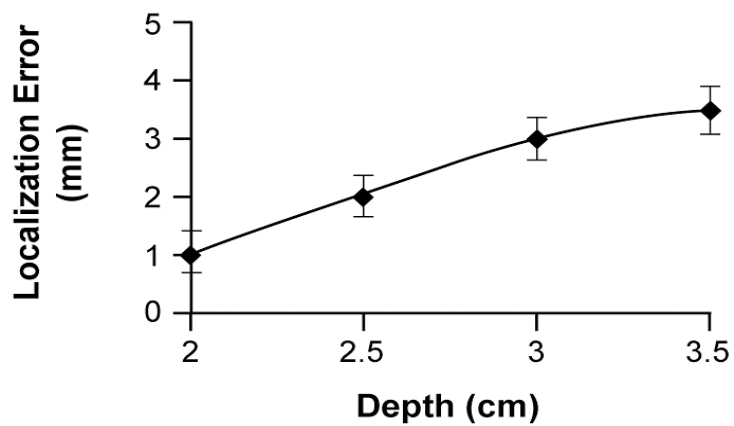
Figure 7-11: Illustration of localization accuracy by fine needle insertion.

### 7.2.2 System Performance

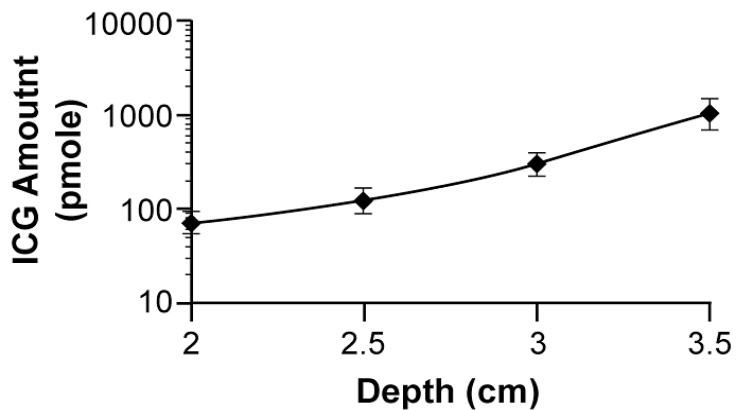
Figure 7-12 summarizes a series of tests on the relationship of signal strength (phase) and the localization accuracy with respect to the object depth, as well as the detection limit in terms of the minimum amount of ICG. Figure 7-12(a) and (b) are tested with a 5 mm sphere filled with 1 nano-mole ICG, and the optical properties of the scattering medium are the same as aforementioned. The phase transition signal decreases with the increase of the object depth, which is corresponding to the decreased perturbation when the object is further away. The localization error increases with the increase of object depth, due to the decrease of signal to noise ratio. From these charts, sufficient signal within the appropriate accuracy range can be obtained up to 3.5 cm deep inside the turbid medium. Figure 7-12(c) is obtained with the same size of object, but various ICG concentrations. To detect the fluorescent object at the 3.50 cm depth, the minimum amount of ICG is around 1 nano-mole.



(a)



(b)



(c)

Figure 7-12: The relationship of (a) phase signal and (b) localization error with respect to the object depth (5 mm diameter spherical object with 1 nano-mole ICG). (c) The limit of detection (minimum amount of ICG) versus the object depth (5 mm diameter spherical object). (Note: The error bars are coming from average of 3 independent measurements)

### 7.2.3 Animal Model I – Intra-tumor Injection

To explore the feasibility of applying the phased cancellation system to the localization of tumors, preliminary tests with animal tumor models are performed. The first animal model is the submerged mouse model with an intra-tumor injection. This approach will leave out the issue of delivery efficiency of the contrast agent and focus on the detection of fluorescence signals from the tumor. We use Athymic nude mouse with the implantation of the RIF-1 tumor (Radiation Induced Fibrosarcoma) on the right thigh. Then, the mouse is submerged into the scattering medium (Intralipid + ink) in different depths after euthanasia. To simulate the local high contrast of the fluorescence contrast agent, intra-tumor injections of ICG are performed (Figure 7-13(a)). After euthanasia, ICG is mainly remaining inside the tumor area. The distribution of ICG inside the tumor is validated after the experiment by *ex vivo* scanning through different slices of the tumor using a three-dimensional low temperature scanner (Figure 7-13(b)). The instrument basically scans the frozen-trapped tissue sample maintained at low temperature (in liquid nitrogen), and the fluorescence signals of ICG from the surface are recorded. The spatial resolution of this instrument can reach  $40 \times 40 \times 10 \mu\text{m}^3$  [153,154]. From Figure 7-13(b) we can see that the ICG signals mainly reside within the tumor margin.

The localization image of the detected ICG-labeled tumor is shown in Figure 7-14. The 8 mm x 10 mm diameter tumor is submerged at a depth of 2.5 cm. The localization error for this tumor is about 3.5 mm.

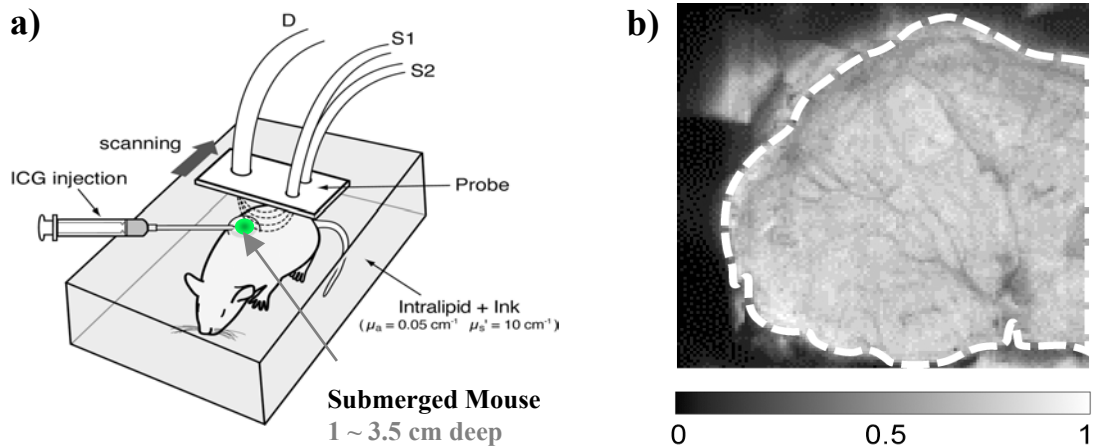


Figure 7-13: (a) Experimental set-up for animal tumor model test. (b) One representative slice of the fluorescent image in the tumor area obtained by the low temperature scanner (1 cm x 1 cm). The dashed white curve is the tumor margin.

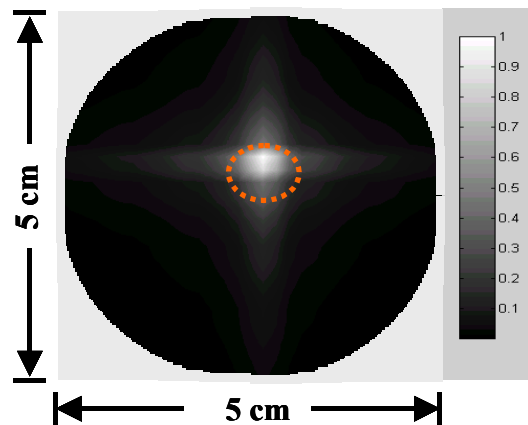


Figure 7-14: The two-dimensional localization of the 8 mm x 10 mm submerged mouse tumor with intra-tumor injection of 200  $\mu$ l ICG at a concentration of 5  $\mu$ M.

The tumor is submerged 2.5 cm deep inside the media.

After the determination of the tumor position via four consecutive scans as described previously, a fine needle is inserted to simulate the clinical biopsy procedure to verify the localization of the tumor. As illustrated in Figure 7-15, the

needle is targeting on the mouse tumor, with a 3.5 mm mean distance from the place of ICG needle injection. While considering the heterogeneous distribution of ICG in the tumor area, as illustrated in Figure 7-13(b), the capability of detecting small fluorescent heterogeneity in the animal model with reasonable accuracy is demonstrated.

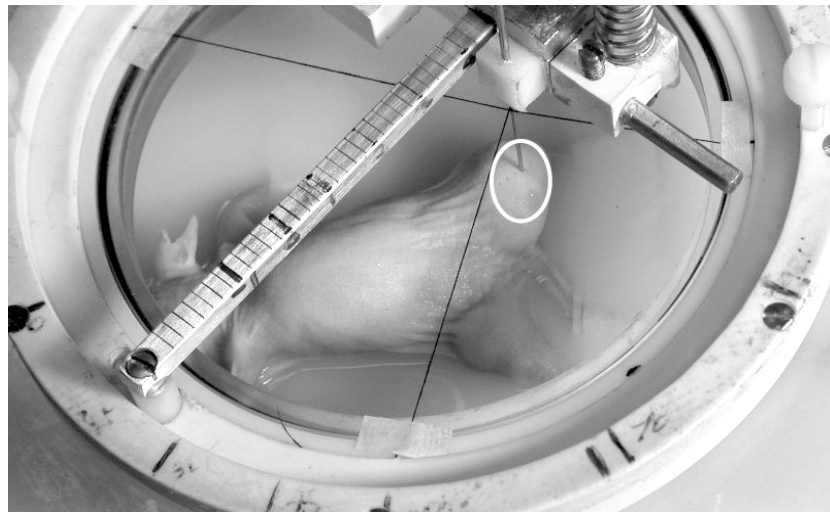


Figure 7-15: Illustration of the fine needle localization of 2.5 cm deep 8 mm x 10 mm RIF-1 tumor injected with ICG (the tumor margin is outlined).

#### 7.2.4 Animal Model II – In Vivo Systematic Administration

The results from the submerged mouse model demonstrated that our system can sensitively detect the contrast agent delivered into the tumor, so the next step is to image the *in vivo* uptake of the contrast agent by the tumor. The Athymic nude mouse with the implantation of the AR42J tumor (pancreatic acinar carcinoma) on the right thigh is injected with 200  $\mu$ l 1 mg/ml NIRF-2-D-Glucosamide after 12 hours fasting. The injection process is infusion through the tail vein. The imaging is performed 3.5 hours after the injection with the mouse submerged in the scattering medium

(Intralipid + ink) after anesthesia (Figure 7-16(a)). The scattering media has the same optical properties described in Section 7.2.1, and is warmed to retain the physiological temperature ( $\sim 37^\circ$ ). The tumor cells are hyper-metabolic compared with normal cells, thus will take up more NIRF-2-D-Glucosamide into the tumor cell. NIRF-2-D-Glucosamide has similar spectral properties as ICG. The mouse is kept alive throughout the experiment. The distribution of NIRF-2-D-Glucosamide inside the tumor is also examined after the experiment by *ex vivo* scanning (Figure 7-16(b)). As comparison, the same amount of ICG is also injected intravenously on another mouse and imaged after 3.5 hours.

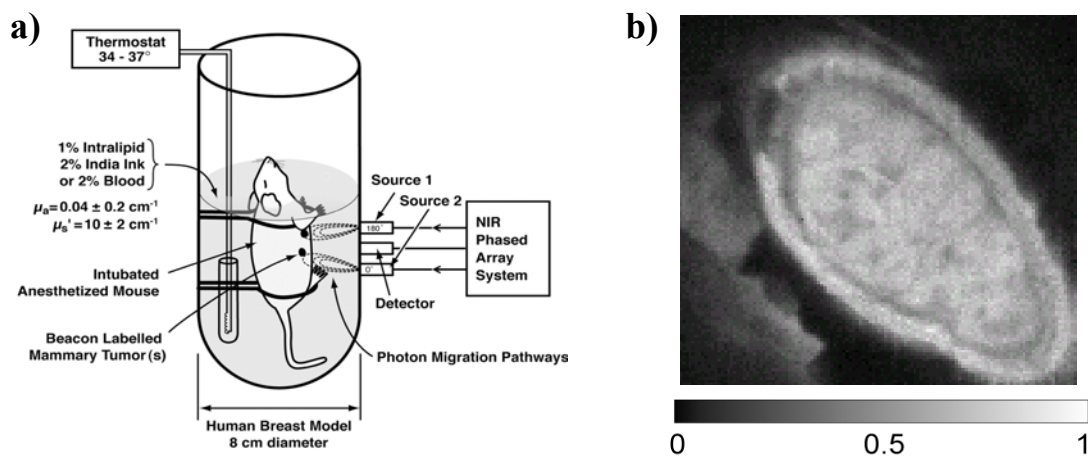


Figure 7-16: (a) Experimental set-up for *in vivo* animal tumor model test. (b) One representative slice of a fluorescent image in the tumor area obtained by the low temperature scanner (1 cm x 1 cm).

Figure 7-17(a) plots the two-dimensional imaging of hyper-metabolism using the NIR804-2-D-Glucosamide. The tumor region is enhanced. The mouse tumor is submerged with a depth of 1.5 cm with the localization error of 2.0 mm. As comparison, Figure 7-17(b) shows the two-dimensional imaging of the tail-vein

injection of ICG. There is no significant enhancement in the tumor region, suggesting that the ICG could not provide high contrast between tumor and the normal tissue after 3.5 hours. This result is in agreement with the non-tumor-specificity of ICG and the depletion of ICG from the circulation system rapidly by the liver [40].

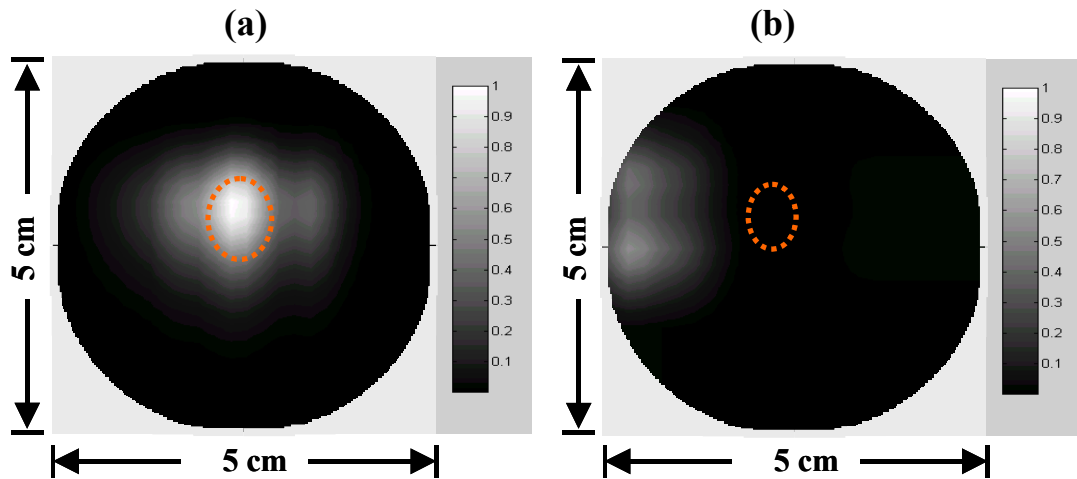


Figure 7-17: (a) The two-dimensional localization of the 10 mm x 5 mm submerged mouse tumor with tail vein injection of 200  $\mu$ l 1 mg/ml NIR804-2-D-Glucosamide. The tumor is 1.5 cm deep inside the media. (b) The two-dimensional localization of the 8 mm x 4 mm submerged mouse tumor with tail vein injection of 200  $\mu$ l 1 mg/ml ICG. The tumor is 1.5 cm deep inside the media.

It has been demonstrated that the clearance of ICG is quick by the hepatobiliary excretion [40], thus after 3.5 hours, the phased array imaging system could not detect the contrast between tumor and the normal tissue using ICG. The fluorochrome labeled 2-Deoxy-Glucose (NIR804-2-D-Glucosamide) showed an accumulation in the tumor area, which is in correspondence with the higher rate of glycolysis associated with hyper-metabolism in tumor cells. The above results

confirm that molecular specific contrast agents can be used as a marker to enhance the detection sensitivity in tumor imaging. We have also obtained the localization images of subsurface tumors labeled with other NIRF-2-D-Glucosamide conjugate contrast agents. Figure 7-18 demonstrates the examples using the Cypate-mono-2-D-Glucosamide. From Figure 7-18(a), we can see that the localization of the tumor with a depth of 1.5 cm is accurately resolved, with a localization error of 2.0 mm. When we increase the depth of the tumor to 2 cm, we can still detect the tumor, and the localization error is 3.0 mm (Figure 7-18(b)). Also, we note that the FWHM of  $\chi^2$  fitting map is getting broader due to the decrease of the signal-to-noise ratio associated with the increase of the tumor depth.

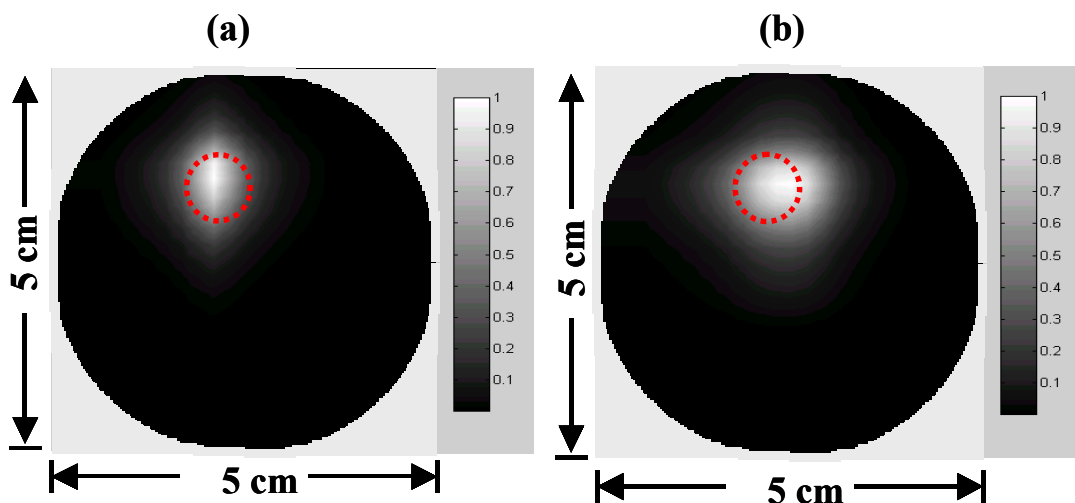


Figure 7-18: (a) The two-dimensional localization of the 8 mm x 8 mm submerged mouse tumor with tail vein injection of 200  $\mu$ l 1 mg/ml Cypate-mono-2-D-Glucosamide. The tumor is 1.5 cm deep inside the media. (b) The two-dimensional localization of the 8 mm x 8 mm submerged mouse tumor with tail vein injection of 200  $\mu$ l 1 mg/ml Cypate-mono-2-D-Glucosamide. The tumor is 2.0 cm deep inside the media.

Figure 7-19 illustrated another case with Bacteriochlorophyll (BChl)-2DG, same dosage as other contrast agents. We also accurately detected the position of the contrast-enhanced tumor with the localization error of 3 mm (Figure 7-19(a)). Figure 7-19(b) also shows a negative control animal model result, without the injection of the contrast agent, thus the fluorescence phased array system does not detect the signals from the tumor.

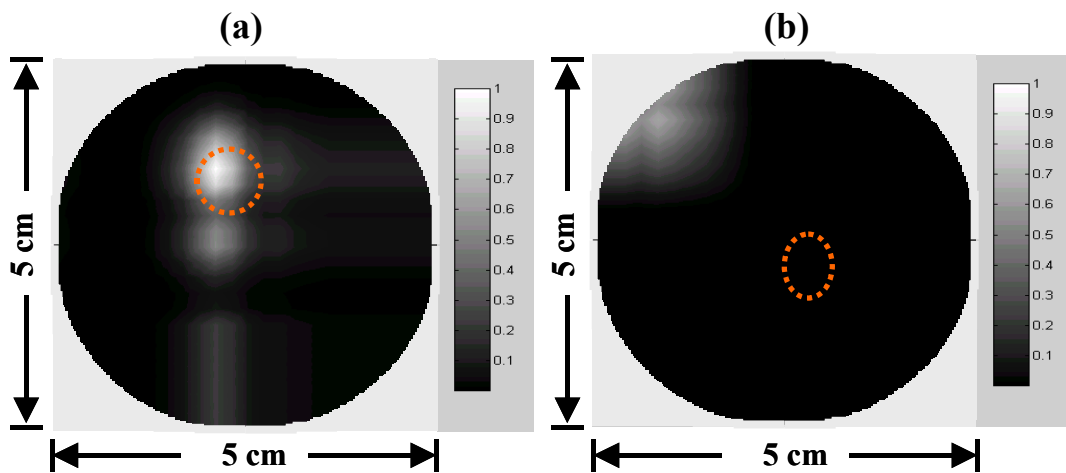


Figure 7-19: (a) The two-dimensional localization of the 8 mm x 8 mm submerged mouse tumor with tail vein injection of 200  $\mu$ l 1 mg/ml BChl-2-D-Glucosamide. The tumor is 1.5 cm deep inside the media. (b) The two-dimensional localization of the 8 mm x 6 mm submerged mouse tumor without injection of any type of contrast agent.

The tumor is 1.5 cm deep inside the media.

### 7.2.5 Discussion

We have demonstrated an efficient instrument for detection and localization of a tumor labeled by the molecular specific fluorescence contrast agent inside the scattering media. The localization error is within a few millimeters. This instrument can sensitively detect the fluorescence signal from less than 1 nano-mole contrast

agent in the phantom experiment. It is promising for the early detection of cancer through the joint efforts of development of novel molecular targeting contrast agents and non-invasive optical instruments.

The experiments presented the ability of the NIR phased array system in tumor localization via the enhanced contrast in metabolism in the animal model. This device can probe not only the contrast in the metabolism pathway, but also other molecular hallmarks of tumor cells, provided the fluorescent contrast agents linking to specific molecular processes have been developed. For instance, contrast agents have been designed to probe the over-expression of certain receptors in tumor cells [40] and enhanced activity of proteolytic enzymes [44]. Thus, the device will have wide applications in cancer diagnosis and drug development.

This system is safe, economic and portable for hospital usage. It could be readily adapted for the imaging of other fluorescent contrast agents by changing the sources and the optical filter. The accuracy of this instrument suggests that it could be applied to early tumor detection and could be helpful for clinical fine needle biopsy. This portable device would be complementary to X-ray mammogram and provide add-on information on early diagnosis and localization of a breast tumor.

### **7.3 Breast Cancer Detection with Amplitude Cancellation System**

The ultimate goal of the development of optical imaging techniques and the molecular specific contrast agents is aiming for the clinical diagnosis of early breast cancer. Because of the FDA regulations, the new contrast agents need to be approved before they can be used clinically. Thus most of the current clinical trials still focus on the intrinsic contrasts [12,21,56,179-182] or the non-specific contrast agents such as

ICG [14,130]. Here we would like to present some clinical data acquired by the Amplitude Cancellation imaging system based on the intrinsic contrasts.

### 7.3.1 Blood Model Experiments

The detailed instrumentation of Amplitude Cancellation system has been introduced in Section 6.2.5. To verify the performance of the instrument, we have tested the system through a series of blood model experiments.

Based on the extinction coefficients of oxygenated and deoxygenated hemoglobin, we use the following empirical relationship to extract the blood volume and oxygenation.

$$\text{Blood Volume} = 0.3 * \text{signal (750 nm)} + \text{signal (830 nm)}, \quad (7-5a)$$

$$\text{Oxygenation} = \text{signal (830 nm)} - \text{signal (750 nm)}. \quad (7-5b)$$

Figure 7-20 shows the setup of the blood model test. An object (small cylinder or coil), is placed in the background (Intralipid + ink) and can be moved in three dimensions. The blood is pumped through the object and the saturation of blood is controlled by bubbling oxygen or nitrogen into the flask.

A testing object (8 mm × 5 mm cylinder with 10% blood) is placed in the fish tank with Intralipid, 1.5 cm away from the wall where the imager pad is attached. The testing object is moved across the imaging area, and the real positions and the object position obtained from images are compared in Figure 7-21. The result suggests that the imaging system can accurately localize the embedded object.

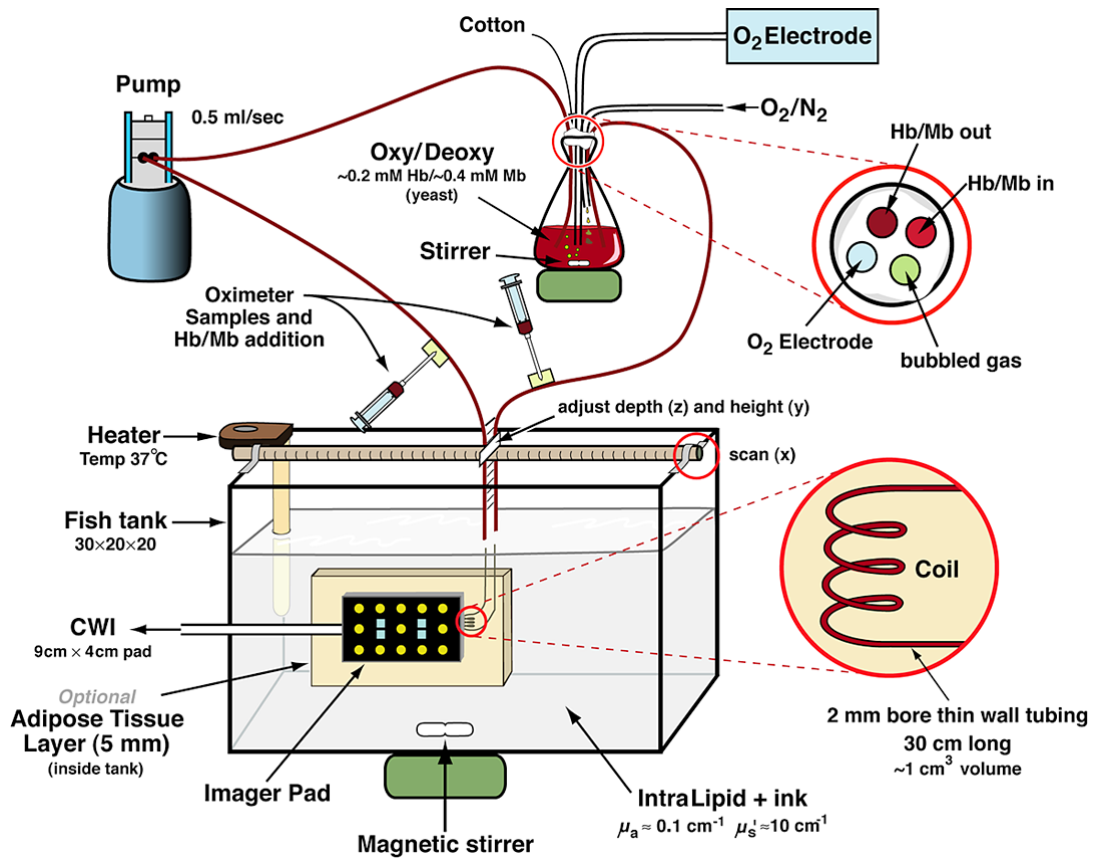


Figure 7-20: The set-up of blood model test.

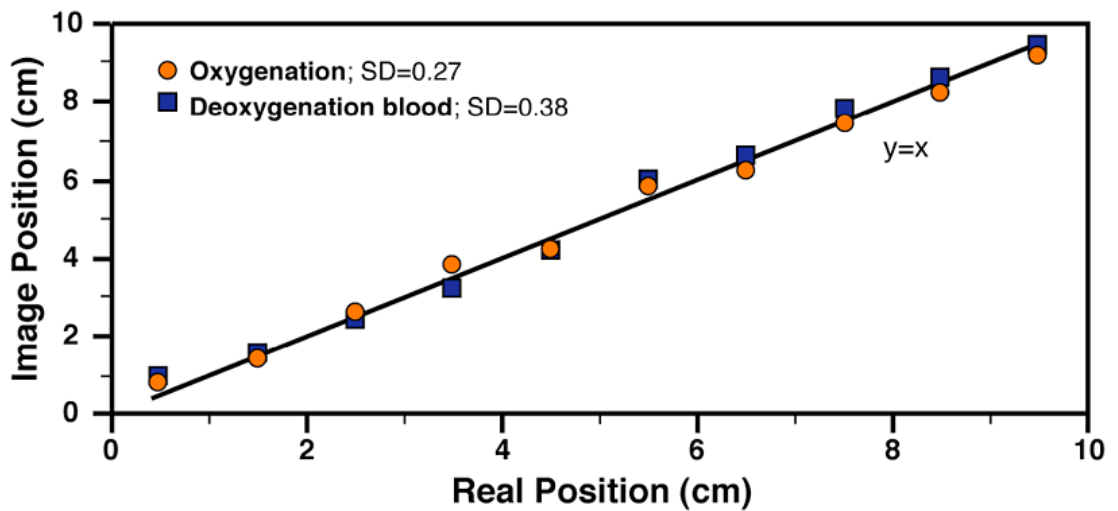


Figure 7-21: The relationship between the real position and measured position for both oxygenated and deoxygenated blood. The relations are linear.

Figure 7-22 shows the pictures for deoxygenated blood and oxygenated blood. From this picture, we can see that for the 10% blood sample, the blood volume does not change, but the differences of oxygenation is prominent.

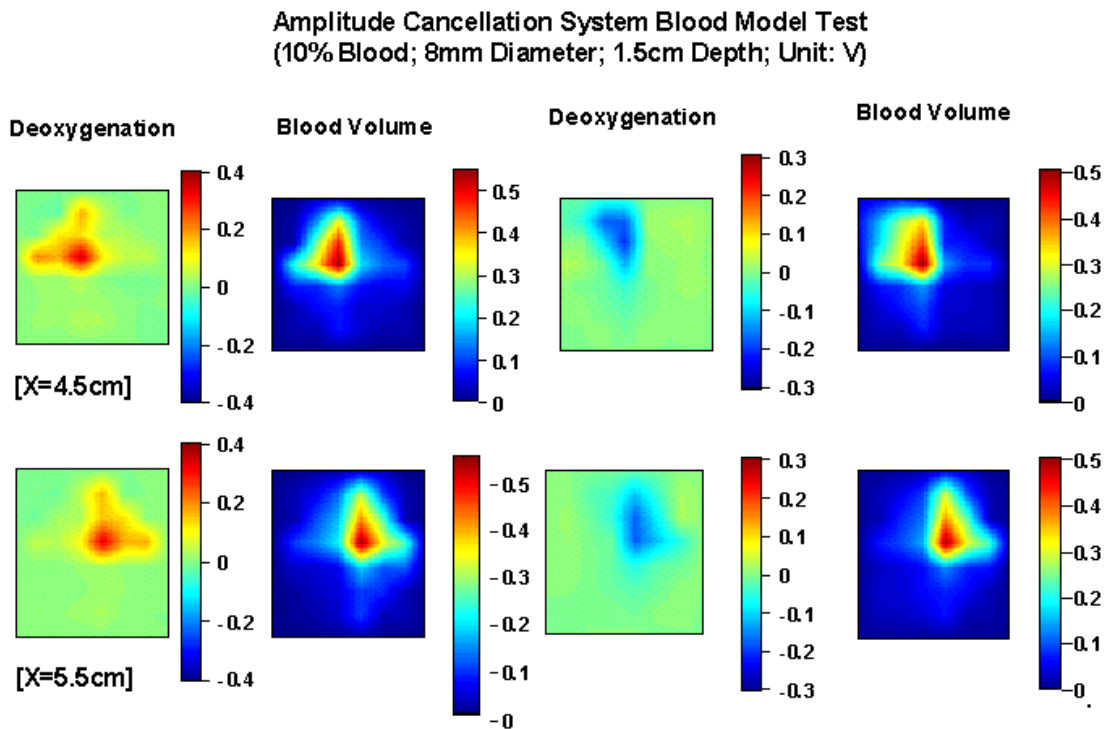


Figure 7-22: Imaging of deoxygenated blood and oxygenated blood. The 10% blood is pumped through the 8 mm object.

### 7.3.2 Preliminary Human Studies

We have applied the dual-wavelength amplitude cancellation image system to clinical breast cancer study, and it can probe the blood volume and blood deoxygenation change for a breast tumor. The experimental set-up has been outlined in Figure 6-15.

Figure 7-23 shows the results of a human breast test. Images of the tumor bearing breast (right breast) and normal breast (left breast) versus a breast model ( $\mu_a = 0.04 \text{ cm}^{-1}$ ,  $\mu_s' = 10 \text{ cm}^{-1}$ ) are illustrated. Blood volume is calculated using Eq. (7-5). In this case the right breast has high deoxygenation and blood volume. The congruence of the blood volume and deoxygenation images indicates the high possibility of a breast tumor, which is verified by biopsy as malignant [183].

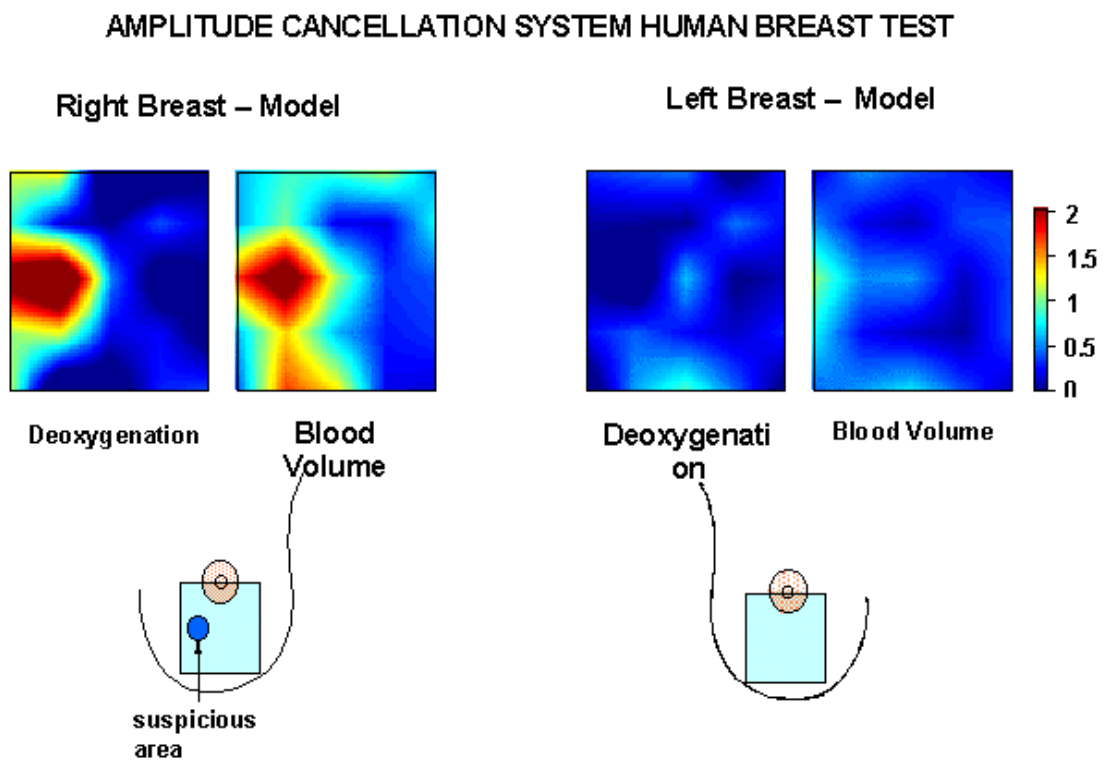


Figure 7-23: Breast tumor image. The right breast has suspicious mass.

We have observed relatively large signals from a small tumor, as small as several millimeters. The breast tumor has high deoxygenation and blood volume, in combination with the spatial congruence of the blood volume and the deoxygenation images, thus the Amplitude Cancellation system has great potential for diagnosis of a tumor mass with high sensitivity and specificity. Most of the masses were detected

when we used the criteria of the congruence of blood volume and deoxygenation signals. A nipple can also be seen in images that are compared with a model. The effect of the nipple can be subtracted by the image difference between the right and the left breast; in this case the probe is placed in the mirror locations of both breasts.

## 7.4 Tomographic Image Reconstruction

In Chapter 5 and Section 6.2.4, we had introduced the theoretical and instrumental background of tomographic image reconstruction using the phased array configuration. In this section, we will present some examples of image reconstruction with both absorptive and fluorescent heterogeneity.

### 7.4.1 Imaging Absorptive Heterogeneity

The data measurement was performed on slab geometry with  $8 \times 5 \text{ cm}^2$  rectangular area as described in Section 7.2.4. For phased array configuration, the sources (source pair) and detector were scanned in parallel with 1 cm step (in total  $9 \times 9$  measurements). The data with and without the object were collected so that the perturbative Rytov scattered wave  $\phi_{sc}$  was obtained. For image reconstruction, the above area was discretized into  $32 \times 20$  voxels ( $0.25 \times 0.25 \text{ cm}^2$ ). The reconstruction is limited to a slice for computational efficiency. We chose the real part of the weight matrix, which corresponds to the amplitude measurements only. We also perform the image reconstruction with conventional single-source configuration. In this case, each of the 9 source and detector positions are placed oppositely. We use both the algebraic reconstruction technique (SIRT) and the subspace methods (TSVD) for the image reconstruction.

Reconstruction with SIRT: Figure 7-24 shows the reconstructed object embedded inside the highly scattering media (Intralipid and ink mixture) using SIRT. The background optical properties are:  $\mu_a = 0.04 \text{ cm}^{-1}$ ,  $\mu_s' = 10.0 \text{ cm}^{-1}$ . The object is a 5 mm diameter cylindrical tube (thin wall NMR tubing) containing a mixture of the background solution with Indocyanine Green (ICG) added to provide an absorption contrast of 10 versus the background.

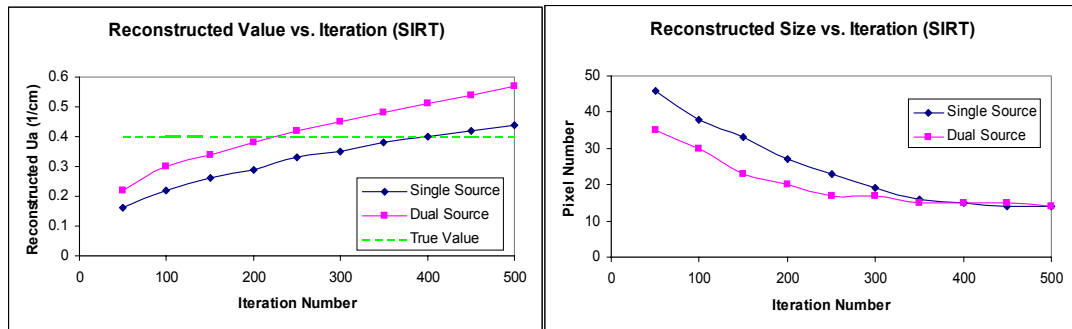


Figure 7-24: Image reconstruction using SIRT.

We perform both single-source illumination and dual-interfering-source configuration to validate the weight function and algorithm for phased array imaging experimentally. The resultant reconstructed image is shown in Figure 7-24. From Figure 7-24 we can see that they are congruent in localization. Here the reconstructed image appears to be elongated along the y-axis which could be a result of our sampling interval (the separation between adjacent detectors) being quite sparse (1 cm), and the higher sensitivity for voxels close to the sources and detectors in transmission geometry. Increasing the number of sources and detectors and rescaling the weight matrix sensitivity will improve the image quality [155].

In SIRT, when we increase the iteration number, the reconstructed absorption will also increase and the size of the reconstructed object (the number of pixels with value larger than half maximum) will decrease [65]. We plot the reconstructed  $\Delta\mu_a$

and the number of pixels larger than half maximum with the iteration number. As we can see in Figure 7-25, the dual-interfering-source method achieves the expected value and the converged pixel number with less iteration numbers, hence less reconstruction time.



(a)

(b)

Figure 7-25: Reconstructed absorption vs. iteration number (a) and the object size (the number of pixels with the value larger than half maximum) vs. iteration number (b).

Reconstruction with TSVD: Figure 7-26 shows the results from the TSVD method. In Figure 7-26, the reconstructed objects are obtained with the best regularization parameters estimated from L-curve (Figure 7-27), which gave different parameters for single- and dual-interfering-source. In the central plane ( $y = 2.5$  cm), regularization parameters  $\alpha_c$  for single- and dual-interfering-source are 0.001 and 0.004 respectively, while in the edge plane ( $y = 0$  cm and 5 cm), regularization parameters  $\alpha_e$  are 0.1 and 0.2 for single- and dual-interfering-source. From Figure 7-26, we can see that the object size and contrast are well reconstructed with spatially variant regularization.

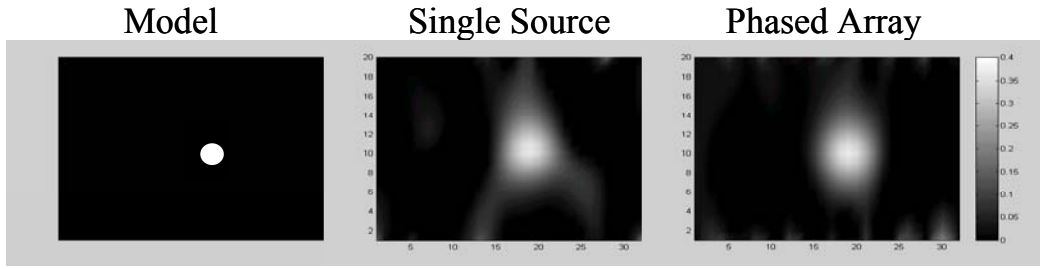


Figure 7-26: Image reconstruction using TSVD.

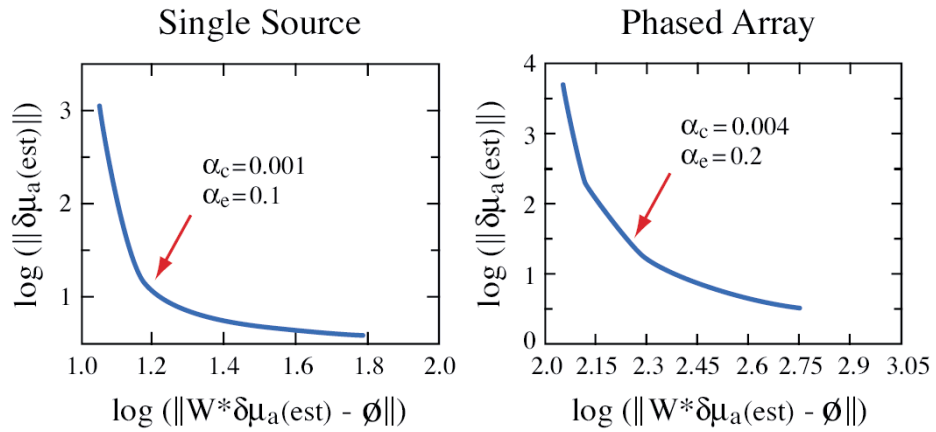


Figure 7-27: L-Curve analysis for TSVD.

Singular Value Analysis: From SVD we obtain the singular matrix  $\mathbf{S}$  that contains the singular values associated with the physical model. Through the analysis of the distribution of the singular values, we will have a better understanding on the influence of several parameters such as modulation frequency, source pair separation and dataset size on the quality of reconstruction.

The singular value dispersion (the shape of the spectra) can be used to analyze the stability of the singular matrix. One of the useful criteria is the resolution, which is  $\sim 2L/\sqrt{k_a}$ , where  $L$  is the dimension of the voxelated region and  $k_a$  is the number of

singular values were truncated by a regularization parameter  $\alpha$  [156]. In the following analysis, we choose  $\alpha = 0.004$  (which corresponds to a singular value = 0.1).

Figure 7-28 shows the singular value spectra for different configuration parameters for the phased array imaging system. Figure 7-28(a) shows the singular value spectra for different modulation frequencies: 50, 100, 200 and 300 MHz. The apparent difference is in the first 9 singular values, which are corresponding to the detectors on the null planes. The higher the modulation frequency, the higher sensitivity (gain) for those singular values. For the rest of the projections, the spectra are almost the same for different frequencies (singular values #10 - #81 are almost same for 4 frequencies in Figure 7-28(a)). The truncating index for those four singular value spectra decreases with the increase of the initial singular value (since we use fixed regularization parameters), which suggests a trade-off between the detection sensitivity and the resolution.

Figure 7-28(b) shows the singular value spectra for different source pair separations from 1 cm to 4 cm. Figure 7-28(b) shows 1 cm source separation has the highest resolution, and the resolution decreases with the increase of separation. However, those differences are not very prominent. Figure 7-28(c) shows the effects of different numbers of source-detector combinations. We compared 5 source-pairs & 5 detectors, 9 source-pairs & 9 detectors, and 17 source-pairs & 17 detectors. The graph shows 17 source-pairs & 17 detectors gives the largest number for the singular value index, and hence has the highest resolution. From the chart, we estimated the resolution for 5, 9 and 17 source-detectors are 32.0, 22.6 and 16.8. Here the resolution is just a relative value to indicate the smallest wavelength of eigenvector we are choosing in image reconstruction.

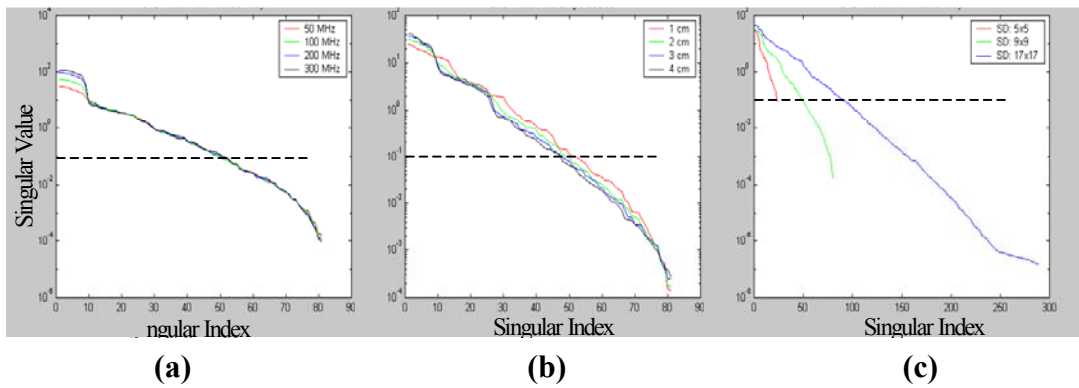


Figure 7-28: Singular value spectra for phased array with (a) different modulation frequency; (b) different source separation; (c) different measurement number.

In this section, we have demonstrated the validity of imaging an absorption perturbation embedded in turbid media using dual-interfering-source illumination. Besides the sensitive information on object localization, the phased array imaging system can also reconstruct the object's size and absorption coefficient through tomographic imaging. By this way, we can utilize the high precision localization information from phased array detection, and the information from multiple projections would also help the phased array detection to differentiate multiple objects, providing the information of object depth and quantifying the optical properties of the object. We also show that the singular value analysis method is a good quantitative way to compare the effects of different configuration parameters for the phased array imaging system. From our analysis, significant improvement of the system will come from the increasing of the source-detector numbers. This approach could help us to optimize our system in future applications.

### 7.4.2 Imaging Fluorescent Heterogeneity

In Section 5.5.2 we have derived the equation for tomographic reconstruction of the fluorescent object (Eq. (5-62)). Here we demonstrate the possibility of resolving the fluorescent heterogeneity inside the scattering media experimentally.

The imaging geometry is similar to those described in Section 7.4.1. This time the data measurement area is  $5 \times 5 \text{ cm}^2$ . Again, the source pair and detector were scanned in parallel with a 1 cm step (in total  $5 \times 5$  measurements). The data with and without the fluorescent filter (absorption and fluorescence) are both recorded. From the previous section, we found that the TSVD method with spatially variant regularization gives better results than the SIRT; thus, we use the same approach for the image reconstruction.

Figure 7-29 shows the results from the TSVD method. The fluorescent object is the 5 mm diameter cylindrical bar filled with  $1 \mu\text{M}$  ICG. The regularization parameters are:  $\alpha_c = 0.005$  and  $\alpha_e = 0.25$ . From Figure 7-29, we can see that the object size and contrast are well reconstructed (the color-bar indicates the concentration of the fluorophore in  $\mu\text{M}$ ).

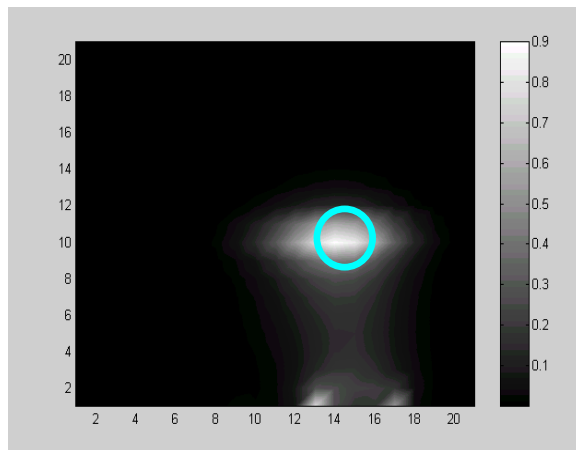


Figure 7-29: Image reconstruction of fluorescent object (ICG) using TSVD. The blue circle indicates the true object size and position and the color-bar is in unit of  $\mu\text{M}$ .

## 7.5 Rat Brain Oxygenation Correlated with BOLD MRI

As mentioned in the previous section, near-infrared spectroscopy (NIRS) has been developing rapidly in recent years as a promising non-invasive technique for quantifying the concentration of tissue chromophores; thus, it has great potential application in measurement of cerebral blood volume and blood oxygenation saturation for clinical monitoring [157]. Theories and instruments have been developed to improve the measurement sensitivity and quantification accuracy of NIRS [116,164-167,198-201]. Comparison of NIRS results with other non-invasive imaging modalities such as magnetic resonance imaging (MRI) can provide more information on the co-registered region, and thus has attracted a lot of interest recently [91,168-174].

Functional MRI (fMRI) is a well-established technique for measuring changes in microvasculature surrounding metabolically active brain tissue. Specifically, fMRI can detect changes in the magnetic state of brain tissue dependent on the degree of oxygenation [175]. The BOLD (blood-oxygenation-level-dependent) effect has been seen with  $T_2^*$ -weighted gradient echo sequences.  $T_2^*$  relaxation is susceptible to paramagnetic deoxygenated hemoglobin and, thus, is sensitive to changes in the level of oxygen bound to hemoglobin in blood. It is of interest to correlate NIRS and MRI in order to improve their individual and simultaneous utility towards detecting the underlying physiology and pathophysiology. In this study, we analyzed the correlation of relative changes in the deoxygenated hemoglobin concentration measured by NIRS and the conventional  $T_2^*$ -weighted BOLD MRI signal for the *in vivo* rat model during inhalation of gas with different concentrations of oxygen ( $F_{iO_2}$ ).

### 7.5.1 Experimental Protocol and Set-up

The instrumentation used for NIRS measurement is the frequency-domain homodyne I & Q spectrometer (Section 6.2.1). Female Sprague-Dawley rats were anesthetized with Nembutol<sup>®</sup> (50mg/kg), and kept at 37°C core body temperature throughout the experiment using a heated waterbed. A mixture of oxygen and nitrogen was delivered to them through gas flow meters and a cylindrical mask. The head of the rat was inserted into the mask with its nose and mouth region inside. The inspired oxygen concentration ( $FiO_2$ ) was incremented evenly from 20% to 100% by 20% steps, and returned back to baseline (20%) after each perturbation. The stimulation period lasted about 60s and the resting period was around 80s. The rat was placed in prone position. The source and detector fibers, separated by 1.5 cm, were placed extradermally over the frontoparietal region of the rat brain.

For the MRI measurements, a solenoid volume coil optimized (SNR = 50) for rat brain imaging was mounted onto a motion-resistant platform. The rats were secured in place, and a cylindrical mask was mounted inside the coil.  $FiO_2$  was adjusted with calibrated gas flow meters, and only oxygen and nitrogen were delivered to the mask as described previously. MRI studies were done on a separate cohort of 3 rats under a similar experimental paradigm, with 80 minutes of stimulation and 200 minutes of recovery.

To measure the BOLD effect,  $T_2^*$ -weighted fast gradient recall echo (FGRE) MRI was conducted (TR = 70 ms, TE = 10 ms, FOV = 5 cm × 5 cm, matrix size = 256 × 128, slice thickness = 3 mm, and scan time = 10 s) at the field strength of 4 Tesla. Data were collected for a single coronal brain slice, as shown in Figure 7-30, anatomically consistent for all three animals [176].

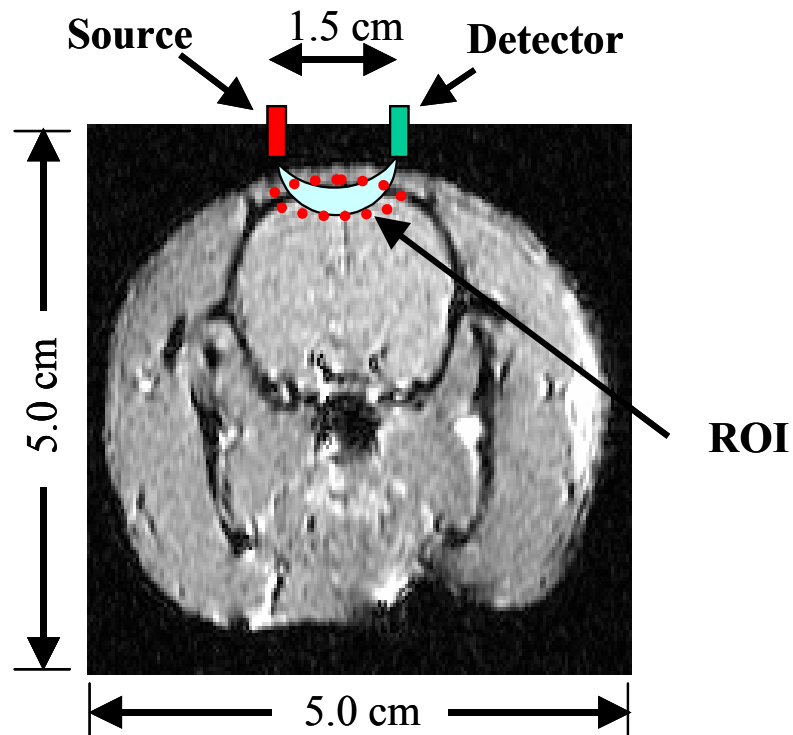


Figure 7-30: Diagram illustrating the NIR probe position and the selection of region of interest (ROI) in the coronal MR images. The ROI is chosen based on the estimated region on the central part of the banana pattern for diffused photons.

### 7.5.2 Near-Infrared (NIR) Spectroscopy Data

The algorithm used to calculate the oxygenated and deoxygenated hemoglobin has been detailed in Section 5.2. Here we present the data during the oxygenation modulation.

Figure 7-31 plots the measured absorption and reduced scattering coefficients during the experiment for rat #1. Here two representative wavelengths, 780 nm and 830 nm, are selected for illustration. The absorption coefficients change corresponding to the perturbation of  $\text{FiO}_2$  and return to the baseline during the

recovery. Notice that  $\mu_a$  at 780 nm and 830 nm change in an antiparallel fashion, and the corresponding  $\mu'_s$  change slightly (i.e. less than 2%) during the FiO<sub>2</sub> modulation.

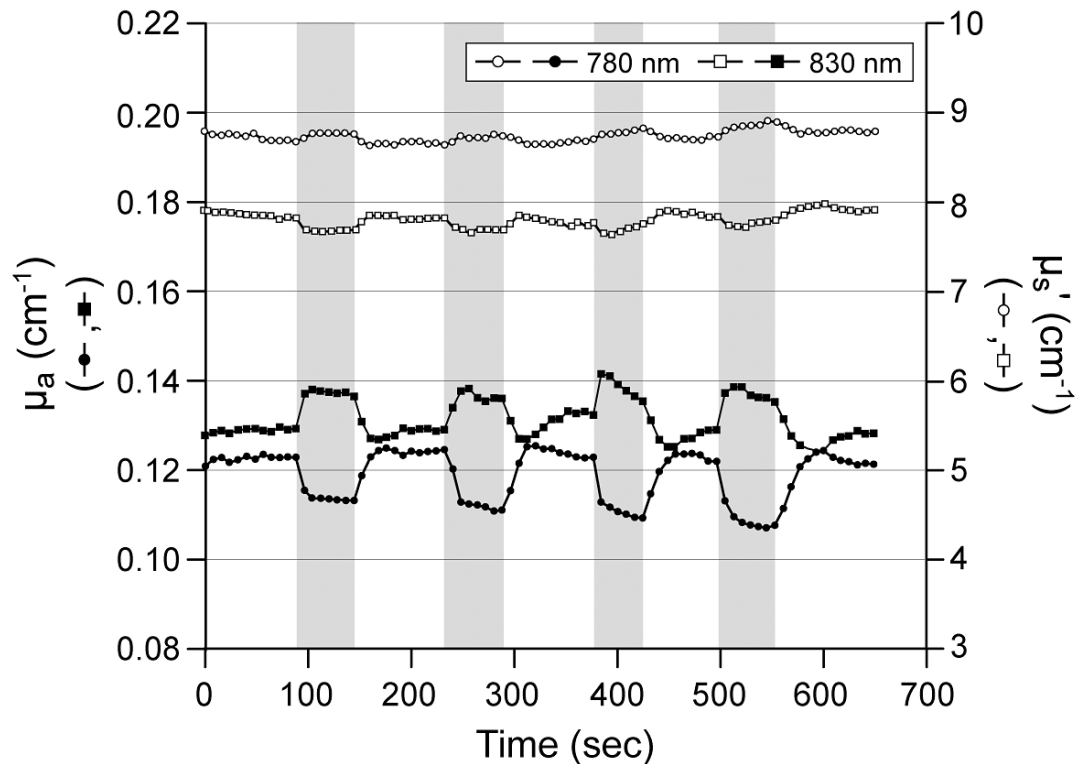


Figure 7-31: Time traces of the optical coefficients (absorption coefficient  $\mu_a$  and reduced scattering coefficient  $\mu'_s$ ) during the experiment. Shaded areas correspond to the stimulation periods.

Figure 7-32 shows the changes of oxygenated hemoglobin, deoxygenated hemoglobin and total hemoglobin concentrations during the FiO<sub>2</sub> modulation on the same rat. The oxygenated hemoglobin concentration increases in response to the increased FiO<sub>2</sub> perturbation and the deoxygenated hemoglobin concentration decreases accordingly, showing that the concentration changes are directly related to the inhaled oxygen concentration. The total hemoglobin concentration changes are small compared to the changes in oxygenated and deoxygenated hemoglobin

concentrations during the entire duration, with slight decrease during the increased  $\text{FiO}_2$  state.

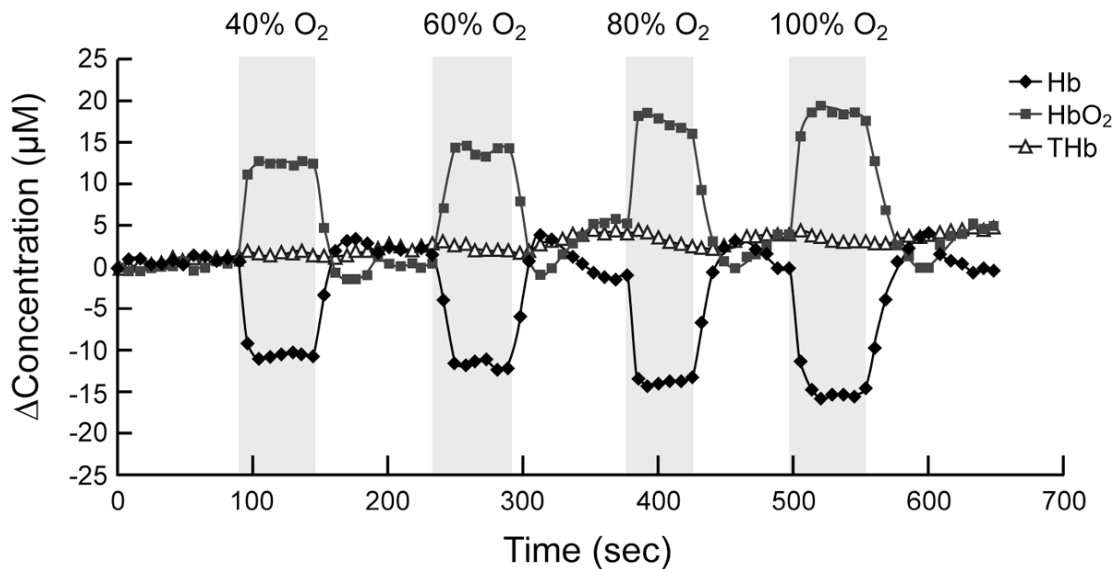
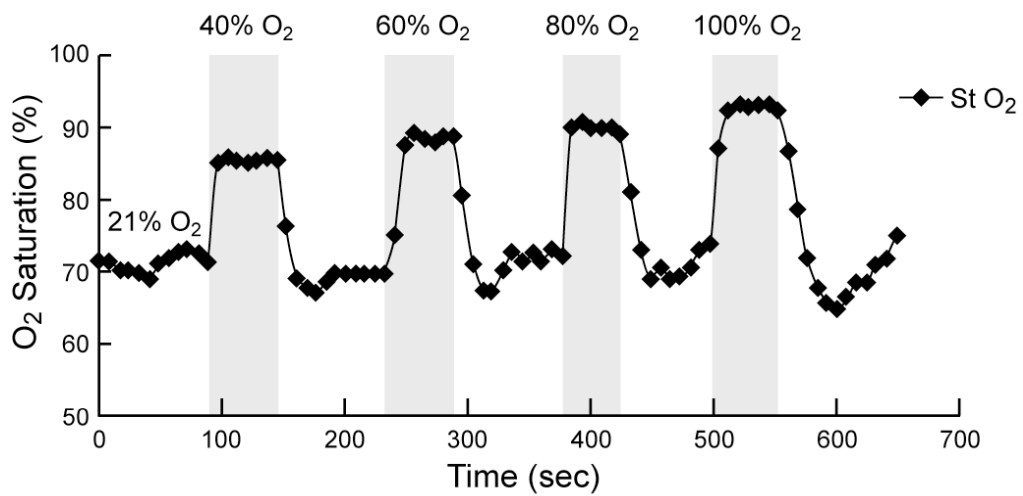


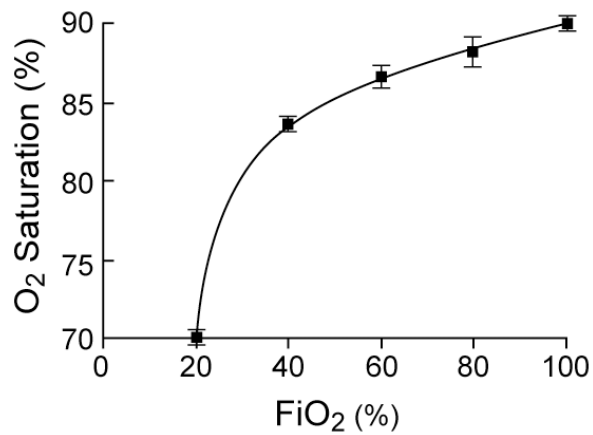
Figure 7-32: Changes of deoxygenated hemoglobin (HB), oxygenated hemoglobin (HBO<sub>2</sub>), and total hemoglobin (THB) concentrations during the inspiration of gas with different  $\text{FiO}_2$  from rat #1.

Figure 7-33(a) depicts the results in the saturation change during the protocol for the same rat. In the normal state (21% O<sub>2</sub> in the inspired air), the tissue saturation ( $\text{StO}_2$ ) is approximately 70%. After inspiration of gas with a higher oxygen concentration than the normal state, the tissue oxygen saturation ( $\text{StO}_2$ ) increases to above 85%. With the continuing increment of the  $\text{FiO}_2$ , the  $\text{StO}_2$  still increases, but much more slowly. The tissue saturation returns to the baseline during the recovery period, with an initial undershoot lower than 70%  $\text{StO}_2$ . This trend was reproduced in the other two rats, although there existed slight subject-specific differences in absolute measurement. Our results are in agreement with the values from other investigators. For example, Hueber *et al* [165] observed a normal saturation of 60% – 70% with the inhalation of 21% oxygen on the piglet brain, and rises to about 85% – 90 % during

the inhalation of 100% oxygen. The increment is large from normal physiological state to the hyperoxic state, and the increases are much slower with further increasing the  $FiO_2$ . From the normal hemoglobin-oxygenation equilibrium curve [177], the oxygen saturation changes with the oxygen pressure in a sigmoidal shape. The measured tissue oxygen saturation and the  $FiO_2$  demonstrated this relationship (part of sigmoid, see Figure 7-33(b)).



(a)



(b)

Figure 7-33: (a) Change of oxygen saturation ( $StO_2$ ) during the inspiration of gas with different  $FiO_2$  (rat #1); (b) Relationship of tissue oxygenation saturation with the inspired  $FiO_2$  (rat #1).

### 7.5.3 Correlation with MRI BOLD Signals

Figure 7-34 depicts representative normalized mean BOLD-MRI pixel intensities for a region of interest (ROI) consisting of the bilateral frontoparietal cortex in a single coronal brain slice obtained per animal under the aforementioned  $\text{FiO}_2$  paradigm. The BOLD signal shows the physiological changes brought on by variations in  $\text{FiO}_2$ .

To study the relative quantitative relationship between the NIRS and BOLD MRI signals, the change in each type of signal was normalized to 1 (i.e., set the difference between the mean signal value at 100%  $\text{FiO}_2$  and the baseline to 1). For the NIRS signal, monitoring of the deoxygenated hemoglobin concentration was selected. For the MRI signal, as stated previously, the conventional  $T_2^*$ -weighted BOLD signal was chosen.

Figure 7-35(a) and (b) plot the normalized NIRS signal (deoxygenated hemoglobin concentration) and the BOLD MRI signal. Since we are mainly interested in the response of both NIRS and BOLD MRI signals due to different stimulus-contrast levels, normalized NIR signal changes and the BOLD MRI signal changes (perturbation from baseline) are presented in Figure 7-35(c). The relationship for both types of perturbation is linear with a correlation coefficient greater than 0.99. This supports the assumption that BOLD signal is linearly proportional to the changes in deoxygenated hemoglobin concentration [169].

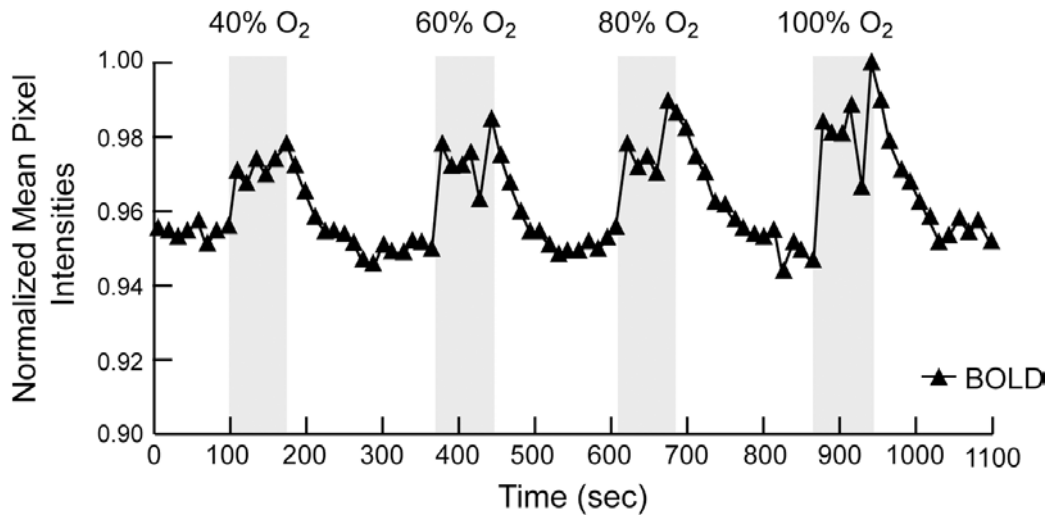


Figure 7-34: The MRI signal (BOLD) of the selected ROI during the inspiration of gas with different  $F_{iO_2}$  for the rat brain mapping.

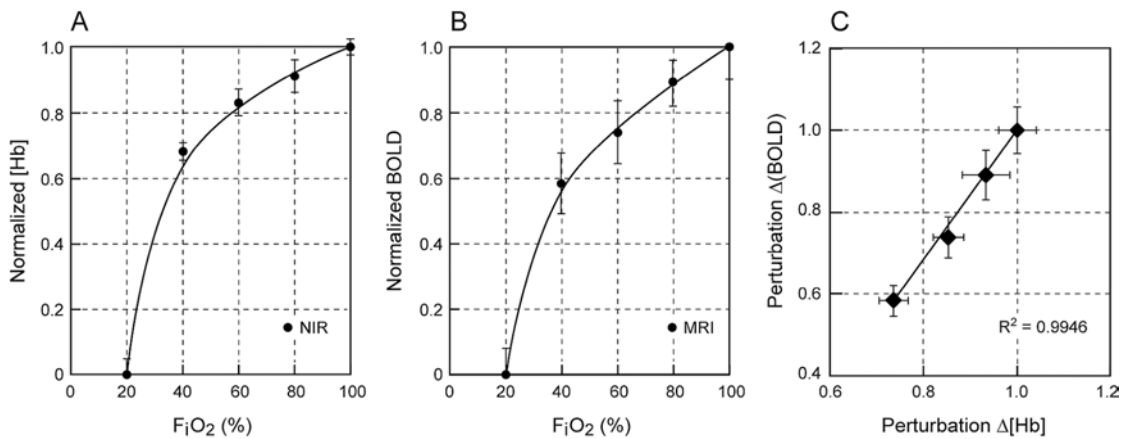


Figure 7-35: (a) Normalized change of deoxygenated hemoglobin concentration measured by NIRS; (b) Normalized change of MRI BOLD signal; (c) Correlation between the normalized BOLD signal change and the normalized deoxygenated hemoglobin concentration change. Four points are corresponding to four perturbations (40%  $F_{iO_2}$ , 60%  $F_{iO_2}$ , 80%  $F_{iO_2}$  and 100%  $F_{iO_2}$ ) from the baseline, normalized with the maximum change. Data include all rats.

This study is a first step in the exploration of the relative quantitative correlation between the NIRS signal and the BOLD MRI signal. Simultaneous co-registration of NIRS and BOLD MRI, which will be our next step, will be better suited for studying the time-correlation [169,170,172] of these signals and for removing subject-specific differences. More studies are required in order to further investigate the relevance of correlation between MRI and NIRS signals.

The linear correlation observed in our study may be used for calibrating BOLD MRI, which cannot otherwise quantify deoxygenated hemoglobin concentration directly. The maximum fractional change of the BOLD MRI signal is only 4%, while in NIRS a 15 $\mu$ M change in the deoxygenated hemoglobin concentration is observed, which corresponds to about 20% of total hemoglobin concentration. This may be due to the fact that the BOLD MRI signal measures the effect of paramagnetic deoxygenated hemoglobin upon the relaxation of water in several spaces including the water within the blood vessel and exterior to the blood vessel, while NIRS measures the vascular bed directly. The relationship between these two physiological processes needs to be further investigated. Also, though MRI has been widely used to study brain function, the exact relationship between the BOLD signal and the underlying neuronal activity still remains unclear, though a linear relationship between normalized BOLD MRI signal and the normalized changes in the intracortical recording potential has been reported [178]. A cross-validation between BOLD MRI and NIRS may help elucidate the neurovascular mechanisms responsible for functional BOLD MRI.

In summary, we have observed significant NIRS signal changes from ambient to significantly increased FiO<sub>2</sub> inhalation, from which we calculated the changes in blood oxygenation saturation and hemoglobin concentration. The changes in

deoxygenated hemoglobin correlate well with the BOLD MRI signal changes sampled in the co-localized region. This correlation encourages further investigation, which may help to probe the tissue oxygen saturation and hemoglobin concentration more accurately for both modalities and to better understand the underlying physiology.

## **7.6 Brain Mapping with Phased Array Topography**

In Section 6.2.4 we also introduce the instrument of phased array topography and here we would like to input more results we obtained using the phased array topographer on brain functional imaging.

Noninvasive measurement of brain activity has been of increasing interest in recent years. Functional activation of the human brain is coupled to the localized changes in cerebral blood volume and oxygenation saturation [157]. Currently, Positron Emission Tomography (PET) and functional Magnetic Resonance Imaging (fMRI) are widely used to obtain images of brain activation related to various kinds of stimulation. Near-infrared imaging (NIRI) is a novel technique for measuring brain activity. Compared with PET and fMRI, NIRI has the advantages of portability, real-time measurement and low cost.

Since Jobsis [9] first showed that the absorption of hemoglobin could be observed in the neonatal brain with near-infrared transillumination, and Brazy *et al* [158] applied the optical method to monitor brain oxygenation levels of newborn infants, much research work has been done in this the area of non-invasive diagnosis of brain function by means of near-infrared spectroscopy [159-161]. Imaging of adults and neonates has been implemented by continuous light [162] and pulsed light [163,193] successfully.

Using frequency-domain techniques, the single-wavelength phased array topographer (Section 6.2.4) can be used for imaging sensorimotor and cognitive activation of adult and pre- and full-term neonate human brain function [91]. The single-wavelength instrument uses 780 nm light source, which is more sensitive to deoxygenated hemoglobin, thus it is comparable to BOLD fMRI (Section 7.5.3). Figure 7-36 demonstrates the co-registered image of brain activation during the finger-tapping task. To access the information of both the oxygenated and deoxygenated hemoglobin, we have developed the dual-wavelength (750 nm and 830 nm) phased array imaging (PAI) system (Section 7.2.4) for human brain function imaging. This system can provide information on blood concentration and oxygenation in a localized region. Figure 7-37 shows the time dependent image of a finger-tapping task. We have observed an increase of phase perturbation signal related with the activation, and the signal decreases after the recovery. The signal location is corresponding to the motor cortex area.

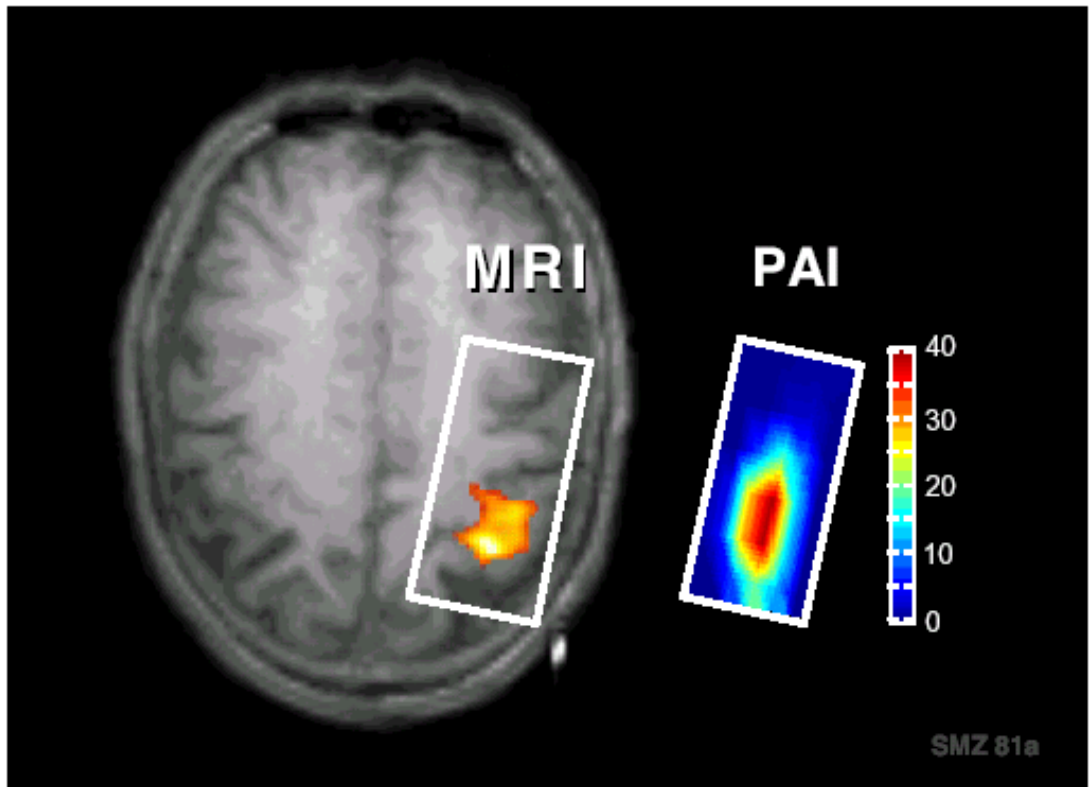


Figure 7-36: The co-registration of the single-wavelength phased array image (PAI) with a concurrent fMRI image, water and CuSO<sub>4</sub> in capillaries define the four corners of the PAI imager on the head and were imaged by MRI allowing co-registration of the shape of the images on the brain (rectangle shown over the MRI). (Adopted from Ref. [91])

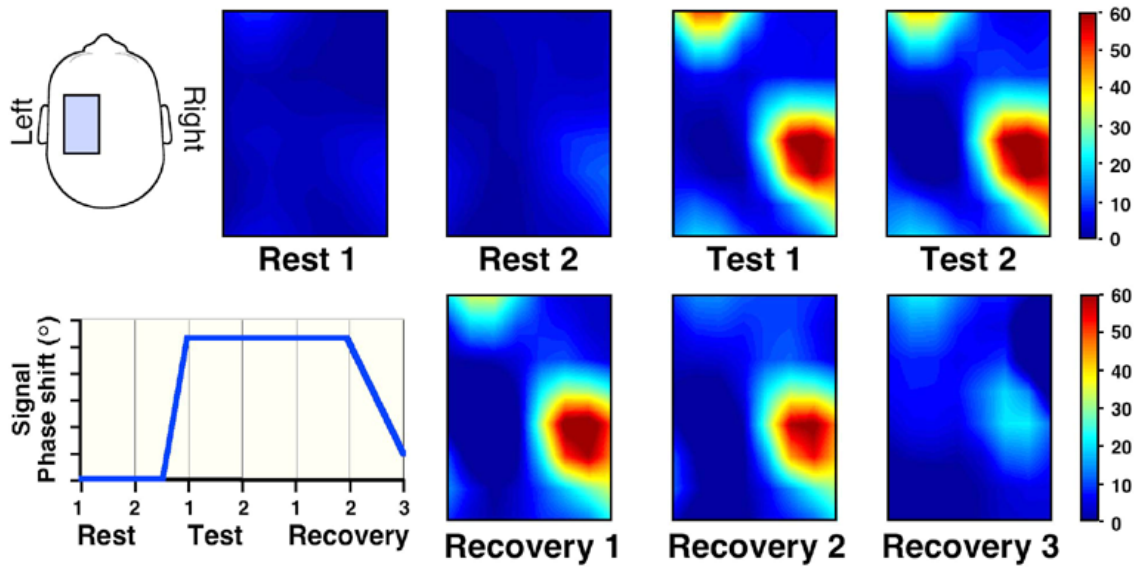


Figure 7-37: Finger-tapping test. Signal increases with the right finger tapping and decreases after the recovery.

### 7.6.1 Phantom Experiment

In the Intralipid + Ink medium with proper optical properties as human brain tissue ( $\mu_a = 0.10 \text{ cm}^{-1}$ ,  $\mu_s' = 12 \text{ cm}^{-1}$ ), a 4 x 4 x 8 mm cellophane chamber is placed with 2.5 cm depth away from the imager pad. The chamber is connected to a pump for oxygenated or deoxygenated blood. Filled with a certain concentration of blood (typically 8 mM), this chamber can be moved to various positions within the model. The perturbation of phase are plotted in Figure 7-38, which shows the difference between two wavelength signals, *i.e.*,  $|\Delta\Phi(830 \text{ nm})| - |\Delta\Phi(750 \text{ nm})|$ . From Figure 7-38, the changes for oxygenated and deoxygenated blood are in opposite directions, and for the black absorber, which has similar absorption coefficients for both wavelengths, shows almost a zero signal after subtraction. In the dual-wavelength system, the wavelengths we had chosen were on different sides of the isosbestic point ( $\sim 800 \text{ nm}$ ). For oxygenated hemoglobin,  $\mu_a(750 \text{ nm}) < \mu_a(830 \text{ nm})$  while for deoxygenated hemoglobin,  $\mu_a(750 \text{ nm}) > \mu_a(830 \text{ nm})$ , the difference of these two

wavelengths can indicate the oxygenation/deoxygenation information. Thus we take  $|\Delta\Phi(830)| - |\Delta\Phi(750)|$ , which can reveal oxygenation changes; and  $\Delta\Phi(830) + \Delta\Phi(750)$ , which can reveal the blood volume changes, as the signal for evaluation.

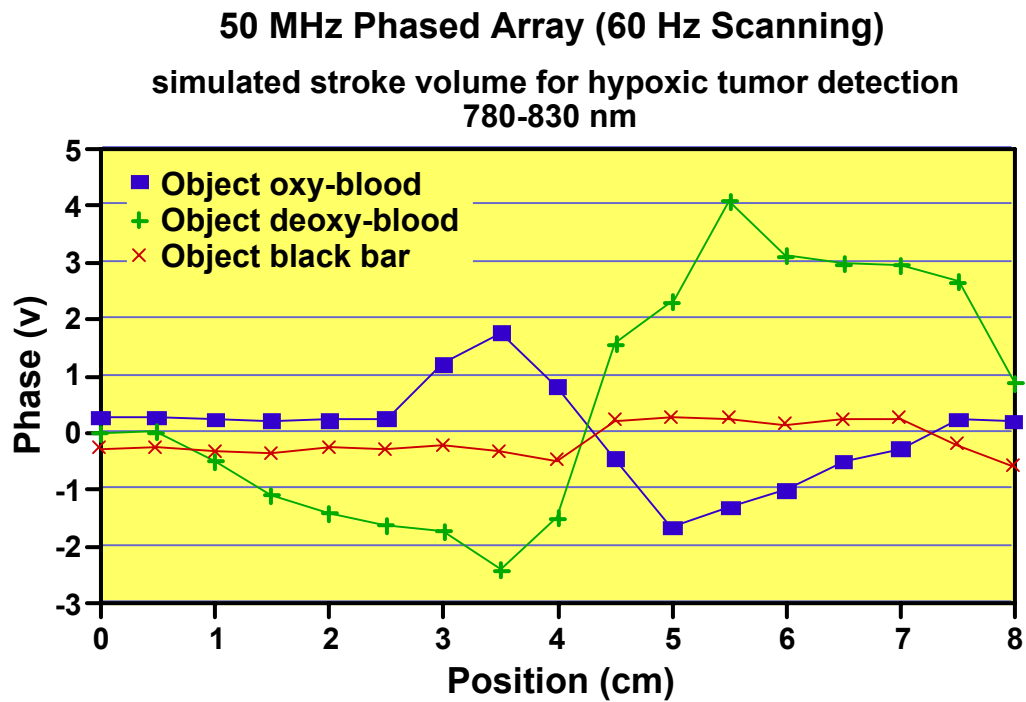


Figure 7-38:  $|\Delta\Phi(830 \text{ nm})| - |\Delta\Phi(750 \text{ nm})|$  varies with the displacement of the absorber. Also note the opposite trends for oxygenated blood and deoxygenated blood, and almost no change for the neutral absorber (black delrin cylinder). (Phase is expressed in volt, which is proportional to phase angle in degree)

### 7.6.2 Functional Imaging for Neonate

We have studied totally 7 neonates for a period of about two months, with the IRB approved informed consent from the mothers of neonates. Six of the neonates are pre-term (gestation:  $27 \pm 4$  weeks) and their average age is  $30 \pm 18$  days. Three of them have brain trauma (bleeding or epilepsy), while others are considered normal.

The imager pad is placed on the middle region of neonates' head centered at *fonticulus* to cover the sensorimotor cortex, with a plastic wrap to prevent direct contact on the neonate's skin. During the experiments, the neonates are stimulated by separately touching the four extremities and recording the signals in the contralateral sensorimotor cortex. The experimental protocol is that after the recording of the baseline, the physician gently and continuously touches the infant's four extremities (left hand, right hand, left foot and right foot) sequentially using swabs with equal intensity. The duration of each stimulation is 30 seconds and there is 30 seconds resting state between two stimulations.

*Normal Brain vs. Diseased Brain:* We have obtained the signals due to the blood volume and oxygenation changes caused by the sensory stimulation. Our results illustrate the difference in the response patterns and signal intensities of normal neonates and those who have diseased brain conditions. In normal neonates, we get reproducible responses. Figure 7-39(a) gives one example of the blood volume and oxygenation changes during a touching task. For subject S., a 33-wk gestational age infant with normal conditions, the signal changes occur in the region contralateral to the stimulus side. We observed the increases of blood volume and oxygenation saturation in the left side of the brain sensorimotor area during the stimulation. For instance, we stimulated the right foot of the neonate, and on the left part of the sensory area, we observed large responses (Oxygenation image:  $\Delta\Phi = 60^\circ$ ; Blood Volume image:  $\Delta\Phi = 90^\circ$ ; total signal (the sum of Oxygenation and Blood Volume:  $\Delta\Phi = 150^\circ$ ). The recovery of the signal is observed after 30 seconds of rest (Oxygenation image:  $\Delta\Phi \sim 5^\circ$ ; Blood Volume image:  $\Delta\Phi \sim 10^\circ$ ; See Figure 7-39(b)). In neonate with brain dysfunction, patient N., 27-wk gestational age with epilepsy, the signal is lower and non-localized (Oxygenation image:  $\Delta\Phi < 5^\circ$ ; Blood Volume

image:  $\Delta\Phi < 5^\circ$ ; See Figure 8-37(c)). The image taken after 30s recovery also has low signal intensity.

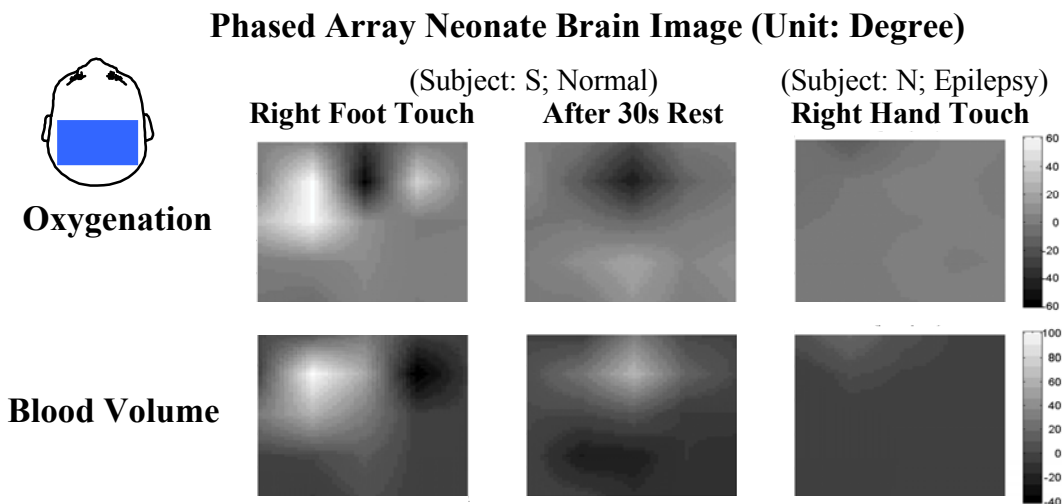


Figure 7-39: Response to stimulation task from normal ((a) and (b)) and abnormal (c) subjects. (a) the signal corresponding to contralateral parietal stimulation; (b) the disappearance of signal 30 seconds after the stimulation ends; (c) for brain dysfunction neonate, no clear signal is observed. (For Oxygenation Images, “+” indicates oxygenation, and “-” indicates deoxygenation; For Blood Volume Images, “+” indicates increase and “-” indicates decrease in blood volume)

Statistical analysis of the total signals from the responding voxels (not including the background) for normal and diseased populations with the Student *t*-test shows there is a significant difference in the mean of total responding signals (For normal subjects, mean and standard deviation =  $109.5^\circ \pm 15.3^\circ$ ; For abnormal subjects, mean and standard deviation =  $26.1^\circ \pm 11.8^\circ$ ;  $P = 0.004$ ).

Case Study of Cardiac Arrest Neonate: We have been able to study subject W (24-wk gestational age) over 21 days, postpartum. This subject had cardiac arrest for

30 minutes during delivery. Figure 7-40(a) and (b) show a large response to parietal stimulation and complete disappearance of the signal after 30 seconds rest period on the 1st day after resuscitation, which indicates the brain function was quite active. The 2nd day this infant had a neonatal seizure, and no parietal response was observed on the tests on the following day (3rd day) (Figure 7-40(c)). Then, the infant gradually recovered and returned to functional condition. The response to the stimulation can be observed again.

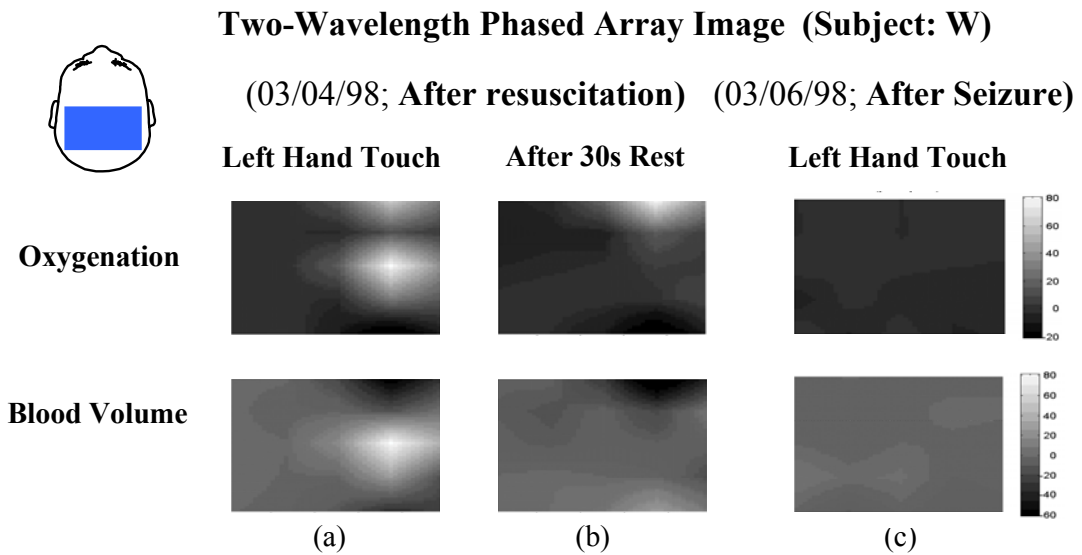


Figure 7-40: Results of phased array imaging before and after seizure: response of stimulation (a) and disappearance of signal (b) after stimulation before seizure and no response (c) to parietal stimulation after seizure. (Image gray scale code same as Figure 7-39)

To examine the longitudinal tendency of the brain functional response, we plot the summation of phased array total signal intensity ( $|\text{blood volume}| + |\text{oxygenation}|$ ) corresponding to all the four sensory stimulation in one day versus the test date in Figure 7-41. Here we observed summation of the total signal varied with the date after

birth (resuscitation). On the first day after resuscitation, the neonate had partial response to the stimulation (strong response to Left Hand Touch, while no obvious response to other stimulations), and the sum of the total signal is  $190^\circ$ . After the seizure, the neonate was inactive so that the sum of the signal is only  $\sim 10^\circ$  on date 3. On date 6, the infant seemed recovered and a little bit hypersensitive to the stimulation, and we got an overshooting in the sum of total signal ( $440^\circ$ ). Then the infant's condition fluctuated but remained at a certain level (date 8:  $130^\circ$ ; date 10:  $170^\circ$ ; date 13:  $100^\circ$ ). Thereafter, the neonate recovered gradually and became more sensitive to the stimulation (date 16:  $280^\circ$ ; date 21:  $360^\circ$ ). On date 21, the infant behaved normally and if we look at the average total signal for each stimulation, the result is roughly  $90^\circ$  ( $= 360^\circ/4$ ), which is comparable to the mean of total signal for normal neonates we got above ( $109.5^\circ$ ), considering the standard deviation is  $15.3^\circ$ . On date 22, the infant had completely recovered and left the hospital. The basic assumption here is the coupling between neuronal activation and the changes in local cerebral oxygenation and blood volume. Thus the signal variance with date could be related to the neonate's brain condition.

### Phase Array Signal vs. Date

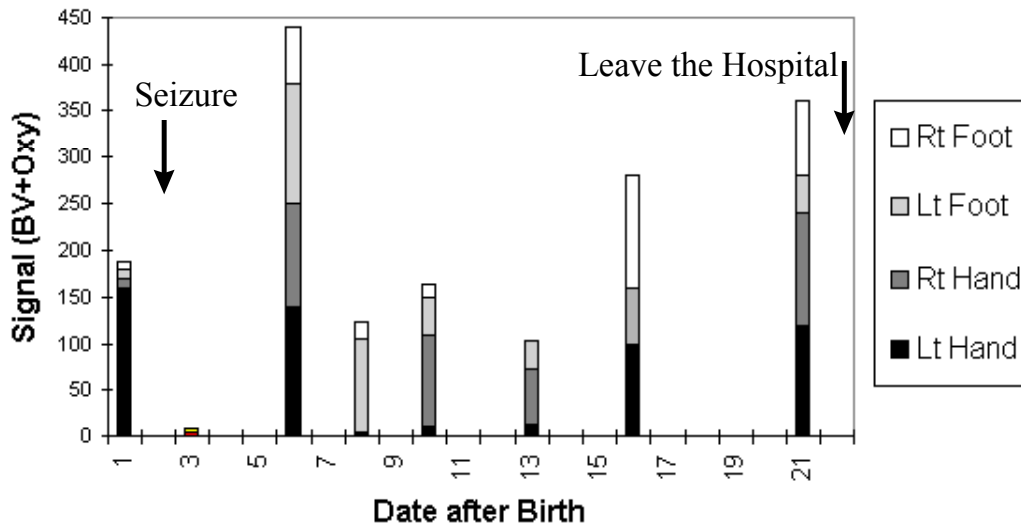


Figure 7-41: The summation of total signals from four stimuli on one day versus the date of testing (indicated by the date after birth and resuscitation), which shows the signal variation with different brain conditions. Note that there is almost no signal after the seizure (date 3) and the signal recovered gradually and finally reached a normal value before the infant was discharged (date 21).

We have shown above that the dual-wavelength phased array imaging system can successfully reveal the changes in blood concentration and oxygenation in functional brain activation for pre- and full-term neonates. Since this system is portable, it can be used for bedside monitoring and imaging of the infants' neurological development and detecting brain dysfunctions.

## 8 Summary and Perspective

In this thesis I have presented the theory, instrumentation and experimental results of utilizing the dual-interfering-source for sensitive object localization, especially with the application of early tumor detection in association with the fluorescent contrast agents. Other applications include the brain oxygenation monitoring correlated with BOLD MRI and functional brain mapping are presented as well. Our results demonstrated that near-infrared diffuse optical spectroscopy and imaging, as emerging technologies in biomedical imaging, hold a promising future for clinical diagnosis and other important medical applications.

Here, I would also like to further discuss some specific aspects regarding the future developments of diffuse optical spectroscopy and imaging, including the combination of other imaging modalities, the synergic development of molecular probes and imaging techniques, and the potential medical application of the phased array imager.

## 8.1 Image Fusion

An exciting application of optical technology is the combination with other imaging modalities, such as X-ray mammography [196], ultrasound [184,185], MRI [14,110,169,172] and PET [197], etc. The development of the hybrid system that can simultaneously image biological samples will offer more insights into the physiology and pathophysiology under investigation. Optical techniques possess the unique ability to probe the tissue functional information, including oxygenated and deoxygenated hemoglobin, as well as molecular imaging techniques with the molecular specific fluorescence contrast agents, which can offer complementary information to the structural imaging modalities; hence, improving the diagnosis specificity. On the other hand, the structural information provided by the high-resolution modalities might serve as *a priori* information for optical techniques (both the spectroscopy and tomography) to improve the quantification accuracy and spatial resolution.

## 8.2 Molecular Imaging

Molecular imaging has been a growing research field in recent years which aims to probe the malignancy in the cellular and molecular level, rather than the traditional morphological imaging. Optical techniques, especially the near-infrared (NIR) technology, holding the great strength of deep tissue penetration, open a window to resolve the molecular targets and pathways *in vivo* [186,187]. The synergic efforts in the developments of molecular specific imaging probes (including the chemical dyes [26,29] and nano-materials such as quantum dots [188], among others) and the advancements of optical imaging technologies (including the novel instrumentation and imaging algorithm [190,191]) will lead to a new tool for early

disease diagnosis and drug discovery. Although the barriers of delivering those probes into the designated area still remains to be understood and overcome [192].

### **8.3 Prospects of Phased Array Imaging**

Although the preliminary results of imaging cancer with molecular specific contrast agents are only demonstrated in small animals mostly, this technology has great potential for clinical applications. The key issues are the development of novel molecular contrast agents and their approval from FDA for human studies. Instrumentation wise, this technology can be readily adapted to clinical study. NIR light has been shown to penetrate through tissue deeply [193], thus has unique merit in detecting tumors inside large organs such as the human breast. Considering the breast imaging systems, several patient-device interfaces have been proposed. The system can use planar geometry similar to X-ray mammography, or the pendent breast geometry like CT fan beam scan (Figure 8-1(a) and (b)).

The principle of phase cancellation can be applied to low frequency range such as the audio frequency (kHz). Then the size and cost of the instrument can be further reduced owing to the integrated audio components. A handheld scanner similar to the ultrasound probe could be designed as a convenient self-examination device using the cancellation principles (Figure 8-2(c)).

Another interesting prospect is to seamlessly combine the detection and therapy together. One possible approach is to use the Bacteriochlorophyll (BChl)-2-Deoxy-Glusamide as the contrast agent. As demonstrated in Section 7.2.4, BChl-2DG shows detectable contrast between the tumor and the surrounding normal tissue. Since BChl is the Photodynamic therapy (PDT) agent itself, the two-dimensional tumor localization image provided by the phased array scanner could be used to guide the

position to shine high power laser light for tumor ablation or PDT treatment. In this case, the two-dimensional localization information will be sufficient for guiding the treatment.

Compared with X-ray or nuclear imaging modalities, the NIR imaging system has no ionizing radiation, thus is safe for the patients. Also it is inexpensive compared with MRI or PET system. Hence, the NIR imaging system will be an attractive modality for clinical diagnosis in the near future.

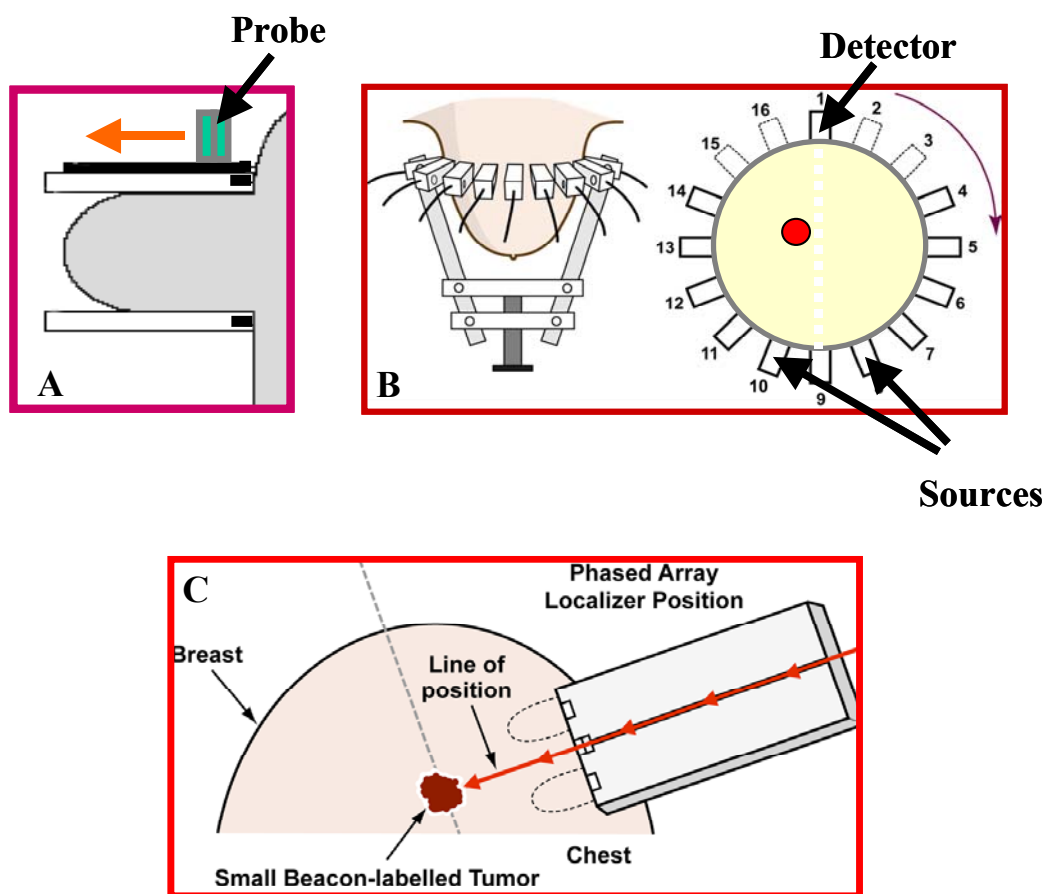


Figure 8-1: Proposed patient-device interface for NIR phased array imaging system.

(A: Planar Geometry; B: Pendant Geometry; C: Handheld System)

## 9 References

1. American Cancer Society: Cancer Facts & Figures – 2002, *American Cancer Society* (2002).
2. Roberts M.M., Alexander F.E., Anderson T.J., Chetty U., Donnan P.T., Forrest P., Hepburn W., Huggins A., Kirkpatrick A.E. and Lamb J., Edinberg trial of screening for breast cancer: mortality at seven years, *Lancet*, **335**, 241-246 (1990).
3. Cross M.J., Harms S.E., Cheek J.H., Peters G.N. and Jones R.C., New horizons in the diagnosis and treatment of breast cancer using magnetic resonance imaging, *Am. J. Surg.*, **166**, 749-755 (1993).
4. Forouhi P., Walsh J.S., Anderson T.J. and Chetty U., Ultrasonography as a method of measuring breast tumor size and monitoring response to primary systemic treatment, *Brit. J. Surg.*, **81**, 223-225 (1994).
5. Cerussi A.E., Berger A.J., Bevilacqua F., Shah N., Jakubowski D., Butler J., Holcombe R.F. and Tromberg B.J., Sources of absorption and scattering

- contrast for near-infrared optical mammography, *Acad. Radiol.*, **8**, 211-218 (2001).
6. Uno K., Yoshikawa K., Imazeki K., Okada J., Minoshima S. and Arimizu N., FDG-PET evaluation of breast cancer – a diagnostic role for primary or metastatic and recurrent lesions, *Radiology*, **185**, 108-108 (1992).
  7. Cutler M., Transillumination as an aid in the diagnosis of breast lesions, *Surg. Gynecol. Obstet.*, **48**, 721-729 (1929).
  8. Chance B. (Ed.), *Photon Migration in Tissues*, Plenum Press, New York (1989).
  9. Jobsis F.F., Noninvasive infrared monitoring of cerebral and myocardial oxygen sufficiency and circulatory parameter, *Science*, **198**, 1264-1267 (1977).
  10. Yodh A.G. and Chance B., Spectroscopy and imaging with diffusing light, *Phys. Today*, **48**, 34-40 (1995).
  11. Arridge S.R., Optical tomography in medical imaging, *Inverse Problems*, **15**, R41-R93 (1999).
  12. Franceschini M.A., Moesta K.T., Fantini S., Gaida G., Gratton E., Jess H., Mantulin W.W., Seeber M., Schlag P.M. and Kaschke M., Frequency-domain techniques enhance optical mammography: initial clinical results, *Proc. Natl. Acad. Sci. USA*, **94**, 6468-6473 (1997).
  13. Pogue B.W., Poplack S.P., McBride T.O., Wells W.A., Osterman S., Osterberg U.L. and Paulsen K.D., Quantitative hemoglobin tomography with diffuse near-infrared spectroscopy: pilot results in the breast, *Radiology*, **218**, 261-266 (2001).
  14. Ntziachristos V., Yodh A.G., Schnall M. and Chance B., Concurrent MRI and diffuse optical tomography of breast after indocyanine green enhancement, *Proc. Natl. Acad. Sci. USA*, **97**, 2767-2772 (2000).

15. Quaresima V., Matcher S.J. and Ferrari M., Identification and quantification of intrinsic optical contrast for near-infrared mammography, *Photochem. Photobiol.*, **67**, 4-14 (1998).
16. McBride T.O., Pogue B.W., Gerety E.D., Poplack S.P., Osterberg U.L. and Paulsen K.D., Spectroscopic diffuse optical tomography for the quantitative assessment of hemoglobin concentration and oxygen saturation in breast tissue, *Appl. Opt.*, **38**, 5480-5490 (1999).
17. Folkman J., Angiogenesis and breast cancer, *J. Clin. Oncol.*, **12**, 441-443 (1994).
18. Vaupel P., Schlenger K., Knoop C. and Hockel M., Oxygenation of human tumors: Evaluation of tissue oxygen distribution in breast cancers by computerized O<sub>2</sub> tension measurements, *Cancer Res.*, **51**, 3316-3322 (1991).
19. Vaupel P., Kallinowski F. and Okunieff P., Blood flow, oxygen and nutrient supply, and metabolic microenvironment of human tumors: A review, *Cancer Res.*, **49**, 6449-6465 (1989).
20. Tromberg B.J., Coquoz O., Fishkin J., Pham T., Anderson E.R., Butler J., Cahn M., Gross J.D., Venugopalan V. and Pham D., Non-invasive measurements of breast tissue optical properties using frequency-domain photon migration, *Phil. Trans. Roy. Soc. Lond. B*, **352**, 661-668 (1997).
21. Tromberg B.J., Shah N., Lanning R., Cerussi A., Espinoza J., Pham T., Svaasand L. and Butler J., Non-invasive in vivo characterization of breast tumors using photon migration spectroscopy, *Neoplasia*, **2**, 26-40 (2000).
22. Chance B, Near-infrared (NIR) optical spectroscopy characterizes breast tissue hormonal and age status, *Acad. Radiol.*, **8**, 209-210 (2001).

23. Ntziachristos V. and Chance B., Probing physiology and molecular function using optical imaging: applications to breast cancer, *Breast Cancer Res.*, **3**, 41-46 (2001).
24. Ebert B., Sukowski U., Grosenick D., Wabnitz H., Moesta K.T., Licha K., Becker A., Semmler W., Schlag P.M. and Pinneberg H., Near-infrared fluorescent dyes for enhanced contrast in optical mammography: phantom experiments, *J. Biomed. Opt.*, **6**, 134-140 (2001).
25. Troy T.L., Page D.L. and Sevick-Muraca E.M., Optical properties of normal and diseased breast tissues: Prognosis for optical mammography, *J. Biomed. Opt.*, **1**, 342-355 (1996).
26. Bornhop D.J., Contag C.H., Licha K. and Murphy C.J., Advances in contrast agents, reporters, and detection, *J. Biomed. Opt.*, **6**, 106-110 (2001).
27. Hawrysz D.J. and Sevick-Muraca E.M., Developments toward diagnostic breast cancer imaging using near-infrared optical measurements and fluorescent contrast agents, *Neoplasia*, **2**, 388-417 (2000).
28. Sevick-Muraca E.M., Houston J.P. and Gurfinkel M., Fluorescence-enhanced, near infrared diagnostic imaging with contrast agents, *Curr. Opin. Chem. Biol.*, **6**, 642-650 (2002).
29. Licha K., Contrast agents for optical imaging, *Top. Curr. Chem.*, **222**, 1-29 (2002).
30. Desmettre T., Devoisselle J.M. and Mordon S., Fluorescence properties and metabolic features of indocyanine green (ICG) as related to angiography, *Surv. Ophthalmol.*, **45**, 15-27 (2000).
31. Gulsen G., Yu H., Wang J., Nalcioglu O., Merritt S., Bevilacqua F., Durkin A.J., Cuccia D.J., Lanning R. and Tromberg B.J., Congruent MRI and near-

- infrared spectroscopy for functional and structural imaging of tumors, *Technology in Cancer Research & Treatment*, **1**, 1-9 (2002).
32. Kusaka T., Isobe K., Nagano K., Okubo K., Yasuda S., Kondo M., Itoh S. and Onishi S., Estimation of regional cerebral blood flow distribution in infants by near-infrared topography using indocyanine green, *Neuroimage*, **13**, 944-952 (2001).
  33. Licha K., Riefke B., Ntziachristos V., Becker A., Chance B. and Semmler W., Hydrophilic cyanine dyes as contrast agents for near-infrared tumor imaging: Synthesis, photophysical properties and spectroscopic in vivo characterization, *Photochem. Photobiol.*, **72**, 392-398 (2000).
  34. Sevick-Muraca E.M. and Burch C.L., Origin of phosphorescence signals reemitted from tissues, *Opt. Lett.*, **19**, 1928-1930 (1994).
  35. Li X.D., Beauvoit B., White R., Nioka S., Chance B. and Yodh A.G., Tumor localization using fluorescence of indocyanine green (ICG) in rat models, *Proc. Soc. Photo-Opt. Ins.*, **2389**, 789-797 (1995).
  36. Sevick-Muraca E.M., Lopez G., Reynolds J.S., Troy T.L. and Hutchinson C.L., Fluorescence and absorption contrast mechanisms for biomedical optical imaging using frequency-domain techniques, *Photochem. Photobiol.*, **66**, 55-64 (1997).
  37. Reynolds J.S., Troy T.L., Mayer R.H., Thompson A.B., Waters D.J., Cornell K.K., Snyder P.W. and Sevick-Muraca E.M., Imaging of spontaneous canine mammary tumors using fluorescent contrast agents, *Photochem. Photobiol.*, **70**, 87-94 (1999).
  38. Gurfinkel M., Thompson A.B., Ralston W., Troy T.L., Moore A.L., Moore T.A., Gust J.D., Tatman D., Reynolds J.S., Muggenburg B., Nikula K., Pandey

- R., Mayer R.H., Hawrysz D.J. and Sevick-Muraca E.M., Pharmacokinetics of ICG and HPPH-car for the detection of normal and tumor tissue using fluorescence, near-infrared reflectance imaging: A case study, *Photochem. Photobiol.*, **72**, 94-102 (2000).
39. Becker A., Riefke B., Ebert B., Sukowski U., Rinneberg H., Semmler W. and Licha K., Macromolecular contrast agents for optical imaging of tumors: Comparison of indotricarbocyanine-labeled human serum albumin and transferrin, *Photochem. Photobiol.*, **72**, 234-241 (2000).
40. Achilefu S., Dorshow R.B., Bugaj J.E. and Rajagopalan R., Novel receptor-targeted fluorescent contrast agents for *in vivo* tumor imaging, *Invest. Radiol.*, **35**, 479-485 (2000).
41. Bugaj J.E., Achilefu S., Dorshow R.B. and Rajagopalan R., Novel fluorescent contrast agents for optical imaging of *in vivo* tumors based on a receptor-targeted dye-peptide conjugate platform, *J. Biomed. Opt.*, **6**, 122-133 (2001).
42. Becker A., Hassenius C., Licha K., Ebert B., Sukowski U., Semmler W., Wiedenmann B. and Grotzinger C., Receptor-targeted optical imaging of tumors with near-infrared fluorescent ligands, *Nat. Biotechnol.*, **19**, 327-331 (2001).
43. Zheng G., Li H., Yang K., Blessington D., Licha K., Lund-Katz S., Chance B. and Glickson J.D., Tricarbocyanine cholesteryl laurates labeled LDL: New near infrared fluorescent probes (NIRFs) for monitoring tumors and gene therapy of *Familial hypercholesterolemia*, *Bioorg. Med. Chem. Lett.*, **12**, 1485-1488 (2002).
44. Weissleder R., Tung C.H., Mahmood U. and Bogdanov A., *In vivo* imaging of tumors with protease-activated near-infrared fluorescent probes, *Nat. Biotechnol.*, **17**, 375-378 (1999).

45. Weissleder R. and Mahmood U., Molecular imaging, *Radiology*, **219**, 316-333 (2001).
46. Case K.M. and Zweifel P.F., *Linear Transport Theory*, Addison-Wesley, MA (1967).
47. Ishimaru A., *Wave Propagation and scattering in random media*, Academic, New York (1978).
48. Patterson M.S., Chance B. and Wilson B.C., Time resolved reflectance and transmittance for the non-invasive measurement of tissue optical properties, *Appl. Opt.*, **28**, 2331-2336 (1989).
49. Fishkin J.B. and Gratton E., Propagation of photon-density waves in strongly scattering media containing an absorbing semi-infinite plane bounded by a straight edge, *J. Opt. Soc. Am. A*, **10**, 127-140 (1993).
50. Boas D.A., O'Leary M.A., Chance B. and Yodh A.G., Scattering of diffuse photon density waves by spherical inhomogeneities within turbid media: Analytical solution and applications, *Proc. Natl. Acad. Sci. USA*, **91**, 4887-4891 (1994).
51. Boas D.A., *Diffuse photon probes of structural and dynamical properties of turbid media: theory and biomedical applications*, Dissertation in Physics, University of Pennsylvania (1996).
52. Pogue B.W. and Patterson M.S., Frequency-domain optical absorption spectroscopy of finite tissue volumes using diffusion theory, *Phys. Med. Biol.*, **39**, 1157-1180 (1994).
53. Haskell R.C., Svaasand L.O., Tsay T.T., Feng T.C., McAdams M.S. and Tromberg B.J., Boundary conditions for the diffusion equation in radiative transfer, *J. Opt. Soc. Am. A*, **11**, 2727-2741 (1994).

54. Aronson R., Boundary conditions for diffusion of light, *J. Opt. Soc. Am. A*, **12**, 2532-2539 (1995).
55. Suzuki K., Yamashita Y., Ohta K., Kaneko M., Yoshida M. and Chance B., Quantitative measurement of optical parameters in normal breasts using time-resolved spectroscopy: *in vivo* results of 30 Japanese women, *J. Biomed. Opt.*, **1**, 330-334 (1996).
56. Durduran T., Choe R., Culver J.P., Zubkov L., Holboke M.J., Giammarco J., Chance B. and Yodh A.G., Bulk optical properties of healthy female breast tissue, *Phys. Med. Biol.*, **47**, 2847-2861 (2002).
57. Firbank M., Hiraoka M., Essenpreis M. and Delpy D.T., Measurement of the optical properties of the skull in the wavelength range 650-950 nm, *Phys. Med. Biol.*, **38**, 503-510 (1993).
58. Hueber D.M., Franceschini M.A., Ma H.Y., Zhang Q., Ballesteros J.R., Fantini S., Wallace D., Ntziachristos V. and Chance B., Non-invasive and quantitative near-infrared haemoglobin spectrometry in the piglet brain during hypoxic stress, using a frequency-domain multidistance instrument, *Phys. Med. Biol.*, **46**, 41-62 (2001).
59. O'Leary M.A., Boas D.A., Chance B. and Yodh A.G., Refraction of diffuse photon density waves, *Phys. Rev. Lett.*, **69**, 2658-2661 (1992).
60. Schmitt J.M., Knuttel A. and Knutson J.R., Interference of diffuse light waves, *J. Opt. Soc. Am. A*, **9**, 1832-1843 (1992).
61. Knuttel A., Schmitt J.M., Barnes R. and Knutson J.R., Acousto-optic scanning and interfering photon density waves for precise localization of an absorbing (or fluorescent) body in a turbid medium, *Rev. Sci. Instrum.*, **64**, 638-644 (1993).

62. Knuttel A., Schmitt J.M. and Knutson J.R., Spatial localization of absorbing bodies by interfering diffusive photon-density waves, *Appl. Opt.*, **32**, 381-389 (1993).
63. Chance B., Kang K., He L., Weng J. and Sevick-Muraca E.M., Highly sensitive object location in tissue models with linear in-phase and anti-phase multi-element optical arrays in one and two dimensions, *Proc. Natl. Acad. Sci. USA*, **90**, 3423-3427 (1993).
64. Chance B., Kang K., He L., Liu H. and Zhou S., Precision localization of hidden absorbers in body tissues with phased-array optical systems, *Rev. Sci. Instrum.*, **67**, 4324-4332 (1996).
65. O'Leary M.A., *Imaging with diffuse photon density waves*, Dissertation in Physics, University of Pennsylvania (1996).
66. O'Leary M.A., Boas D.A., Chance B. and Yodh A.G., Experimental images heterogeneous turbid media by frequency-domain diffusing-photon tomography, *Opt. Lett.*, **20**, 426-428 (1995).
67. Gonatas C.P., Ishii M., Leigh J.S. and Schotland J.C., Optical diffusing imaging using a direct inversion method, *Phys. Rev. E*, **52**, 4361-4365 (1995).
68. Keijzer M., Star W.M. and Storchi P.R.M., Optical diffusion in layered media, *Appl. Opt.*, **27**, 1820-1824 (1988).
69. O'Leary M.A., Boas D.A., Chance B. and Yodh A.G., Reradiation and imaging of diffuse photon density waves using fluorescent inhomogeneities, *J. Lumin.*, **60&61**, 281-286 (1994).
70. Li X.D., *Fluorescence and diffusive wave diffraction tomographic probes in turbid media*, Dissertation in Physics, University of Pennsylvania (1998).

71. Souris J.S., *Diffusing wave emission tomography in highly-scattering systems*, Dissertation in Biochemistry and Molecular Biophysics, University of Pennsylvania (1999).
72. Richards-Kortum R. and Sevick-Muraca E.M., Quantitative optical spectroscopy for tissue diagnosis, *Annu. Rev. Phys. Chem.*, **47**, 555–606 (1996).
73. Fantini S., Franceschini M.A. and Gratton E., Semi-infinite-geometry boundary problem for light migration in highly scattering media: a frequency-domain study in the diffusion approximation, *J. Opt. Soc. Am. B*, **11**, 2128-2138 (1994).
74. Boas D.A., O’Leary M.A., Chance B. and Yodh A.G., Detection and characterization of optical inhomogeneities with diffuse photon density waves: a signal-to-noise analysis, *Appl. Opt.*, **36**, 75-92 (1997).
75. Feng S., Zeng F. and Chance B., Photon migration in the presence of a single defect: a perturbation analysis, *Appl. Opt.*, **34**, 3826-3837 (1995).
76. Walker S.A., Boas D.A. and Gratton E., Photon density waves scattered from cylindrical inhomogeneities: theory and experiments, *Appl. Opt.*, **37**, 1935-1944 (1998).
77. Li X.D., O’Leary M.A., Boas D.A., Chance B. and Yodh A.G., Fluorescent diffuse photon density waves in homogeneous and heterogeneous turbid media: analytic solutions and applications, *Appl. Opt.*, **35**, 3746-3758 (1996).
78. Li X.D., Chance B. and Yodh A.G., Fluorescent heterogeneities in turbid media: limits for detection, characterization, and comparison with absorption, *Appl. Opt.*, **37**, 6833-6844 (1998).
79. Wu J., Perelman L., Dasari R.R. and Feld M.S., Fluorescence tomographic imaging in turbid media using early-arriving photons and Laplace transforms, *Proc. Natl. Acad. Sci. USA*, **94**, 8783-8788 (1997).

80. Kang K.A., Bruley D.F., Londono J.M. and Chance B., Localization of a fluorescent object in highly scattering media via frequency response analysis of near infrared-time resolved spectroscopy spectra, *Ann. Biomed. Eng.*, **26**, 138-145 (1998).
81. Hielscher A.H., Alcouffe R.E. and Barbour R.L., Comparison of finite-difference transport and diffusion calculations for photon migration in homogenous and heterogeneous tissues, *Phys. Med. Biol.*, **43**, 1285-1302 (1998).
82. Lakowicz J.R., *Principles of Fluorescence Spectroscopy*, Plenum Press, New York (1983).
83. Kang K., Bruley D.F. and Chance B., Feasibility study of a single- and multiple-source near-infrared phase-modulation device for characterizing biological systems, *Biomed. Instrum. Technol.*, **31**, 373-389 (1997).
84. Intes X., Chance B., Holboke M.J. and Yodh A.G., Interfering diffusive photon-density waves with an absorbing-fluorescent inhomogeneity, *Opt. Express*, **8**, 223-231 (2001).
85. Wu G.L., Luo Q.M., Zeng S.Q., Mu C.P., Liu X.D. and Chance B., Theoretical study of a phased-array system using the diffraction model, *J. Mod. Opt.*, **48**, 181-187 (2001).
86. Lindquist C., Pifferi A., Berg R., Andersson-Engels S. and Svanberg S., Reconstruction of diffuse photon-density wave interference in turbid media from time-resolved transmittance measurements, *Appl. Phys. Lett.*, **69**, 1674-1676 (1996).

87. Erickson M.G., Reynolds J.S. and Webb K.J., Comparison of sensitivity for single-source and dual-interfering-source configurations in optical diffusion imaging, *J. Opt. Soc. Am. A*, **14**, 3083-3092 (1997).
88. Chen Y., Mu C.P., Intes X. and Chance B., Signal-to-noise analysis for detection sensitivity of small absorbing heterogeneity in turbid media with single-source and dual-interfering-source, *Opt. Express*, **9**, 212-224 (2001).
89. Intes X., Chen Y., Li X.D. and Chance B., Detection limit enhancement of fluorescent heterogeneities in turbid media by dual-interfering excitation, *Appl. Opt.*, **41**, 3999-4007 (2002).
90. Zhu Q., Sullivan D., Chance B. and Dambro T., Combined ultrasound and near infrared diffused light imaging in a test object, *IEEE Trans. Ultrason. Ferroelectrics & Freq. Control*, **46**, 665-678 (1999).
91. Chance B., Nioka S., Zhou S., Hong L., Worden K., Li C., Murray T., Ovetsky Y., Pidikiti D. and Thomas R., A novel method for fast imaging of brain function, non-invasively, with light, *Opt. Express*, **2**, 411-423 (1998).
92. Chen Y., Zhou S., Xie C., Nioka S., Delivoria-Papadopoulos M., Anday E. and Chance B., Preliminary evaluation of dual wavelength phased array imaging on neonatal brain function, *J. Biomed. Opt.*, **5**, 194-200 (2000).
93. Chen Y., Mu C., Intes X., Zhou L., Blessington D. and Chance B., Near-infrared phase cancellation instrument for fast and accurate localization of fluorescent heterogeneity, *Rev. Sci. Instrum.* (in press, 2003).
94. Intes X., Ntziachristos V. and Chance B., Analytical model for dual-interfering sources diffuse optical tomography, *Opt. Express*, **10**, 2-14 (2002).
95. Chen Y., Mu C.P., Intes X. and Chance B., Diffuse optical tomography using dual-interfering-source, *Proc. Soc. Photo-Opt. Ins.*, **4536**, 253-260 (2002).

96. Chen Y., Intes X., Zhou S., Mu C., Holboke M., Yodh A.G. and Chance B., Detection sensitivity and optimization of phased array system, *Proc. Soc. Photo-Opt. Ins.*, **4250**, 211-218 (2001).
97. Morgan S.P. and Yong K.Y., Controlling the phase response of a diffusive wave phased array system, *Opt. Express*, **7**, 540-546 (2000).
98. Papaioannou D.G., Hooft G.W., Colak S.B. and Oostveen J.T., Detection limit in localizing objects hidden in a turbid medium using an optically scanned phased array, *J. Biomed. Opt.*, **1**, 305-310 (1996).
99. Zhang Q., Brukilacchio T., Gaudett T., Wang L., Li A. and Boas D.A., Experimental comparison of using continuous-wave and frequency-domain diffuse optical imaging systems to detect heterogeneities, *Proc. Soc. Photo-Opt. Ins.*, **4250**, 219-238 (2001).
100. Chance B., Cope M., Gratton E., Ramanujam N. and Tromberg B., Phase measurement of light absorption and scatter in human tissue, *Rev. Sci. Instrum.*, **69**, 3457-3481 (1998).
101. Oldham N., Kramar J., Hetrick P. and Teague E., Electronic limitations in phase meters for heterodyne interferometry, *Precis. Eng.*, **15**, 173-179 (1993).
102. Pogue B.W. and Patterson M.S., Error assessment of a wavelength tunable frequency domain system for noninvasive tissue spectroscopy, *J. Biomed. Opt.*, **1**, 311-323 (1996).
103. Fantini S., Franceschini M.A., Maier J.S., Walker S.A., Barbieri B. and Gratton E., Frequency domain multichannel optical detector for non-invasive tissue spectroscopy and oximetry, *Opt. Eng.*, **34**, 32-42 (1995).

104. Yang Y., Liu H., Li X.D. and Chance B., Low-cost frequency-domain photon migration instrument for tissue spectroscopy, oximetry and imaging, *Opt. Eng.*, **36**, 1562-1569 (1997).
105. Cope M. and Delpy D.T., System for long-term measurement of cerebral blood and tissue oxygenation on newborn infants by near infrared transillumination, *Med. Biol. Eng. Comput.*, **26**, 289-294 (1988).
106. Quaresima V., Matcher S.J. and Ferrari M., Identification and quantification of intrinsic optical contrast for near-infrared mammography, *Photochem. Photobiol.*, **67**, 4-14 (1998).
107. Cooper C.E., Cope M., Springett R., Amess P.N., Penrice J., Tyszczuk L., Punwani S., Ordidge R., Wyatt J. and Delpy D.T., Use of mitochondrial inhibitors to demonstrate that cytochrome oxidase near-infrared spectroscopy can measure mitochondrial dysfunction noninvasively in the brain, *J. Cerebr. Blood F. Met.*, **19**, 27-38 (1999).
108. Robertson C.S., Gopinath S.P. and Chance B., Use of near-infrared spectroscopy to identify traumatic intracranial hematomas, *J. Biomed. Opt.*, **2**, 31-41 (1997).
109. Casavola C., Paunescu L.A., Fantini S., Franceschini M.A., Lugara P.M. and Gratton E., Application of near-infrared tissue oxymetry to the diagnosis of peripheral vascular disease, *Clin. Hemorheol. Micro.*, **21**, 389-393 (1999).
110. Ntziachristos V., Yodh A.G., Schnall M. and Chance B., MRI-guided diffuse optical spectroscopy of malignant and benign breast lesions, *Neoplasia*, **4**, 347-354 (2002).
111. Graaff R., Aarnoudse J.G., Zijp J.R., Sloot P.M., de Mul F.M., Greve J. and Koelink M.H., Reduced light-scattering properties for mixtures of spherical

- particles: A simple approximation derived from Mie calculations *Appl. Opt.*, **31**, 1370-1376 (1992).
112. Liu H.L., Beauvoit B., Kimura M. and Chance B., Dependence of tissue optical properties on solute-induced changes in refractive index and osmolarity, *J. Biomed. Opt.*, **1**, 200-211 (1996).
  113. Cubeddu R., Pifferi A., Taroni P., Torricelli A. and Valentini G., Noninvasive absorption and scattering spectroscopy of bulk diffusive media: An application to the optical characterization of human breast, *Appl. Phys. Lett.*, **74**, 874-876 (1999).
  114. Chance B., Mayevsky A., Guan B. and Zhang Y.T., Hypoxia/ischemia triggers a light scattering event in rat brain, *Adv. Exp. Med. Biol.*, **428**, 457-467 (1997).
  115. Woodard H.Q. and White D.R., The composition of body tissues, *Brit. J. Radiol.*, **59**, 1209-1219 (1986).
  116. Ma H.Y., Xu Q., Ballesteros J.R., Ntziachristos V., Zhang Q. and Chance B., Quantitative study of hypoxia stress in piglet brain by IQ phase modulation oximetry, *Proc. Soc. Photo-Opt. Ins.*, **3597**, 642-649 (1999).
  117. Golub G. and van Loan C., *Matrix Computations*, John Hopkins Univ. Press (1989).
  118. Nelder J.A. and Mead R., A simplex method for function minimization, *Computer J.*, **7**, 308-313 (1964).
  119. Sevick-Muraca E.M., Chance B., Leigh J., Nioka S. and Maris M., Quantitation of Time- and Frequency-Resolved Optical Spectra for the determination of Tissue Oxygenation, *Anal. Biochem.*, **195**, 330-351 (1991).
  120. Villringer A. and Chance B., Non-invasive optical spectroscopy and imaging of human brain function, *Trends. Neurosci.*, **20**, 435-442 (1997).

121. Hintz S.R., Benaron D.A., Siegel A.M., Zourabian A., Stevenson D.K. and Boas D.A., Bedside functional imaging of the premature infant brain during passive motor activation, *J. Perinat. Med.*, **29**, 335-343 (2001).
122. Nioka S., Moser D., Lech G., Evengelisti M., Verde T., Chance B. and Kuno S., Muscle deoxygenation in aerobic and anaerobic exercise, *Adv. Exp. Med. Biol.*, **454**, 63-70 (1998).
123. Farrell T., Patterson M. and Wilson B.C., A diffuse theory model of spatially resolved, steady-state diffuse reflectance for the noninvasive determination of tissue optical properties *in vivo*, *Med. Phys.*, **19**, 879-888 (1992).
124. Liu H., Boas D.A., Zhang Y., Yodh A.G. and Chance B., Determination of optical properties and blood oxygenation in tissue using continuous NIR light, *Phys. Med. Biol.*, **40**, 1983-1993 (1995).
125. Ramanujam N., Mitchell M.F., Mahadevan A., Warren S., Thomsen S. and Richards-Kortum R.R., *In Vivo* diagnosis of cervical intraepithelial neoplasia (CIN) using 337 nm laser induced fluorescence, *Proc. Natl. Acad. Sci. USA*, **91**, 10193-10197 (1994).
126. Backman V., Gurjar R., Badizadegan K., Itzkan L., Dasari R.R., Perelman L.T. and Feld M.S., Polarized light scattering spectroscopy for quantitative measurement of epithelial cellular structures *in situ*, *IEEE J. Sel. Top. Quant.*, **5**, 1019-1026 (1999).
127. Hanlon E.B., Manoharan R., Koo T.W., Shafer K.E., Motz J.T., Fitzmaurice M., Kramer J.R., Itzkan I., Dasari R.R. and Feld M.S., Prospects for *in vivo* Raman spectroscopy, *Phys. Med. Biol.*, **45**, R1-R59 (2000).

128. Boas D.A., Gaudette T., Strangman G., Cheng X.F., Marota J.J.A and Mandeville J.B., The accuracy of near infrared spectroscopy and imaging during focal changes in cerebral hemodynamics, *Neuroimage*, **13**, 76-90 (2001).
129. Kak A. and Slaney M., *Principles of computerized tomographic imaging*, IEEE Press, New York (1988).
130. Intes X., Ripoll J., Chen Y., Nioka S., Yodh A.G. and Chance B., *In vivo* continuous wave optical breast imaging enhanced by Indocyanine Green, *Med. Phys.* (in press, 2003).
131. Gaudette R., Brooks D., DiMarzio C., Kilmers M., Miller E., Gaudette T. and Boas D.A., A comparison study of linear reconstruction techniques for diffuse optical tomographic imaging of absorption coefficient, *Phys. Med. Biol.*, **45**, 1051-1070 (2000).
132. Engl H., Hanke M. and Neubauer A., *Regularization of inverse problems*, Kluwer Academic Publishers (1996).
133. Ntziachristos V. and Weissleder R., Experimental three-dimensional fluorescence reconstruction of diffuse media by use of a normalized Born approximation, *Opt. Lett.*, **26**, 893-895 (2001).
134. Lee J. and Sevick-Mucara E.M., Fluorescence-enhanced absorption imaging using frequency-domain photon migration: tolerance to measurement error, *J. Biomed. Opt.*, **6**, 58-67 (2001).
135. Boas D.A., Gaudette T.J. and Arridge S.R., Simultaneous imaging and optode calibration with diffuse optical tomography, *Opt. Express*, **8**, 263-270 (2001).
136. Pogue B., McBride T., Prewitt J., Osterberg U. and Paulsen K., Spatially variant regularization improves diffuse optical tomography, *Appl. Opt.*, **38**, 2950-2961 (1999).

137. Hansen P. and O'Leary D., The use of L-curve in the regularization of discrete ill-posed problems, *SIAM J. Sci. Comput.*, **14**, 1487-1503 (1993).
138. Boas D.A., Brooks D.H., Miller E.L., DiMarzio C.A., Kilmer M., Gaudette R.J. and Zhang Q., Imaging the body with diffuse optical tomography, *IEEE Signal Proc. Mag.*, **18**, 57-75 (2001).
139. Tu T., Chen Y., Zhang J., Intes X. and Chance B., Analysis of performance and optimization of frequency-domain near-infrared instruments, *J. Biomed. Opt.*, **7**, 643-649 (2002).
140. Chance B., Cope M., Gratton E., Ramanujam N. and Tromberg B., Phase measurement of light absorption and scatter in human tissue, *Rev. Sci. Instrum.*, **69**, 3457-3481 (1998).
141. Nioka S., Luo Q. and Chance B., Human brain functional imaging with reflectance CWS, *Adv. Exp. Med. Biol.*, **428**, 237-242 (1997).
142. Fantini S., Hueber D., Franceschini M.A., Gratton E., Rosenfeld W., Stubblefield P.G., Maulik D. and Stankovic M.R., Non-invasive optical monitoring of the newborn piglet brain using continuous-wave and frequency-domain spectroscopy, *Phys. Med. Biol.*, **44**, 1543-1563 (1999).
143. Lin Y.Q., Lech G., Nioka S., Intes X. and Chance B., Noninvasive, low-noise, fast imaging of blood volume and deoxygenation changes in muscles using light-emitting diode continuous-wave imager, *Rev. Sci. Instrum.*, **73**, 3065-3074 (2002).
144. Ntziachristos V., Ma X.H. and Chance B., Time-correlated single photon counting imager for simultaneous magnetic resonance and near-infrared mammography, *Rev. Sci. Instrum.*, **69**, 4221-4233 (1998).

145. Hillman E.M.C., Hebden J.C., Schweiger M., Dehghani H., Schmidt F.E.W., Delpy D.T. and Arridge S.R., Time resolved optical tomography of the human forearm, *Phys. Med. Biol.*, **46**, 1117-1130 (2001).
146. Zhou S., Chen Y., Zou Q., Nioka S., Li X., Pfaff L., Cowan C. and Chance B., Portable dual-wavelength amplitude cancellation image system for the determination of human breast tumor, *Proc. Soc. Photo-Opt. Ins.*, **3597**, 571-579 (1999).
147. Liu Q., Chen Y., Chance B. and Luo Q., Handheld Low Frequency Phased Array Near-Infrared Breast Cancer Localizer, *Proc. Soc. Photo-Opt. Ins.* (in press, 2003).
148. Chen Y., Taylor D.R., Intes X. and Chance B., Correlation between near-infrared spectroscopy and magnetic resonance imaging of rat brain oxygenation modulation, *Phys. Med. Biol.*, **48**, 417-427 (2003).
149. Chen Y., Mu C., Intes X. and Chance B., Adaptive calibration for object localization in turbid media with interfering diffuse photon density waves, *Appl. Opt.*, **41**, 7325-7333 (2002).
150. Zhang M., Zhang Z.H., Blessington D., Li H., Busch T.M., Madrak V., Miles J., Chance B., Glickson J.D. and Zheng G., Pyropheophorbide 2-Deoxyglucosamide: a new photosensitizer targeting at glucose transporters, *Bioconjugate Chem.* (in press, 2003).
151. Pauwels E.K., Ribeiro M.J., Stoot J.H., McCready V.R., Bourguignon M. and Maziere B., FDG accumulation and tumor biology, *Nucl. Med. Biol.*, **25**, 317-22 (1998).

152. Chen W.R., Liu H., Yue W., Wang J. and Nordquist R.E., Dynamically observing intratumor injection of laser-absorbing dye and immunoadjuvant using digital x-ray imaging technique, *Opt. Eng.*, **40**, 1249-1254 (2001).
153. Quistorff B. and Chance B., Simple techniques for freeze clamping and for cutting and milling of frozen tissue at low temperature for the purpose of two- or three-dimensional metabolic studies in vivo, *Anal. Biochem.*, **108**, 237-248 (1980).
154. Gu Y., Qian Z., Chen J., Blessington D., Ramanujam N. and Chance B., High-resolution three-dimensional scanning optical image system for intrinsic and extrinsic contrast agents in tissue, *Rev. Sci. Instrum.*, **73**, 172-178 (2002).
155. Pei Y., Graber H. and Barbour R., Normalized-Constraint algorithm for minimizing inter-parameter cross-talk in DC optical tomography, *Opt. Express*, **9**, 97-109 (2001).
156. Culver J., Ntziachristos V., Holboke M. and Yodh A., Optimization of optode arrangements for diffuse optical tomography: a singular-value analysis, *Opt. Lett.*, **26**, 701-703 (2001).
157. Villringer A. and Chance B., Noninvasive optical spectroscopy and imaging of human brain function, *Trends Neurosci.*, **20**, 435-442 (1997).
158. Brazy J.E., Lewis D.V., Mitnick M.H. and Jobsis F.F., Noninvasive monitoring of cerebral oxygenation in pre-term infants: preliminary observations, *Pediatrics*, **75**, 217-225 (1985).
159. Chance B., Zhuang Z., UnAh C., Alter C. and Lipton L., Cognition activated low frequency modulation of light absorption in human brain, *Proc. Natl. Acad. Sci. USA*, **90**, 2660-2774 (1993).

160. Hoshi Y., Onoe H., Wanatabe Y., Anderson J., Bergstrom M., Lilja A., Langstrom B. and Tamura M., Non-synchronous behavior of neuronal activity, oxidative metabolism and blood supply during mental tasks in man, *Neurosci. Lett.*, **172**, 129-133 (1994).
161. Cope M. and Delpy D.T., System for the long-term measurement of cerebral blood and tissue oxygenation on newborn infants by near infrared transillumination, *Med. Biol. Eng. Comput.*, **26**, 289-294 (1988).
162. Chance B., Luo Q., Nioka S., Alsop D.C. and Detre J.A., Optical investigation of physiology: a study of biochemical intrinsic and extrinsic contrast, *Phil. Trans. R. Soc. Lond. B*, **352**, 707-716 (1997).
163. Hintz S.R., Cheong W.F., Van Houten J.P., Stevenson D.K. and Benaron D.A., Bedside imaging of intracranial hemorrhage in the neonate using light: comparison with Ultrasound, Computed Tomography, and Magnetic Resonance Imaging," *Pediatr. Res.*, **45**, 54-59 (1999).
164. Franceschini M.A., Boas D.A., Zourabian A., Diamond S.G., Nadgir S., Lin D.W., Moore J.B. and Fantini S., Near-infrared spirometry: noninvasive measurements of venous saturation in piglets and human subjects, *J. Appl. Physiol.*, **92**, 372-384 (2002).
165. Hueber D.M., Franceschini M.A., Ma H.Y., Zhang Q., Ballesteros J.R., Fantini S., Wallace D., Ntziachristos V. and Chance B., Non-invasive and quantitative near-infrared haemoglobin spectrometry in the piglet brain during hypoxic stress, using a frequency-domain multidistance instrument, *Phys. Med. Biol.*, **46**, 41-62 (2001).
166. Fantini S., Hueber D.M., Franceschini M.A., Gratton E., Resonfeld W., Stubblefield P.G., Maulik D. and Stankovic M.R., Non-invasive optical

- monitoring of the newborn piglet brain using continuous wave and frequency domain spectroscopy, *Phys. Med. Biol.*, **44**, 1543-1563 (1999).
167. Ntziachristos V., Kohl M., Ma H.Y. and Chance B., Oximetry based on diffuse photon density wave differentials, *Med. Phys.*, **27**, 410-421 (2000).
168. Wolf M., Weber O., Keel M., Golay X., Scheidegger M., Bucher H.U., Kollias S., Boesiger P. and Banziger O., Comparison of cerebral blood volume measured by Near Infrared Spectroscopy and contrast enhanced Magnetic Resonance Imaging, *Adv. Exp. Med. Bio.*, **471**, 767-773 (1999).
169. Toronov V., Webb A., Choi J.H., Wolf M., Michalos A., Gratton E. and Hueber D.M., Investigation of human brain hemodynamics by simultaneous Near-Infrared Spectroscopy and functional Magnetic Resonance Imaging, *Med. Phys.*, **28**, 521-527 (2001).
170. Toronov V., Webb A., Choi J.H., Wolf M., Safonova L., Wolf U. and Gratton E., Study of local cerebral hemodynamics by frequency-domain near-infrared spectroscopy and correlation with simultaneously acquired functional magnetic resonance imaging, *Opt. Express*, **9**, 417-427 (2001).
171. Imabayashi E., Ohnishi T., Matsuda H., Kawachi T., Okabe S., Wada Y., Oda I. and Konishi I., fMRI analysis with simultaneous measurements of optical topography during finger tapping, in *8<sup>th</sup> International Conference on Functional Mapping of Human Brain* (Sendai, Japan, 2002).
172. Strangman G., Culver J.P., Thompson J.H. and Boas D.A., A quantitative comparison of simultaneous BOLD fMRI and NIRS recordings during functional brain activation, *Neuroimage*, **17**, 719-731 (2002).
173. Chen Y., Intes X., Taylor D., Regatte R., Ma H., Ntziachristos V., Leigh J., Reddy R. and Chance B., Probing rat brain oxygenation with Near-Infrared

- (NIR) Spectroscopy and Magnetic Resonance Imaging (MRI),” *Adv. Exp. Med. Biol.*, **510**, 199-204 (2003).
174. Dunn J.F., Zaim-Wadghiri Y., Pogue B.W. and Kida I., Bold MRI vs. NIR spectrophotometry - will the best technique come forward? *Adv. Exp. Med. Biol.*, **454**, 103-113 (1998).
175. Ogawa S., Lee T.M., Nayak A.S. and Glynn P., Oxygenation-sensitive contrast in magnetic resonance image of rodent brain at high magnetic fields, *Magnet. Reson. Med.*, **14**, 68-78 (1990).
176. Tailor D.R., *Indirect <sup>17</sup>O Magnetic Resonance Imaging of cerebral blood flow and metabolism*, Dissertation in Bioengineering, University of Pennsylvania (2002).
177. Berne R.M. and Levy M.N. (eds), *Principles of Physiology*, St. Louis, Mosby-Year Book (1996).
178. Logothetis N.K., Pauls J., Augath M., Trinath T. and Oeltermann A., Neurophysiological investigation of the basis of the fMRI signal, *Nature*, **412**, 150-157 (2001).
179. McBride T.O., Pogue B.W., Jiang S.D., Osterberg U.L., Paulsen K.D. and Poplack S.P., Initial studies of *in vivo* absorbing and scattering heterogeneity in near-infrared tomographic breast imaging, *Opt. Lett.*, **26**, 822-824 (2001).
180. Dehghani H., Pogue B.W., Poplack S.P. and Paulsen K.D., Multiwavelength three-dimensional near-infrared tomography of the breast: initial simulation, phantom, and clinical results, *Appl. Opt.*, **42**, 135-145 (2003).
181. Jiang H.B., Iftimia N.V., Xu Y., Eggert J.A., Fajardo L.L. and Klove K.L., Near-infrared optical imaging of the breast with model-based reconstruction, *Acad. Radiol.*, **9**, 186-194 (2002).

182. Colak S.B., van der Mark M.B., Hooft G.W., Hoogenraad J.H., van der Linden E.S. and Kuijpers F.A., Clinical optical tomography and NIR spectroscopy for breast cancer detection, *IEEE J. Sel. Top. Quant.*, **5**, 1143-1158 (1999).
183. Zhu Q., Conant E. and Chance B., Optical imaging as an adjunct to sonograph in differentiating benign from malignant breast lesions, *J. Biomed. Opt.*, **5**, 229-236 (2000).
184. Chen N.G., Guo P.Y., Yan S.K., Piao D.Q. and Zhu Q., Simultaneous near-infrared diffusive light and ultrasound imaging, *Appl. Opt.*, **40**, 6367-6380 (2001).
185. Holboke M.J., Tromberg B.J., Li X., Shah N., Fishkin J., Kidney D., Butler J., Chance B. and Yodh A.G., Three-dimensional diffuse optical mammography with ultrasound localization in a human subject, *J. Biomed. Opt.*, **5**, 237-247 (2000).
186. Ntziachristos V., Tung C.H., Bremer C. and Weissleder R., Fluorescence molecular tomography resolves protease activity *in vivo*, *Nat. Med.*, **8**, 757-760 (2002).
187. Weissleder R. and Ntziachristos V., Shedding light onto live molecular targets, *Nat. Med.*, **9**, 123-128 (2003).
188. Chan W.C.W., Maxwell D.J., Gao X.H., Bailey R.E., Han M.Y. and Nie S.M., Luminescent quantum dots for multiplexed biological detection and imaging, *Curr. Opin. Biotech.*, **13**, 40-46 (2002).
189. Ntziachristos V. and Weissleder R., Charge-coupled-device based scanner for tomography of fluorescent near-infrared probes in turbid media, *Med. Phys.*, **29**, 803-809 (2002).

190. Ntziachristos V., Ripoll J. and Weissleder R., Would near-infrared fluorescence signals propagate through large human organs for clinical studies? *Opt. Lett.*, **27**, 333-335 (2002).
191. Eppstein M.J., Hawrysz D.J., Godavarty A. and Sevick-Muraca E.M., Three-dimensional, Bayesian image reconstruction from sparse and noisy data sets: near-infrared fluorescence tomography, *Proc. Natl. Acad. Sci. USA*, **99**, 9619-9624 (2002).
192. Jain R.K., Delivery of molecular and cellular medicine to solid tumors, *Adv. Drug Deliver. Rev.*, **46**, 149-168 (2001).
193. Hebden J.C., Gibson A., Yusof R.M., Everdell N., Hillman E.M.C., Delpy D.T., Arridge S.R., Austin T., Meek J.H. and Wyatt J.S., Three-dimensional optical tomography of the premature infant brain, *Phys. Med. Biol.*, **47**, 4155-4166 (2002).
194. Yaroslavsky A.N., Schulze P.C., Yaroslavsky I.V., Schober R., Ulrich F. and Schwarzmaier H.J., Optical properties of selected native and coagulated human brain tissues *in vitro* in the visible and near infrared spectral range, *Phys. Med. Biol.*, **47**, 2059-2073 (2002).
195. Contini D., Martelli F. and Zaccanti G., Photon migration through a turbid slab described by a model based on diffusion approximation. I. Theory, *Appl. Opt.*, **36**, 4587-4599 (1997).
196. Brukilacchio T.J., Zhang Q., Stott J., Li A., Boas D.A., Wu T., Moore R.H. and Kopans D.B., Instrumentation for imaging of breast lesions based on co-registered diffuse optical and X-ray tomography, *in OSA Biomedical Topical Meetings, OSA Technical Digest*, 178-180 (Optical Society of America, Washington DC, 2002).

197. Ohmae E., Ouchi Y., Oda M., Suzuki T., Nobesawa S., Kannno T., Yoshikawa E., Futatsubashi M., Okada H. and Yamashita Y., Assessment of light sampling depth in Near-infrared Spectroscopy: Correlation with simultaneous PET measurements, in *Proceedings of Asian Symposium on Biomedical Optics and Photomedicine*, 190-191 (Sapporo, Japan, 2002).
198. Cheung C., Culver J.P., Takahashi K., Greenberg J.H. and Yodh A.G., *In vivo* cerebrovascular measurement combining diffuse near-infrared absorption and correlation spectroscopies, *Phys. Med. Biol.*, **46**, 2053-2065 (2001).
199. Culver J.P., Furuya D., Durduran T., Cheung C, Greenberg J.H. and Yodh A.G., Diffuse optical measurement of hemoglobin and cerebral blood flow in rat brain during hypercapnia, hypoxia and cardiac arrest, *Adv. Exp. Med. Biol.*, **510**, 293-298 (2003).
200. Yu G., Durduran T., Furuya D., Greenberg J. and Yodh A.G., Frequency domain multiplexing system for *in vivo* diffuse light measurements of rapid cerebral hemodynamics, *Appl. Opt.* (in press, 2003).
201. Culver J.P., Furuya D., Durduran T., Cheung C., Greenberg J.H. and Yodh A.G., Diffuse optical tomography of cerebral blood flow, oxygenation and metabolism in rat during focal ischemia, *J. Cerebr. Blood F. Met.* (in press, 2003).